12-2017

Evaluation of a Semi-Analytical/Numerical Method for Modeling Matrix Diffusion Effects in Groundwater Chemical Transport

Noelia Susana Muskus Ruiz
Clemson University

EVALUATION OF A SEMI-ANALYTICAL/NUMERICAL METHOD FOR MODELING MATRIX DIFFUSION EFFECTS IN GROUNDWATER CHEMICAL TRANSPORT

A Thesis
Presented to
the Graduate School of
Clemson University

In Partial Fulfillment
of the Requirements for the Degree
Master of Science
Environmental Engineering and Science

---

by
Noelia Susana Muskus Ruiz
December 2017

Accepted by:
Dr. Ronald Falta, Committee Chair
Dr. David Freedman
Dr. Lawrence Murdoch

ABSTRACT

Secondary sources of contamination, such as dissolved chemicals in low permeability zones result in plume persistence and limitations for plume remediation as a consequence of the process of matrix diffusion (Mackay and Cherry, 1989; Chapman and Parker, 2005). Existing numerical transport simulators are capable of modeling matrix diffusion; however, they require fine discretization, resulting in large computational effort. An alternative approach was developed combining numerical and analytical modeling to simulate matrix diffusion effects. The semi-analytical/numerical (referred to as semi-analytical for short) approach used here was adapted from geothermal reservoir modeling of transient heat conduction in low permeability cap rocks (Vinsome and Westerveld, 1980). The semi-analytical method discretizes the high permeability parts of the aquifer in the numerical model and the matrix diffusion flux is approximated at the sub-grid scale without modifying the grid.

The objective of this research is to test the semi-analytical method for the simulation of matrix diffusion effects in groundwater transport. To achieve this goal the semi-analytical method was used to simulate laboratory-scale studies and the results were compared to experimental data. In addition, various test scenarios representing heterogeneous environments were developed and compared to results from a commercial numerical simulator.

Two implementations of the matrix diffusion analysis were tested in this research. Initially, a Visual Basic program in Excel® was compared to experimental results from two published studies from University of Florida and Colorado State University. Results

from the Visual Basic code were also compared to fine-grid numerical simulations of two-layer systems. A FORTRAN version of this program, called REMChlor-MD was evaluated by comparing to results from large fine-grid numerical models (approximately 3 million gridblocks) with highly heterogeneous material distributions.

The results indicate that the semi-analytical method matches both experimental data and fine grid numerical simulations, even for systems with highly complex heterogeneities. Besides the visual comparison, coefficients of determination were estimated for the cases studied, obtaining values from 0.724 to 0.998, demonstrating good accuracy of the matrix diffusion semi-analytical method for most practical purposes. The semi-analytical model is highly efficient, requiring only a fraction (approximately 1/10000) of the run times of the fine grid numerical simulations used as comparison basis.

This evaluation is one of the stages of the project funded by the DoD's Environmental Security Technology Certification Program (ESTCP) and supported in part by the Department of Energy. The project aims to develop and implement a new generation of the screening level transport model REMChlor that considers matrix diffusion in the plume: REMChlor-MD.

DEDICATION

In memory of Fabiola Mercado, you were the best godmother and sister I could have ever asked for. You will always be remembered and loved.

To my mom Alicia, my uncle Alfredo, and my sisters Diana and Mafe: *gracias por su amor incondicional y apoyo en mis decisiones; aunque éstas me hayan llevado a kilómetros de distancia, siempre los llevo en mi corazón, los amo*. To my other half, Chip: Thank you for being with me every step of the way and always having my back; I truly found my home away from home in you. To my wonderful friends from Colombia and Clemson: Thank you for always making time for me and having words of encouragement when needed.

ACKNOWLEDGMENTS

First and foremost, I want to thank my advisor Dr. Ron Falta for believing in me and giving me the opportunity and financial support to work on his project. I am gratefully indebted for his boundless guidance and patience. Dr. Falta was always available and willing to share his knowledge whenever I ran into an issue or had a question about the research or my writing. For that and more I feel extremely lucky to have had him as my advisor.

I want to express gratitude to my committee members, Dr. Lawrence Murdoch and Dr. David Freedman, for their guidance and valuable comments on this thesis work. I would also like to thank my fellow classmates and research group mates, especially to Kien Pham for his cooperation throughout this past year and helping me see aspects of the research that I might have otherwise missed.

Many thanks to Dr. James Jawitz and Dr. Minjune Yang at University of Florida for kindly sharing their research results with us, providing the comparison basis for our initial simulations. I would also like to acknowledge the United States Department of Defense through the Environmental Security Technology Certification Program (ESTCP) for providing the funding to carry out this research.

TABLE OF CONTENTS

Page

Table of Contents (continued)

Page

LIST OF TABLES

Page

List of Tables (continued)

Page

LIST OF FIGURES

Page

List of Figures (continued)

Page

List of Figures (continued)

Page

List of Figures (continued)

Page

List of Figures (continued)

Page

List of Figures (continued)

Page

List of Figures (continued)

Page

List of Figures (continued)

Page

List of Figures (continued)

Page

List of Figures (continued)

Page

List of Figures (continued)

Page

List of Figures (continued)

Page

List of Figures (continued)

Page

1. INTRODUCTION

Groundwater represents the largest and most important source of fresh potable water in the world (Howard and Gelo, 2002). More than half of the population relies on groundwater as a source for drinking water (Solley et al., 1998). Thus, the quality of groundwater is a matter of great significance (Fetter, 2008). Organic contaminants are the most common chemicals detected in groundwater with health threatening properties, with industrial solvents and aromatic hydrocarbons from petroleum products being the most common (Mackay and Cherry, 1989). The causes of groundwater contamination of this type are attributed largely to leakage, spillage, or disposal of organic liquids immiscible with water (nonaqueous-phase liquids, NAPLs) into the ground (Mackay and Cherry, 1989; Pankow and Cherry, 1996).

NAPLs are divided into two classes depending to whether they are more or less dense than water: light NAPLs (LNAPLs, i.e. gasoline) have a specific gravity less than one and float on water. Conversely, dense NAPLs (DNAPLs) such as trichloroethylene, sink through water. (National Research Council, 1994; Domenico and Schwartz, 1998).

To an important extent, the complexity of a contamination problem is determined by whether NAPLs are present because contaminants can be distributed among different phases. Following a NAPL spill, the liquid will move mainly downward due to a density-driven flow. The NAPL may dissolve into pore water, volatilize into air in the pores or remain as a residual liquid trapped within the pores. Lateral spreading is also possible due to capillary forces, vapor phase migration, and the presence of heterogeneities. After reaching the water table, NAPLs will behave differently due to the difference in density.

LNAPLs will float at the water table and flow primarily downgradient. Upon contact with the water table, there is dissolution of the DNAPL and subsequent transport of the dissolved chemicals (such as VOCs), forming a contaminant plume that flows predominantly in the horizontal direction. The remainder of DNAPL has the ability to move downward to the base of the aquifer, leaving a trail of liquid at residual saturation. Relatively impermeable materials (such as clay lenses) promote lateral spreading and DNAPL pool formation. The DNAPL present as an entrapped residual fluid or "pooled" on low permeability areas also dissolves into groundwater contributing to the existing plume. Therefore, DNAPLs can become significant subsurface sources of secondary contamination (Mackay and Cherry, 1989; National Research Council, 1994; Domenico and Schwartz, 1998). This situation only aggravates when the matrix diffusion effects are considered.

A large number of contaminated sites were being addressed by pump-and-treat systems in the 1980s (Hadley and Newell, 2014). By the end of the decade some issues appeared, such as removing a substantial amount of contaminant mass higher than initially estimated or contamination levels bouncing back after extraction completion (Travis and Doty, 1990). The inefficiency to completely remediate the contaminated sites by pump-and-treat systems led to a discussion and research about possible causes and solutions. The first journal article describing matrix diffusion as a contaminant transport process appeared years before in 1975, authored by Stephen Foster: "The Chalk Groundwater Tritium Anomaly—A Possible Explanation" (Foster, 1975; Hadley and Newell, 2014). Multiple projects followed (Goodall and Quigley, 1977; Gillham et al., 1984; Sudicky et al., 1985) until the scientific community recognized that low permeability zones act as contaminant

sinks first to later serve as contaminant sources to transmissive zones with flowing groundwater due to matrix diffusion (Mackay and Cherry, 1989; Chapman and Parker, 2005; Falta, 2005; Seyedabbasi et al., 2012).

Matrix diffusion is the process of mass transfer of solutes between high permeability zones and surrounding low permeability zones due to a concentration gradient. This process is known as forward diffusion when the transport is from high to low permeability zones. Forward diffusion takes place during a "loading period", usually when contaminants reach the aquifer. After the contaminant source has been removed, the concentration gradient reverses and diffusion goes from low to high permeability zones, resulting in back diffusion (Liu and Ball, 2002; Chapman and Parker, 2005; Falta, 2005; Parker et al., 2008; Sale et al., 2008; Falta and Wang, 2017).

Back diffusion of contaminants from low permeability areas can result in plume persistence and limitations in remediation efforts (Chapman and Parker, 2005; Rasa et al., 2011; Seyedabbasi et al., 2012; Yang et al., 2014). There are analytical solutions available to model matrix diffusion (Tang et al., 1981; Sudicky and Frind, 1982; Liu and Ball, 2002; Sale et al., 2008; Yang et al., 2015); however, they are constrained to simple geometries corresponding to ideal cases (Falta and Wang, 2017). Numerical simulations studies of matrix diffusion (Chapman and Parker, 2005; Parker et al., 2008; Rasa et al., 2011; Chapman et al., 2012; Chapman and Parker, 2013) have shown the ability to reproduce the transient matrix diffusion effects. Nevertheless, very fine discretization is required in order to reproduce the diffusive fluxes at the high permeability/low permeability interfaces, usually controlled by concentration gradients in the scale of centimeters to millimeters.

High resolution grids result in large computational effort (Pruess and Wu, 1988; Chapman et al., 2012; Falta and Wang, 2017).

A lot of research projects have focused on matrix diffusion as a contaminant source, its effects and modeling efforts. Ball et al. (1997) conducted extensive studies at the Dover Air Force Base in Delaware, using independent estimates of sorption and diffusion properties in the aquitard layers and mathematical modeling based on diffusion in laminate slabs to deduce the arrival of the plume and historical concentration in the overlying aquifer. Also at the Dover Air Force Base, Liu and Ball (2002) used core samples over time to validate an analytical model to predict concentration profiles at the site, considering matrix diffusion effects. Chapman and Parker (2005) carried out a study at an industrial site in Connecticut, where a DNAPL source isolation was performed in a sand aquifer overlying a clayey silt aquitard. Groundwater and core sampling, together with numerical modeling of site conditions allowed them to show that the distribution of TCE in the aquifer is explained by vertical back diffusion from the aquitard combined with advection and dispersion in the transmissive zone. They also concluded that the impact of back diffusion in the aquifer TCE concentration was such that it would remain above the MCL for centuries.

Sale et al. (2008) studied how reductions in loading of contaminants to plumes affect downgradient water quality by conducting a set of laboratory experiments for an idealized two-layer scenario. At the same time, an analytical solution was developed and tested with the experimental data, obtaining satisfactory results (Sale et al., 2008). Parker and Chapman (2008) carried out a field study of a contaminated site in Florida, isolating the

contaminant source and monitoring the downgradient area groundwater quality. The site was modeled using a fine grid numerical model and matrix diffusion was found to be the cause of contaminant persistence in the aquifer after source isolation.

Chapman et al. (2012) performed a test of high resolution numerical simulations of matrix diffusion effects using three different models: HydroGeosphere (Brunner and Simmons, 2012), FEFLOW (Trefry and Muffels, 2007), and MT3DMS (Zheng and Wang, 1999), and obtaining close match to experimental data from a lab scale sandbox study. Seyedabbasi et al. (2012) used a hypothetical DNAPL source zone architecture with different size pools and fingers and a defined low permeability layer below each pool to investigate the relative contribution of DNAPL dissolution versus matrix diffusion processes to the longevity of chlorinated source zones. Several analytical models were used to describe the resulting source attenuation curves and the results showed that matrix diffusion has the potential of becoming an important factor in the persistence of contamination sources and it might play a higher role than DNAPL dissolution alone.

More recently, Chapman and Parker (2013) developed a set of hypothetical two-dimensional numerical simulations in order to determine if popular numerical groundwater models can match an analytical solution. Additional numerical simulations were performed for different scenarios representative of real life conditions, including both porous media and fractured rock configurations to demonstrate effects of mass storage and release for “type site” conditions. Comparison with experimental data was also performed. For most cases, the numerical models matched well with the analytical solutions and experimental data, but required very fine temporal and spatial discretization. The “type

site" simulations showed that long-term persistence of the plume takes place after the source removal, due to slow back diffusion of mass stored in low permeability zones. The effect of sorption and degradation in low permeability zones was assessed, finding that higher sorption increases the storage capacity and rates of forward and back diffusion, leading to longer-term tailing. It was also found that even very slow degradation rates can have substantial impact on plume attenuation. Chapman and Parker (2013) limited their study to a two-dimensional domain due to computational limitations caused by very fine spatial and temporal discretization. At the time of this research work, there are no three-dimensional studies about matrix diffusion effects to the extent of the author's knowledge

Yang et al. (2015) carried out a series of laboratory experiments in a two-dimensional flow chamber to calculate solute diffusion from sand into and out of thin clay layers. One dimensional analytical solutions were developed for diffusion in a finite aquitard with mass transfer with an adjacent aquifer using the method of images, obtaining very good agreement with measured breakthrough curves and aquitard concentration distributions.

A different modeling approach combines analytical and numerical modeling. This method was developed in petroleum reservoir engineering to calculate heat conductive flux from a permeable reservoir to an impermeable caprock. Additionally, it has been successfully used in fractured reservoir configurations. The semi-analytical method discretizes only the high permeability parts of the aquifer in the numerical model, and the heat conduction flux is treated as a temperature dependent source/sink term calculated analytically in each gridblock at every time step (Vinsome and Westerveld, 1980; Pruess and Wu, 1988; Pruess and Wu, 1993). This semi-analytical method was adapted to the

matrix diffusion process given that the matrix diffusion equations and heat conduction equations are analogous (Bear et al., 1994; Wang, 2014; Falta and Wang, 2017). Wang (2014) and Falta and Wang (2017) implemented the matrix diffusion semi-analytical method for the case of an aquifer in contact with a thick aquitard and verified its accuracy with analytical solutions obtaining excellent results.

The purpose of this project is to further evaluate the matrix diffusion semi-analytical model with experimental results and fine grid numerical simulations for cases where there are local embedded low permeability zones in the aquifer. In Chapters 4 and 5 of this document, the Visual Basic version of the semi-analytical method was used to model previously published laboratory-scale experiments. For Chapters 6 and 7, different scenarios were created to test the FORTRAN version of the semi-analytical method against numerical simulations, from ideal layered setups to complex heterogeneous systems, obtaining good-to-excellent results (R^2 = 0.849 -0. 998).

2. SEMI-ANALYTICAL METHOD DESCRIPTION

This chapter presents the explanation of the conventional heat conduction semi-analytical method and the implementation to the matrix diffusion process for the case of finite heterogeneities embedded in the high permeability material, which works under the assumption of a well-mixed high *k* material zone.

2.1. Vinsome and Westerveld heat conduction method

Oil recovery schemes use steam and hot water injection as common practices to enhance the recovery from permeable oil reservoirs. The conductive transfer of heat from the reservoir into adjacent low permeability zones represents heat loss that can become large, affecting process economics. An accurate numerical model of thermal recovery must include the heat exchange with impermeable areas, discretizing them alongside the reservoir. Thus, the number of gridblocks grows considerably, leading to increasing simulation run times. A simple semi-analytical approximation for the heat conduction losses replaces the discretization of the confining bed with a temperature dependent heat source/sink term added only to the gridblocks adjacent to confining units (Vinsome and Westerveld, 1980; Pruess and Wu, 1988).

Vinsome and Westerveld (1980) recognized that the process of heat conduction in confining units is mainly one-directional. The semi-analytical method represents the temperature profile in the confining beds with a trial function that is updated at every time step:

$$T_l(z_l, t) = (T^{t+\Delta t} + pz_l + qz_l^2)e^{-z_l/d} \quad (1)$$

where z_l (m) is the distance into the low permeability material, $T^{t+\Delta t}$ (ºC) is the current temperature at the interface between the reservoir and confining bed, and d (m) is the time dependent thermal penetration depth, described by:

$$d = \frac{\sqrt{\kappa_h t}}{2} \quad ; \quad \kappa_h = \frac{k_h}{\rho C_r} \tag{2}$$

where κ_h (m^2/s) is the thermal diffusivity, k_h (W/m-ºC) is the thermal conductivity, ρ (kg/m^3) is the density and C_r (J/kg-ºC) is the heat capacity.

The parameters p (ºC/m) and q (ºC/m^2) are time dependent fitting parameters determined by two energy balance constraints. The first one is that the partial differential equation for heat conduction must be satisfied at the interface between the reservoir and caprock:

$$\rho C_r \frac{\partial T}{\partial t} = k_h \frac{\partial^2 T}{\partial z_l^2}\bigg|_{z_l=0} \tag{3}$$

The second constraint requires that the rate of change of energy in the low permeability material must equal the conductive heat flux across the interface:

$$\frac{\partial}{\partial t}\int_0^\infty \rho C_r T dz_l = -k_h \frac{\partial T}{\partial z_l}\bigg|_{z_l=0} \tag{4}$$

The parameters p and q are calculated at each time step for every gridblock adjacent to a low permeability material. The conductive heat flux across the reservoir/caprock interface, F_h (W/m^2), is defined by Fourier's Law, substituting for the temperature with the fitting function in Equation 1:

$$F_h = -k_h \frac{\partial T}{\partial z_l}\bigg|_{z_l=0} = k_h\left(\frac{T^{t+\Delta t}}{d} - p\right) \tag{5}$$

Therefore, the heat flux is treated as a temperature dependent source/sink term in gridblocks at the interface with the caprock. This method reduces the computational work needed to model heat conduction in and out of low permeability zones by simulating the conductive response in confining units, eliminating the need to discretize them.

2.2. Matrix diffusion method

The governing equation for matrix diffusion is analogous to the heat conduction partial differential equation (Equation 3), with the exception of a first order decay term included in the matrix diffusion equation. The governing one-dimensional matrix diffusion equation assuming decay only in the aqueous phase is:

$$R_l \frac{\partial C_l}{\partial t} = \tau_l D \frac{\partial^2 C_l}{\partial z_l^2} - \lambda_l C_l \tag{6}$$

The subscript l refers to the low permeability material. C_l (kg/m^3) is the aqueous concentration, R_l is the retardation factor, τ_l is the tortuosity, D (m^2/s) is the molecular diffusion coefficient, and λ_l (s^{-1}) is the first order decay rate.

Bear et al. (1994) and Falta and Wang (2017) use a fitting function from Vinsome and Westerveld (1980) adapted to the concentration in the low permeability zones:

$$C_l(z_l, t) = (C^{t+\Delta t} + pz_l + qz_l^2) e^{-z_l/d} \tag{7}$$

where $C^{t+\Delta t}$ (kg/m^3) is the current concentration at the interface between high permeability and low permeability zones. The concentration penetration depth, d (m), is defined by:

$$d = \frac{\sqrt{\kappa_l t}}{2} \quad ; \quad \kappa_l = \frac{\tau_l D}{R_l} \tag{8}$$

The zero level of the concentrations in Equation 7 correspond to the initial (uniform) concentration in the low permeability zone, which is usually zero. The fitting parameters p (kg/m^4) and q (kg/m^5) are determined by two conservation of mass laws. The first constraint requires the fitting function to satisfy the governing equation at the high permeability/low permeability interface (Falta and Wang, 2017):

$$R_l \frac{\partial C_l}{\partial t} = \tau_l D \left. \frac{\partial^2 C_l}{\partial z_l^2} \right|_{z_l=0} - \lambda_l C_l|_{z_l=0} \tag{9}$$

In order to discretize the equation, a first-order finite difference approximation is applied to the time derivative. C_l is replaced with the trial function on the right hand side, which results in:

$$R_l \left(\frac{C^{t+\Delta t} - C^t}{\Delta t} \right) = \tau_l D \left(\frac{C^{t+\Delta t}}{d^2} - \frac{2p}{d} + 2q \right) - \lambda_l C^{t+\Delta t} \tag{10}$$

The second constraint is the mass conservation in the low permeability material, and requires the rate of change of total mass in the matrix to equal the mass flux across the interface minus the rate of decay in the matrix. For an ideal infinite aquitard case, the integral of distance into low permeability areas is defined from zero to infinity (Falta and Wang, 2017):

$$R_l \frac{\partial}{\partial t} \int_0^\infty C_l dz_l = -\tau_l D \left. \frac{\partial C_l}{\partial z_l} \right|_{z_l=0} - \lambda_l \int_0^\infty C_l dz_l \tag{11}$$

This research project deals with finite heterogeneities, such as low permeability lenses or layers. Thus, the mass conservation constraint must account for a finite diffusion distance. The characteristic average diffusion length, L (m) corresponds to the depth or

vertical distance of diffusion into the low permeability material. The second constraint becomes:

$$R_l \frac{\partial}{\partial t} \int_0^L C_l dz_l = -\tau_l D \left. \frac{\partial C_l}{\partial z_l} \right|_{z_l=0} - \lambda_l \int_0^L C_l dz_l \tag{12}$$

The solution of the concentration integral in Equation 12 using the trial function is:

$$I(t) = \int_0^L C_l dz_l = C(t)d + pd^2 + 2qd^3 - (C(t)d + pdL + pd^2 + qL^2 d + 2qd^2 L + 2qd^3)e^{-L/d} \tag{13}$$

Following Pruess and Wu (1988, 1993), this can be written as a weighted function of *C(t)*, *p*, and *q*:

$$I(t) = \delta C(t) + \gamma p + \beta q \tag{14}$$

where

$$\delta = d - de^{-L/d} \tag{15}$$

$$\gamma = d^2 - (dL + d^2)e^{-L/d} \tag{16}$$

$$\beta = 2d^3 - (L^2 d + 2d^2 L + 2d^3)e^{-L/d} \tag{17}$$

For the special case of an ideal infinite aquitard, where $L \rightarrow \infty$:

$$\delta = d \quad ; \quad \gamma = d^2 \quad ; \quad \beta = 2d^3$$

corresponding to the definition of *I(t)* in Falta and Wang (2017). Replacing the derivative in Equation 12 with a finite difference approximation of the concentration integral, and substituting C_l with the fitting function in the space derivative and decay term gives:

$$R_l \left(\frac{\delta C^{t+\Delta t} + \gamma p + \beta q - I^t}{\Delta t} \right) = \tau_l D \left(\frac{C^{t+\Delta t}}{d} - p \right) - \lambda_l (\delta C^{t+\Delta t} + \gamma p + \beta q) \tag{18}$$

Solving Equation 10 for *q*:

$$q = \frac{R_l}{2\tau_l D}\left(\frac{C^{t+\Delta t} - C^t}{\Delta t}\right) - \frac{C^{t+\Delta t}}{2d^2} + \frac{p}{d} + \frac{\lambda_l C^{t+\Delta t}}{2\tau_l D} \tag{19}$$

Multiplying by $2d^2/2d^2$ and rearranging:

$$q = \frac{\frac{(C^{t+\Delta t} - C^t)d^2}{\kappa_l \Delta t} - C^{t+\Delta t} + 2dp + \frac{\lambda_l C^{t+\Delta t} d^2}{R_l \kappa_l}}{2d^2} \tag{20}$$

Which is the same expression for q for the infinite aquitard case (Falta and Wang, 2017). Rearranging Equation 18:

$$\delta C^{t+\Delta t} + \gamma p + \beta q - I^t = \kappa_l \Delta t\left(\frac{C^{t+\Delta t}}{d} - p\right) - \frac{\lambda_l \Delta t}{R_l}(\delta C^{t+\Delta t} + \gamma p + \beta q) \tag{21}$$

$$\left(\beta + \frac{\lambda_l \Delta t}{R_l}\beta\right) q + \left(\gamma + \kappa_l \Delta t + \frac{\lambda_l \Delta t}{R_l}\gamma\right) p + \left(\delta - \frac{\kappa_l \Delta t}{d} + \frac{\lambda_l \Delta t}{R_l}\delta\right) C^{t+\Delta t} = I^t \tag{22}$$

Let:

$$A = \beta + \frac{\lambda_l \Delta t}{R_l}\beta \tag{23}$$

$$B = \gamma + \kappa_l \Delta t + \frac{\lambda_l \Delta t}{R_l}\gamma \tag{24}$$

$$E = \delta - \frac{\kappa_l \Delta t}{d} + \frac{\lambda_l \Delta t}{R_l}\delta \tag{25}$$

Then Equation 22 can be written as:

$$Aq + Bp + EC^{t+\Delta t} = I^t \tag{26}$$

Substituting the expression for q (Equation 19) in Equation 26:

$$A\left(\frac{(C^{t+\Delta t} - C^t)}{2\kappa_l \Delta t} - \frac{C^{t+\Delta t}}{2d^2} + \frac{p}{d} + \frac{\lambda_l C^{t+\Delta t}}{2R_l \kappa_l}\right) + Bp + EC^{t+\Delta t} = I^t \tag{27}$$

Rearranging:

$$\left(\frac{A}{d}+B\right)p = I^t - EC^{t+\Delta t} - \frac{A(C^{t+\Delta t}-C^t)}{2\kappa_l \Delta t} + \frac{AC^{t+\Delta t}}{2d^2} - \frac{A\lambda_l C^{t+\Delta t}}{2R_l\kappa_l} \quad (28)$$

Solving for *p*:

$$p = \frac{I^t - EC^{t+\Delta t} - A\left(\frac{C^{t+\Delta t}-C^t}{2\kappa_l \Delta t} - \frac{C^{t+\Delta t}}{2d^2} + \frac{\lambda_l C^{t+\Delta t}}{2R_l\kappa_l}\right)}{\frac{A}{d}+B} \quad (29)$$

Unique values of *p* and *q* are calculated in the aquifer gridblocks containing low permeability zones, and they are updated at each time step to represent the changing concentration profile in the low permeability zones. The concentration integral *I(t)* is recalculated at every time step in every gridblock using Equation 14 and it is stored for use in the next time step (I^t). This results in a nearly perfect mass balance.

2.2.1. Matrix diffusion mass flow

The matrix diffusion mass flow entering (+) or leaving (-) the high permeability zone is described by Fick's first law of diffusion. Substituting the low permeability material concentration by the trial function:

$$\dot{m} = A_{md}\phi_l\tau_l D\left.\frac{\partial C_l}{\partial z_l}\right|_{z_l=0} = A_{md}\phi_l\tau_l D\left(-\frac{C^{t+\Delta t}}{d}+p\right) \quad (30)$$

where ϕ_l is the porosity of the low permeability material and A_{md} (m^2) is the matrix diffusion area, defined as the interfacial area between the high permeability and low permeability zones. The equation for *p* can be rewritten as:

$$p = aC^{t+\Delta t} + b \quad (31)$$

With

$$a = \frac{-E - \frac{A}{2\kappa_l \Delta t} + \frac{A}{2d^2} - \frac{A\lambda_l}{2R_l\kappa_l}}{\frac{A}{d} + B} \tag{32}$$

$$b = \frac{I^t + \frac{AC^t}{2\kappa_l \Delta t}}{\frac{A}{d} + B} \tag{33}$$

And the expression for the mass rate, $\dot{m}$ (kg/s), turns into:

$$\dot{m} = A_{md}\phi_l\tau_l D\left(\left(a - \frac{1}{d}\right)C^{t+\Delta t} + b\right) \tag{34}$$

The matrix diffusion mass flow becomes a concentration-dependent source/sink term added in the numerical transport model gridblocks that contain low permeability materials.

2.2.2. Numerical formulation

The integral finite difference mass balance equation (Narasimhan and Witherspoon, 1976) for an element *i* is given in Equation 35. Only transmissive zones are considered due to the working assumptions of the semi-analytical method.

$$V_i \frac{dM_i}{dt} = \sum_j F_{ij}A_{ij} + Q_i \tag{35}$$

where

$$M_i = mass\ of\ contaminant\ per\ unit\ volume$$

$$F_{ij} = mass\ flux\ entering\ i\ from\ neighbouring\ elements\ j$$

$$A_{ij} = interfacial\ area\ between\ i\ and\ j$$

$$Q_i = source/sink\ term\ in\ element\ i\ (mass/time)$$

The mass term in the high permeability material is (Falta and Wang, 2017):

$$M = \phi RC \tag{36}$$

Here, ϕ is the porosity of the high permeability material, and R is the solute retardation factor in the high permeability material.

The right-hand side in the mass balance expression corresponds to the accumulation of mass. Following the conventional approach for numerical modeling, the sum of mass fluxes includes advection and hydrodynamic dispersion (Freeze and Cherry, 1979; Fetter, 2008), and the internal source/sink term includes reactions. With the semi-analytical approach, diffusion is included in the source/sink term as a mass rate and not in the sum of fluxes, like in traditional numerical modeling. Therefore, the internal source/sink term also includes the matrix diffusion mass flow when element i is adjacent to or includes low permeability materials (Falta and Wang, 2017).

Following Falta and Wang (2017), the transport equation using the semi-analytical approach was expressed for a three-dimensional system, using Cartesian coordinates. The system assumes uniform groundwater flow in the horizontal direction and dispersion in all three directions (i, j, k). Additional conditions included first-order decay in the aqueous phase in the high permeability zone, and matrix diffusion with decay in low permeability zones. A uniform grid with spacing of Δx, Δy, and Δz was used, along with a finite difference approximation for the concentration gradients in the dispersive fluxes, and upstream weighting for the advective term. Under these conditions, the transport equation with a fully implicit formulation is equal to:

$$\begin{aligned}\Delta x\Delta y\Delta z\phi R\left(\frac{C_{i,j,k}^{t+\Delta t}-C_{i,j,k}^{t}}{\Delta t}\right) &= v_x\Delta y\Delta z\left(C_{i-1,j,k}^{t+\Delta t}-C_{i,j,k}^{t+\Delta t}\right)\\ &+\frac{\phi D_x\Delta y\Delta z}{\Delta x}\left(C_{i-1,j,k}^{t+\Delta t}-2C_{i,j,k}^{t+\Delta t}+C_{i+1,j,k}^{t+\Delta t}\right)\\ &+\frac{\phi D_y\Delta x\Delta z}{\Delta y}\left(C_{i,j-1,k}^{t+\Delta t}-2C_{i,j,k}^{t+\Delta t}+C_{i,j+1,k}^{t+\Delta t}\right)\\ &+\frac{\phi D_z\Delta x\Delta y}{\Delta z}\left(C_{i,j,k-1}^{t+\Delta t}-2C_{i,j,k}^{t+\Delta t}+C_{i,j,k+1}^{t+\Delta t}\right)\\ &-\Delta x\Delta y\Delta z\phi\lambda C_{i,j,k}^{t+\Delta t}\\ &+A_{md,i,j,k}\phi_l\tau_l D\left(\left(a-\frac{1}{d}\right)C_{i,j,k}^{t+\Delta t}+b_{i,j,k}^{t}\right)\end{aligned} \tag{37}$$

where

$$v_x = Darcy\ velocity\ in\ the\ x\ direction$$

$$D_x = horizontal\ dispersion\ coefficient$$

$$D_y = transverse\ dispersion\ coefficient$$

$$D_z = vertical\ dispersion\ coefficient$$

$$\lambda = aqueous\ decay\ rate\ in\ high\ k\ material$$

As defined before, the last term in Equation 37 contains the matrix diffusion flux into or out of the high permeability material, multiplied by the interfacial matrix diffusion area to convert to mass rate units. The matrix diffusion term is only applicable to the gridblocks adjacent to or containing low permeability materials. Equation 37 produces a simultaneous system of linear algebraic equations with only one unknown, $C^{t+\Delta t}$. REMChlor-MD uses a Gauss Siedel iterative method to solve the resulting system of equations (Falta and Wang, 2017).

3. RESEARCH OBJECTIVES

The main goal of this investigation is to evaluate the ability of the semi-analytical method to simulate matrix diffusion effects in groundwater chemical transport for finite embedded heterogeneity scenarios. The specific objectives are:

- Apply the matrix diffusion application of the semi-analytical method (Visual Basic version) to model existing laboratory-scale flow chamber studies of layered and heterogeneous systems and test the accuracy of the method to reproduce the experimental results.
- Design and develop different test scenarios of transport of chlorinated volatile organic compounds (CVOCs) in layered and heterogeneous settings to provide a basis for comparison.
- Run fine-grid flow field and chemical transport simulations of the test scenarios using the numerical simulator MT3DMS (Zheng and Wang, 1999).
- Model the test scenarios with the FORTRAN version of the semi-analytical method and assess its ability to match the results from fine-grid numerical simulations.

4. SEMI-ANALYTICAL SIMULATION OF MATRIX DIFFUSION FROM A THIN LOW PERMEABILITY LAYER

4.1. Experimental data

Laboratory-scale tracer experiments were conducted by Yang et al. (2015) at University of Florida to study forward and back diffusion in a thin clay layer underlain by a sand layer. A 28×1.2×12 cm flow chamber as designed by Yang et al. (2014) was filled with 20/30 mesh Accusand for the transmissive zone. A layer of kaolinite (Fluka) was laid on top to act as the low permeability zone. The experiments consisted of displacing tracer solutions through the flow chamber for a determined number of days followed by flushing without tracers for an additional period of time. The experimental setup is shown in Figure 1:

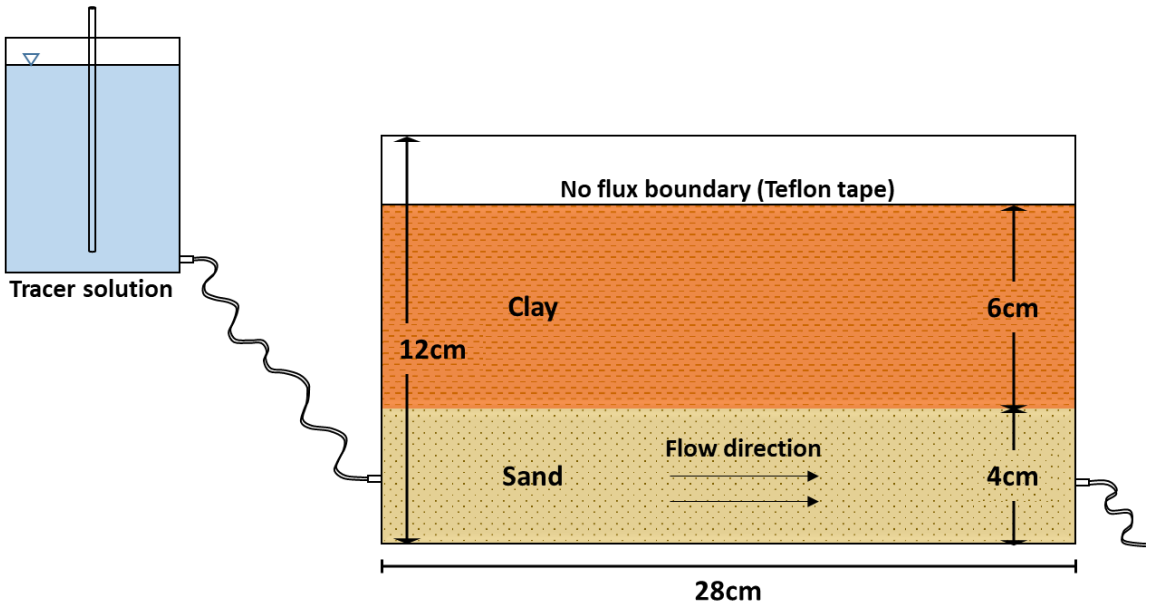

Figure 1. Flow chamber experimental setup (experiment I). Adapted from Yang et al. (2015).

The first experiment was carried out as shown in Figure 1. A 4-cm-thick sand layer was placed at the bottom of the flow chamber, followed by a 6-cm-thick layer of kaolinite. A solution containing 200 mg/L of bromide was flushed through the sandbox at a rate of 0.018 mL/min for 22 days. Immediately after the tracer, flushing continued with clean water for 32 days.

The experiment was repeated using a sand thickness of 3 cm and a clay thickness of 2 cm. The tracer solution was flushed for 10 days followed by clean water for 30 days. The solution was injected at a flow rate of 0.01mL/min. The conditions of the experiments of interest are summarized in Table 1:

Table 1. Summary of conditions in Yang et al. (2015) experiments.

Description	**Value**	
Experiment	I	III
Solute	Bromide	Bromide
Initial concentration (mg/L)	200	200
Flow rate, *Q* (mL/min)	0.018	0.01
Clay thickness (cm)	6	2
Sand thickness (cm)	4	3
Loading time, *T* (days)	22	10
Flushing time, *t*-*T* (days)	32	30

4.2. Semi-analytical model

The semi-analytical method was implemented as a Visual Basic program in Excel®. It was initially set up as a single gridblock representing the high permeability zone with an embedded matrix diffusion area for the low *k* material, defining the high/low permeability distribution by volume fractions. The bromide concentrations were initialized to zero. At time zero the inlet bromide concentration was set to 200 mg/L, and maintained at this value

for 22 and 10 days for experiments I and III, respectively. To account for the flushing with clean water, the inlet concentration was set to zero again for 32 and 30 days, respectively.

The input parameters for the model were obtained directly and calculated from Yang et al. (2015), and Yang and Jawitz (personal communication, 2016). They are listed in Table 2:

Table 2. Input parameters used in model for back diffusion from low permeability layers.

Description	**Value**	
Experiment	I	III
Darcy velocity, v_x (m/yr)	7.884	8.76
Sand porosity, ϕ	0.3	0.3
Matrix porosity, ϕ_l	0.6	0.6
Sand retardation, R	1	1
Matrix retardation, R_l	1	1
Matrix tortuosity, τ_l	0.15	0.15
Diffusion coefficient, D (m^2/yr)	6.35E-2	6.35E-2
Source concentration, C_0 (mg/L)	200	200
Δx (m)	0.28	0.28
Δy (m)	0.012	0.012
Δz (m)	0.1	0.05
Matrix diffusion area, A_{md} (m^2)	3.36E-3	3.36E-3
Sand volume fraction, ~~V_f~~	0.4	0.6
Characteristic diffusion length, L (m)	0.06	0.02
Number of elements (x-dir)	1	1
Number of cells in y direction	1	1
Number of layers (z-dir)	1	1
Source time duration (yr)	6.03E-2	2.74E-2
Δt (yr)	2.66E-4	5.99E-4
Number of time steps	556	183

The parameters Δx, Δy, and Δz refer to the grid spacing in the x, y, and z direction, respectively. Since there is only one gridblock (number of elements in Table 2), the grid spacing is equal to the geometry of the sand/clay structure. Since the layers of sand and

clay are stacked one on top of the other, the Δz used is the sum of the sand and clay thicknesses. The Darcy velocity is calculated as the volumetric flow rate divided by the cross-sectional area of flow; that is, Q divided by $\Delta y \Delta z$.

The matrix diffusion area, A_{md}, is the interfacial area between the high permeability and low permeability zones. For the simple 2-layer clay/sand configuration the matrix diffusion area corresponds to the product of the grid spacing in the x and y directions, Δx and Δy, respectively.

The sand volume fraction, V_f, is defined as the ratio of the sand layer volume (product of Δx, Δy, and thickness of sand) to the total volume (product of Δx, Δy, and Δz).

The characteristic average diffusion length parameter, L, corresponds to the depth or vertical distance into the low permeability material. Because this configuration shows only one sand/clay interface with a no-flow boundary, the characteristic diffusion length is equal to the total thickness of the clay layer.

4.3. Testing

The accuracy of the semi-analytical model was tested by comparison with the experimental data, obtained directly from Yang and Jawitz (personal communication, 2016). The effluent breakthrough curves obtained for experiments I and III are shown in Figures 2 and 3, showing the pore volumes in the x axis.

a)

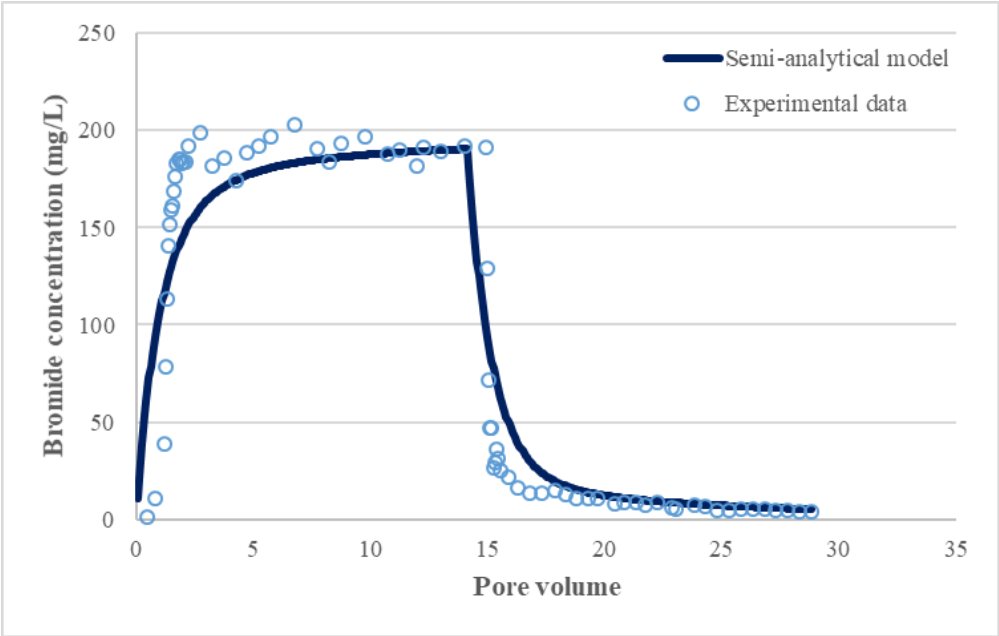

b)

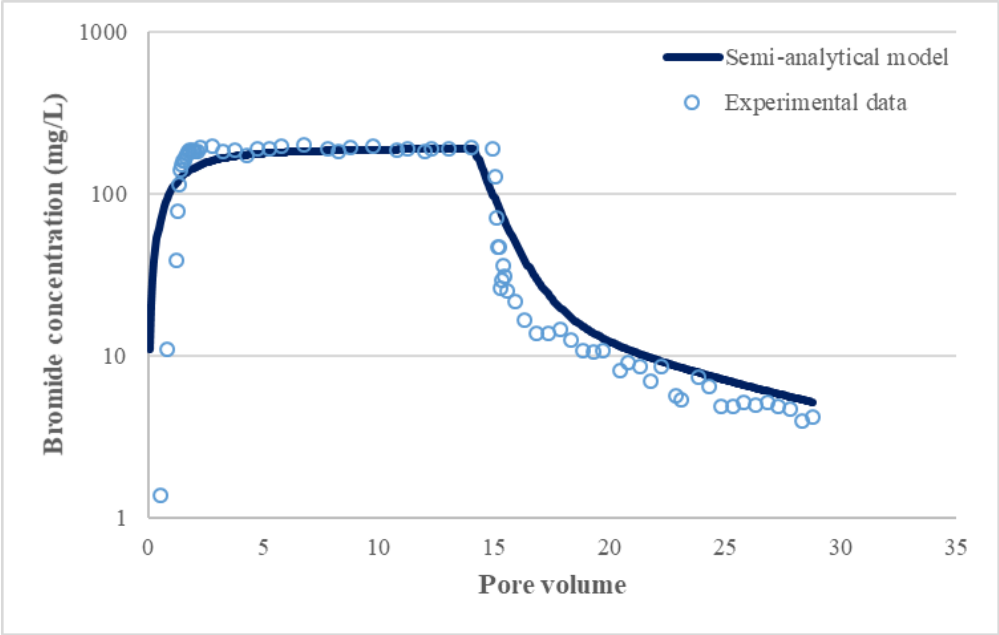

Figure 2. Effluent bromide concentration vs pore volume profile comparing the semi-analytical model with experimental data for experiment I in a) linear scale and b) log scale, simulated using one active gridblock.

a)

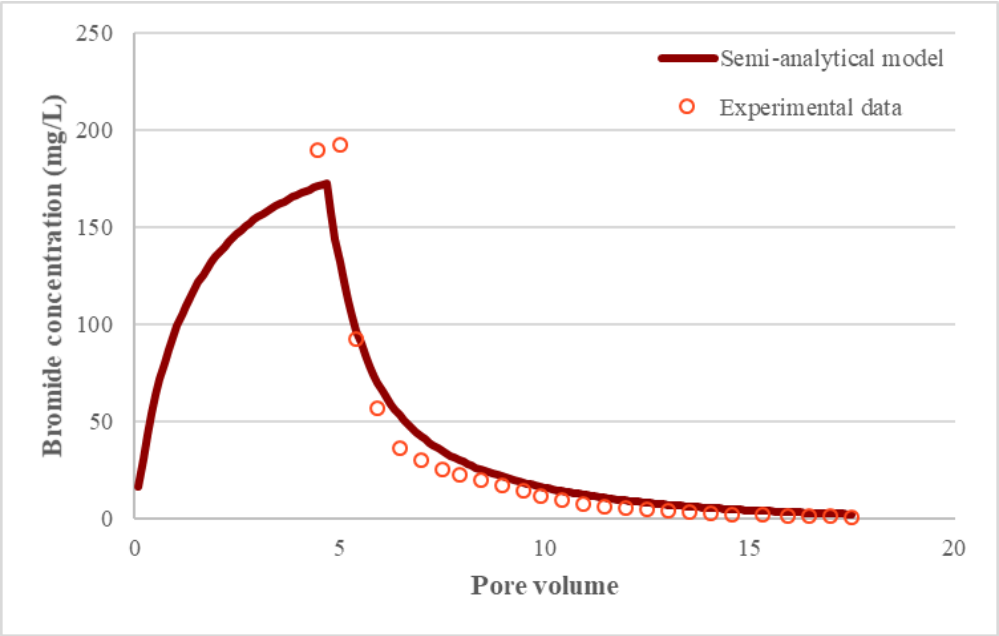

b)

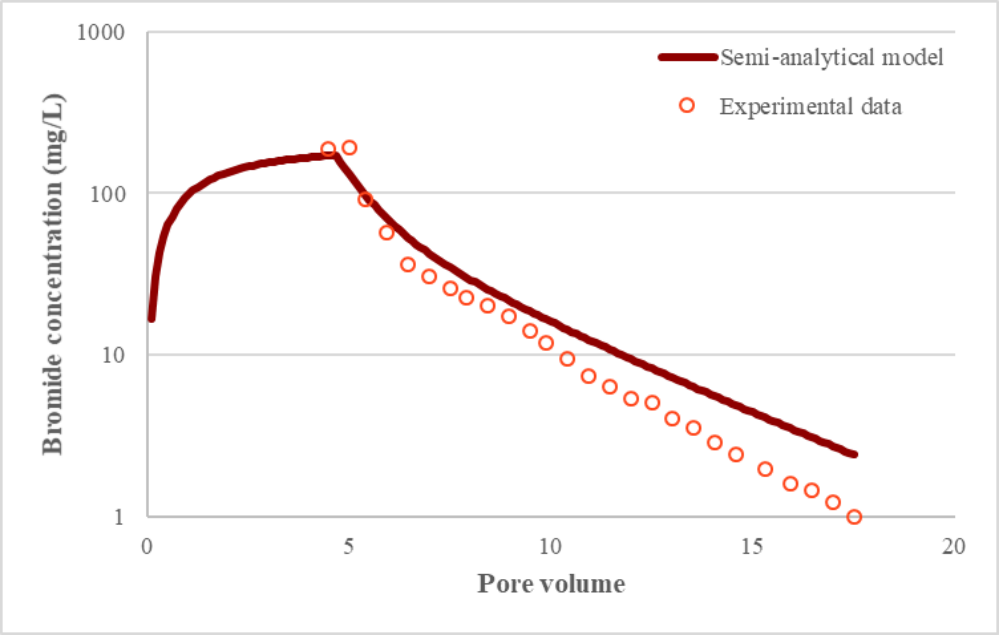

Figure 3. Effluent bromide concentration vs pore volume profile comparing the semi-analytical model with experimental data for experiment III in a) linear scale and b) log scale, simulated using one active gridblock.

The coefficient of determination R^2 evaluates the "goodness of fit" of a model (Anderson, 2010). R^2 takes values between 0 and 1 and is defined as:

$$R^2 = \frac{SSR}{SST} = 1 - \frac{SSE}{SST} \tag{38}$$

Where:

$$SSR = sum\ of\ squares\ due\ to\ regression = SST - SSE \tag{39}$$

$$SSE = sum\ of\ squares\ due\ to\ error = \sum_i (y_i - \hat{y}_i)^2 \tag{40}$$

$$SST = total\ sum\ of\ squares = \sum_i (y_i - \bar{y})^2 \tag{41}$$

Where y_i is the observed value (experimental data), $\hat{y}_i$ is the estimated value (model), and $\bar{y}$ is the mean of the experimental data.

The time to reach a specified effluent bromide concentration was used as an additional parameter for comparison. The target bromide concentration for both experiments was chosen as the lowest concentration provided in the experimental data available for comparison with the simulated dataset. This value was 4.197 mg/L for experiment I and 1.97 mg/L for experiment III. The approximate arrival times and target concentration for the semi-analytical model were extracted from the raw simulated dataset.

The calculated R^2 values and approximate times to reach the target bromide concentration ($t_{targetC}$) for the two simulations are shown in Table 3:

Table 3. Coefficient of determination and time to reach target bromide concentration for back diffusion from low permeability layers case using one gridblock.

Experiment	R^2	$t_{targetC}$ (d)	
		Experimental data	Semi-analytical model
I	0.876	52.5	49
III	0.925	30.6	38.5

The bromide concentration sharply decreases after the source is removed, followed by tailing behavior in Figures 2 and 3. The semi-analytical model and experimental data results show differences in the leading edge of the graphs and after the loading period, 14.3 PV and 4.8 PV for experiments I and III, respectively. The experimental concentration rises and drops more rapidly after a sudden change (as the occurrence and removal of the tracer) than the results from the semi-analytical model. The time to reach the target effluent bromide concentration in the semi-analytical model differ with the experimental data by 3.5 days (~6.7%) for experiment I, with the experimental data having a later arrival to the target concentration than the semi-analytical model. For experiment III, the difference between arrival times was about 8 days (~25.7%), with the experimental data reaching the target concentration faster than the semi-analytical model. The visual comparison, estimated coefficients of determination, and times to reach the target effluent bromide concentration suggest an overall good fit of the experimental data.

The behavior in the semi-analytical model is caused by numerical dispersion due to the upstream weighting of the advective term in the numerical solution of the transport equation. Numerical dispersion is a second-order error caused by truncation of the Taylor

series approximation used in finite difference schemes (Ataie-Ashtiani and Hosseini, 2005). This error looks like physical dispersion and leads to smeared spatial gradients of concentration (Fanchi, 2005). The numerical formulation of the model results in a numerical dispersivity equal to $\Delta x/2$ (Zheng and Bennett, 2002).

Since only one gridblock (Δx = total chamber length) was used in the model setup, the numerical dispersion was significant compared to the scale of the experiment. In order to decrease the numerical dispersion and thus improve the simulations, the semi-analytical model was set up as a one-dimensional model with 20 gridblocks (# of elements).

The new 20-gridblock configuration required modifying the grid spacing (Δx) and the matrix diffusion area in the model. This was achieved by dividing the parameters by the number of gridblocks, resulting in a Δx equal to 1.4 cm and a matrix diffusion area of 1.68 cm^2 in each gridblock.

Other geometry-related parameters such as the volume fraction and characteristic average diffusion length were not affected by the configuration change. Even though the change in Δx reduces the volume of sand for a gridblock, this reduction also applies to the total volume by the same factor, cancelling out. The characteristic average diffusion length is not affected since the number of gridblocks pertains to the discretization in the x direction and L corresponds to the vertical distance into the low permeability material. The comparisons with experimental data are shown in Figures 4 and 5. The calculated R^2 values and times to reach the target bromide concentration ($t_{targetC}$) for the two simulations are shown in Table 4.

a)

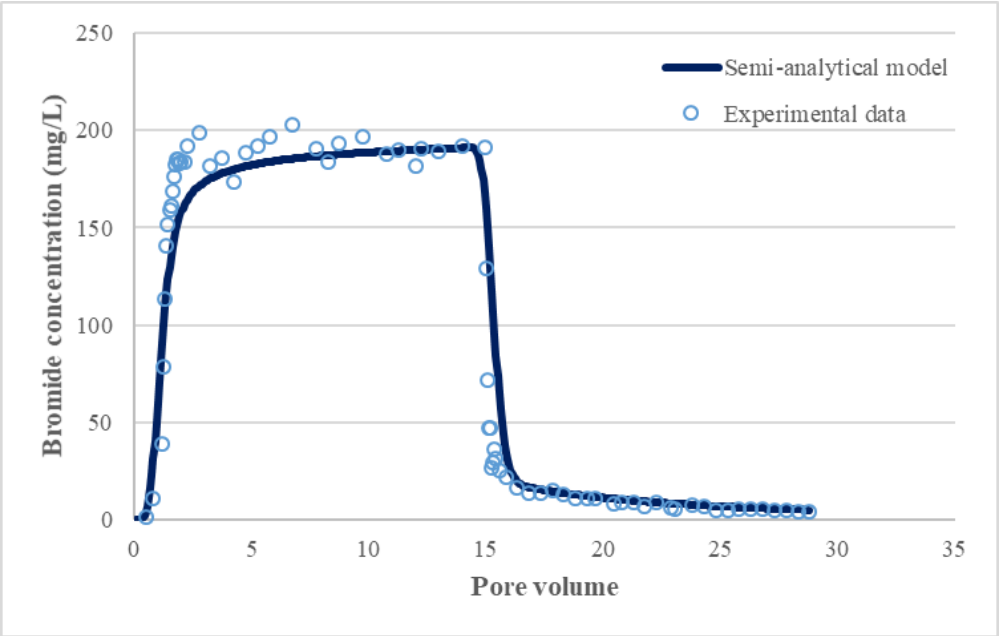

b)

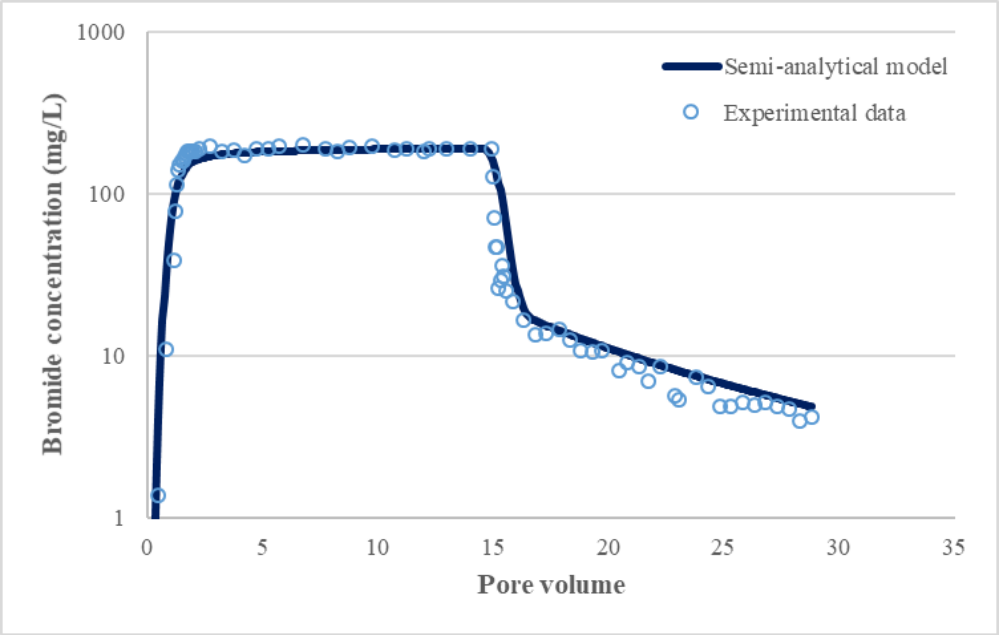

Figure 4. Effluent bromide concentration vs pore volume profile comparing the semi-analytical model using 20 gridblocks with experimental data for experiment I in a) linear scale and b) log scale.

a)

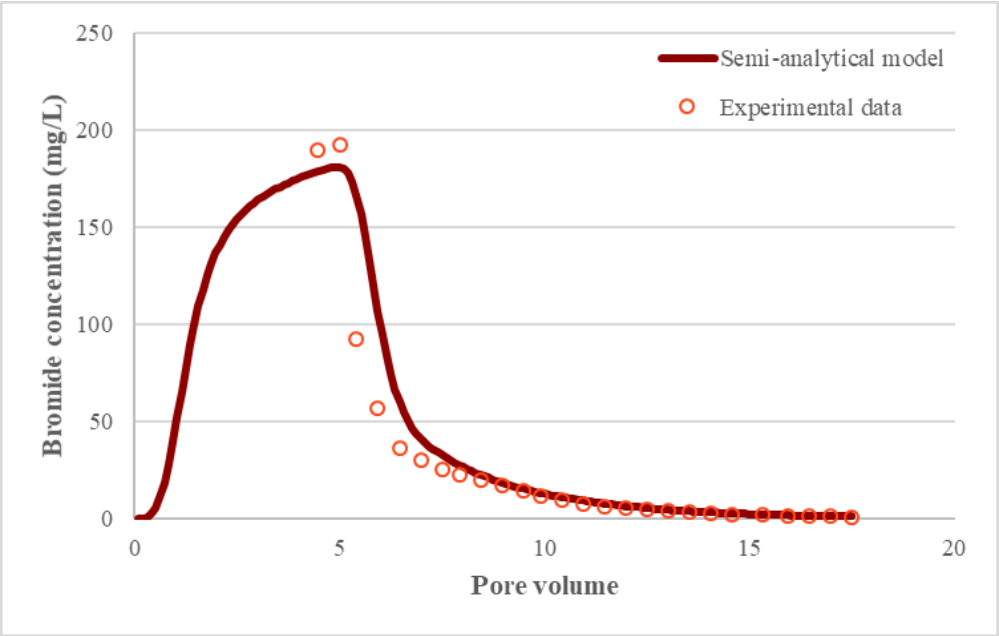

b)

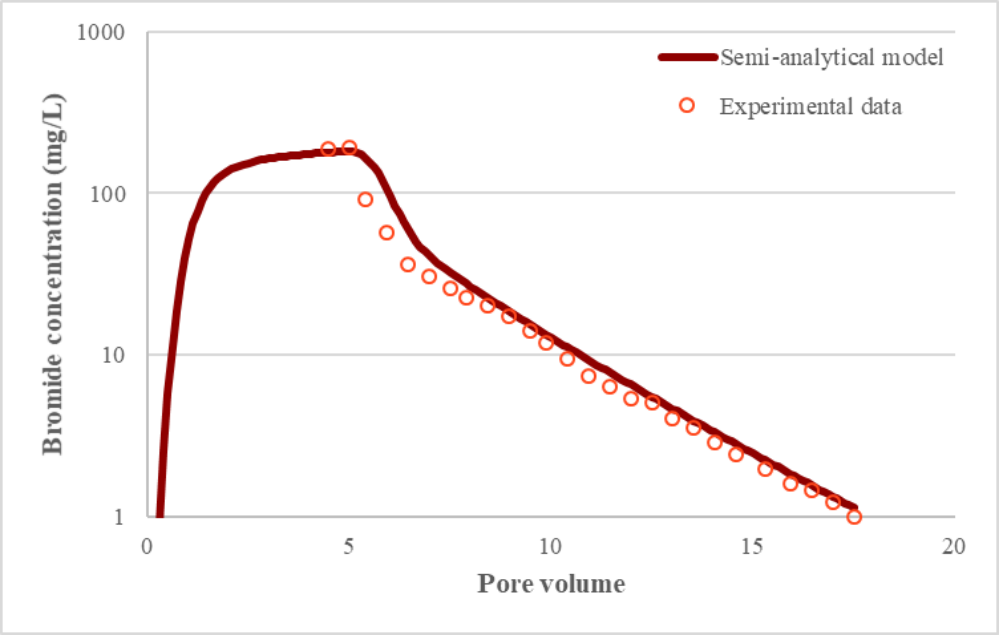

Figure 5. Effluent bromide concentration vs pore volume profile comparing the semi-analytical model using 20 gridblocks with experimental data for experiment III in a) linear scale and b) log scale.

Table 4. Coefficient of determination and time to reach target bromide concentration for back diffusion from low permeability layers case using 20 gridblocks.

Experiment	R^2	$t_{targetC}$ (d)	
		Experimental data	Semi-analytical model
I	0.879	52.5	47.6
III	0.866	30.6	33

The better fit of the simulation is apparent in the graphs, especially in the logarithmic scale because it allows examination of the data over a few orders of magnitude. Increasing the number of gridblocks in the model led to a reduction in the numerical dispersion, as observed in the breakthrough curves in Figures 4 and 5. There is an overall enhancement of the model with the finer grid, with special effect on the sharp rise and drop in concentration for experiment I and the tails for both graphs.

The new calculated coefficient of determination in Table 4 above increased for experiment I. Conversely, the R^2 has decreased for experiment III. The times to reach the target effluent bromide concentration were reduced for the semi-analytical model, although keeping the same behavior as before. The time needed to reach the target concentration for the semi-analytical model slightly moved away from the experimental dataset, from 3.5 days (~6.7%) to about 5 days (~9.3%) for experiment I. On the other hand, this difference improved for experiment III from about 8 days (~25.7%) in the simulation with a single gridblock to less than 2.5 days (~7.9%) for the refined grid.

Even though the visual comparison of experimental and simulated models is more appreciable when the data are displayed in logarithmic scale, the coefficient of determination in Table 4 corresponds to the linear scale graph since the data were never

transformed. The improvement of the tail in the graph of experiment III is apparent (see Figure 5b) with the use of a finer grid. However, there is a slight deviation of the results from the semi-analytical model at the highest portion of the curve. While there are only four or five points not met by the semi-analytical model results, they are dominating the calculation of the R^2 because these small number of points are the highest values in the set of experimental data (2 order of magnitude difference from the smaller data points). This can be easily proved by removing the first four or five data points from the calculation, altering the last four or five data points to deviate from the experimental data (5 times their original values), and evaluating their effect on R^2. The results are shown in Table 5:

Table 5. Effect of changes in small and large magnitude data points over R^2 calculation.

Changes made	**R^2**
None	0.866
Removal of first four data points	0.922
Removal of first five data points	0.978
Increase of last four simulated data points (×5)	0.864
Increase of last five simulated data points (×5)	0.862

As observed, the effect of the small values is minimal and the estimation of R^2 is dominated by large magnitude data points.

In this chapter, the semi-analytical method was used to model laboratory-scale tracer experiments conducted by Yang et al. (2015), obtaining an approximate match between the semi-analytical and experimental data when only one active gridblock was used and an overall improvement of the fit to the experimental data when the numerical dispersion of the model was reduced by using a 20-gridblock grid for the simulation.

5. SEMI-ANALYTICAL SIMULATION OF MATRIX DIFFUSION FROM SUSPENDED LOW PERMEABILITY ZONES

5.1. Experimental data

Doner (2008) carried out a set of laboratory experiments at Colorado State University using a 1.07×0.03×0.84 m tank filled with sand (US Silica; F-95 "Ottawa Sand") and four suspended clay lenses (unamended sodium bentonite, Black Hills Bentonite Co.). A tracer solution was flushed through the sandbox followed by flushing of clean water. Influent and effluent concentrations were monitored throughout the experiments. The setup of the sandbox experiment is shown in Figure 6:

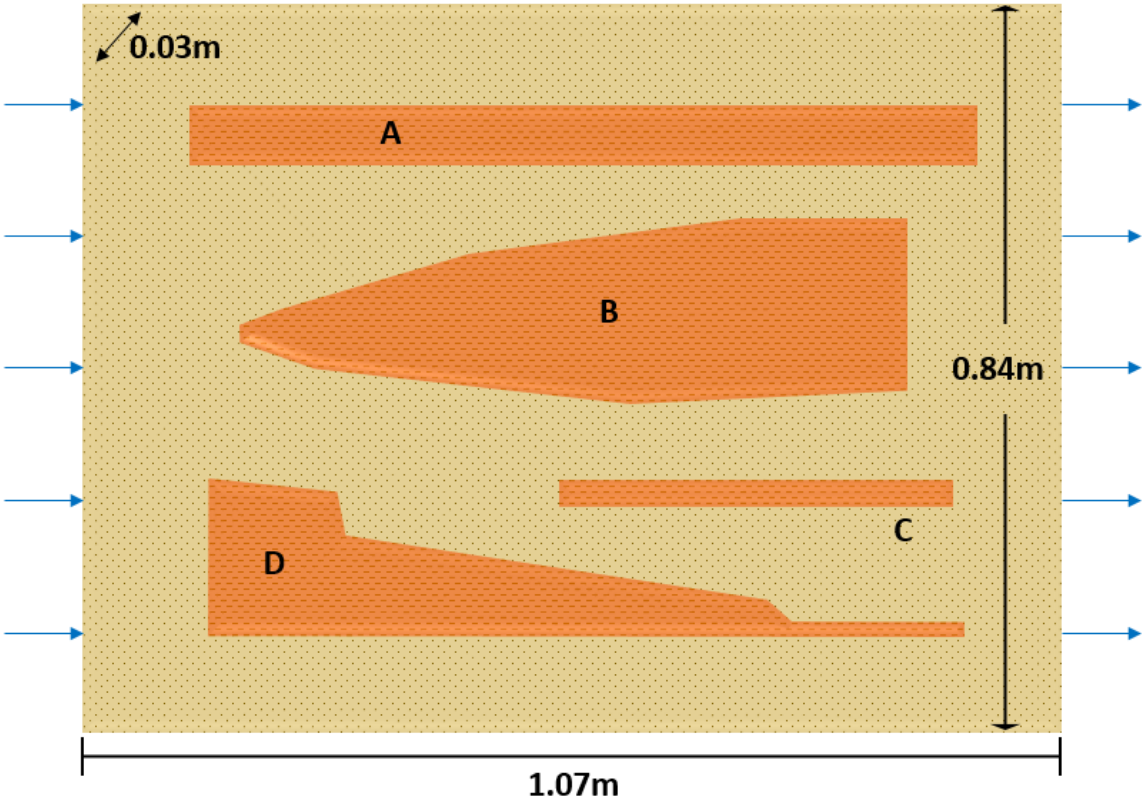

Figure 6. Sandbox experiment setup. Adapted from Doner (2008).

More recently, Chapman et al. (2012) simulated this experiment numerically to study the validity of several high resolution numerical models to simulate diffusion in and out of low permeability areas. The tested models showed close match to the experimental data, requiring fine grids (~9,000-24,000 gridblocks) and temporal discretization.

The tracer solution used in the experiment consisted of de-aired tap water containing 400 mg/L of fluorescein and 90 mg/L of bromide. The flow rate during the experiment was not constant. During the first 10 days, the solution flowed through the sandbox at a rate of 0.9 mL/min and it was later increased to and held constant at 1.5 mL/min. This inflow was maintained for 22 days and then switched by clean water for 100 more days. Table 6 summarizes the experiment conditions:

Table 6. Sandbox experiment conditions.

Parameter	Symbol	Value	Units
Total inflow/outflow (days 0–10)	Q_1	0.9	mL/min
Total inflow/outflow (day 10–end)	Q_2	1.5	mL/min
Input concentration (Bromide)	C_0	90	mg/L
Input concentration (Fluorescein)	C_0	400	mg/L
Source duration	T	22	days
Flushing duration	t-T	100	days

Note: Modified from Chapman et al. (2012).

5.2. Semi-analytical model

A single gridblock was used to simulate the high permeability zone, with an embedded matrix diffusion area representing the clay lenses. The matrix diffusion area was calculated approximating the geometry of the irregular clay lenses. This was accomplished by digitizing (Rohatgi, 2017) the clay lenses from a picture of the experimental setup (Doner,

2008) and scaling the clay dimensions from the sandbox dimensions. The values are shown in Figure 7:

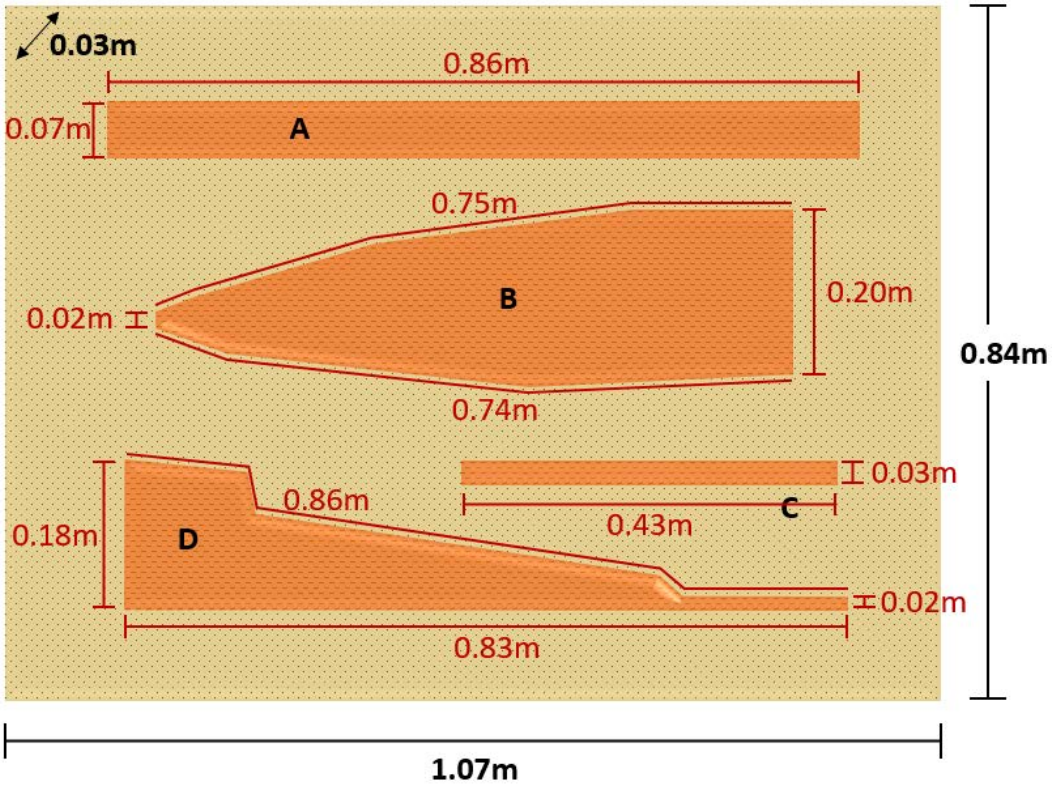

Figure 7. Approximate dimensions of clay lenses estimated from Doner (2008).

The matrix diffusion area for every clay lens is the sum of each face length times the thickness of the sandbox. The total matrix diffusion area, A_{md}, is the sum of the individual lens matrix diffusion areas and it was estimated as 0.1923 m^2.

As before, the use of a single active gridblock yielded a grid spacing equal to the geometry of the sandbox. The high/low permeability zone distribution was specified by volume fractions. The volume of sand required for the volume fraction calculation was computed from the overall sand area (0.26 m^2) specified in Chapman et al. (2012). The estimated sand volume fraction, ~~V_f~~, was 0.711.

The Darcy velocity was calculated as Q divided by the product of Δy and Δz. However, the experiment was carried out with a variable volumetric rate and the current formulation of the semi-analytical method uses a constant value. The value of Q_2 in Table 6 was chosen to be used in the semi-analytical method because it was implemented for a longer period of time during the sandbox testing.

The difference of volumetric flow rates between the experiment and the semi-analytical model will impact the results of the simulation, increasing any existing deviation from the experimental results. By choosing the higher volumetric rate the expected effluent concentrations during the first 10 days of the experiment are achieved at a faster time. Therefore, a shift to the left is expected in the leading edge of the simulated concentration versus time profile.

The characteristic average diffusion length, L, is a complex parameter to establish directly since all the clay lenses have different shapes. However, it can be estimated from other parameters. From a simple geometric perspective, the product of the interfacial area and the diffusion length should be equal to the volume of the low permeability zone. This is:

$$A_{md}L = V_{gridblock}\left(1 - \cancel{V_f}\right) \tag{42}$$

The right-hand side of the equation represents a diffusion related volume. Multiplying the volume of a gridblock by the volume fraction of the low permeability material yields a low permeability material volume, satisfying the equality. Since the matrix diffusion area and the sand volume fraction were already specified, the characteristic average diffusion length was estimated rearranging Equation 42:

$$L = \frac{V_{gridblock}\left(1 - \overline{V_T}\right)}{A_{md}} \tag{43}$$

The calculated value for L was 0.0405 m. Given that this value is only an estimate, additional simulations were carried out varying the characteristic average diffusion length to evaluate its effect on the results.

At time zero the inlet bromide and fluorescein concentrations were set to the specified values in Table 6, maintaining these concentrations constant for 22 days (loading period). After this time, the tracer inlet concentrations were reset to zero for 100 more days.

The input parameters for the semi-analytical model are presented in Table 7. They are the same for both bromide and fluorescein, except for the diffusion coefficients and sand retardation factors. The parameter values other than A_{md} and L were obtained and calculated from Chapman et al. (2012) and Doner (2008).

Table 7. Input parameters used in model for matrix diffusion from suspended low *k* zones.

Description	Value
Darcy velocity, v_x (m/yr)	31.29
Sand porosity, ϕ	0.45
Matrix porosity, ϕ_l	0.6
Sand retardation (Br), R	1
Sand retardation (Fl), R	1.39
Matrix retardation, R_l	1
Matrix tortuosity, τ_l	0.6
Diffusion coefficient (Br), D (m^2/yr)	6.34E-02
Diffusion coefficient (Fl), D (m^2/yr)	1.73E-02
Source concentration (Br), C_0 (mg/L)	90
Source concentration (Fl), C_0 (mg/L)	400
Δx (m)	1.07
Δy (m)	0.03
Δz (m)	0.84
Matrix diffusion area, A_{md} (m^2)	0.1923
Sand volume fraction, V_f	0.711
Characteristic diffusion length, L (m)	0.0405
Number of elements (x-dir)	1
Number of elements (y-dir)	1
Number of layers (z-dir)	1
Source time duration (yr)	6.03E-02
Δt (yr)	1.37E-03
Number of time steps	240

5.3. Testing

The experimental data were compared to the simulation results. The effluent concentration versus time profiles obtained for the bromide and fluorescein experiments are shown in Figure 8:

a)

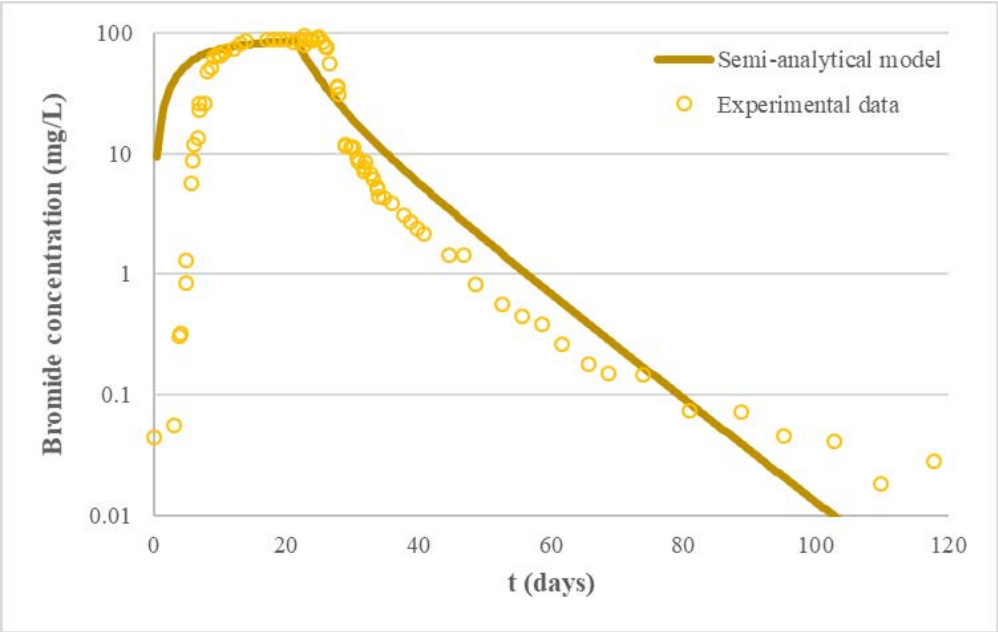

b)

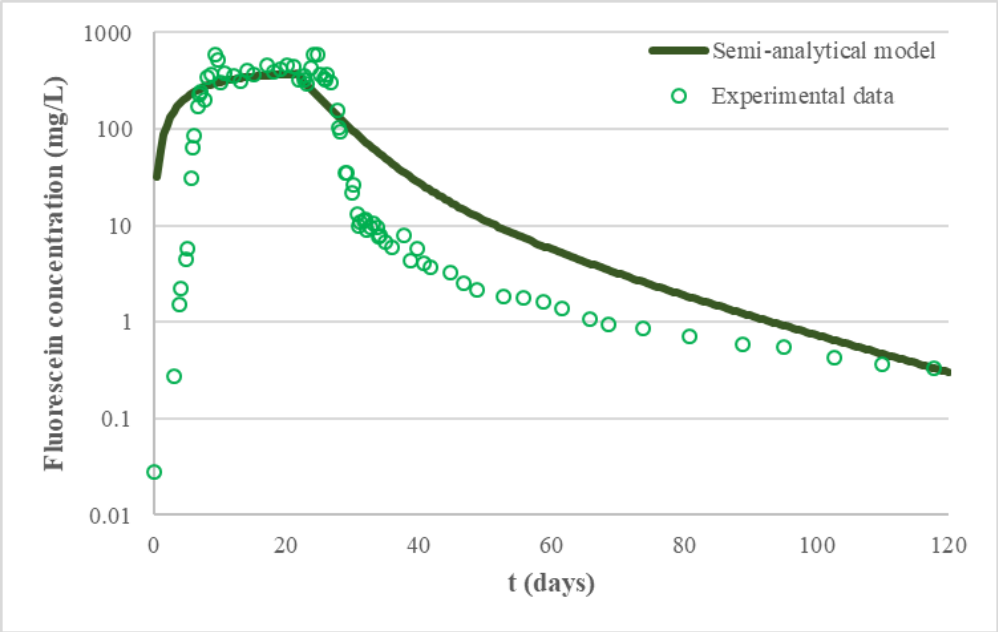

Figure 8. Effluent concentration vs time profile comparing the semi-analytical model with experimental data for Doner (2008) for a) bromide and b) fluorescein using a single gridblock to represent the entire experiment.

The concentration profiles for the experimental data in Figure 8 show a sharp rise and decrease of concentration after the sudden occurrence of the tracer solutions at time zero, and later on, after the removal of the tracer source at 22 days, followed by a tailing effect on the graphs at later times. This behavior is not observed in the semi-analytical method concentration profile, which presents smeared concentration fronts. The simulated concentration time series also exhibits the shift to the left due to the higher volumetric flow rate used in the Darcy velocity estimation, discussed previously.

Calculating the coefficient of determination for these curves was not done directly because the independent variable (time) was not equally distributed in the experimental dataset. Instead, a cubic spline was used to interpolate between the data points of the simulated data to match the exact time from the experimental data.

A cubic spline is a hybrid polynomial function of order three, created by individual cubic polynomials sections joined at adjacent data points. Fitting curves generated by cubic splines are smooth, meaning that the slope of the curve on each side of a data point matches. Thus, the functions are twice differentiable at these points. (Choudhry and Lizzio, 2004; Adidharma and Temyanko, 2007)

With the interpolated data, there is a one-to-one correspondence for the independent variable (time) and the coefficient of determination can be calculated. Further information about the cubic spline interpolation can be found in appendix A.

For the arrival time comparison, the target bromide and fluorescein concentration were chosen again as the lowest concentration provided in the experimental data available for comparison with the simulated dataset. The values for bromide and fluorescein were

0.018 mg/L and 0.327 mg/L, respectively. The R^2 and time to reach target bromide and fluorescein concentrations are given in Table 8:

Table 8. Coefficient of determination and time to reach target bromide and fluorescein concentration for matrix diffusion from suspended low *k* zones case.

Experiment	R^2	$t_{targetC}$ (d)	
		Experimental data	Semi-analytical model
Bromide	0.557	109.8	96.5
Fluorescein	0.663	117.7	118

The time to reach the target effluent bromide concentration in the semi-analytical model differ with the experimental data by about 13 days (~12.1%), with the experimental data having a later arrival to the target concentration than the semi-analytical model. For the fluorescein, the difference between arrival times was less than a day (~0.26%), with the experimental data reaching the target concentration faster than the semi-analytical model.

The visual comparison, coefficients of determination, and arrival time comparisons suggest an overall moderate fit to the experimental data with some deviation, including the shift to the left on the leading edge previously discussed. As with the case studied before in Chapter 4, the fit can be improved by decreasing the numerical dispersion caused by the large spacing in the x-direction.

Consequently, the semi-analytical model was set up as a 1-D model with 50 gridblocks. The matrix diffusion area for each of the 50 gridblocks became 0.3846 cm. Fine discretization reduced the grid spacing in the x-direction to 2.14 cm. The concentration profiles for the 50-gridblock simulation can be seen in Figure 9:

a)

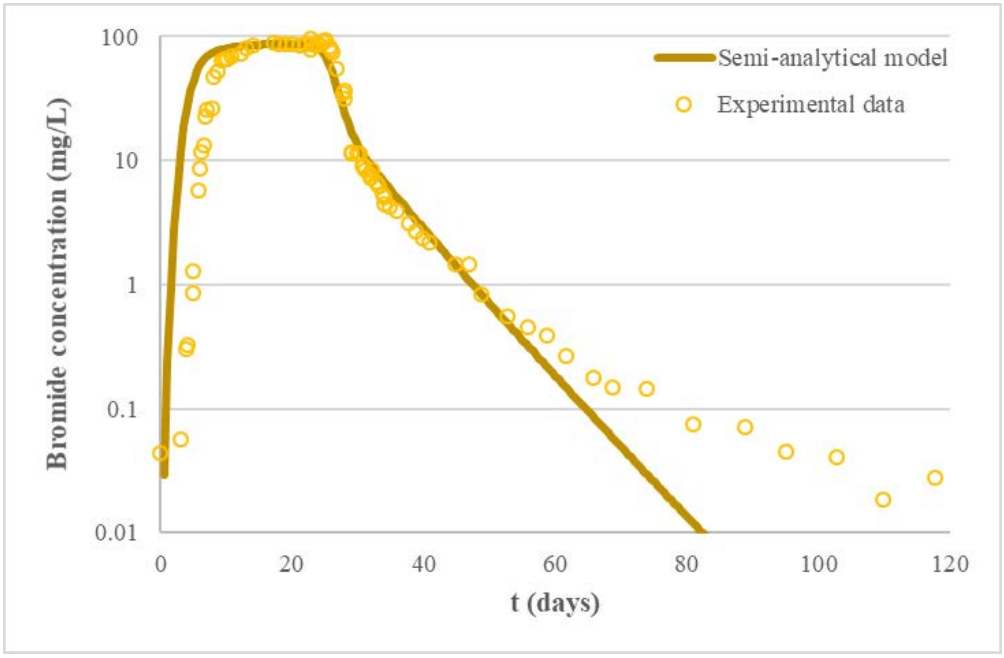

b)

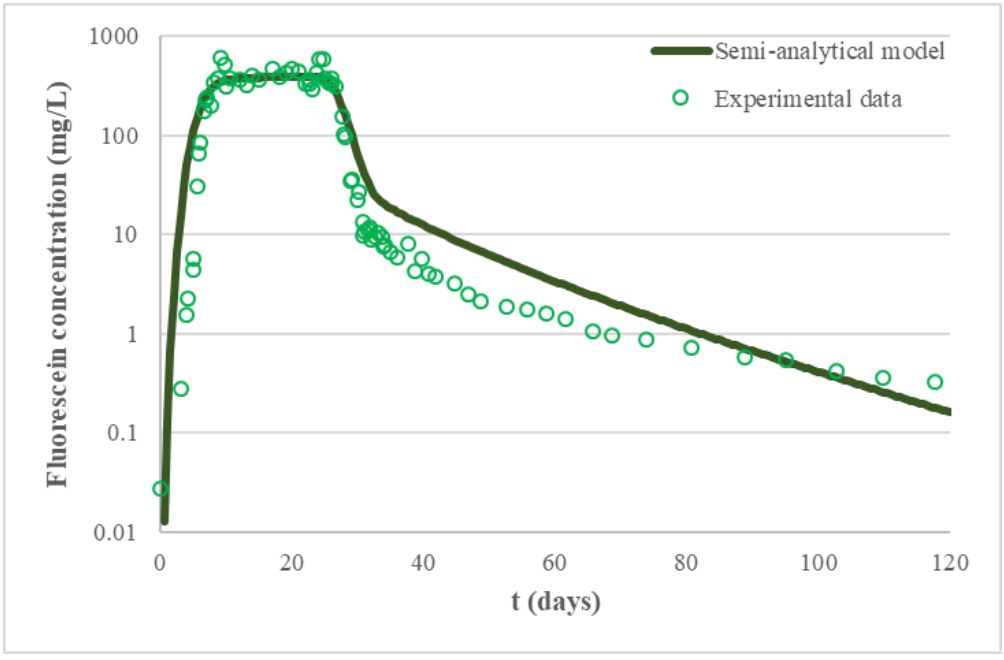

Figure 9. Effluent concentration vs time profile comparing the semi-analytical model using 50 gridblocks with experimental data for Doner (2008) for a) bromide and b) fluorescein.

The improvement of the fit is apparent in both curves, especially during the unloading period, after the tracer source has been turned off and the sharp decrease in concentration takes place. However, at later times (>60 days) the experimental bromide concentration profile is not met by the semi-analytical model results.

The new coefficients of determination and times to reach the target concentration are reported in Table 9:

Table 9. Coefficient of determination and time to reach target bromide and fluorescein concentration for matrix diffusion from suspended low *k* zones case using 50 gridblocks.

Tracer	**R^2**	**$t_{targetC}$ (d)**	
		Experimental data	**Semi-analytical model**
Bromide	0.724	109.8	77.5
Fluorescein	0.880	117.7	105

The recalculated values of the R^2 increased with respect to the simulations with one gridblock, confirming the improvement of the fit by reducing numerical dispersion.

The time it took the semi-analytical model to reach the target bromide concentration decreased, increasing the difference from the experimental dataset, from about 13 days (~12.1%) to about 32 days (~29.4%). Likewise, the difference for the fluorescein curves moved up from less than a day (~0.26%) in the simulation with a single gridblock to about 13 days (~10.8%) for the 50-gridblock configuration.

The new arrival times support the visual comparison, in which the simulated bromide concentration decreases faster than the experimental concentration at later times and the simulated fluorescein curve crosses from being above the experimental curve to below it at approximately 90 days.

Despite the difference in the bromide curve tail, the visual and quantitative comparisons point out to an overall enhancement of the match between the semi-analytical model and the experimental data, suggesting that the semi-analytical method does a good job of predicting the matrix diffusion processes.

5.3.1. Effect of the diffusion length

Since all the clay lenses had different dimensions and the characteristic average diffusion length was approximated, the effect of this parameter on the results was studied.

Additional simulations were carried out for diffusion lengths of 3 cm, 5 cm, 6 cm, and 8 cm and compared to the experimental data. Since the characteristic average diffusion length was fixed, Equation 42 was used to estimate the correspondent matrix diffusion area for each case.

Figure 10 displays the resulting curves, including the original results (L = 4.05 cm) for comparison. The graphs presented show how the different effluent concentration profiles are basically the same up to around the time the source is removed, 22 days. After this time, and up to 35 days for the bromide profile, the curves for each L start to separate, starting with L = 3cm at the top and going down with increasing diffusion length. From 35 to 60 days, the curves start to cross over, and after 60 days shorter diffusion lengths lead to lower concentrations at the exit of the sandbox and larger diffusion lengths cause the concentrations to be higher at the effluent.

a)

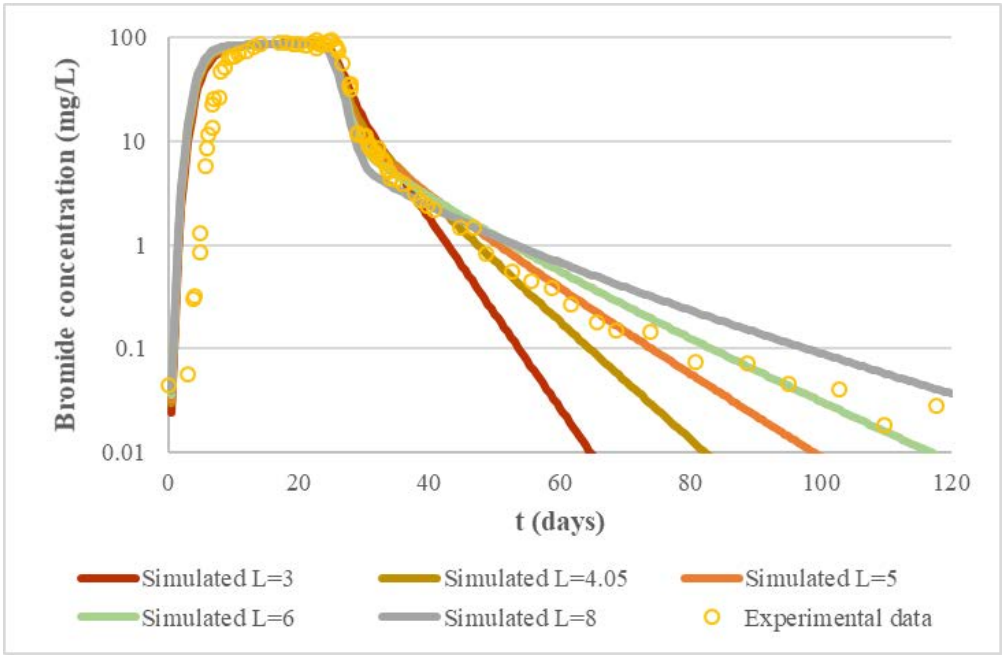

b)

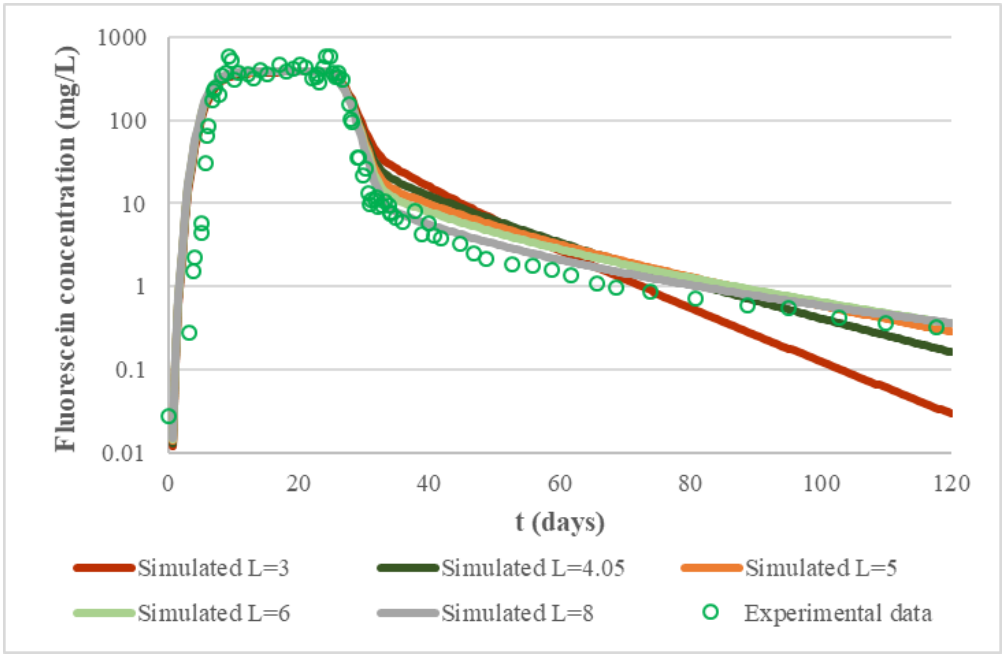

Figure 10. Effect of diffusion length on effluent concentration profile for the case of matrix diffusion from suspended low *k* zones for a) bromide and b) fluorescein.

This behavior is also observed in the fluorescein effluent concentration time series. From time zero up until the source is removed the curves are almost the same. After source removal, when the sharp concentration front occurs, the curves start to separate with increasing diffusion length top to bottom until about 40 days. From 40 to 70 days the crossover occurs and, after 70 days, there are higher tails with increasing L.

There is a proportional relationship between the diffusion length and the effluent concentration at large times. This effect can be explained by the slower diffusive mass flux that occurs with an increased diffusion length and a decreased matrix diffusion area. After cleaning the source, the mass in the low permeability zones is depleted more quickly for the shorter diffusion lengths with larger A_{md}.

The calculated R^2 and approximate time to reach the target effluent concentration for each curve are presented in Table 10:

Table 10. Coefficient of determination and time to reach target bromide and fluorescein concentration for diffusion length study in the case of matrix diffusion from suspended low k zones.

	R^2		$t_{targetC}$ (d)			
			Bromide (br)		Fluorescein (fl)	
L (cm)	br	fl	Experimental data	Semi-analytical model	Experimental data	Semi-analytical model
3	0.7754	0.8751	109.8	62	117.7	87
4.05	0.7242	0.8795	109.8	77.5	117.7	105
5	0.6844	0.8804	109.8	92.5	117.7	116
6	0.6496	0.8803	109.8	108	117.7	$>t_{sim}$
8	0.5986	0.8793	109.8	$>t_{sim}$	117.7	$>t_{sim}$

As discussed before, because the changes made happened in the low order of magnitude values, they have a small effect in the coefficient of determination. This is particularly observed when the changes are small, such as the ones in the fluorescein curve.

The arrival times for the semi-analytical model increase with increasing diffusion length, corresponding to the proportional relationship between L and effluent concentration previously discussed.

Taking into account the visual and quantitative comparisons for both tracer solutions, a diffusion length of 5 cm would be the best option to use for the simulations to get an overall match to the experimental data.

6. COMPARISON OF THE SEMI-ANALYTICAL METHOD WITH NUMERICAL SIMULATION USING MT3DMS FOR TWO-LAYER SCENARIO

6.1. Grid refinement study

The next step in the evaluation of the semi-analytical method was a comparison with the MT3DMS numerical model (Zheng and Wang, 1999). The number of gridblocks affects the accuracy of the model and computational effort to provide a solution so, a grid refinement study was carried out to find an appropriate discretization. The interest was dedicated to the vertical direction (z) to effectively approximate matrix diffusion fluxes between high and low permeability zones.

The grid refinement study consisted of modeling a two-layer scenario using different discretization in the vertical direction until the results converge. A 500 m × 1 m × 2 m (L×W×H = x, y, z) two-layer system was set up with a 1 m thick layer of clay underlain by an identical layer of sand, as seen on Figure 11:

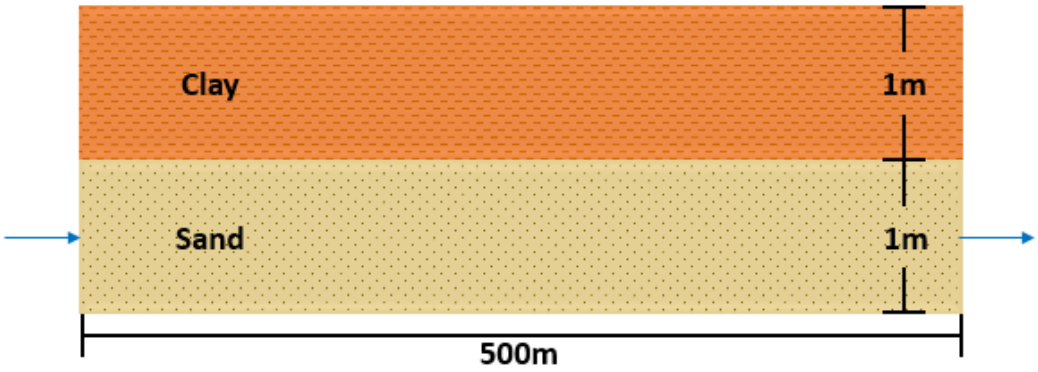

Figure 11. Clay/sand system modeled in grid refinement studies.

6.1.1. MT3DMS/MODFLOW model

The numerical model was set up using the Aquaveo GMS interface for MODFLOW (McDonald and Harbaugh, 1988) and MT3DMS (Zheng and Wang, 1999). The MT3DMS/MODFLOW model used grid spacing of 5 m in the horizontal direction (Δx) and 1 m in the y direction (Δy). Vertical grid spacings (Δz) of 0.02 m, 0.1 m, 0.2 m, 0.5 m, and 1 m were used. The hydraulic conductivity of clay and the porosity of the sand and clay were set up using common values for clay and sand (Domenico and Schwartz, 1998; Schwartz and Zhang, 2003). The hydraulic conductivity of the sand was set to 9 m/day, which falls within the typical values.

The minimum hydraulic head was set to the maximum elevation of the model (2 m). The maximum hydraulic head was calculated from the minimum head and a hydraulic gradient of 1%, obtaining a value of 7 m.

After creating the flow field with MODFLOW, a 200-year mass transport model was built with MT3DMS. An extra column (x) was added to the inlet face of the model to place a source of TCE at solubility of 1.1×10^6 ppb. The TCE source was placed only in the sand layers and kept constant for 10 years. After this time, the source concentration was set to zero to simulate clean water flushing for the remaining 190 years. The diffusion coefficient for TCE of $1\times10^{-9}m^2/s$ was taken from literature (Pankow and Cherry, 1996; Chapman and Parker, 2013). The value entered in MT3DMS is the effective diffusion coefficient, D_{TCE}^*, calculated as the product of tortuosity of the low permeability material, τ_l, and the molecular diffusion coefficient, D_{TCE}:

$$D_{TCE}^* = \tau_l D_{TCE} \tag{44}$$

Tortuosity values were estimated from the values of porosity used the equation below, (Millington and Quirk, 1961) yielding a low *k* tortuosity of 0.794.

$$\tau = \phi^{1/3} \tag{45}$$

The Finite Difference Method with Upstream weighting was used for the advection package, since it is the type of discretization used in the semi-analytical method. Sorption and retardation were considered for the model. The retardation factors were assigned as 1 and 2 for sand and clay, respectively. They were specified using the Chemical reaction package within MT3DMS, defining bulk densities and soil-water distribution coefficients. The values from density of the materials were taken from literature (VanLoon, 2000) and the partition coefficients were calculated from the equation for *R*:

$$K_D = \frac{(R-1)\phi}{\rho_b} \tag{46}$$

where K_D is the soil-water distribution coefficient, R is the retardation factor, and ρ_b is the bulk density of the material.

Degradation was also specified with the chemical reaction package, requiring a reaction rate constant. The reaction rate is calculated from the first-order decay equation:

$$\ln \frac{C}{C_0} = -\lambda t \tag{47}$$

Half-life is the time required to reduce the initial contaminant concentration in half:

$$\ln 0.5 = -\lambda t_{1/2} \tag{48}$$

$$\lambda = \frac{\ln 2}{t_{1/2}} \tag{49}$$

For a half-life of 10 years, the reaction rate constant calculated is 0.0693/year.

The horizontal dispersivity was defined as 0.01 m, and the transverse and vertical dispersivities were set as 1×10^{-3} m. These parameters were input in the Dispersion package of MT3DMS.

The time discretization was set as 0.02 years to ensure stability of the simulation in GMS. A Δt study was carried out beforehand and the .out file from MT3DMS provided a value of $\Delta t = 3.773\times10^{-2}$ yrs as the stability criterion for the advective term. Table 11 summarizes the parameters used in the MT3DMS/MODFLOW model.

Table 11. Parameters used in MT3DMS/MODFLOW model for grid refinement study.

Description	**Sand**	**Clay**
Porosity, ϕ	0.3	0.5
Hydraulic conductivity, K (m/yr)	3285	3.65E-3
Density, ρ (kg/m^3)	1500	1200
Effective diffusion coefficient, *DMCOEF* (m^2/yr)	2.503E-2	2.503E-2
Soil-water distribution coefficient, K_D (m^3/kg)	4.1667E-4	0
Reaction rate constant, λ (yr^{-1})	0.0693	0.0693
TCE source concentration, C_0 (ppb)	1.1E6	
Maximum hydraulic head, h_{max} (m)	7	
Minimum hydraulic head, h_{min} (m)	2	
Longitudinal dispersivity, α_x (m)	0.01	
Transverse dispersivity, α_y (m)	1E-3	
Vertical dispersivity, α_z (m)	1E-3	
Length in x (m)	505	
Length in y (m)	1	
Length in z (m)	2	
Number of cells in x	101	
Number of cells in y	1	
Number of cells in z	100, 20, 10, 4, 2	
Δt (yr)	0.02	
Source time duration, t_1 (yr)	10	
Release period (yr)	190	

The parameter to compare was the TCE concentration at the outlet of the model. The outlet face corresponds to the last row (x) of the model and its location is highlighted in Figure 12 for the vertical spacing of 0.5m.

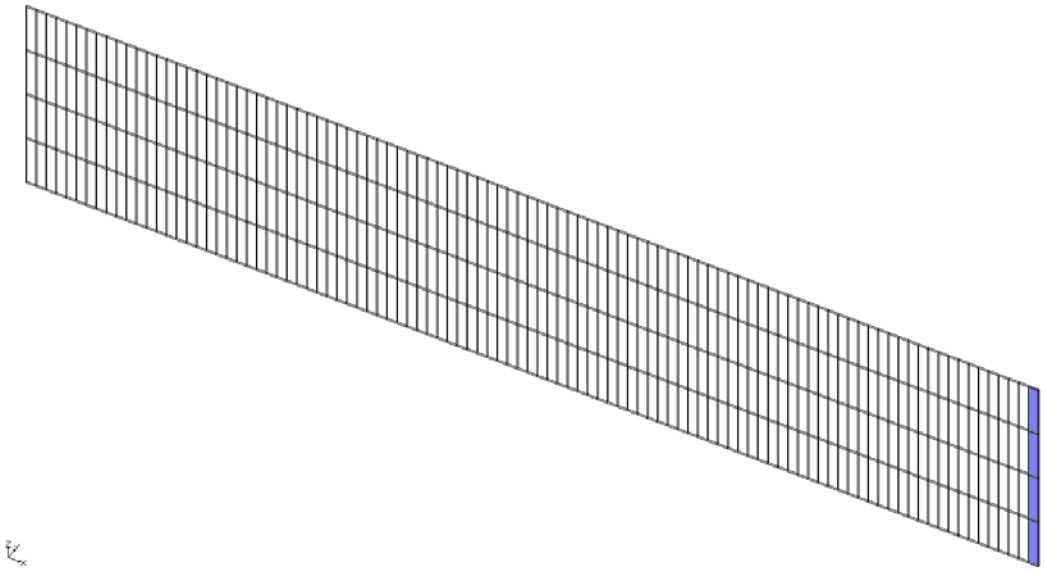

Figure 12. Location of outlet face of MODFLOW/MT3DMS model (Δz = 0.5m, z magnification = 50).

Figures 13 and 14 provide the TCE concentration at the outlet of the model with respect to time for the different levels of discretization used. The concentration profile was divided into two separate graphs to show as much detail as possible. The overall shape of the curves is the same. However, the results for the grid spacing of 1m display more deviation than those for the finer grids. This can be attributed to estimating the concentrations over larger areas. As the grid is refined, the concentration profiles start to converge and there is almost an overlap between the concentration profiles for Δz = 0.1 m and Δz = 0.2 m. A vertical spacing of 0.1 m appears to provide enough accuracy when compared with other grid size results. Hence, it was chosen as the vertical spacing for numerical simulations to follow.

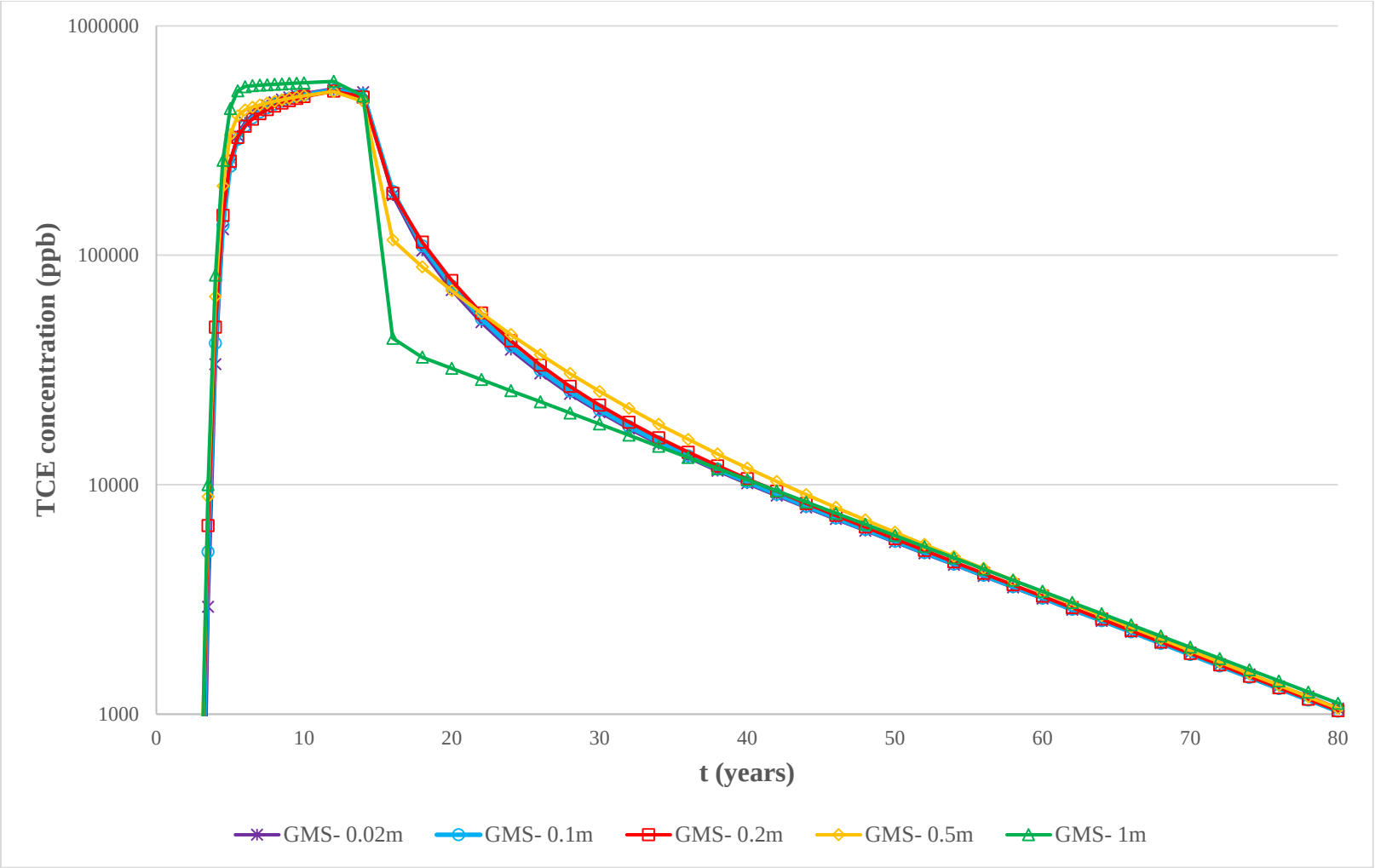

Figure 13. TCE outlet concentration for different levels of grid refinement (0-80 years).

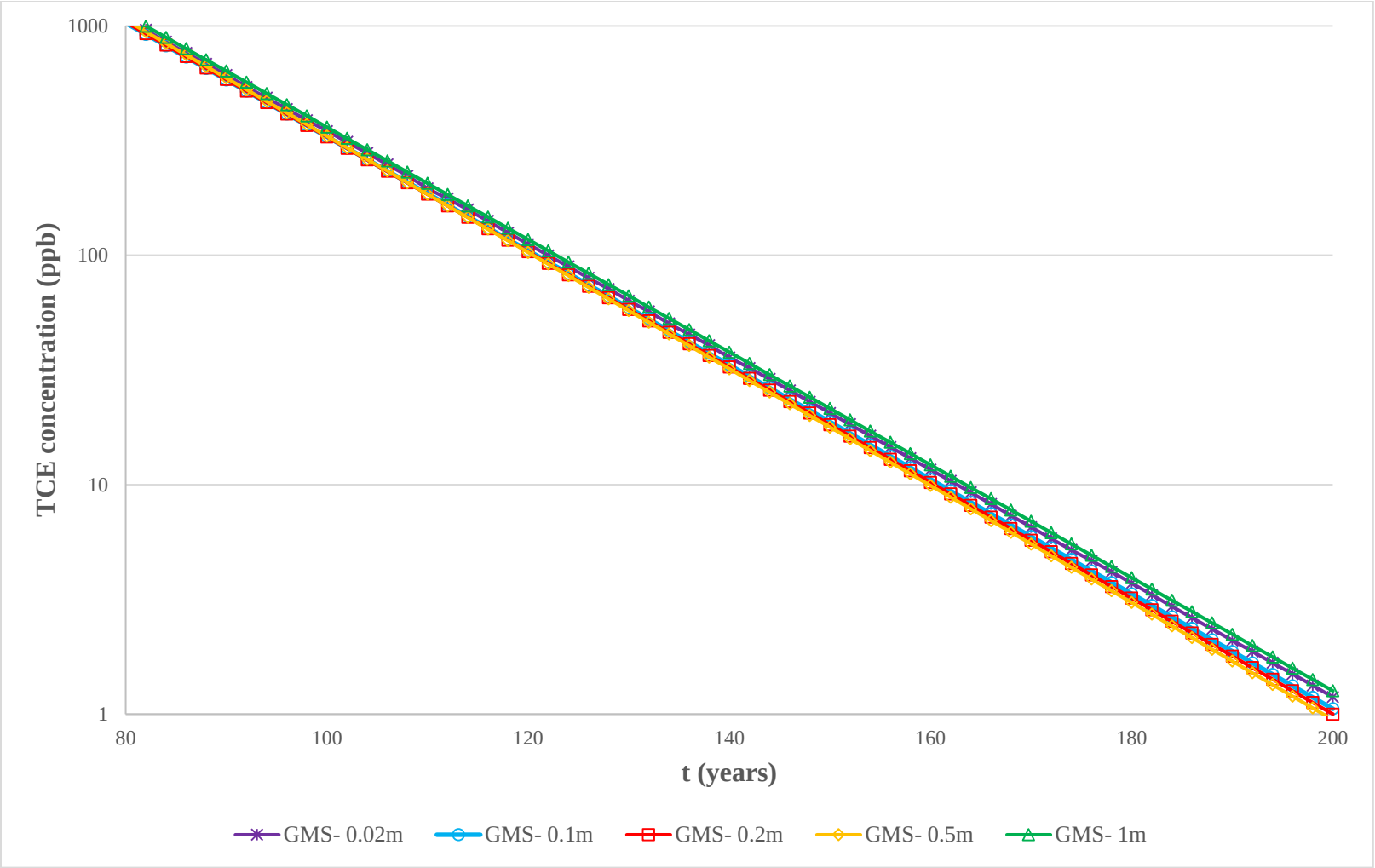

Figure 14. TCE outlet concentration for different levels of grid refinement (80-200 years).

6.2. Semi-analytical simulation of two-layer system of equal thickness

The first scenario to simulate kept the 500 m by 1 m in *x* and *y*-dir structure and consisted of a 0.1 m thick layer of clay underlain by a layer of sand of the same thickness. This configuration is shown in Figure 15:

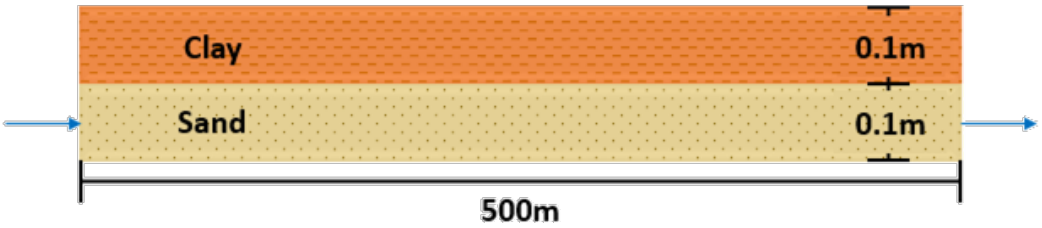

Figure 15. Two-layer clay/sand scenario with equal thickness.

As before, the Darcy flux in the sand was 0.09 m/day. A TCE source at solubility was held constant at the inlet of the sand layer for ten years, followed by flushing with clean water for 190 years. There is sorption in the low permeability area and no sorption in the transmissive zone. Degradation is present in both materials with half-life of 10 years.

6.2.1. MT3DMS model

The numerical model was set up with 101 cells in the horizontal direction, one cell in *y*-dir, and only two layers in the *z* direction. This scenario is almost the same as the one used for the grid refinement study. The difference is the thickness of the sand and clay layers. The new clay thicknesses lead to new hydraulic head values (0.2m and 5.2m) to keep the same Δh and hydraulic gradient. All the other parameters of the model remained unchanged, such as material properties, TCE properties, and loading and flushing times, to name a few. Table 12 contains the parameters used in the MT3DMS model:

Table 12. Parameters used in MT3DMS model for two-layer system of equal thickness scenario.

Description	Sand	Clay
Porosity, ϕ	0.3	0.5
Hydraulic conductivity, K (m/yr)	3285	3.65E-3
Density, ρ (kg/m^3)	1500	1200
Effective diffusion coefficient, *DMCOEF* (m^2/yr)	2.503E-2	2.503E-2
Soil-water distribution coefficient, K_D (m^3/kg)	4.1667E-4	0
Reaction rate constant, λ (yr^{-1})	0.0693	0.0693
TCE source concentration, C_0 (ppb)	1.1E6	
Maximum hydraulic head, h_{max} (m)	5.2	
Minimum hydraulic head, h_{min} (m)	0.2	
Longitudinal dispersivity, α_x (m)	0.01	
Transverse dispersivity, α_y (m)	1E-3	
Vertical dispersivity, α_z (m)	1E-3	
Length in x (m)	505	
Length in y (m)	1	
Length in z (m)	0.2	
Number of cells in x	101	
Number of cells in y	1	
Number of cells in z	2	
Δt (yr)	0.02	
Source time duration, t_1 (yr)	10	
Release period (yr)	190	

The head contours from the flow field created with MODFLOW are shown in Figure 16, and Figure 17 displays TCE concentration contours from the MT3DMS simulation at different times. The times with an asterisk represent flushing times, the amount of time lapsed after the TCE source was removed.

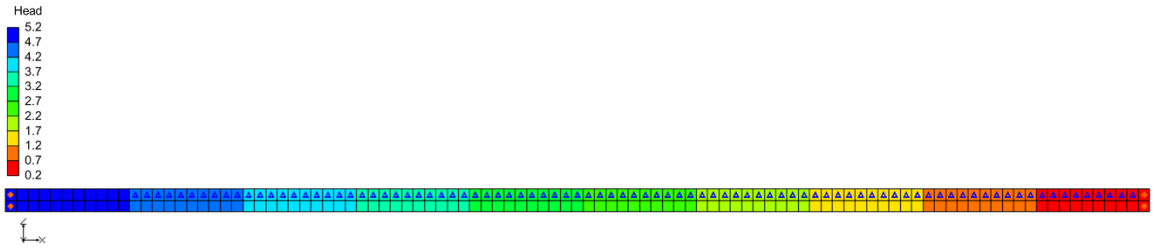

Figure 16. Head contours in MODFLOW model for two-layer system of equal thickness scenario (z magnification = 50).

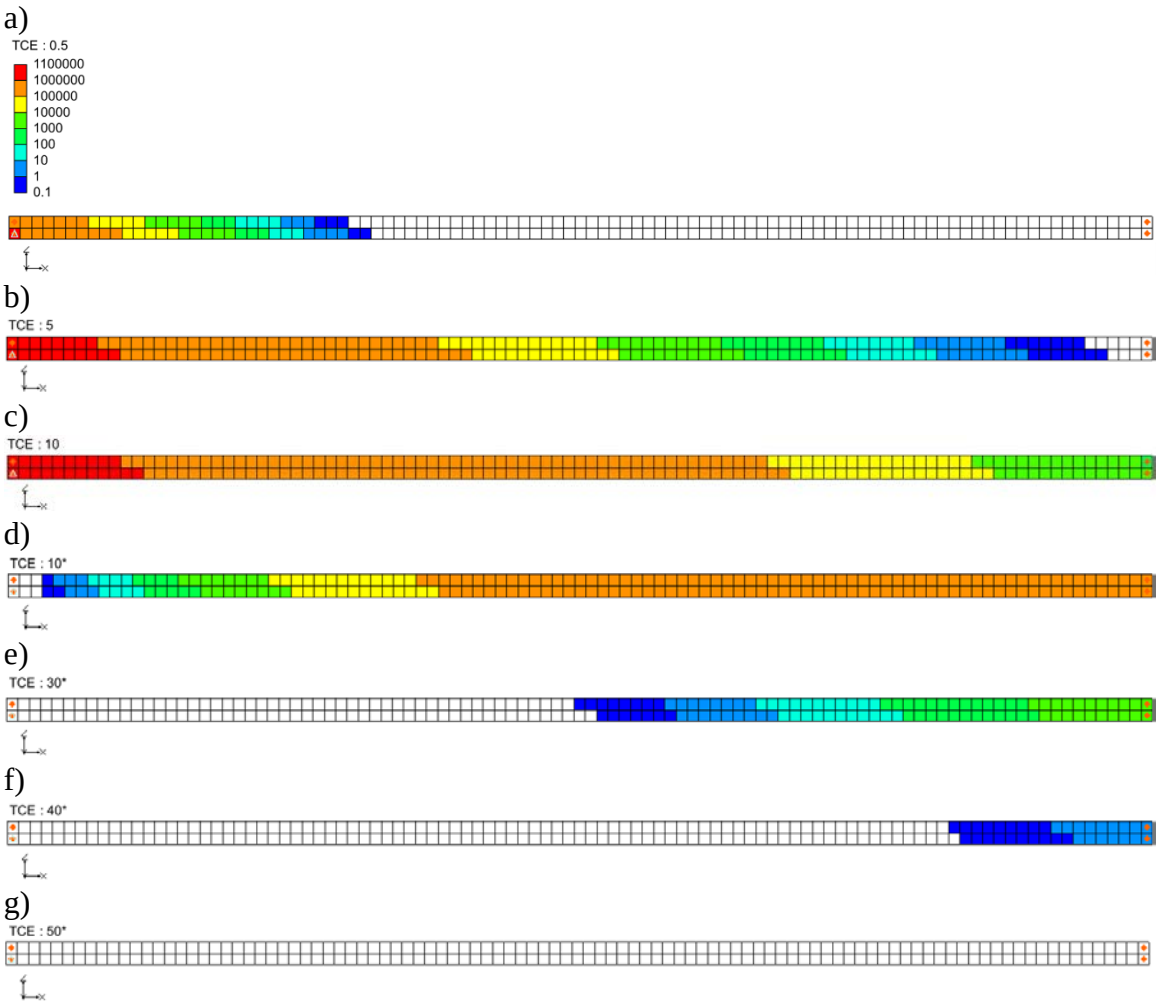

Figure 17. TCE concentration contours at a) 0.5 years, b) 5 years, c) 10 years, d) 10* years (20 yrs) e) 30* years (40 yrs), e) 40* years (50 yrs), and g) 50* years (60 yrs) for two-layer system of equal thickness scenario (z magnification = 50).

The TCE concentration contours in Figure 17 show how the contamination plume moves throughout the model. When the time is lower than the loading period (10 years), the TCE plume increases in a systematic way from the source towards the outlet face of the model, showing a decrease in concentration as it moves in the positive *x*-axis. This illustrates the evolution of the plume in the downgradient direction, caused mainly by advective transport and decay. After the source has been removed, the concentration contours show the opposite behavior, displaying higher concentrations at the outlet face of the model. This represents the flushing of TCE with clean water, reaching concentration values below the MCL (5 ppb) between 40 and 50 years after removing the contamination source.

6.2.2. Semi-analytical model

The semi-analytical model used 100 cells in the *x*-direction to apply the same numerical dispersion from the MT3DMS model. Likewise, only one cell was used in *y*-dir. For the vertical direction, only one gridblock was used to represent both high and low permeability areas, using an embedded matrix diffusion area to account for the heterogeneity in the system. Hence, the grid spacing in *x*, *y*, and *z* were set as 5 m, 1 m, and 0.2 m, respectively. The matrix diffusion area was calculated by analyzing the faces of sand and clay in contact. As before, this parameter corresponds to the product of Δx and Δy for a layered case. The distribution of sand and clay in the model was defined by volume fractions, entering the high *k* volume fraction in the model.

The Darcy velocity input in the semi-analytical model is the Darcy velocity throughout the system, whereas the value calculated from MODFLOW is the Darcy velocity of the

sand. The Darcy flux of the system was obtained multiplying $v_{d,sand}$ by the sand volume fraction. The TCE diffusion coefficient in the semi-analytical model corresponds to the molecular diffusion coefficient found in literature, 1×10^{-9} m^2/s (Pankow and Cherry, 1996; Chapman and Parker, 2013). The characteristic average diffusion length is equal to the clay layer thickness.

An inflow of TCE contaminated water was held for 10 years, with temporal discretization of 0.02 years, for a total simulation time of 200 years. After the loading period, the contamination was removed setting the source concentration to zero.

The Visual Basic implementation of the semi-analytical model used does not account for the horizontal or transverse dispersivities, only vertical dispersion. However, since only one layer was defined in the semi-analytical model, the dispersivity in the *z* direction was specified as zero. Therefore, only numerical dispersion is acting in the semi-analytical simulation. The remaining parameters in Table 13 are the same used in the creation of the semi-analytical model.

Table 13. Input parameters of semi-analytical model for two-layer system of equal thickness scenario.

Description	Value
Darcy velocity, v_x (m/yr)	16.425
Sand porosity, ϕ	0.3
Matrix porosity, ϕ_l	0.5
Sand retardation, R	1
Matrix retardation, R_l	2
Matrix tortuosity, τ_l	0.794
Sand reaction rate constant, λ (yr^{-1})	0.0693
Matrix reaction rate constant, λ (yr^{-1})	0.0693
Diffusion coefficient, D (m^2/yr)	3.15E-2
Source concentration, C_0 (kg/m^3)	1.1
Longitudinal dispersivity, α_x (m)	N/A
Transverse dispersivity, α_y (m)	N/A
Vertical dispersivity, α_z (m)	0
Δx (m)	5
Δy (m)	1
Δz (m)	0.2
Matrix diffusion area, A_{md} (m^2)	5
Sand volume fraction, ~~V_f~~	0.5
Characteristic diffusion length, L (m)	0.1
Number of elements (x-dir)	100
Number of layers (z-dir)	1
Source time duration (yr)	10
Δt (yr)	0.02
Number of time steps	10000

6.2.3. Testing

The outlet TCE concentrations of the MT3DMS and semi-analytical models are compared in Figure 18, with an inset showing a zoomed-in view of the tail. For the MT3DMS model, the concentration over time data was obtained by selecting the last row (x) of sand and using the Plot Wizard in GMS to generate an Active dataset time series. After this, the corresponding data of the plot was retrieved by choosing the “View values”

option. The outlet concentration from the semi-analytical model was a direct output of the Visual Basic program.

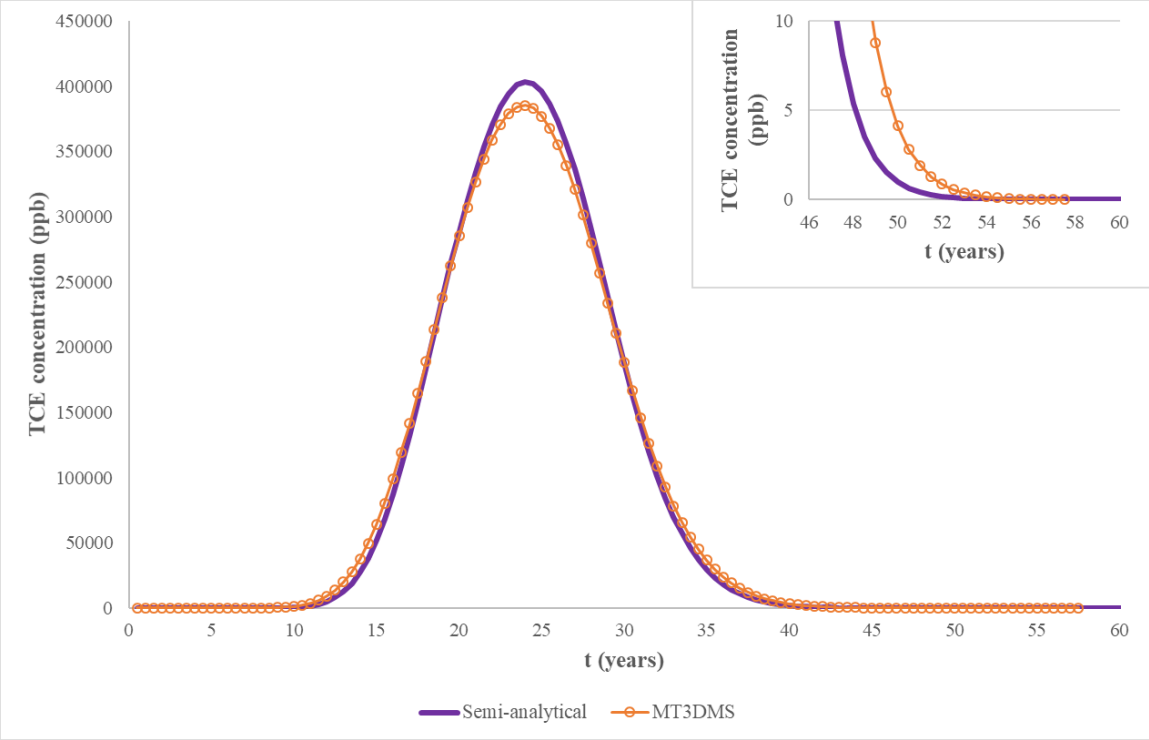

Figure 18. TCE outlet concentration vs time profile comparing the semi-analytical model with MT3DMS data in two-layer system of equal thickness scenario. Inset: zoomed-in view of tail for MCL arrival.

The breakthrough curves in Figure 18 display the progression of the TCE plume in the models. There is an increase in concentration from the beginning of the simulation up to 24 years that represents the downgradient evolution of the plume in Figure 17 a) through c). It also includes the start of the plume recession in Figure 17 d) after the source was removed and the most concentrated portion of the plume reached the outer boundary of the model. At this time the back diffusion process started, where the contaminant stored in the low permeability layer is slowly released into the sand.

After the 24-year mark, there is a sharp decrease in the TCE concentration even though there is contaminant diffusing back into the transmissive layer. This is due to the advective flushing of the contamination through the model, which is much bigger than the diffusive flux of TCE into the sand. Degradation also contributes to the depletion of the plume in the model. This process is represented in Figure 17 e) through g) where the plume is eventually flushed out of the system at around 50 years after source removal (60 years total).

The coefficient of determination calculated for this scenario is 0.998. The target concentration for the comparison of arrival times is the MCL value of 5 ppb. The inlet in Figure 18 and the raw data of both models put the arrival time of the MT3DMS model at about 50 years and the semi-analytical model at about 48 years, yielding a 2-year difference (4%). The visual comparison suggests an excellent match between the two concentration profiles throughout the total simulation period, with a slight difference in the TCE concentration around the 24-year mark, when there is a reversal of the concentration behavior. The visual comparison is supported by the high value of the coefficient of determination and the relatively small difference in times to reach the MCL.

6.3. Semi-analytical simulation of two-layer clay dominated system

Given that the diffusion effects were not very appreciable in the equal layer thickness case, a similar system was set up with higher percentage of clay, having a clay/sand ratio of 5:1. The scenario consisted of a 0.5 m thick clay layer over a sand layer of 0.1 m of thickness. The conditions of the system were kept the same, with a 0.09 m/day inflow of contaminated water at TCE solubility for 10 years followed by advective flushing with

clean water for 190 years, sorption in the clay, and degradation in the high and low *k* areas ($t_{1/2}$ = 10 yrs). The set up for this case is presented in Figure 19:

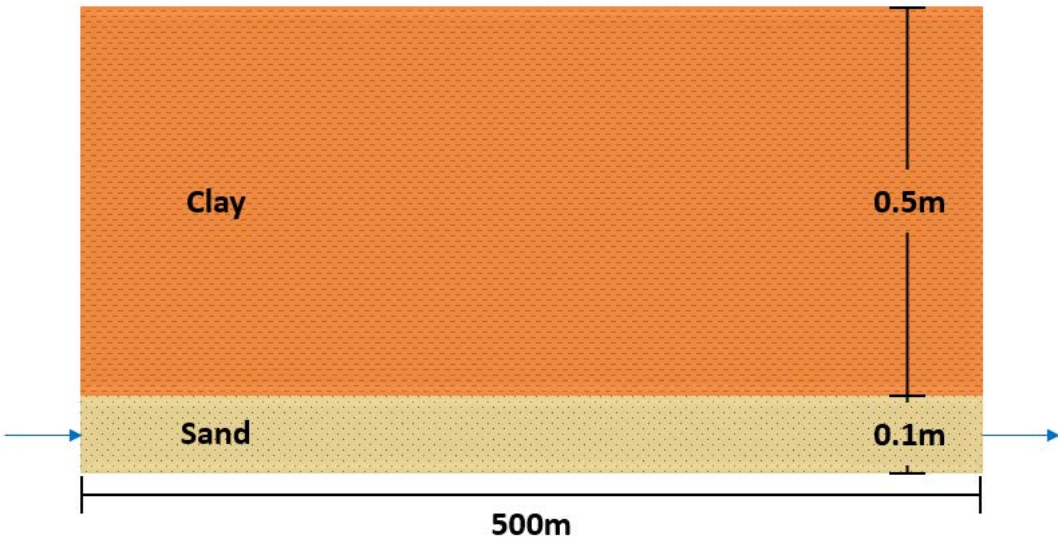

Figure 19. Two-layer clay dominated system.

6.3.1. MT3DMS model

Once again, the MT3DMS numerical model comprised 101 cells in *x* and one cell in the *y* axis. A total of six layers were required in the vertical direction with spacing of 0.1m.

The change in the length of *z* in the model caused the hydraulic head values to be defined as 0.6 m and 5.6 m, in order to keep the same hydraulic gradient. The rest of the parameters were maintained, and they are listed in Table 14:

Table 14. Parameters used in MT3DMS/MODFLOW model for two-layer system dominated by clay.

Description	Sand	Clay
Porosity, ϕ	0.3	0.5
Hydraulic conductivity, K (m/yr)	3285	3.65E-3
Density, ρ (kg/m^3)	1500	1200
Effective diffusion coefficient, D (m^2/yr)	2.503E-2	2.503E-2
Soil-water distribution coefficient, K_D (m^3/kg)	4.1667E-4	0
Reaction rate constant, λ (yr^{-1})	0.0693	0.0693
TCE source concentration, C_0 (ppb)	1.1E6	
Maximum hydraulic head, h_{max} (m)	5.6	
Minimum hydraulic head, h_{min} (m)	0.6	
Longitudinal dispersivity, α_x (m)	0.01	
Transverse dispersivity, α_y (m)	1E-3	
Vertical dispersivity, α_z (m)	1E-3	
Length in x (m)	505	
Length in y (m)	1	
Length in z (m)	0.6	
Number of cells in x	101	
Number of cells in y	1	
Number of cells in z	6	
Δt (yr)	0.02	
Source time duration, t_1 (yr)	10	
Release period (yr)	190	

The contaminant plume throughout the simulation time is shown in Figure 20. The plume evolution is shown in the first ten years, equivalent to the loading period. The growth of the plume is not as fast as in the equal thickness scenario, when comparing the loading period contours. This can be attributable to the larger volume for diffusion in the low permeability zone causing a higher diffusion flux into the clay. This is seen as a spreading of the plume in z, leading to a reduction of the plume progression in the horizontal direction.

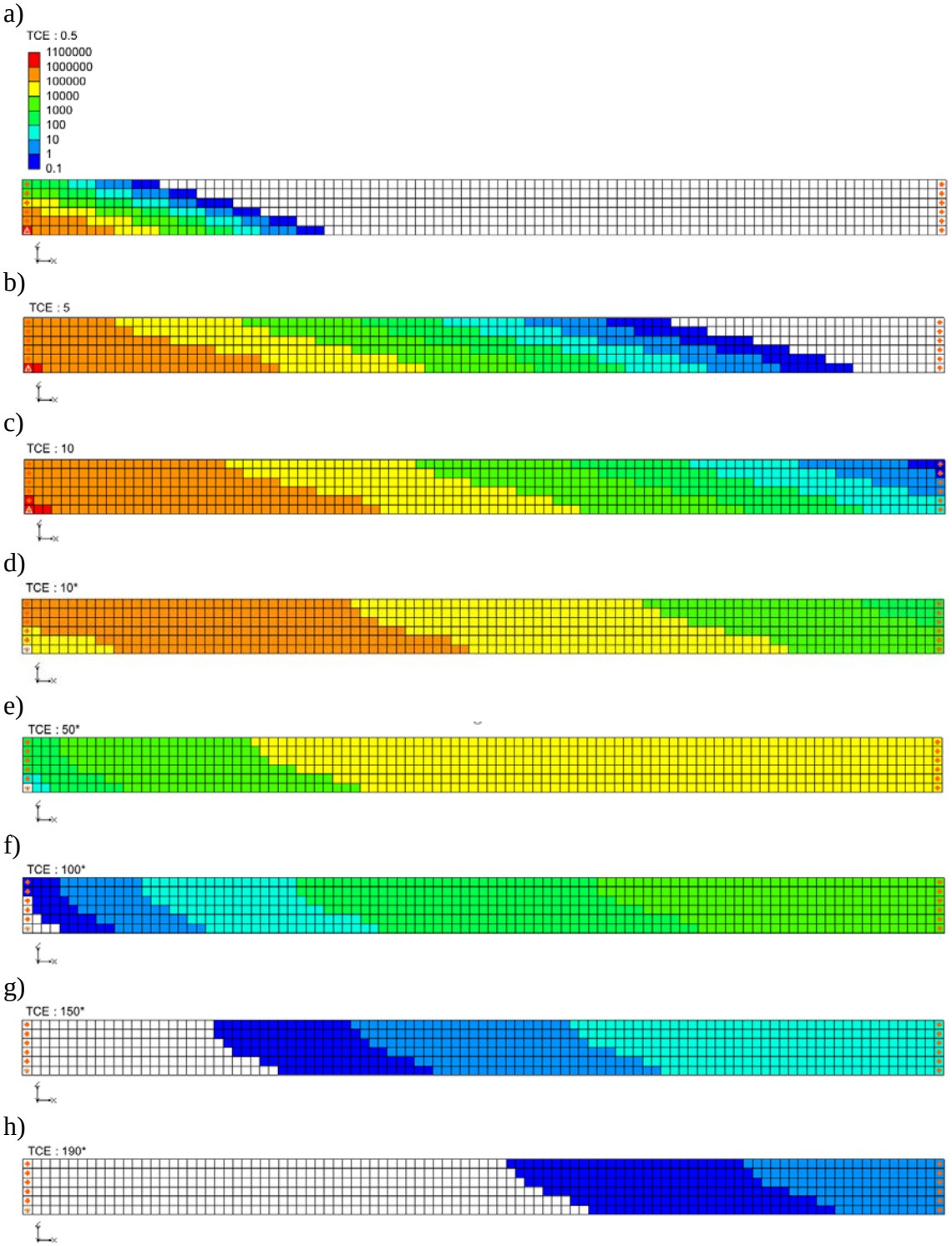

Figure 20. TCE concentration contours at a) 0.5 years, b) 5 years, c) 10 years, d) 10* years (20 yrs) e) 50* years (60 yrs), f) 100* years (110 yrs), g) 150* years (160 yrs), and h) 190* years (200 yrs) for two-layer system of equal thickness scenario (z magnification = 50).

The effect of matrix diffusion is more visible in the flushing period, with a persistent plume that is still present at 200 years, although in a diluted form, with concentrations between 10 ppb (double of MCL) and less than 0.1 ppb (See Figure 20 e-h).

6.3.2. Semi-analytical model

Just as in the equal layer thickness scenario, the semi-analytical model was built with 100 cells in *x*-dir, one cell in *y* axis, and the same horizontal and transverse discretization. The vertical spacing was set as 0.6 m, using only one layer with embedded heterogeneities defined by volume fractions.

The semi-analytical model matrix diffusion area, A_{md}, remained the same as before since this parameter corresponds to the geometry of the *x* and *y* directions and these did not change. The Darcy flux was recalculated as 5.475 m/yr for the new sand volume fraction of 0.167 m. A higher diffusion length, *L*, was defined as 0.5 m, matching the clay layer thickness.

All the parameters needed for the semi-analytical model are summarized in Table 15, where those not mentioned above kept the same values as in the scenario with identical layer thickness.

Table 15. Input parameters in semi-analytical model for two-layer clay dominated system.

Description	Sand	Clay
Darcy velocity, v_x (m/yr)	5.475	-
Porosity, ϕ	0.3	0.5
Retardation factor, R	1	2
Matrix tortuosity, τ_l	-	0.794
Reaction rate constant, λ (yr^{-1})	0.0693	0.0693
Diffusion coefficient, D (m^2/yr)	-	3.15E-2
Source concentration, C_0 (kg/m^3)	1.1	-
Longitudinal dispersivity, α_x (m)	N/A	
Transverse dispersivity, α_y (m)	N/A	
Vertical dispersivity, α_z (m)	0	
Δx (m)	5	-
Δy (m)	1	-
Δz (m)	0.6	-
Matrix diffusion area, A_{md} (m^2)	-	5
Sand volume fraction, ~~V~~$_f$	-	0.167
Characteristic diffusion length, L (m)	-	0.5
Number of elements (x-dir)	100	-
Number of layers (z-dir)	1	-
Source time duration (yr)	10	-
Δt (yr)	0.02	
Number of time steps	10000	

6.3.3. Testing

Figure 21 contains the outlet TCE concentration time series for the MT3DMS model and the semi-analytical model, with the inset providing the zoomed-in view of the TCE outlet concentration reaching the MCL. The effect of the matrix diffusion process is evident in the graphs with the lower concentration reached in the outlet face of the model and the longer period of time needed for reducing the outlet concentration to acceptable levels.

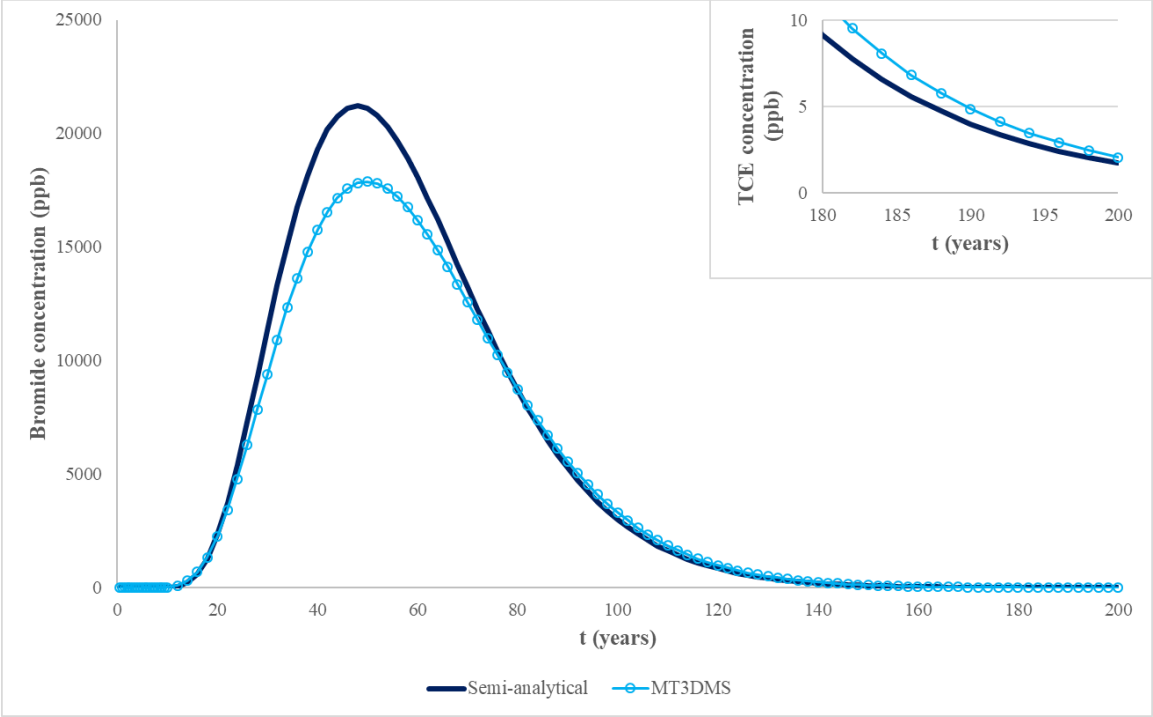

Figure 21. TCE outlet concentration vs time profile comparing the semi-analytical model with MT3DMS data in two-layer clay dominated system. Inset: zoomed-in view of tail for MCL arrival.

Due to the diffusion flux going into the low permeability material, the more of the contaminant is stored in the clay, reducing the amount of mass transported in the transmissive zone, leading to decreased outlet TCE concentrations when compared to the scenario with identical sand and clay layers. When the contaminant source is removed, the concentration gradient is reversed, and the diffusion flux goes from the low permeability material to the sand. Even though the advective flushing is reducing the concentration of TCE in the system, the contribution of the diffusive flux to the total mass is such that it decreases the rate at which the contaminant is being flushed out of the control volume.

The TCE concentration curves in Figure 21 show a rise in concentration from time zero to about 50 years, around the time the maximum TCE concentration is reached in both models; after 50 years the concentration trend reverses and there is a fast decrease in concentration before showing tailing behavior at about 100 years. The numerical model seems to be underestimating the outlet concentrations of TCE, especially at the peak of the curves around 50 years; however, the curves crossover approximately at 80 years and the TCE outlet concentrations estimated by the MT3DMS model are higher than those from the semi-analytical model, as seen in the inset of Figure 21.

The outlet concentration of TCE reaches values below the MCL at 190 yrs and 188 yrs according to the numerical and semi-analytical simulation, respectively. This is more than triple the time needed in the previous case, which only needed 50 years to reach acceptable values. The difference in arrival times between both models is two years (~1.1%), with the semi-analytical simulation achieving the MCL faster. The calculated coefficient of determination for this case was 0.978, which combined with the visual comparison and difference in times to reach the MCL, imply that the results of the semi-analytical method are consistent with the numerical simulation, with some deviation.

In order to further assess the accuracy of the semi-analytical method in this scenario, an additional MT3DMS simulation was run, reducing the size of the gridblocks in the vertical direction to improve the accuracy of the numerical model. The goal was to verify whether it improved the fit with the semi-analytical model or on the contrary, suggested that the semi-analytical approximation disagreed with the fully numerical solution.

The vertical spacing was decreased by an order of magnitude to 1 cm, causing the number of layers to increase to 60 in GMS and providing a numerical model of about 6000 gridblocks. Δz was the only parameter that changed in the simulation.

When this model was run, it resulted in a run-time error and the simulation was aborted by MT3DMS. After checking the .out file for the simulation, it was found that a maximum temporal discretization of 3.7×10^{-4} yrs was necessary for stability of the dispersive term. A new $\Delta t = 2.5\times10^{-4}$ yrs was used for another attempt, running successfully. The results were plotted against the TCE outlet concentrations from the semi-analytical model and the MT3DMS model with 10-cm spacing in Figure 22:

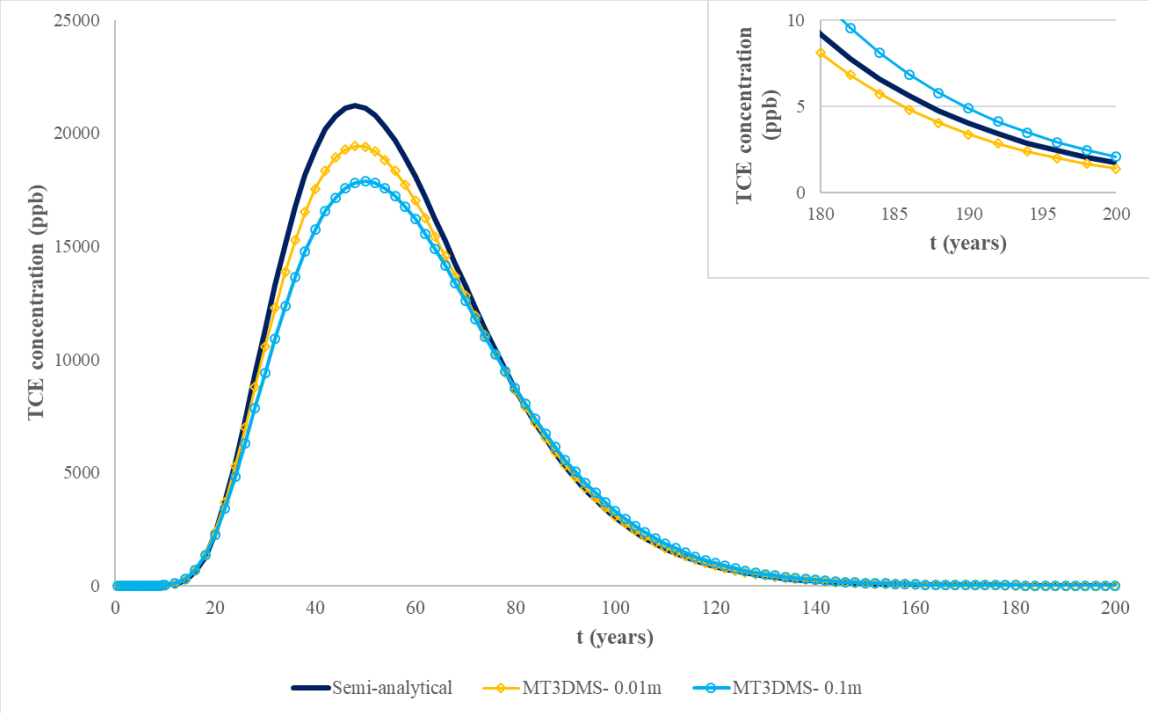

Figure 22. TCE outlet concentration vs time profile comparing the semi-analytical model with MT3DMS data in two-layer clay dominated scenario with spacing of 0.1 m (blue circles) and 0.01 m (yellow diamonds). Inset: zoomed-in view of tail for MCL arrival.

The reduction of the vertical spacing lead to the TCE curves between numerical and semi-analytical simulations being closer, especially at the peak of the graph at 50 years, supporting the hypothesis that the numerical model was underestimating the TCE outlet concentration around the concentration reversal because the gridblock was too big. The coefficient of determination for the model with 1 cm of vertical spacing was 0.995. The new time required for the MT3DMS model to reach values lower than the MCL was 186 years, maintain the same difference of two years, but in this case the numerical model reaches the MCL faster than the semi-analytical model. The visual and quantitative comparisons indicate an excellent fit between datasets. However, this refined grid required a very small temporal discretization (~0.1 day) that would add too much computational effort in bigger and longer models.

A third MT3DMS simulation was run with a finer vertical spacing of half a centimeter to evaluate the response of the numerical model. This resulted in a grid with 120 layers and a total of 12,120 cells. Once more, there was an issue due to stability reasons in the numerical simulation, even with the small $\Delta t = 2.5\times10^{-4}$ yrs.

The .out file showed a maximum value of 9.2×10^{-5} yrs for Δt. Therefore, the temporal discretization was further refined to 5×10^{-5} yrs, taking 18 h and 19 minutes in MT3DMS to complete the numerical simulation. The resulting concentration profile in Figure 23 was plotted alongside the previous MT3DMS models and semi-analytical model for comparison, providing a closer curve to the semi-analytical model around the peak and at later times (inset in Figure 23). The new R^2 was 0.998 and the time simulated by MT3DMS taken to reach values below the MCL was 188 years, matching the time for the semi-

analytical method, which support the visual comparison and verifies the improvement of the match between models.

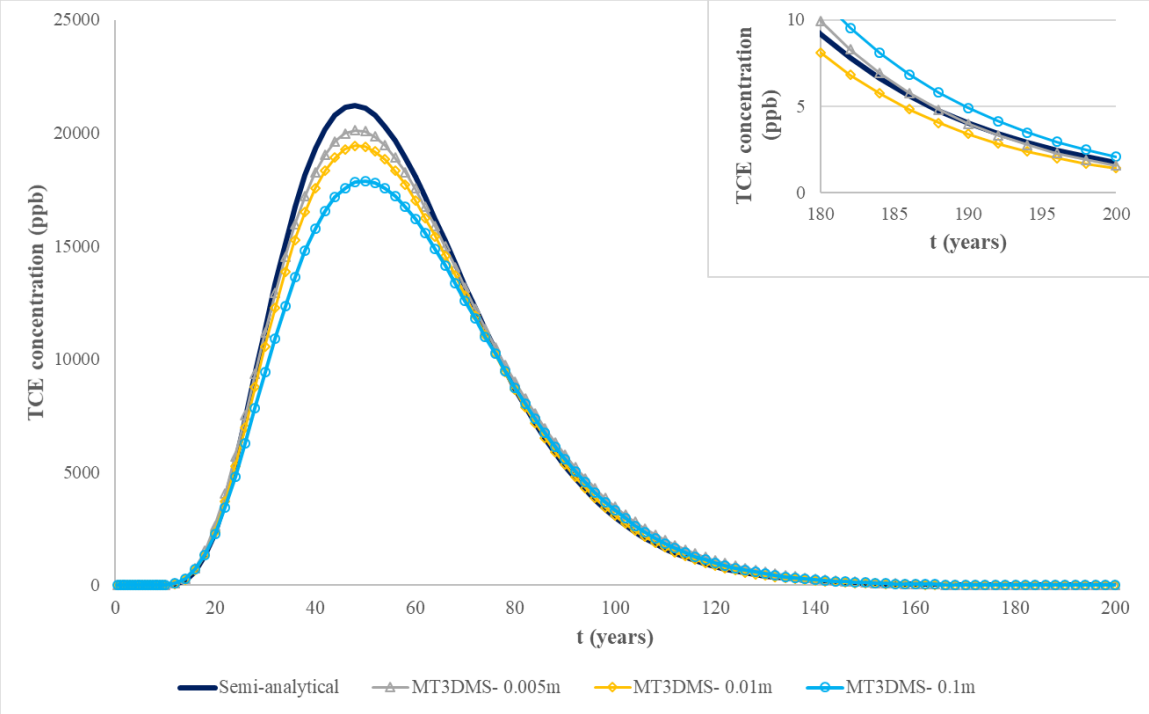

Figure 23. TCE outlet concentration vs time profile comparing the semi-analytical model with MT3DMS data in two-layer clay dominated scenario with spacing of 0.1 m (blue circles), 0.01 m (yellow diamonds), and 0.005 m (grey triangles).

This grid refinement exercise showed the amount spatial and temporal discretization necessary in numerical models to reproduce matrix diffusion effects. The Δt had to be reduced from about a week in the 10-cm vertical spacing to around 2 h for the 1-cm spacing, and 0.4 h for the half-a-cm spacing in MT3DMS for stability requirements.

Furthermore, the increased run-time with grid refinement is an important factor to consider, especially since the simulation time for the semi-analytical model was only about 22 seconds vs approximately 18 hours for the very refined grid. The use of very high resolution grids might not be practical for extensive 3-D models.

7. COMPARISON OF REMChlor's FORTRAN VERSION WITH NUMERICAL SIMULATION FROM T-PROGS MATERIAL DISTRIBUTION

After the excellent results obtained by comparing the semi-analytical method with MT3DMS in simplified scenarios, the evaluation of this method continued by creating a more complex system to model. The purpose of this was to assess the ability of the semi-analytical method to simulate matrix diffusion effects in scenarios that could be found in real-life sites. Two highly heterogeneous scenarios dominated by clay were created using the T-PROGS program (Carle, 1999). The obtained heterogeneous sand/clay distribution was an input to MODFLOW and MT3DMS for the flow field and transport simulation, respectively. This scenario was also modeled with the FORTRAN version of REMChlor-MD and the results obtained from both models were compared to evaluate the performance of the semi-analytical method with complex heterogeneous systems.

The Transition Probability Geostatistical Software (T-PROGS) is a program that uses transition probability geostatistics to generate models of aquifer heterogeneity (Carle, 1999). T-PROGS generates multiple realizations of geologic units or facies, which can be conditioned to borehole data. This capability is part of the GMS software package (Carle, 1999; AQUAVEO, 2016; AQUAVEO, 2017).

The hypothetical site was created modifying the T-PROGS tutorial borehole data (AQUAVEO, 2016), resulting in the 84 boreholes seen in Figure 24. The boreholes are representative of a sand/clay scenario dominated by clay and the borehole data is presented in Appendix B.

Figure 24. Boreholes used for T-PROGS simulation (z magnification = 2).

The borehole data was imported in the T-PROGS module, which analyzed it to determine transitional tendencies, proportions, and mean lengths of the materials. This information is used to generate plots describing the transition probability from one material to the other as seen in Figure 25. The dashed line corresponds to the transition probability measured from the boreholes. The solid green lines are known as Markov Chains and they are used to formulate the equations used by T-PROGS to generate the material sets in the simulation (Carle, 1999; AQUAVEO, 2016).

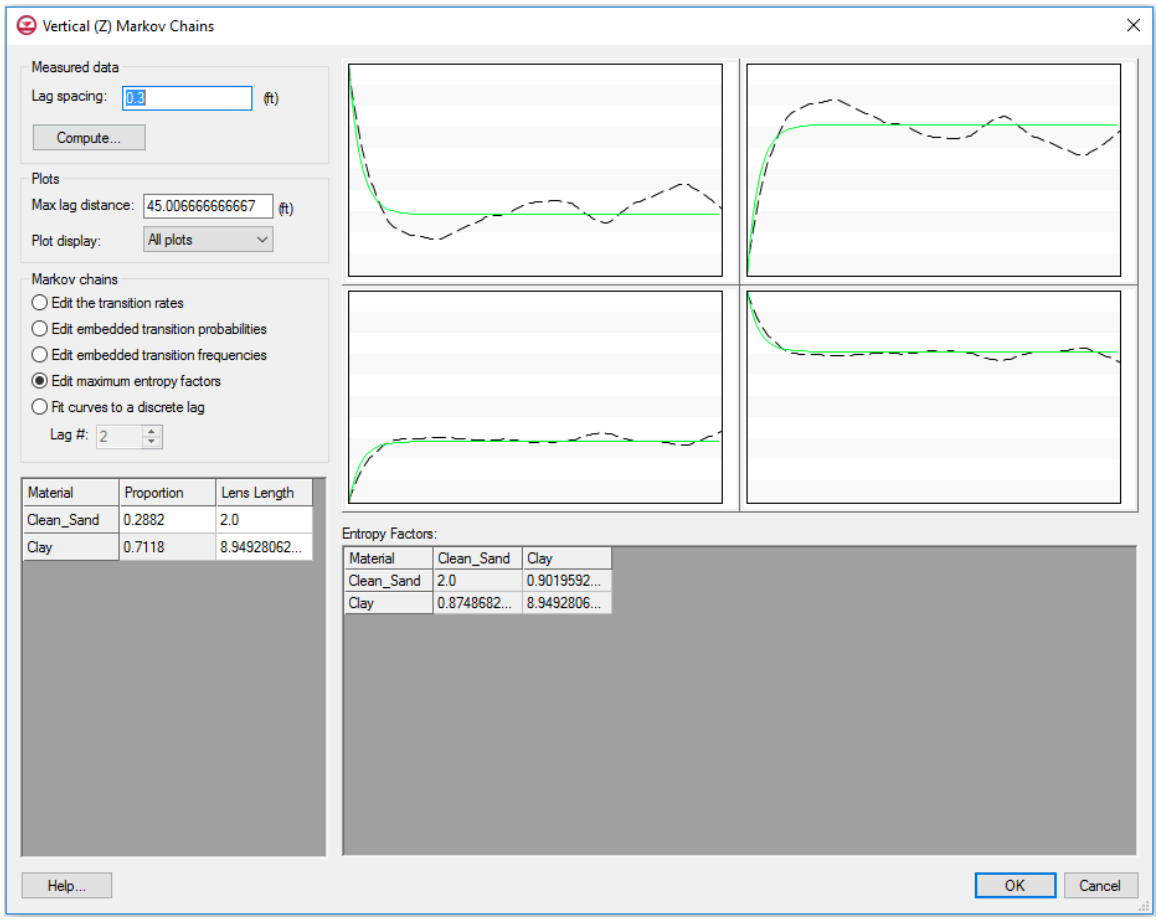

Figure 25. Transition probability in the vertical direction for the T-PROGS interface in GMS.

The Markov Chains are built by plotting transition probability against lag spacing (distances between data pairs under analysis). They are based on the proportions, lens lengths, and transition rates of the materials as shown in Figure 26:

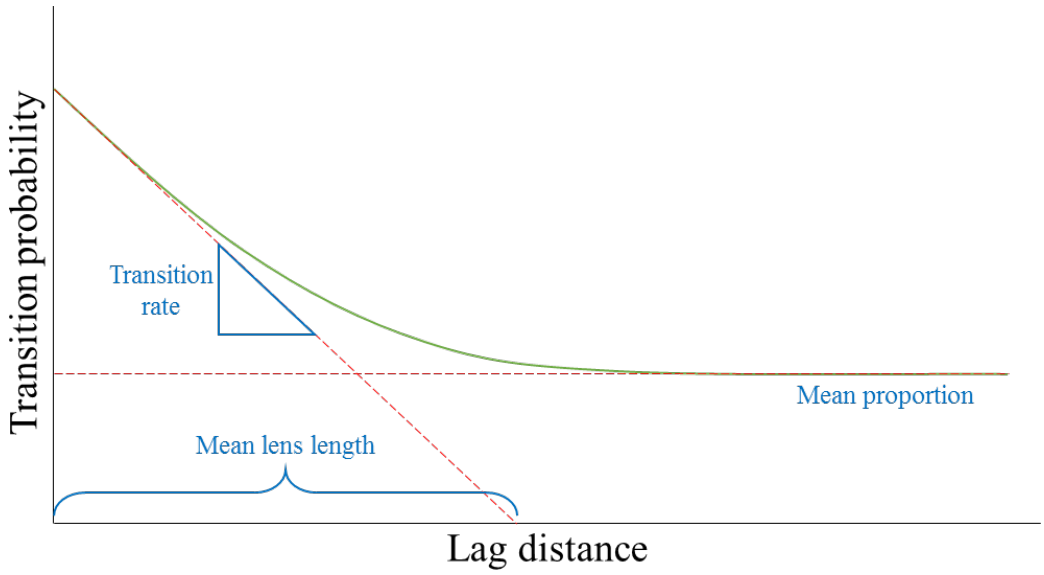

Figure 26. Markov Chain diagram. Modified from T-PROGS tutorial (AQUAVEO, 2016).

The transitions in the vertical direction are developed first, from the borehole data, and T-PROGS makes an automatic attempt to fit the curves, setting the transition rates and mean proportions of the predominant material (clay in this case). The data for the strike (x) and dip (y) directions are calculated from the vertical data (z), defining a lens ratio, as follows:

$$Lens\ ratio = \frac{L_{desired\ direction}}{L_z} \tag{50}$$

After defining the Markov Chains in the three directions, another component of the T-PROGS interface is run to generate the material sets, which can be used as an input for a flow field construction with MODFLOW.

The process of creating the T-PROGS material distributions and subsequent MODFLOW and MT3DMS simulations was an intensive trial and error exercise. Different

parameter combinations were used in the T-PROGS module, such as the proportion and vertical lenses length of the sand, and the length ratios for the strike and dip direction. After this, MODFLOW was run using the Newton solver to create the flow field. The MT3DMS mass transport simulation required numerous attempts to generate a plume that fit within the boundaries of the model, modifying location and size of the source, and TCE concentration. The configuration of the grid had to be modified a few times as well to reduce the computational effort of the simulation to a reasonable level of about 70 hours.

As a result of the different combination of parameters used, two distinct configurations were chosen from the T-PROGS simulation. One of them consisted of a system with suspended long sand zones, as a way to ensure groundwater flow through the model, referred to as the "lens case" from now on. The second configuration used was a visually random distribution of materials in all directions, denominated as the "random case".

Since the MT3DMS/MODFLOW model was initially based on the T-PROGS tutorial it used the same units and grid orientation. The 3-D grid used for both cases was the same, with an extent of 3454.2 ft (1052.84 m) in *x*-dir, 2020 ft (615.7 m) in the *y*-axis, and 135 ft (41.15 m) in the vertical direction. The number of cells in *x* was 101 and 70 in *y*-dir. The grid spacing in the vertical direction was set as 10 cm, based on the grid refinement exercise carried out for the clay dominated scenario in the previous chapter and the size of the model, with the purpose of reducing the computational effort for these simulations. Therefore, the number of layers was set to 400, resulting in a model of 2,828,000 gridblocks. These parameters are summarized in Table 16:

Table 16. Grid configuration in GMS model for T-PROGS material sets generation.

Parameter	Value
Length in *x*	3454.2 ft 1052.84 m
Length in *y*	2020 ft 615.7 m
Length in *z*	135 ft 41.15 m
Δx	34.2 ft 10.42 m
Δy	28.86 ft 8.8 m
Δz	0.3375 ft 0.1029 m
Number of cells in *x*	101
Number of cells in *y*	70
Number of cells in *z*	400

7.1. Lens case

7.1.1. MT3DMS model

After loading the borehole data into GMS and the T-PROGS module, the transition data was calculated automatically by the interface. The sand proportion of 28.82% was left unchanged, while its average length in the vertical direction was decreased from 3.65 ft (1.11 m) to 2 ft (0.61 m). The lens ratios for the *x* and *y* direction are 10 by default; the horizontal ratio was set to 118.67 and the dip lens ratio kept its original value. All of the parameters used for the T-PROGS simulation are listed in Table 17:

Table 17. T-PROGS parameters for lens case.

Parameter	Sand	Clay
Proportion	0.2882	0.7118
Lens length in *z*	2 ft 0.61 m	8.95 ft 2.73 m
Lens ratio in *x*	118.67	65.50
Lens ratio in *y*	10	5.52

The material set generated is shown in Figure 27 and displays elongated sand zones in the horizontal direction, as discussed before. The vertical magnification was set as 2 in order to have a better view of the material distribution. Different views in GMS allow one to appreciate the heterogeneity of the model.

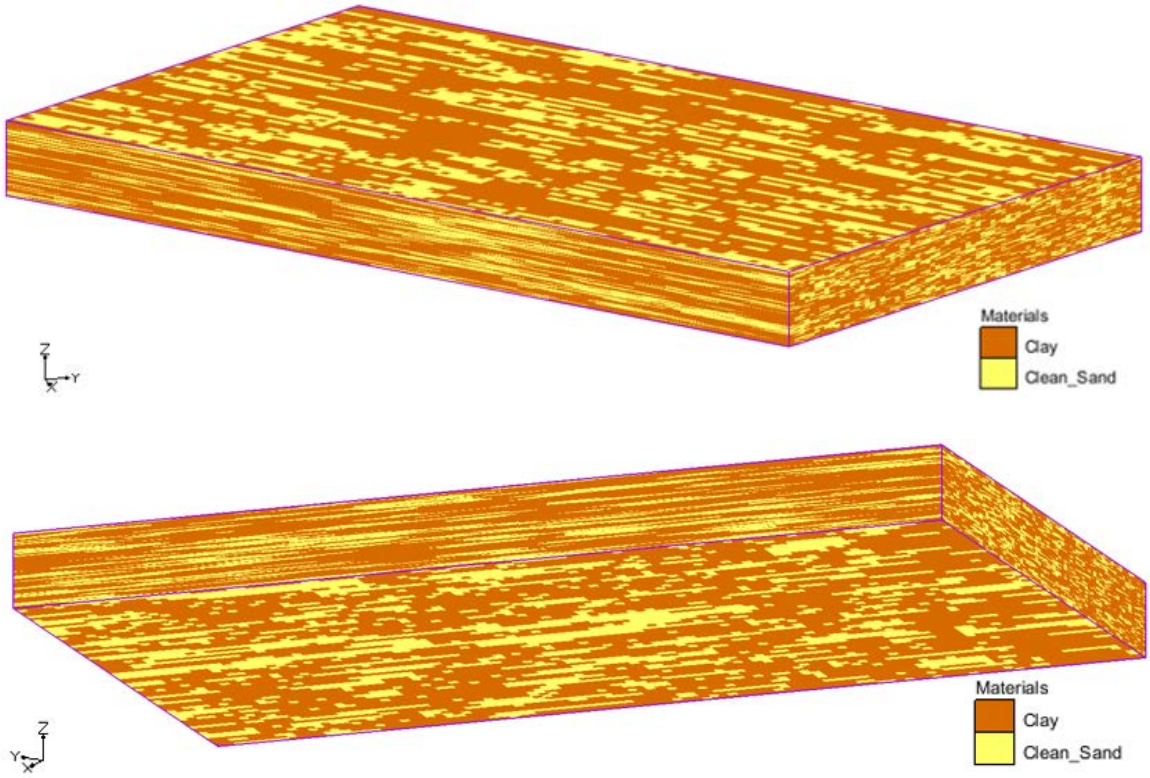

Figure 27. Material distribution from T-PROGS for lens case (z magnification = 2).

In order to create the flow field, the sand and clay properties were edited in the "Materials" window, setting the porosity to previously used values in the MT3DMS/MODFLOW model. The hydraulic conductivity was set as 30 ft/d (9.14 m/d) for the sand and 1×10^{-3} ft/d (3.05×10^{-4} m/d) for the low permeability material.

The flow model is three dimensional, steady-state, heterogeneous, and anisotropic. Two specified head boundary conditions are used to represent the head gradient that causes the flow of groundwater through the model, as shown in Figure 28:

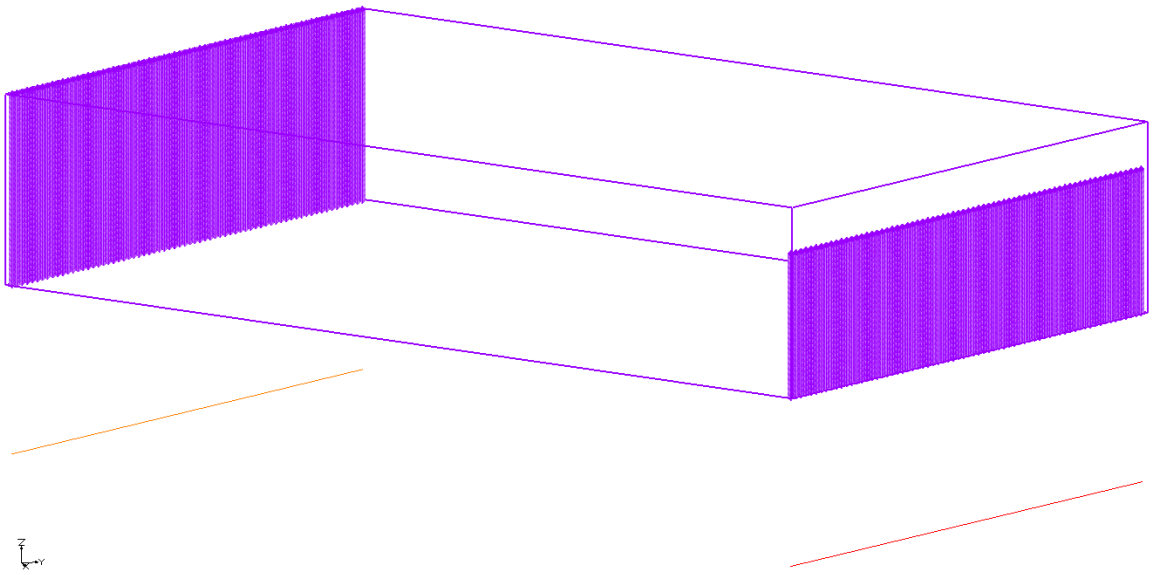

Figure 28. Specified head conditions for the flow field in lens case.

The maximum hydraulic head was set equal to the top elevation of the model. Because the grid had a vertical origin in 119.62 ft (36.46 m) the top elevation and thus, maximum hydraulic head was 254.62 ft (77.61 m). The minimum hydraulic head was estimated from the change in head, which in turn was calculated from the hydraulic gradient needed for a Darcy flux in the sand of 0.09 m/d (107.78 ft/yr). The estimated change in head of 33.66 ft (10.26 m) lead to a minimum hydraulic head calculation of 220.96 ft (67.35 m). The

MODFLOW simulation took about 17 minutes in a workstation with an Intel i7 CPU at 3.60 GHz, and provided the head contours shown in Figure 29:

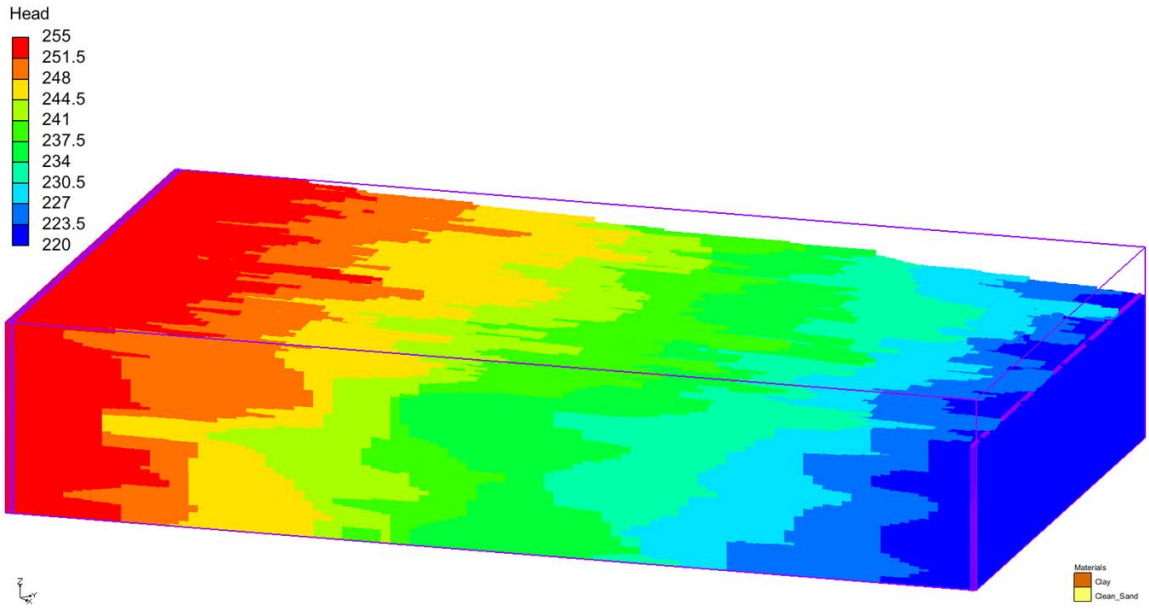

Figure 29. Head contours for lens case.

The simulation time for the mass transport model was set to a total of 230 years. A TCE source of 10,000 ppb was placed downstream from the model inlet (column 15) to reduce the observed lateral dispersion of the plume when the source was located in the first column of the model. The contamination source was laid out over a total area of 389.57 ft^2 (36.19 m^2) comprised by two cells in the *y* direction and 20 gridblocks in the *z* direction. The constant concentration condition was set only in the sand cells of the source area, represented in Figure 30 as blue triangles and outlined by the red square:

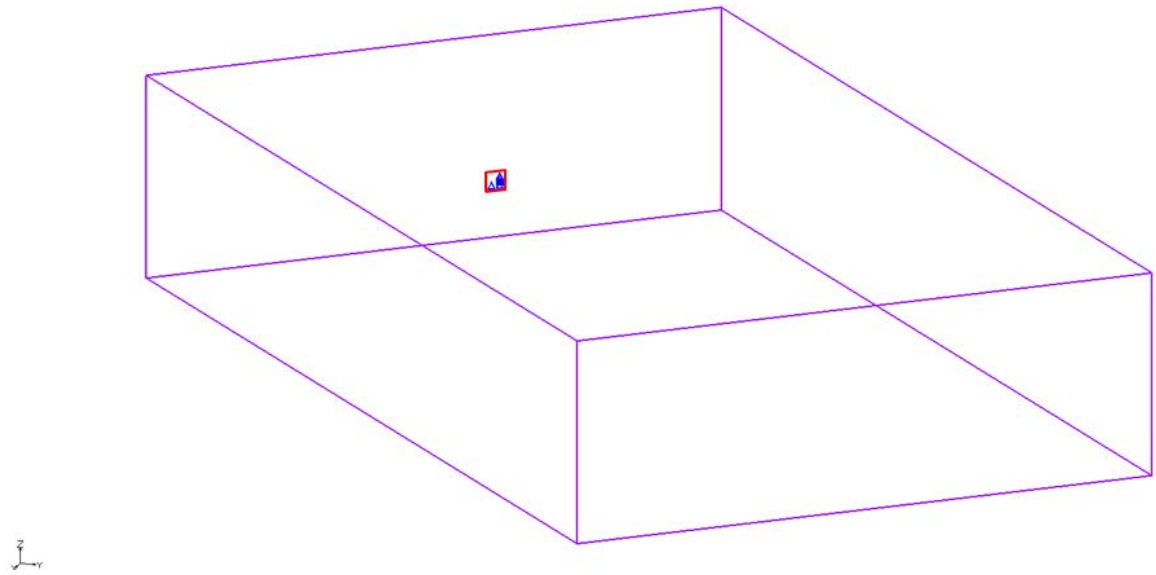

Figure 30. Location of TCE source in lens case.

The contaminated sand cells can be more appreciated by zooming into the source area and showing the distribution of materials as seen below in Figure 31. A closer look into Figure 31 showed that the TCE is located in a total of 18 cells of the MT3DMS model (blue triangles). The TCE source was maintained constant for 30 years, at which point it was removed, and followed by advective flushing for 200 years. As in the previous numerical models, the Δt was defined as 0.02 years.

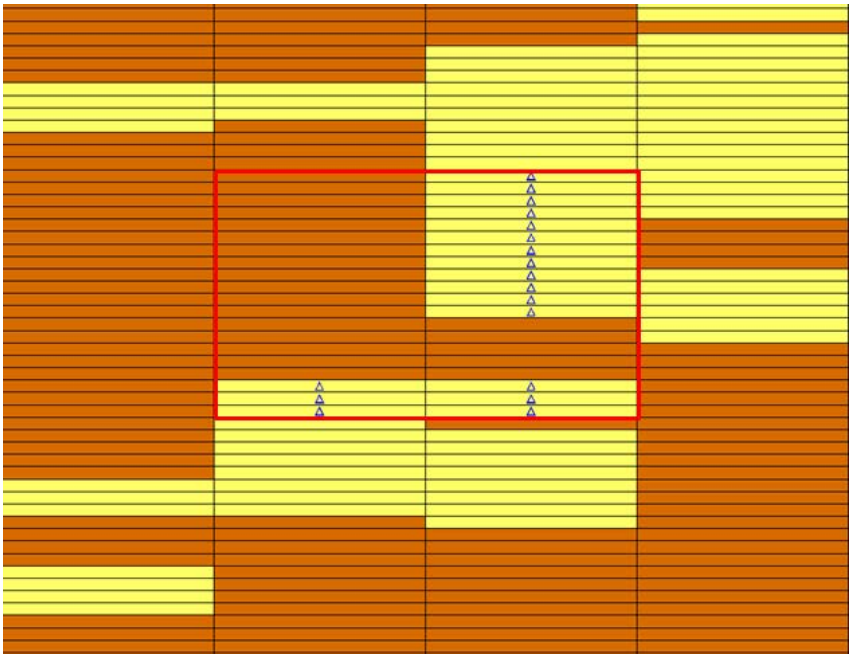

Figure 31. Contamination source in MT3DMS model of lens case.

The effective diffusion coefficient was fixed to 0.2694 ft^2/yr (0.025 m^2/yr). The longitudinal dispersivity was defined as 3.281×10^{-2} ft (1 cm). The transverse and vertical dispersivities were also specified, having equal values of 3.281×10^{-3} ft (1 mm). Retardation and degradation were not considered with the intention of incorporate them after achieving the comparison with this simplified case. However, after finishing the comparisons with REMChlor-MD for the lens and random case time was running short and thus, the incorporation of retardation and degradation was left for future work. The parameters used for the MODFLOW and MT3DMS simulation are condensed in Table 18:

Table 18. Parameters used in MODFLOW and MT3DMS for case of material distribution generated by T-PROGS.

Description	Sand	Clay
Porosity, ϕ	0.3	0.5
Hydraulic conductivity, K	10950 ft/yr 3337.56 m/yr	0.365 ft/yr 0.111 m/yr
TCE source concentration, C_0 (ppb)	10,000	-
Effective diffusion coefficient, D	0.2694 ft^2/yr 0.0250 m^2/yr	
Maximum hydraulic head, h_{max}	254.62 ft 77.61 m	
Minimum hydraulic head, h_{min}	220.96 ft 67.35 m	
Longitudinal dispersivity, α_x	3.281E-2 ft 0.01 m	
Transverse dispersivity, α_y	3.281E-3 ft 1E-3 m	
Vertical dispersivity, α_z	3.281E-3 ft 1E-3 m	
Δt (yr)	0.02	
Source time duration, t_1 (yr)	30	
Release period (yr)	200	

Due to the size and fine discretization of the numerical model, a large computational effort was necessary to run the transport simulation. This resulted in several hours (6-8 h) for the mass transport simulation with the TCE source present, and up to 45 h for the simulation of advective flushing. The resulting TCE concentration contours throughout time are presented in Figure 32. The transparency of the contours had to be set to 70% in order to get a better visualization of the plume.

a)

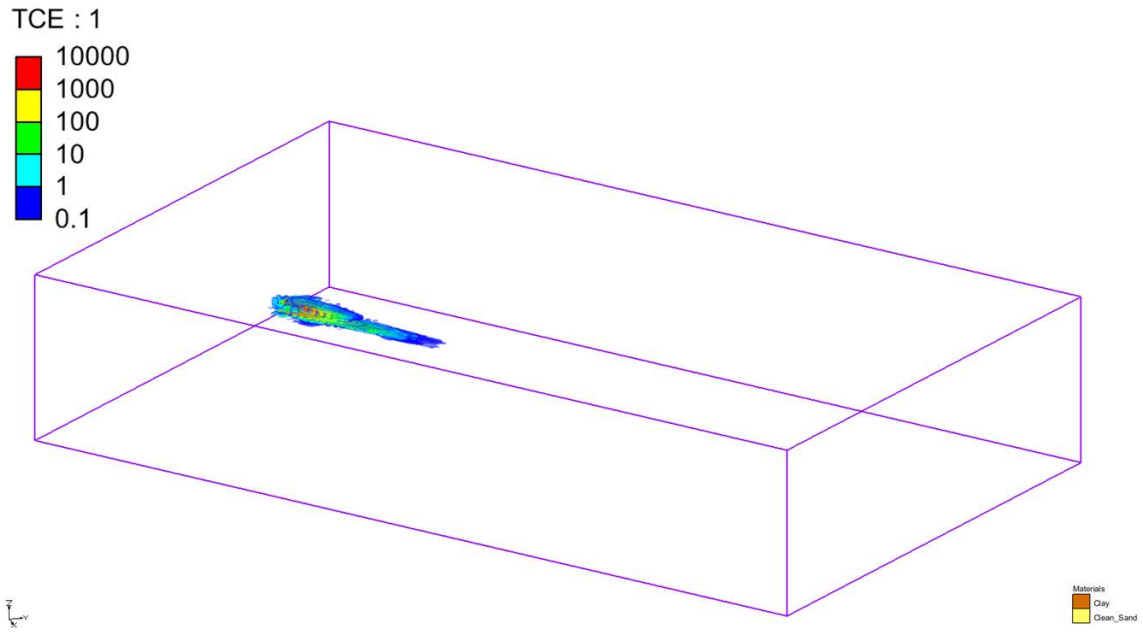
TCE : 1
10000
1000
100
10
1
0.1
Materials
Clay
Clean_Sand

b)

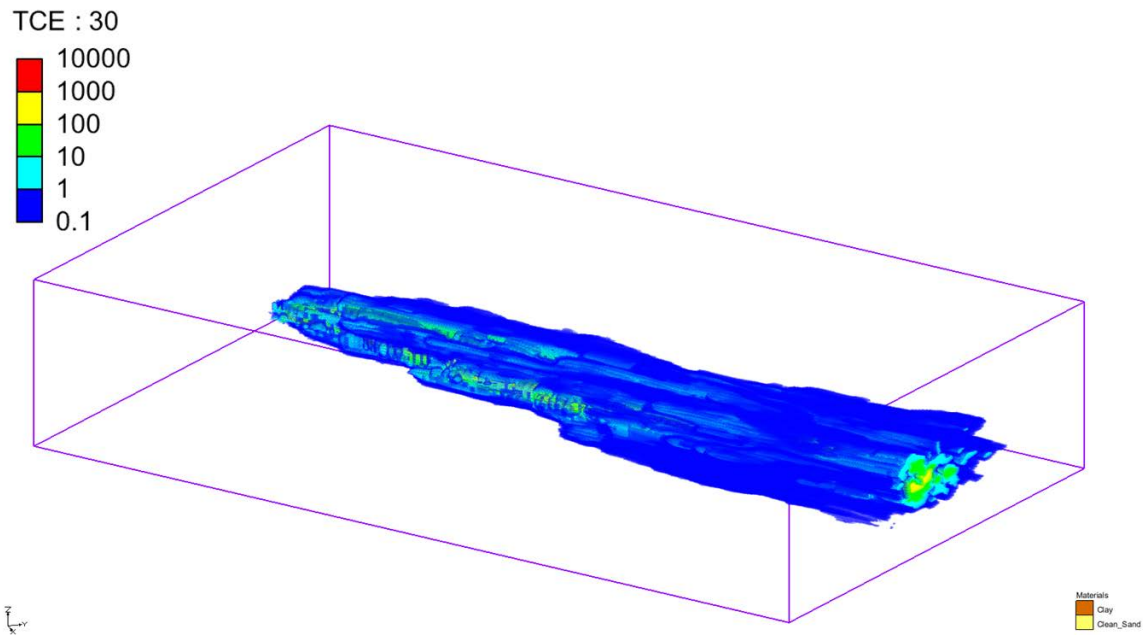
TCE : 30
10000
1000
100
10
1
0.1
Materials
Clay
Clean_Sand

c)

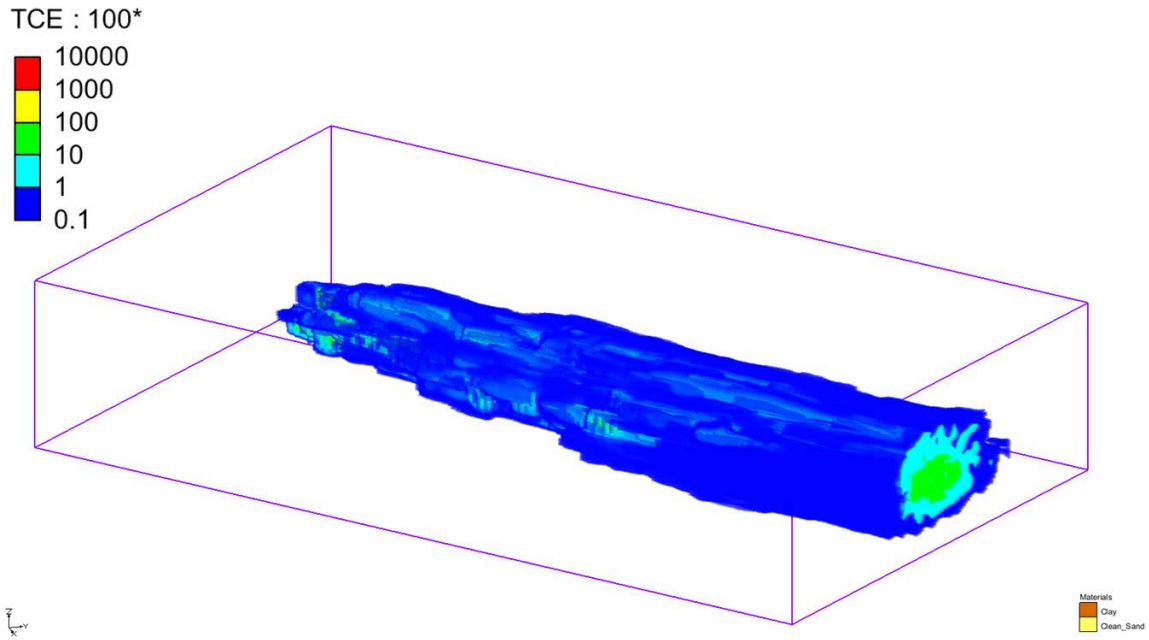

d)

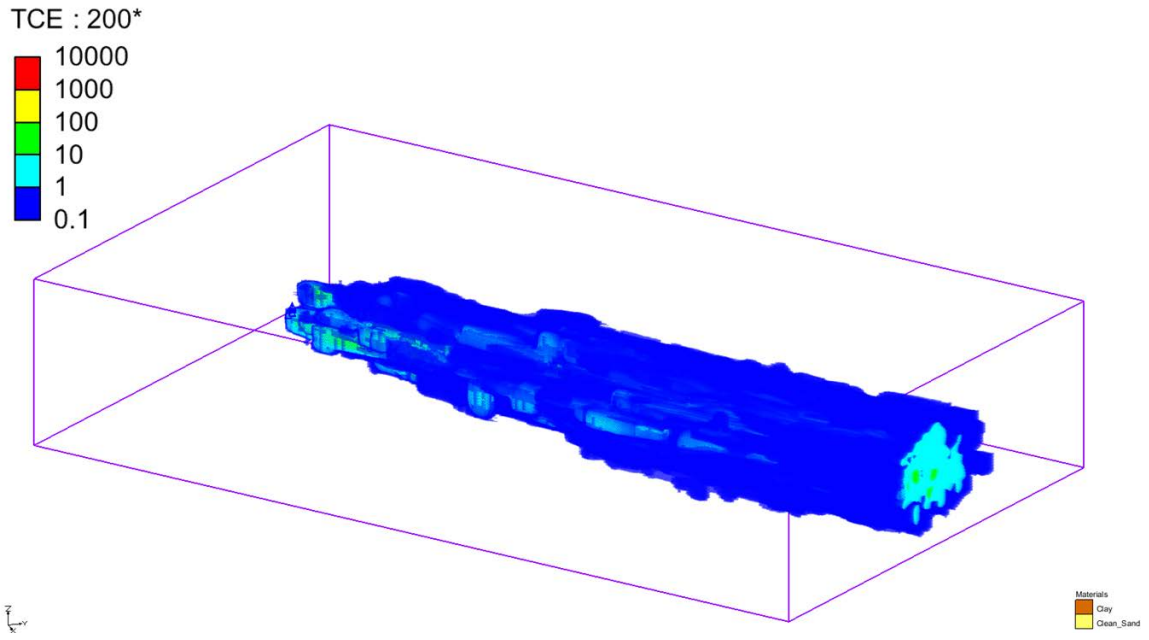

Figure 32. TCE concentration contours at a) 1 year, b) 30 years, c) 100* years (130 yrs), and d) 200* years (230 yrs) for lens case (z magnification = 5).

The concentration contours in Figure 32 show small changes over time once the plume reaches the outlet of the model. The plume achieves some lateral and vertical spreading due to advection through the highly heterogeneous grid. After the source is removed, there is some shrinkage of the contamination plume and a reduction in the concentrations of the outlet face of the model, represented by the color change in the contours. It is recommended to make slices parallel to the horizontal and vertical direction in order to have a better view of the concentration behavior. This will be shown in the testing section (7.1.3) for direct comparison of the plumes from the MT3DMS and semi-analytic models.

7.1.2. REMChlor-MD model

The implementation of the semi-analytical method was performed with the FORTRAN formulation of REMChlor-MD. The information needed to run the model is essentially the same as with the Visual Basic version, with small differences in the input parameters. The REMChlor model uses SI units and therefore, will be presented in such a way.

For the embedded heterogeneity case, the semi-analytical method works under the assumption that the high permeability zone is well mixed. Therefore, the REMChlor-MD model uses a homogeneous, uniform velocity in the transmissive zone.

In this formulation of REMChlor-MD, only half of the model in the y-dir is being simulated due to assumed symmetry about $y = 0$. This assumption is illustrated in Figure 33 below, where the specified grid and source of the REMChlor-MD model is represented by the solid lines and the symmetric counterparts are displayed in the dashed lines.

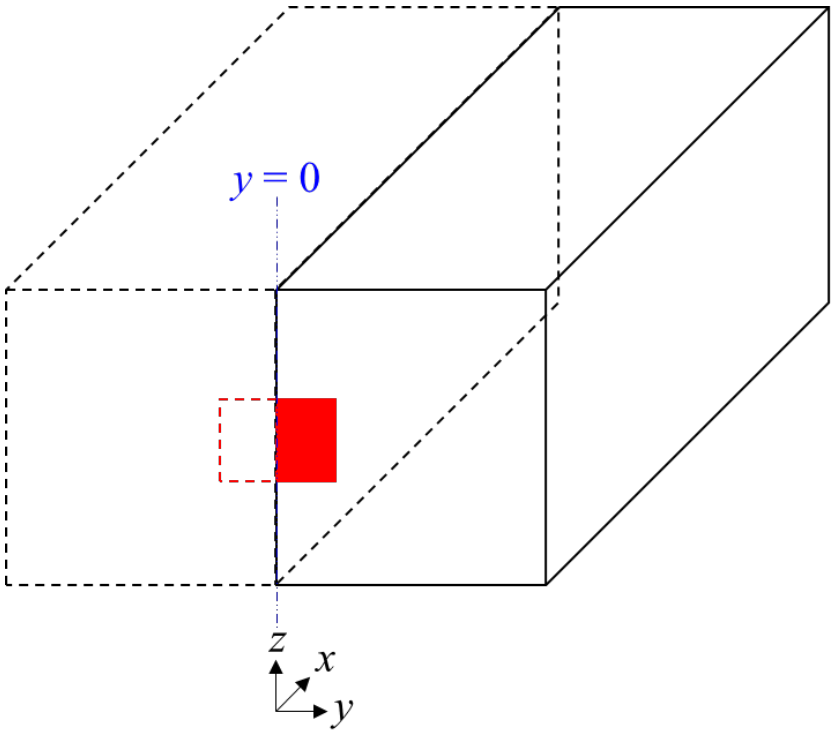

Figure 33. Symmetry about $y = 0$ assumed in REMChlor-MD.

The approach followed to set up the REMChlor-MD model was to fit the approximated area of the source in MT3DMS into one active gridblock of the semi-analytical model, making sure that the mass discharge from the source in REMChlor-MD matched the MT3DMS value. This was accomplished by modifying the initial concentration of TCE in the source gridblock in REMChlor-MD.

The grid spacing in the horizontal direction was set equal to the GMS simulation to maintain its numerical dispersion. Considering only the distance between the contaminant source to the outlet of the model in the GMS model, the calculated number of cells in the horizontal direction was 87. Δy was also set equal to its counterpart in the numerical model in order to fit the contamination source in one active gridblock of the semi-analytical

model. Analyzing the plume extents from the concentration contours in the MT3DMS model and the Δy value specified, it was determined that only 18 cells in the *y* direction were necessary in the REMChlor-MD model to capture the TCE plume obtained from MT3DMS.

An analysis of the contamination source in MT3DMS was made to define the REMChlor-MD discretization in the vertical direction. As discussed before and shown in Figure 31, the contamination (blue triangles) was placed in a total of 18 contaminated sand cells. The TCE source in MT3DMS was approximated as a rectangular area equal to $2\Delta y 9\Delta z$. Subsequently, the vertical spacing in the REMChlor-MD model was set equal to $9\Delta z$ of the MT3DMS model so only one semi-analytical cell contained the vertical extent of the TCE source in MT3DMS. This corresponds to a vertical spacing of approximately 0.926m.

The difference in discretization between MT3DMS and REMChlor-MD for this case can be observed below in Figure 34. The grid for the numerical model is displayed above in Figure 34a), the approximation of the source area in MT3DMS is shown in Figure 34b) to the left, and the semi-analytical model grid is shown in Figure 34b) to the right, with the dashed lines representing the symmetric complement of the REMChlor-MD model. The grid spacing in the *y* direction is the same for the two models. For the vertical direction, one semi-analytical cell is equivalent to nine MT3DMS gridblocks.

a)

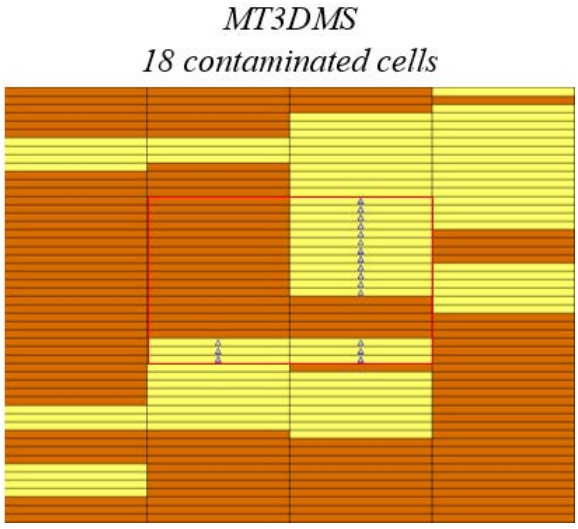

b)

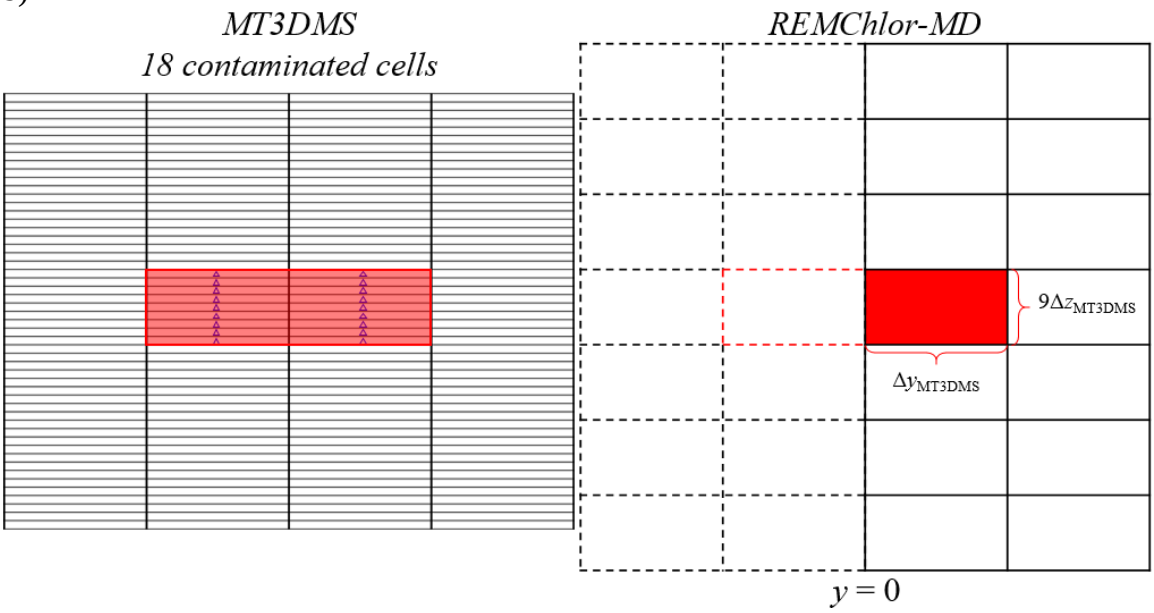

Figure 34. a) Grid spacing in MT3DMS, b) approximation of source area in MT3DMS (left), and grid spacing in REMChlor-MD (right) for lens case.

The plume extents in the *z* direction for the numerical model were also analyzed, concluding that only 36 semi-analytical cells were enough to model the contamination

plume in the vertical direction. This resulted in a much coarser grid than MT3DMS, with a total of 56,376 gridblocks for the REMChlor-MD model.

The Darcy velocity used in REMChlor was calculated as the average between the Darcy velocity in the inlet and outlet face of the MODFLOW model, obtaining 5.614 m/yr. In order to match the contaminant mass rate leaving the source from the MT3DMS model, the average concentration of TCE in the source area was calculated using the Darcy flux and the REMChlor-MD source area:

$$C_{TCE} = \frac{\dot{m}_{MT3DMS}}{v_{d,REMChlor-MD}(2\Delta y \Delta z)} \tag{51}$$

where C_{TCE} is the TCE source concentration in REMChlor-MD , $\dot{m}_{MT3DMS}$ is the mass rate leaving the source from the MT3DMS model, and $v_{d,REMChlor-MD}$ is the Darcy velocity used in the semi-analytical model. Δy and Δz are the REMChlor-MD transverse and vertical grid spacing, respectively.

Because only half of the model in the y direction is simulated in REMChlor-MD (assuming symmetry about $y = 0$), the cross-sectional area of the semi-analytical source gridblock is half of the approximated cross-sectional area of the source in the MT3DMS model. The REMChlor-MD gridblock cross-sectional area is multiplied by a factor of two in order to estimate the volumetric flow rate leaving the MT3DMS source with the REMChlor-MD parameters. The contaminant mass rate leaving the source in the MT3DMS is calculated as:

$$\dot{m}_{MT3DMS} = \sum Q_i C_i \tag{52}$$

The TCE mass flow out of each contaminant cell in the MT3DMS model was analyzed with respect to the neighboring cells, neglecting the flow between fixed concentration cells. The information was extracted from the Flow budget tool in GMS and resulted in a total calculated TCE mass flow rate of 1.588 kg/yr. With this value the source zone concentration averaged over a cross-sectional area of 8.14 m^2 was 17400 ppb.

The source cone was held constant in REMChlor-MD at 17400 μg/L during the loading period. The on-off source condition is defined in REMChlor-MD with the parameters Gamma and *xremove*. Gamma is the exponent on the mass versus concentration relationship, and a value of zero represents a constant source concentration with time until the source is depleted (Falta et al., 2007; Falta, 2008):

$$\frac{C}{C_0} = \left(\frac{M}{M_0}\right)^{\Gamma} \tag{53}$$

The fraction of source mass removed, *xremove* was defined as one, given that all of the TCE is depleted at the time of remediation. The start and end of the remediation time, t_1 and t_2 were set as 30 yrs and 30.1 yrs, respectively. Again, this represents an abrupt total removal of the contaminant at the end of the loading period. There is no decay in the source, so its correspondent decay rate is defined as zero.

The placement of the source in REMChlor-MD is specified by three parameters: *lysource*, *lzsourcemax,* and *lzsourcemin*. The variable *lysource* is the number of cells in the *y* direction containing the source which was set equal to one because only half of *y* is being modeled. The variables *lzsourcemax* and *lzsourcemin* are the top and bottom layer numbers in the vertical direction containing source. These values were both set to 18 since only one

cell contains the TCE source in this case and it was placed in the center of the model. The REMChlor-MD grid and source location are displayed in Figure 35:

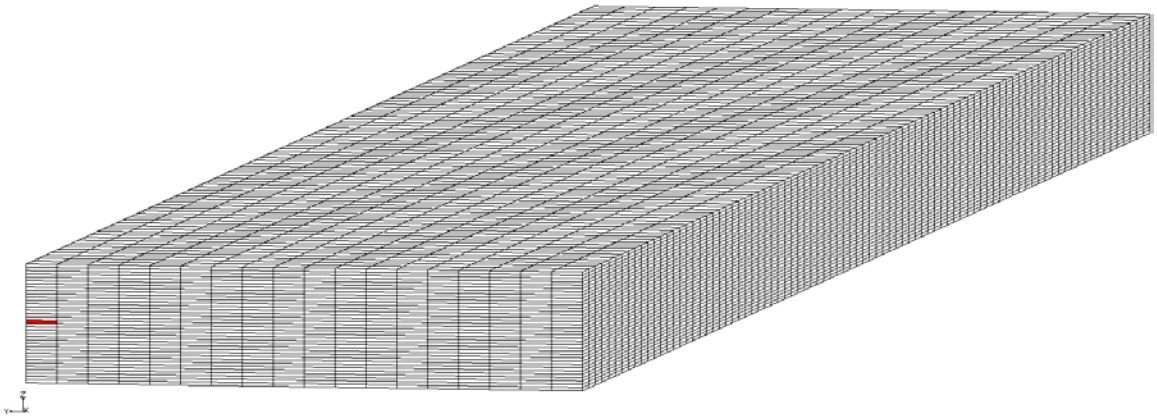

Figure 35. REMChlor-MD grid and source location (red) for lens case.

The parameters for transport in the transmissive zone were set equal to the values used in the MT3DMS/MODFLOW model, with the exception of the transverse and vertical dispersivities, set as 0.5m and 5×10^{-3}m, respectively. These two parameters used larger values than the GMS model to account for the lateral and vertical dispersion caused by the T-PGROS generated material distribution.

The formulation for REMChlor-MD does not use the input for the longitudinal dispersion until the value for α_x is higher than the numerical dispersion ($\Delta x/2$). The values for the transverse and vertical dispersivities were calibrated with the plume extents from the MT3DMS simulation. A trial and error procedure was followed assigning different values for α_y and α_z until the TCE concentration contours from the REMChlor-MD model resembled those from MT3DMS.

A matrix diffusion flag in REMChlor-MD corresponds to the type of scenario being modeled. The case of embedded heterogeneities has an assigned value of 2.

Properties like porosity, tortuosity, and retardation factor in the low permeability zone were set equal to the values in the MT3DMS model. The molecular diffusion coefficient for TCE is the same as used before, 3.15×10^{-2} m^2/yr. The sand volume fraction is equivalent to the 0.288 sand proportion stated in T-PROGS.

To estimate the characteristic average diffusion length, three randomly selected lateral faces of the model were chosen to determine the average thickness of clay in them. The selected faces for the determination of *L* corresponded to the rows (*x*-dir) 30, 68, and 93 in the numerical model. The selected cross-sectional areas are displayed in Figure 36.

Each vertical column in the face was treated as a separate borehole and the thickness of clay in each borehole section was measured and recorded. The clay thickness of the total cross-sectional area was calculated as a volumetric weighted average to give more contribution to higher diffusion lengths to the averaged value.

a)

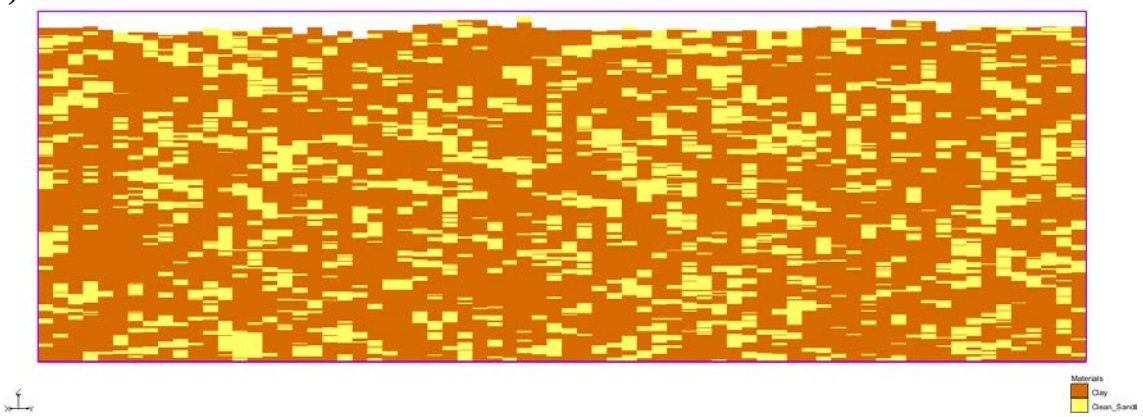

b)

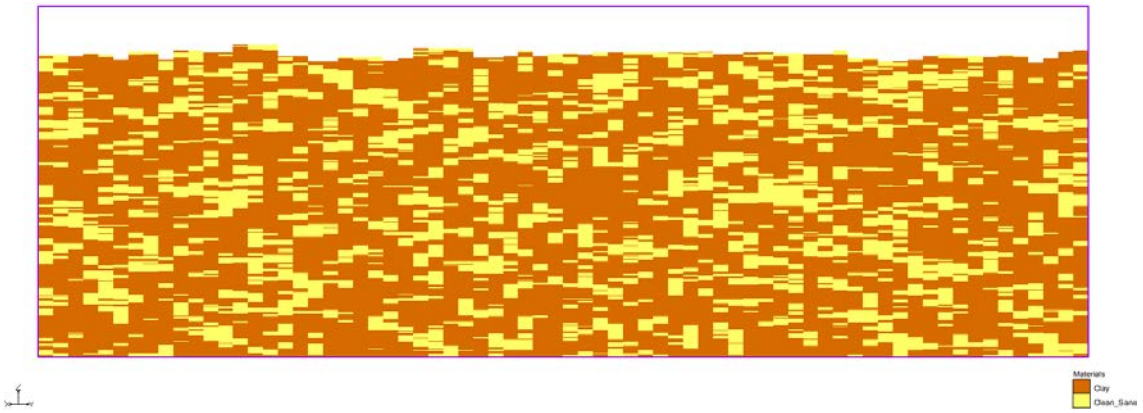

c)

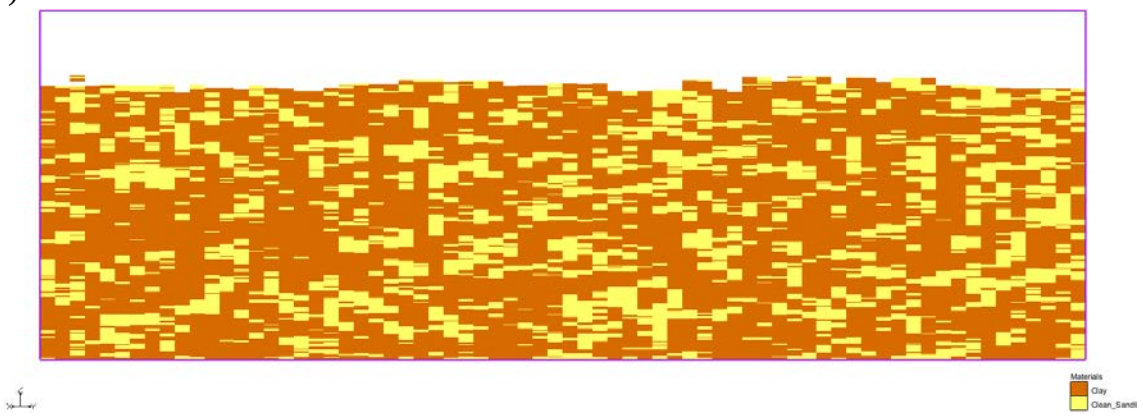

Figure 36. MT3DMS/MODFLOW model faces selected for estimation of *L* in lens case for a) j=30, b) j=68, and c) j=93.

To have a better understanding of how the estimation of *L* was carried out, consider the borehole shown below in Figure 37. The volume fraction of the small clay zone is given by its thickness divided by the total thickness of the borehole. The volume fraction of the big clay zone is calculated in the same manner. The volume weighted average thickness of clay in the borehole is the sum of the individual clay thicknesses weighted by their respective volume fraction, divided by the sum of the fractions.

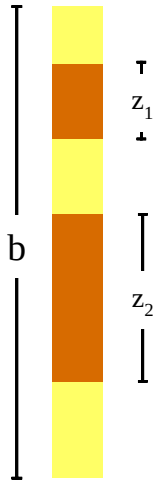

$$f_1 = \frac{z_1}{b} \qquad f_2 = \frac{z_2}{b}$$

$$z_{ave} = \frac{z_1 f_1 + z_2 f_2}{f_1 + f_2} = \frac{z_1^2 + z_2^2}{z_1 + z_2}$$

$$z_{ave} = \frac{\sum z_n^2}{\sum z_n}$$

Figure 37. Illustration of weighted average *L* calculation.

Since clay lenses usually have both top and bottom faces in contact with the transmissive zone, diffusion into the clay from both faces is thought to meet in the middle of the low permeability lens. Thus, the characteristic average diffusion length was calculated as half of the average clay thickness for each cross-sectional area in the MT3DMS/MODFLOW model, resulting in an average value of 1.85 m.

Due to the fact that the value for the sand volume fraction was directly obtained from T-PROGS, $\forall_f$ was kept the same and A_{md} was estimated from Equation 42. The obtained matrix diffusion area was 32.67 m^2.

The retardation factor of the low permeability zone was fixed as 1 since there was no sorption considered in the numerical model. The temporal spacing was set as 0.02 years at first to match the discretization in MT3DMS. It was later defined as half a year after running a small Δt refinement study to reduce computational effort of the REMChlor-MD model and provide essentially the same results.

The input parameters used in the REMChlor-MD model are listed in Table 19. REMChlor-MD is run in the Windows Command Prompt, requiring about a minute for the simulation of this 56,376-gridblock model. Run times of less than a minute have been possible using coarser grids.

Table 19. Input parameters in REMChlor model for lens case.

Description	Value
****Source terms****	
Initial source zone concentration, C_0 (kg/m^3)	1.74E-2
Initial source zone mass, m_{t0} (kg)	100
Gamma exponent, Γ	0
Fraction of source mass removed, *xremove*	1
Remediation start time, t_1 (yr)	30
Remediation end time, t_2 (yr)	30.1
Source zone decay rate constant (1/yr)	0
Source containing cells in *y*, *lysource*	1
Top layer number in *z*, *lzsourcemax*	18
Bottom layer number in *z*, *lzsourcemin*	18
Darcy velocity, v_d (m/yr)	5.614
****Transport terms in high K zone****	
High *K* zone porosity, ϕ	0.3
High *K* zone tortuosity, τ	0.669

Table 19 continued

Description	Value
High *K* zone longitudinal dispersivity, α_x (m)	0.01
High *K* zone transverse dispersivity, α_y (m)	0.5
High *K* zone vertical dispersivity, α_z (m)	5E-3
High *K* zone retardation, *R*	1
****Decay terms in High K zone****	
Zone 1 length for plume decay, x_1	1000
Zone 2 length for plume decay, x_2	2000
Period 1 for plume decay, $tplume_1$ (yr)	250
Period 2 for plume decay, $tplume_2$ (yr)	300
****Transport terms in low K zone****	
Matrix diffusion flag, *mdflag*	2
Low *K* zone porosity, ϕ_l	0.5
Low *K* zone tortuosity, τ_l	0.794
Low *K* zone retardation, R_l	1
Diffusion coefficient, *D* (m^2/yr)	3.15E-2
Matrix diffusion area, A_{md} (m^2)	32.67
Sand volume fraction, V_f	0.288
Characteristic diffusion length, *L* (m)	1.85
****Finite Difference Parameters****	
Δx (m)	10.424
Δy (m)	8.796
Δz (m)	0.926
Number of elements, *nx*	87
Number of *y* cells, *ny*	18
Number of layers, *nz*	36
Δt (yr)	0.5
Number of time steps	460

7.1.3. Testing

The MT3DMS and REMChlor-MD model estimated mass discharge rates in the outlet face of the model were compared to assess the accuracy of the semi-analytical method. The outlet face corresponds to the last row (*x*) of each model and its location is highlighted for

both models in Figure 38. The mass discharge rate was obtained from MT3DMS by activating the Transport observation package before running the simulation. The option to compute the mass rate at source/sinks was selected. After the simulation was completed, the mass rate at each time is automatically calculated by MT3DMS when selecting the specified head boundary condition (BC) located at the output face of the model. The specified head BC is represented by the purple cells in the highlighted area of Figure 38a):

a)

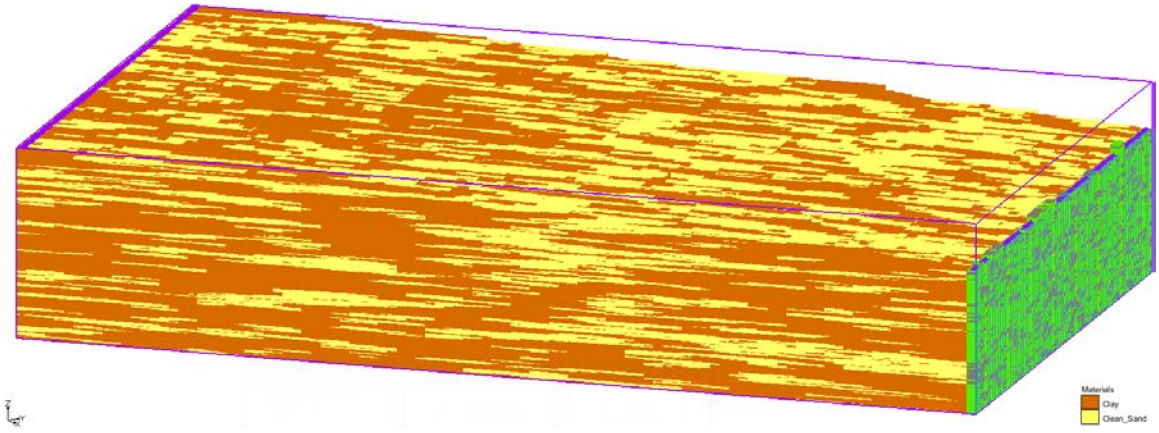

b)

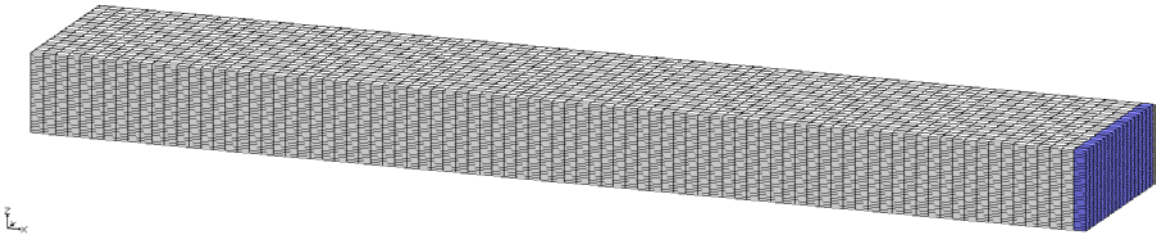

Figure 38. Location of outlet face for a) MT3DMS/MODFLOW and b) REMChlor-MD model.

For REMChlor-MD, the mass rate was calculated with the TCE concentrations given in the output of the model, the Darcy velocity, and total cross-sectional area of the source using the following equation at each time step:

$$\dot{m} = \sum_{\substack{outlet \\ face}} C_i Q_i = \sum_{\substack{outlet \\ face}} C_i v_d (2\Delta y \Delta z) \tag{54}$$

where C_i is the concentration of each gridblock in the outlet face of the model and Q_i is the individual gridblock volumetric flow rate. The graphs of mass discharge rate over time for MT3DMS and REMChlor-MD are displayed in Figure 39:

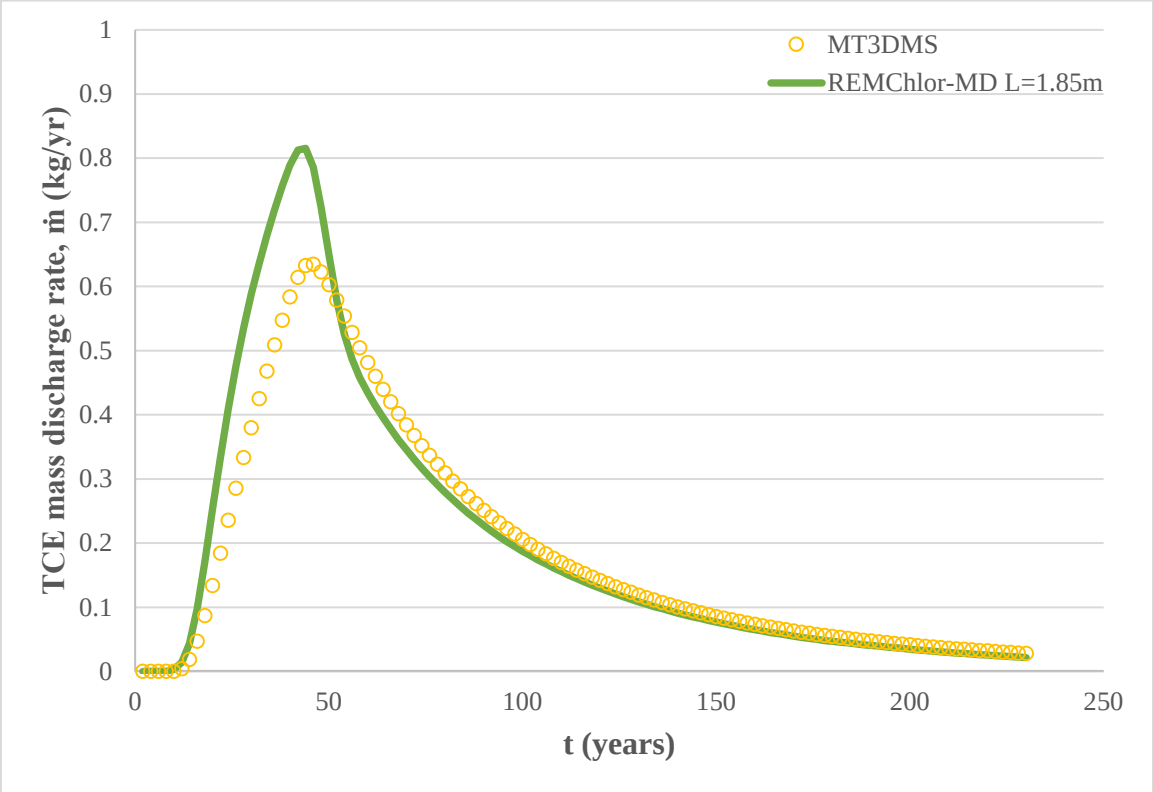

Figure 39. TCE mass discharge rate vs time profile comparing the MT3DMS model with REMChlor-MD for lens case with L = 1.85 m.

The comparison of the mass discharge rate graphs shows a fast rise and decrease of the mass discharge rate, followed by tailing behavior, corresponding to the trend observed in the effluent concentration profiles studied in previous chapters. The calculated coefficient

of determination was 0.849, suggesting an approximate fit of REMChlor-MD to the MT3DMS model, with room for improvement.

In order to compare the times needed to reach the TCE target concentration, the effluent concentration profile was constructed for both models. The concentrations in the outlet face of each model were estimated from the following expression:

$$C_{TCE} = \frac{\dot{m}}{Q} \tag{55}$$

The outlet TCE profile constructed is shown in Figure 40:

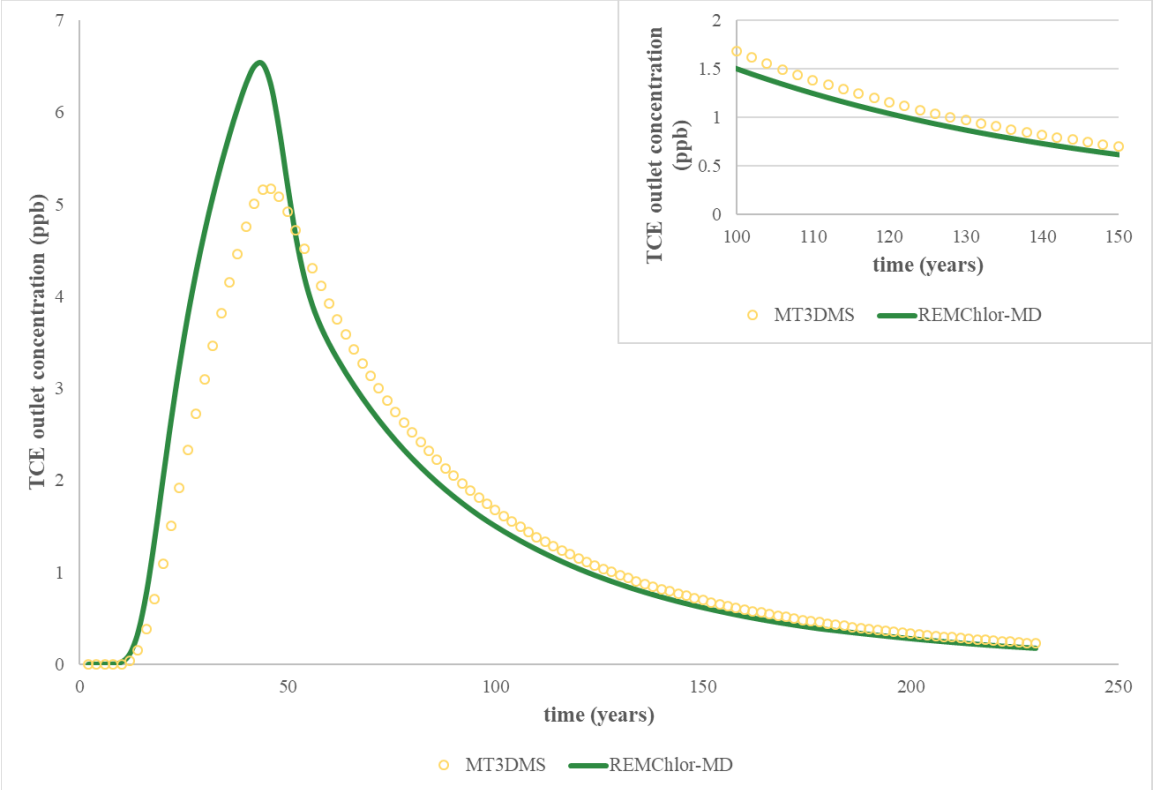

Figure 40. TCE outlet concentration vs time profile comparing the MT3DMS model with REMChlor-MD for lens case with L = 1.85 m. Inset: zoomed-in view of tail for arrival times comparison.

As seen in Figure 40, the concentrations reached by both models at the outlet were low. This is because the more concentrated part of the plume did not reach the outlet face of the models, and will be shown in the concentration plume comparisons later on. The target concentration for this case was 1 ppb, since the MCL (5 ppb) was not located at the tail portion of the curves. The REMChlor-MD results indicate that the TCE values below 1 ppb were reached at approximately 124 years, whereas the MT3DMS model took about 130 years for the same task. The difference in arrival times between the two models is 6 years (~4.6%), with REMChlor-MD showing faster decrease in TCE concentration than MT3DMS.

Furthermore, analyzing the REMChlor curve in Figure 39, the response of the model seems to be a bit too fast, suggesting that the used matrix diffusion area was small. A reduced interfacial area available for mass exchange would result in a smaller diffusion flux going into the low permeability material. Therefore, the mass leaving the semi-analytical model would increase, explaining the higher mass discharge rate observed.

Looking at the relationship of the diffusion parameters in Equation 42, a higher matrix diffusion area could be achieved by slightly decreasing the diffusion length. Small and systematic reductions on the diffusion length were made, concluding than an L of 1.5 m was the best approximation to the overall shape of the mass discharge rate curve with respect to time.

The mass discharge rate comparison between MT3DMS and REMChlor-MD with a diffusion length of 1.5 m is shown in Figure 41:

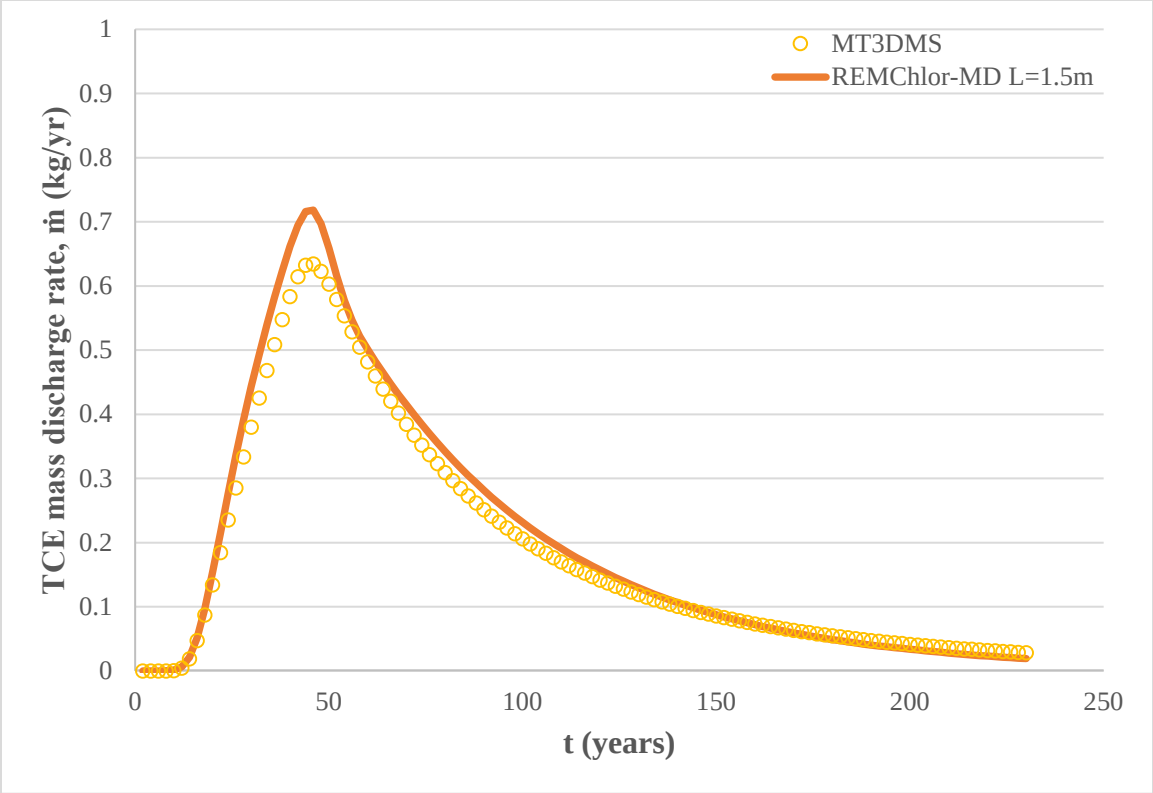

Figure 41. TCE mass discharge rate vs time profile comparing the MT3DMS model with REMChlor-MD for lens case with L = 1.5m.

The mass discharge rate curves in Figure 41 are closer together, showing an improvement from the simulation with diffusion length of 1.85 m. The new calculated coefficient of determination is 0.974, confirming the improvement in the visual comparison. The corresponding TCE outlet concentration profile is presented in Figure 42, with the new REMChlor-MD curve (L = 1.5 m) requiring about 132 years to reach 1 ppb, 2 years (~1.5%) more than the MT3DMS model.

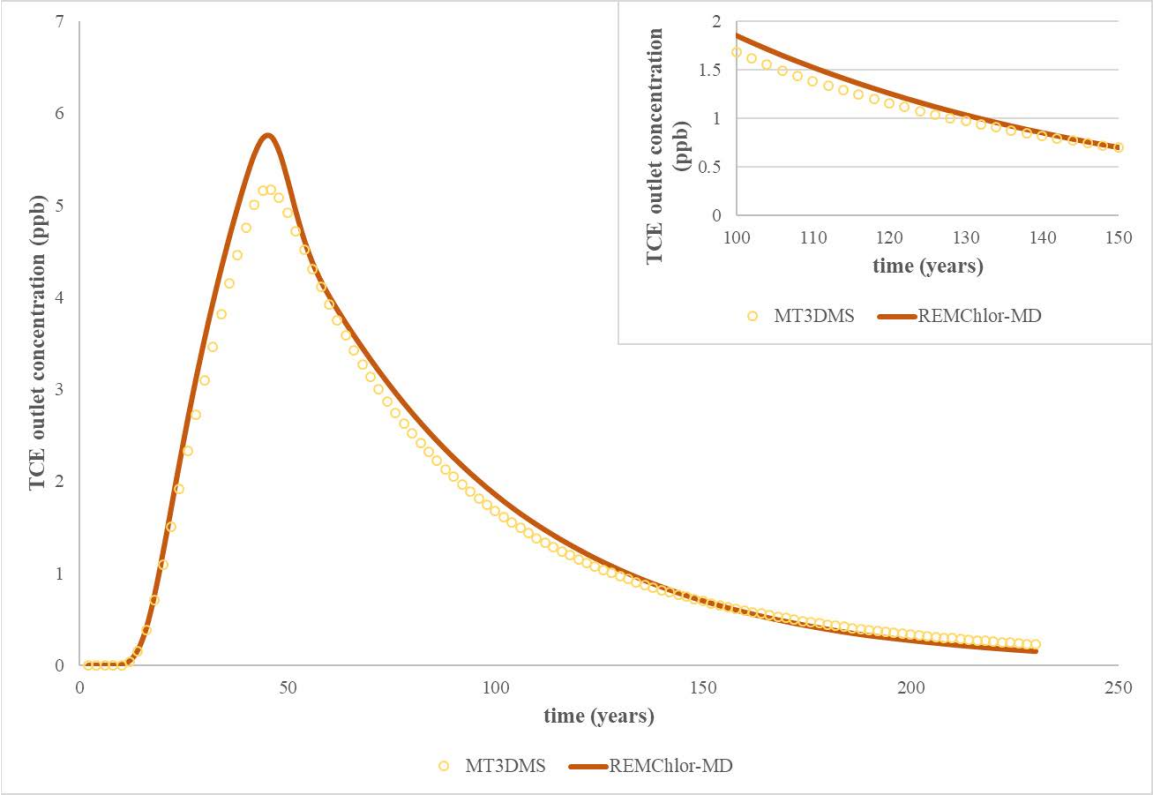

Figure 42. TCE outlet concentration vs time profile comparing the MT3DMS model with REMChlor-MD for lens case with L = 1.5 m. Inset: zoomed-in view of tail for arrival times comparison.

The visual comparison, coefficients of determination, and comparison of arrival times indicate an improvement of the fit between REMChlor-MD and MT3DMS models. There is still a small deviation around the reversal of the mass rate behavior, but it is important to take into account that only the diffusion length was used to improve the fit of the model. Also, the clay dominated layered scenario studied in Section 6.3.3 suggested that Δz =10 cm might be too big to model matrix diffusion effects at very small scales, causing an underestimation of variables. Further refinement of the MT3DMS/MODFLOW grid may

be necessary to test this hypothesis but due to the size of the model the computational effort would be excessive.

As mentioned before, the contour plumes of the MT3DMS and REMChlor-MD models were compared side by side to verify that the plume shape and extents are similar. Since the FORTRAN version of REMChlor-MD used to model this scenario does not have the capability of plotting concentration contours yet, another software package was used to perform this job. The TCE concentration distribution from the REMChlor-MD output file was input to Surfer® (Golden Software, 2017) to create 2-D concentration contour maps.

Vertical and horizontal slices were made in the middle of both models at different times to have a better visualization and comparison of the concentration contours obtained. This is observed in Figure 43 through Figure 48. The graphs are shown in units of feet since this was the default for the MT3DMS/MODFLOW model (T-PROGS tutorial).

The figures represent the TCE plume at 10 years, 30 years, and 130 years. At each simulation time, the concentration contours are shown first in front view (plane *xz*) as a result of a vertical slice in the middle of both models. In MT3DMS this corresponds to cell number 35 in the *y* direction (out of 70). For REMchlor-MD the contours shown are located in the first gridblock in *y*-dir (remember symmetry about $y = 0$). The first graph presented contains the REMChlor-MD contours with 30% transparency superimposed on the MT3DMS contours. This allows to observe the correspondence between the two plumes in different areas of the models. It also serves as a direct comparison of the plume extents resulting from MT3DMS and REMChlor-MD. Subsequently, each contour map is displayed separately with the purpose of showing the individual results for the numerical

and semi-analytical simulation. The MT3DMS TCE plume is presented first followed by the resulting contours from REMChlor-MD. The dashed lines in the MT3DMS graph represent the boundaries of the semi-analytical model.

After the front view contour maps, the TCE plumes are shown from a map view (plane *xy*) resulting from a horizontal slice of the models through the middle of their vertical extents. In MT3DMS this the slice is made at layer 200 (out of 400) whereas in REMChlor-MD the contours are located in layer 18 (out of 36). Again, the superimposed graphs are shown initially, followed by a side by side comparison of the TCE plumes from the MT3DMS model (left) with the results from REMChlor-MD (right).

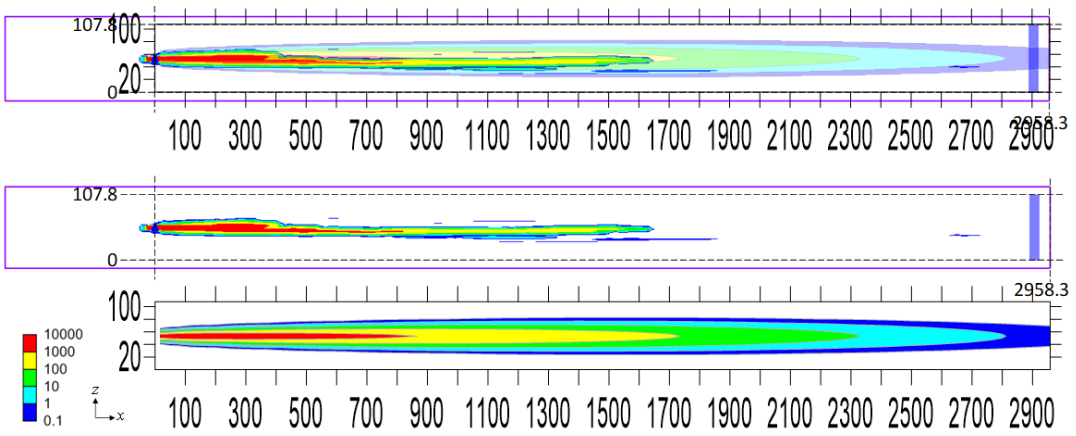

Figure 43. Comparison of MT3DMS (at i = 35) and REMChlor-MD (at first gridblock from center) TCE concentration contours in *xz* plane at *t* = 10yrs for lens case. Above: REMChlor-MD contours over MT3DMS contours. Middle: MT3DMS contours. Below: REMChlor-MD contours.

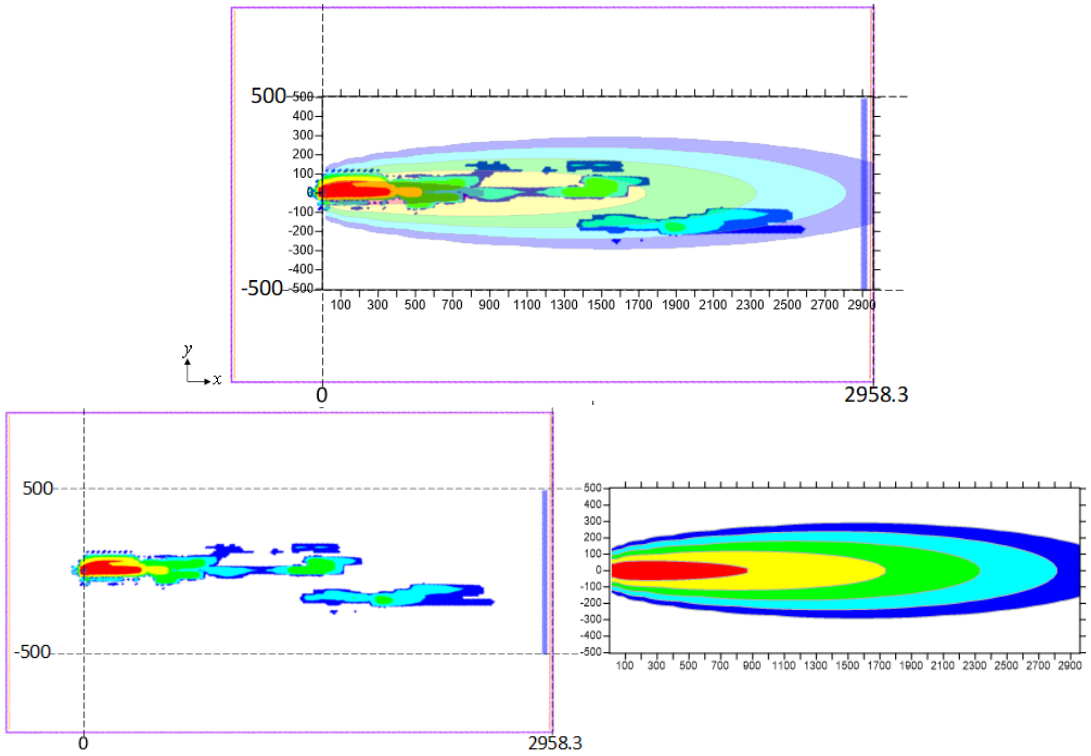

Figure 44. Comparison of MT3DMS (k = 200) and REMChlor-MD (layer #18) models in *xy* plane at *t* = 10yrs for lens case. Above: REMChlor-MD contours over MT3DMS contours. Below: MT3DMS contours (left) and REMChlor-MD contours (right).

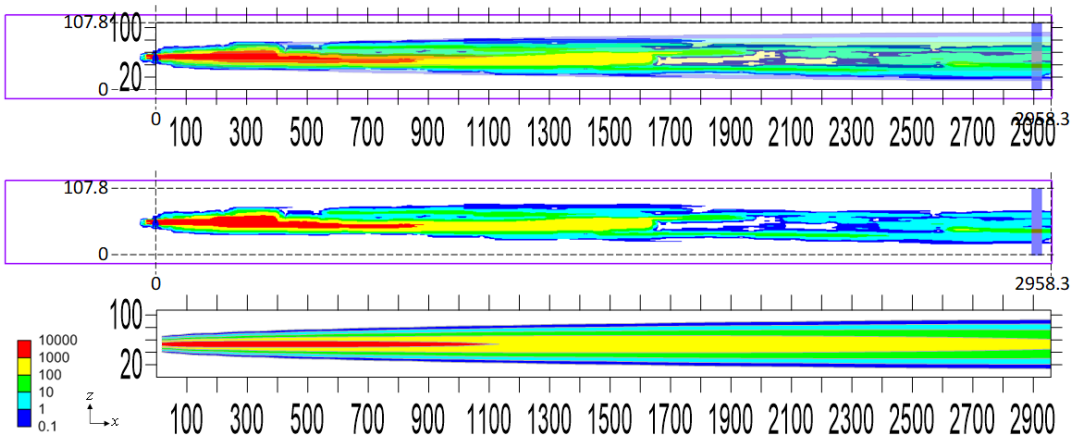

Figure 45. Comparison of MT3DMS (at i = 35) and REMChlor-MD (at first gridblock from center) TCE concentration contours in *xz* plane at *t* = 30yrs for lens case. Above: REMChlor-MD contours over MT3DMS contours. Middle: MT3DMS contours. Below: REMChlor-MD contours.

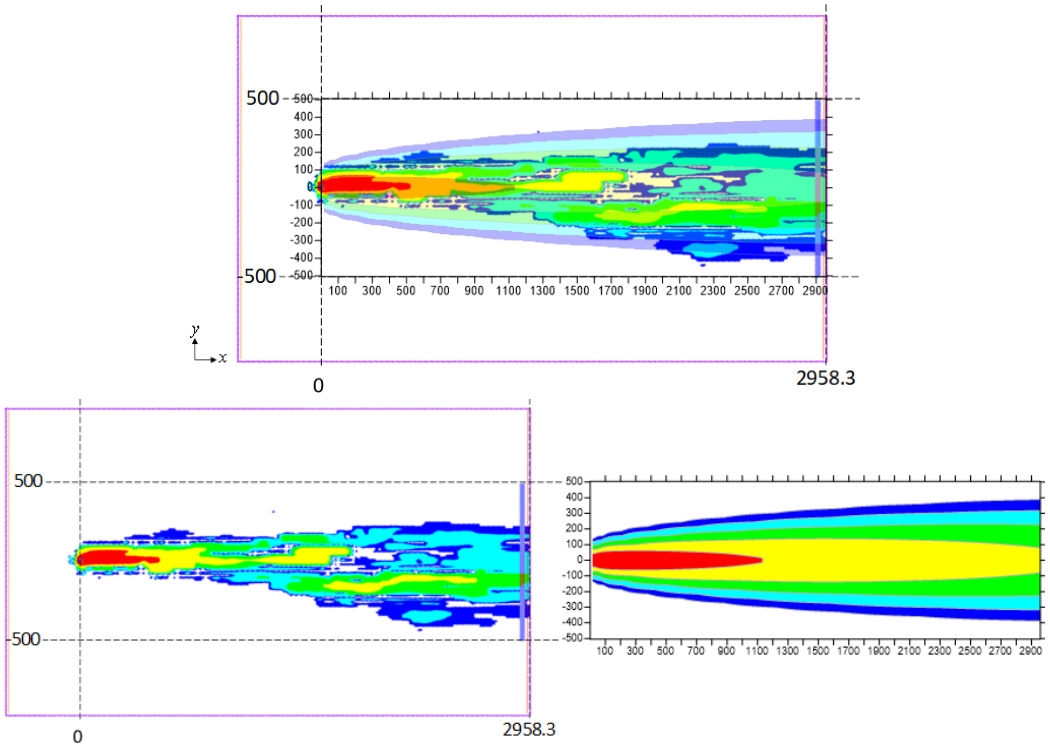

Figure 46. Comparison of MT3DMS (k = 200) and REMChlor-MD (layer #18) models in *xy* plane at *t* = 30yrs for lens case. Above: REMChlor-MD contours over MT3DMS contours. Below: MT3DMS contours (left) and REMChlor-MD contours (right).

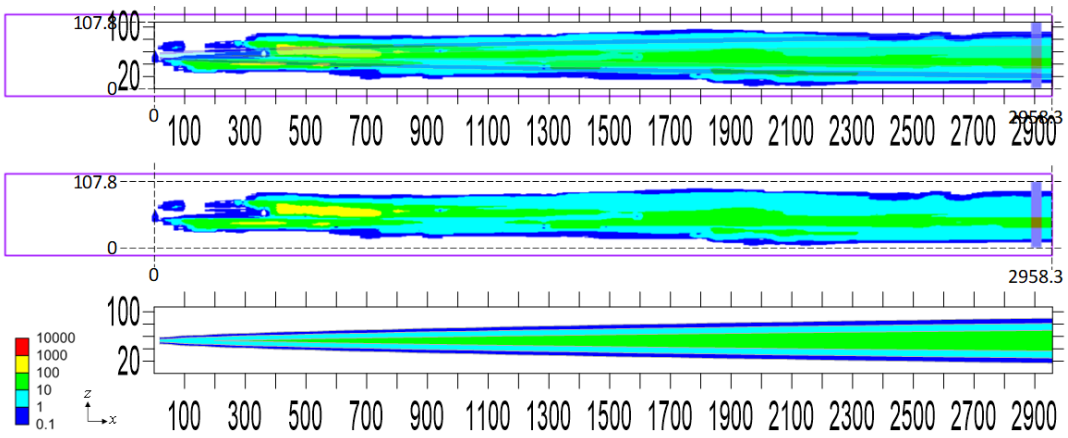

Figure 47. Comparison of MT3DMS (at i = 35) and REMChlor-MD (at first gridblock from center) TCE concentration contours in *xz* plane at *t* = 130yrs for lens case. Above: REMChlor-MD contours over MT3DMS contours. Middle: MT3DMS contours. Below: REMChlor-MD contours.

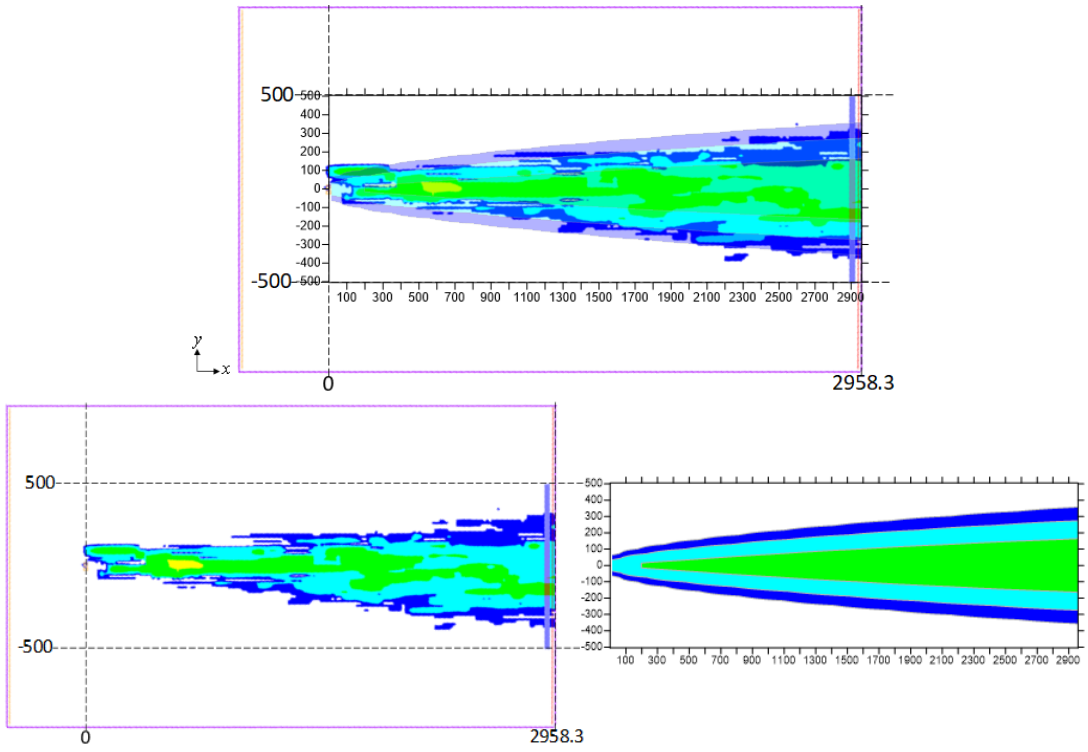

Figure 48. Comparison of MT3DMS (k = 200) and REMChlor-MD (layer #18) models in *xy* plane at *t* = 130yrs for lens case. Above: REMChlor-MD contours over MT3DMS contours. Below: MT3DMS contours (left) and REMChlor-MD contours (right).

The different C_{TCE} contours in Figures 43 through 48 show the evolution of the TCE plume in time. Figures 45 and 46 show the TCE concentration contours at 30 years, right before removing the contaminant source. The horizontal extent (x) of the highest contour zone (1000-10000 ppb) was around 1100 ft (335.3 m). The yellow, green, cyan, and blue contours shown after the 2900 ft (883.9 m) mark indicate that concentrations >1000 to >0.1 ppb reached the outlet face of the models, supporting the low average outlet C_{TCE} seen in Figures 40 and 42. The superimposed and side by side visual comparisons suggest a very good correspondence between MT3DMS and REMChlor-MD, given by the similar extents of each contour zone, thus validating the calibration of the transverse and vertical dispersivities. There are small differences at later times, with MT3DMS showing a more spread plume than REMChlor- MD. This can be attributable to the approximation made in the semi-analytical formulation of only discretize the high k zone. Thus, the TCE concentrations obtained from REMChlor- MD are representative of the high k material, whereas the results from MT3DMS show the concentrations in the high and low k zones.

7.2. Random case

7.2.1. MT3DMS model

As discussed before, the grid and borehole data used for both the lens and random cases were the same. The main difference between the two cases is the material distribution obtained from T-PROGS. The sand proportion for this case had to be increased to 35% to provide enough interconnected transmissive paths to guarantee flow through the model. As with the lens case, the thickness of the sand was reduced to 2 ft to control vertical spreading

of the contaminant plume. The lens ratios for the horizontal and dip (*y*) direction were set as 18 and 7.5, respectively. Again, since the clay is predominant material, its input parameters are automatically adjusted by T-PROGS. The complete set of variables use to prompt the randomized material distribution are summarized in Table 20, and Figure 49 shows the obtained material set from the T-PROGS simulation.

Table 20. T-PROGS parameters for random case.

Parameter	Sand	Clay
Proportion	0.35	0.65
Lens length in *z*	2 ft 0.61 m	8.95 ft 2.73 m
Lens ratio in *x*	17.999	7.471
Lens ratio in *y*	7.499	3.113

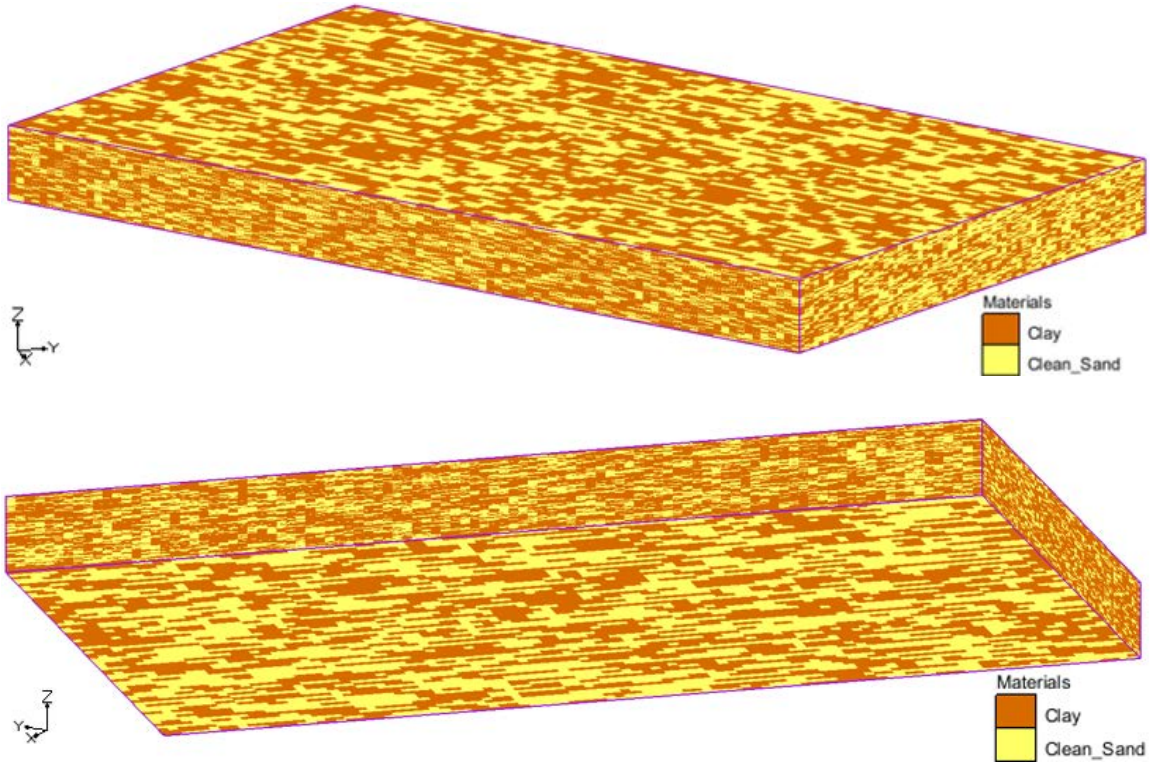

Figure 49. T-PROGS material distribution for random case (z magnification = 2).

The parameters used for the flow field generation and transport simulation were essentially the same as in the lens case. The simulation time for the flushing period had to be increased to 400 years because of plume persistence. As before, the source was placed in the 15th gridblock from the model inlet to reduce lateral dispersion of the plume. However, due to the different material distribution, the location of the TCE contaminated cells changed. This can be seen in Figure 50, which also shows the overall source area (red rectangle) in MT3DMS, placed on a total of 28 sand cells (blue triangles):

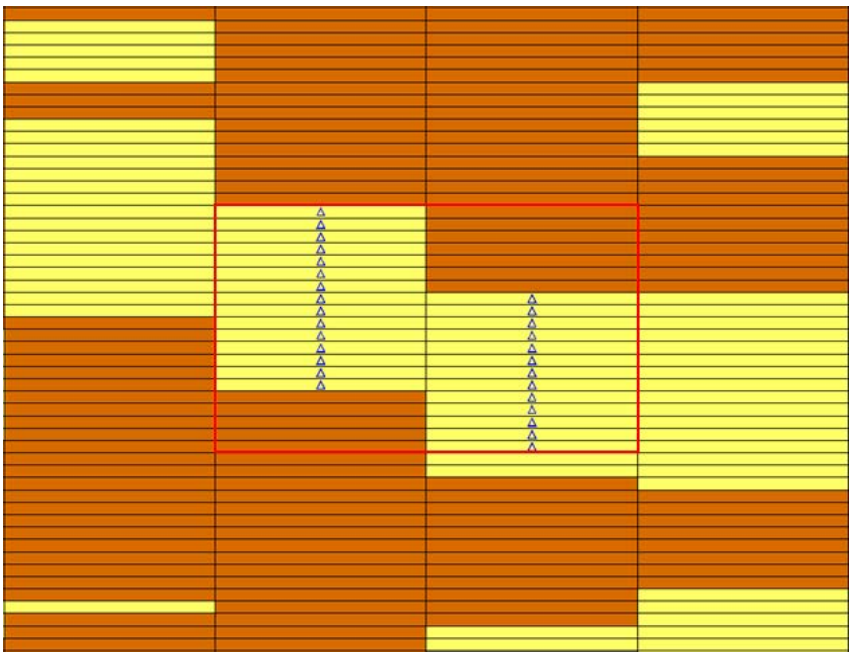

Figure 50. TCE source in MT3DMS model (red rectangle) for random case.

Other than the 400-year flushing period, all of the input parameters for the MT3DMS simulation are the same listed in Table 18. The random case transport simulation with source on ran for 8-10 h in a workstation with an Intel i7 CPU at 3.60 GHz. The run time increased to 60 h for the clean water flushing simulation. This is explained not only by the

size and refinement of the model but also by the added 200 years of simulation in the flushing period. The different concentration contours over time in Figure 51 show a much more spread out plume in comparison with the lens case. The transparency of the contours was set at 30% to be able to see the interior of the plume.

a)

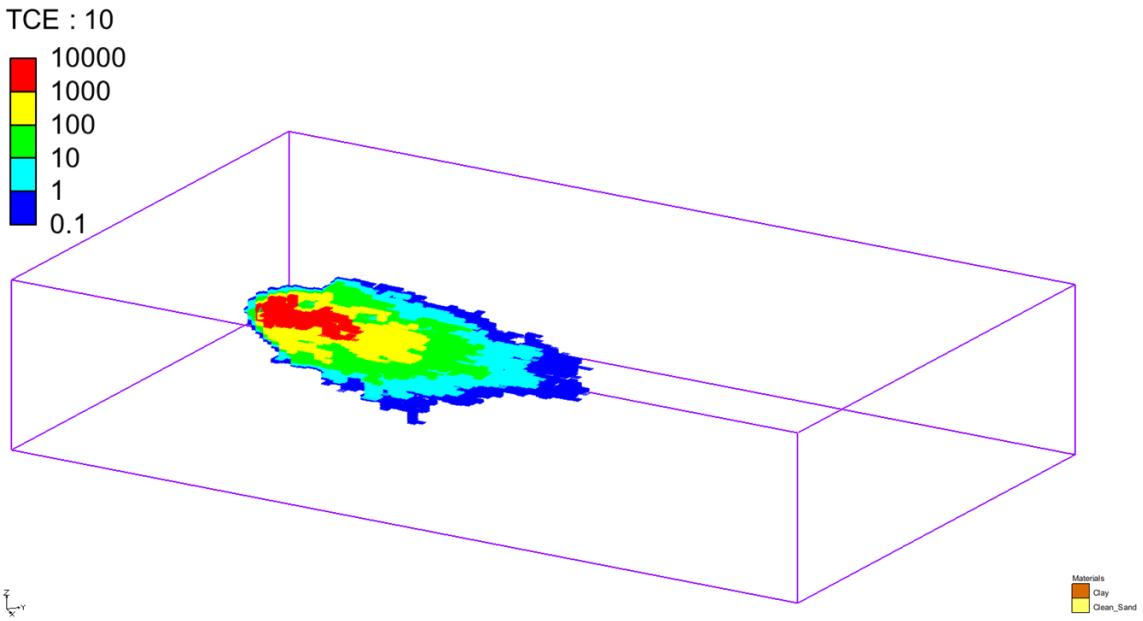

b)

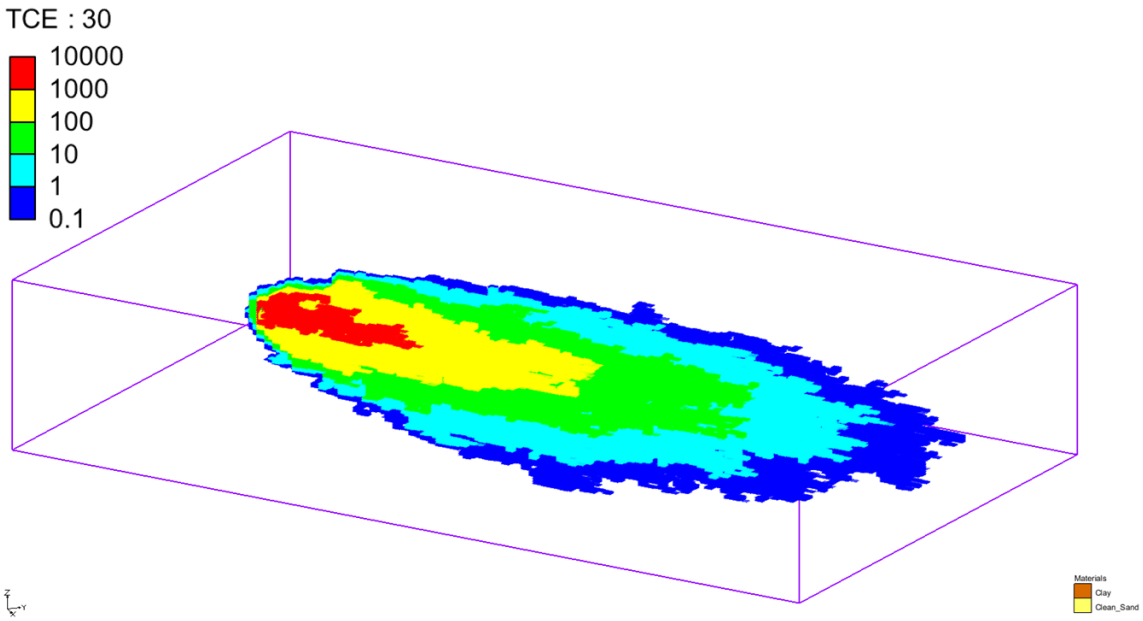

c)

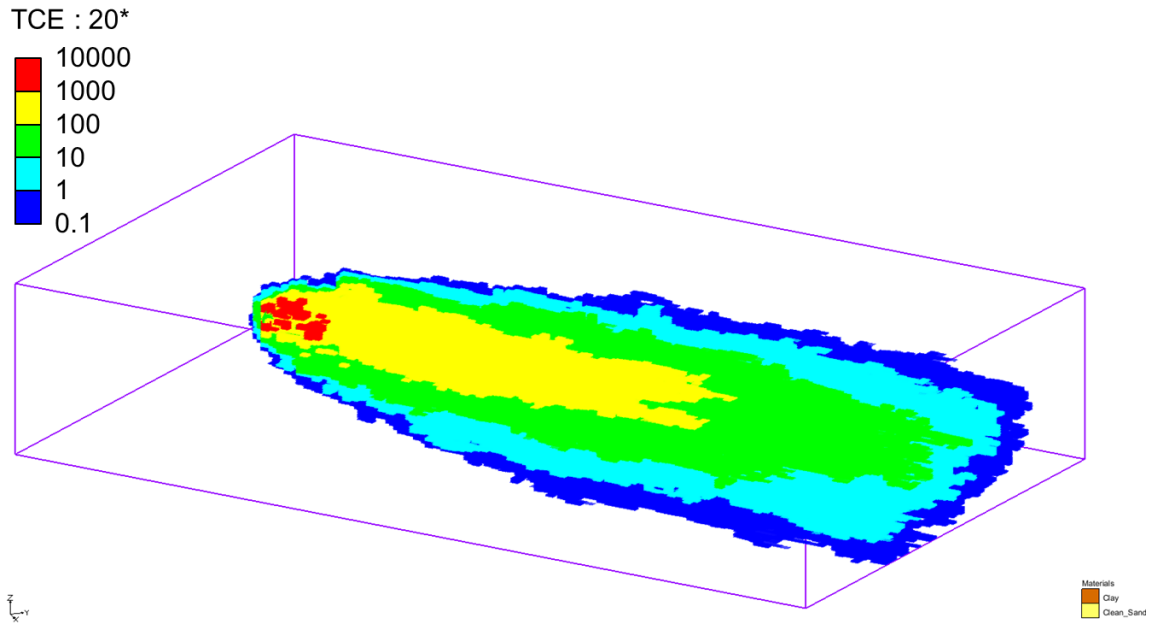
TCE : 20*
10000
1000
100
10
1
0.1
Materials
Clay
Clean_Sand

d)

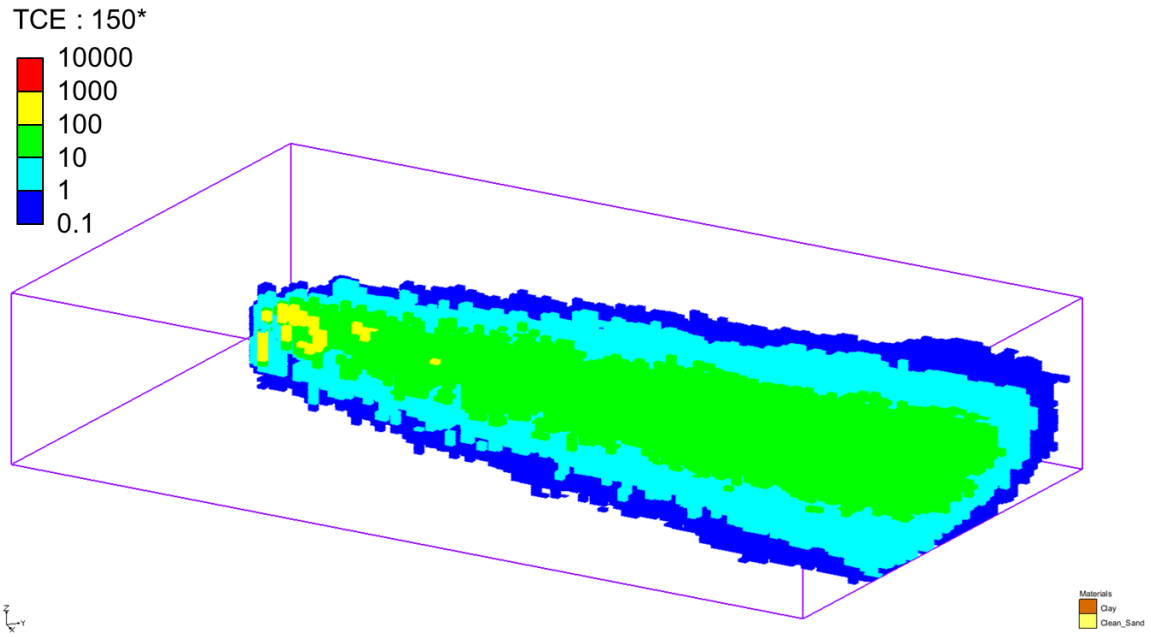
TCE : 150*
10000
1000
100
10
1
0.1
Materials
Clay
Clean_Sand

e)

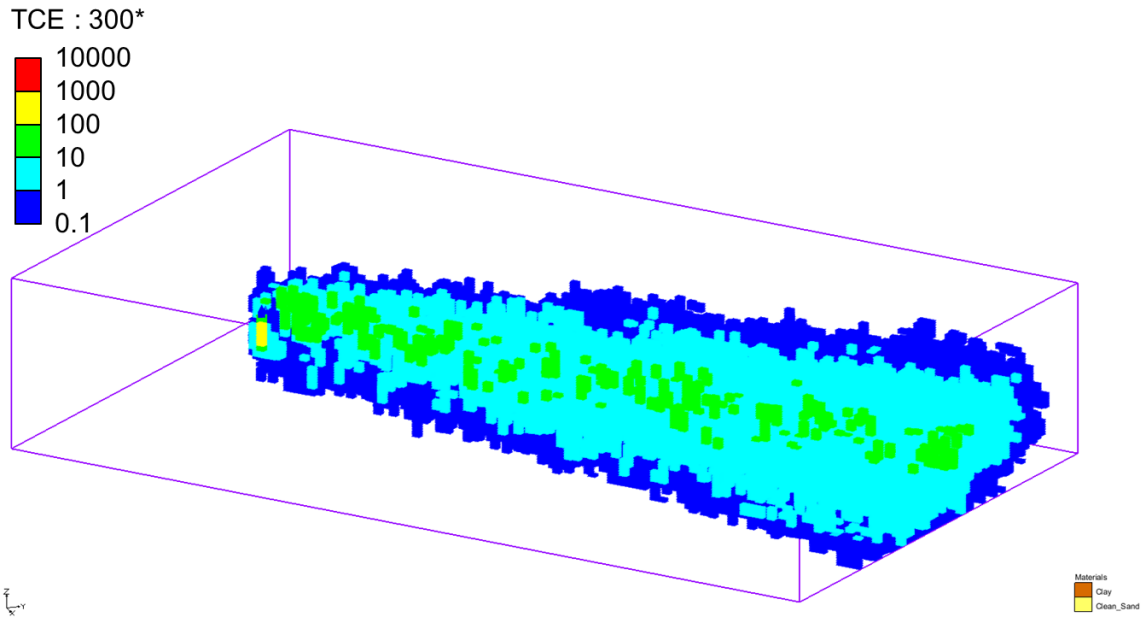

f)

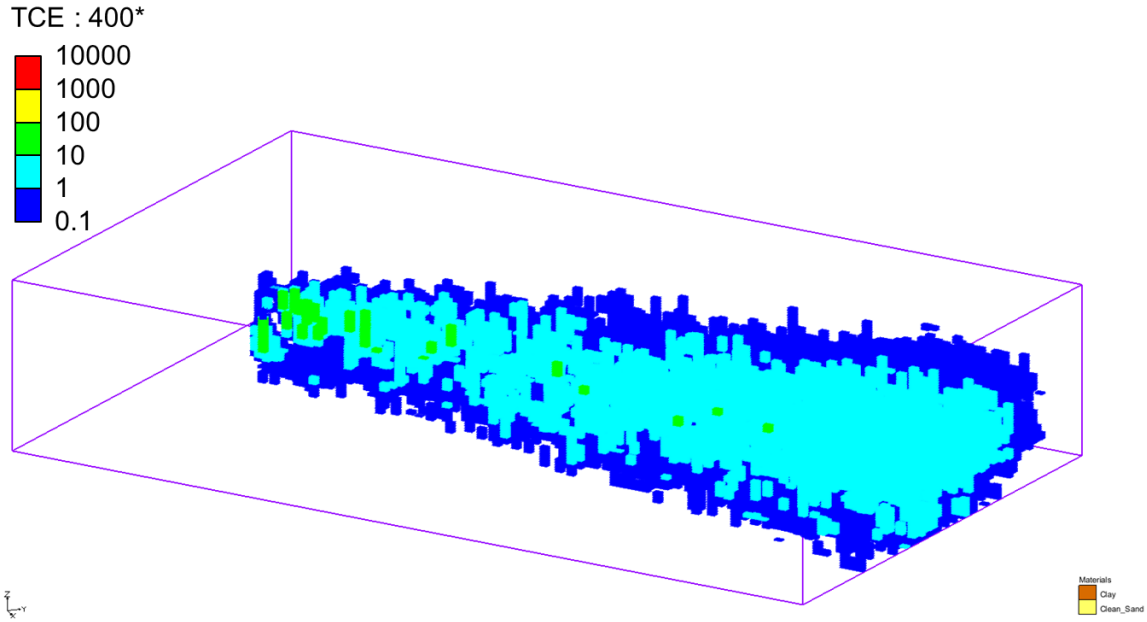

Figure 51. TCE concentration contours at a) 10 years, b) 30 years, c) 20* years (50 yrs), d) 150* years (180 yrs), e) 300* years (330 yrs), and f) 400* years (430 yrs) for random case (z magnification = 5).

The contours allow one to see a tilted plume, with a lot of lateral and vertical spreading due to the randomized material distribution contributing to the advective spreading. When the source is present, the plume displays a more controlled movement through the model, mainly due to the advective transport of TCE.

7.2.2. REMChlor-MD model

The REMChlor-MD model for the random case was set up in the same way as the lens case. However, since the material distribution affects several variables, the values input in the model differed. The length of the model in x and its spacing was set equal to the random case, matching the MT3DMS model and thus, numerical dispersion.

Once again, the discretization in the remaining directions was defined so the source fits in one active gridblock of the REMChlor-MD model (with half of y). Since the source in MT3DMS was placed in two gridblocks in y-dir (from Figure 50), the transverse spacing is set equal to Δy from MT3DMS (8.796m). The length of the model and number of cells was defined with respect to plume extents in MT3DMS. Due to the high lateral spreading of the TCE plume, a total of 32 cells were necessary in the y axis to capture the plume extents obtained from the numerical simulation.

For the vertical direction, an inspection of Figure 50 showed that the TCE constant concentration source was placed over a total of 28 cells in MT3DMS. The corresponding contaminated sand area can is equivalent to $2\Delta y 14\Delta z$. Therefore, the spacing in REMChlor-MD was set as 14 times the vertical spacing in MT3DMS in order to fit the

TCE source into one semi-analytical gridblock. This resulted in Δz = 4.725 ft (1.44 m) in REMChlor-MD, as seen below in Figure 52:

a)

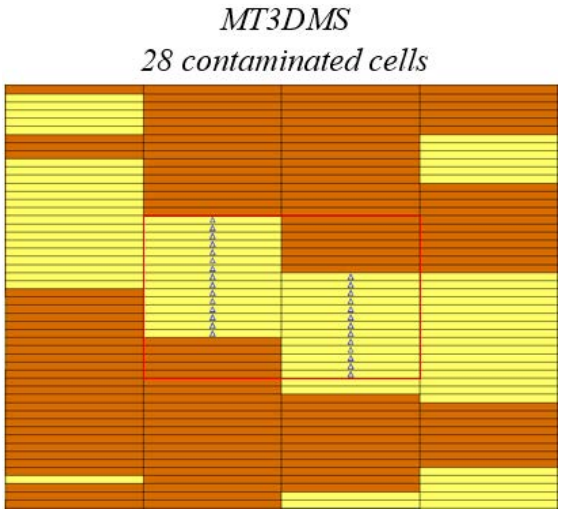

b)

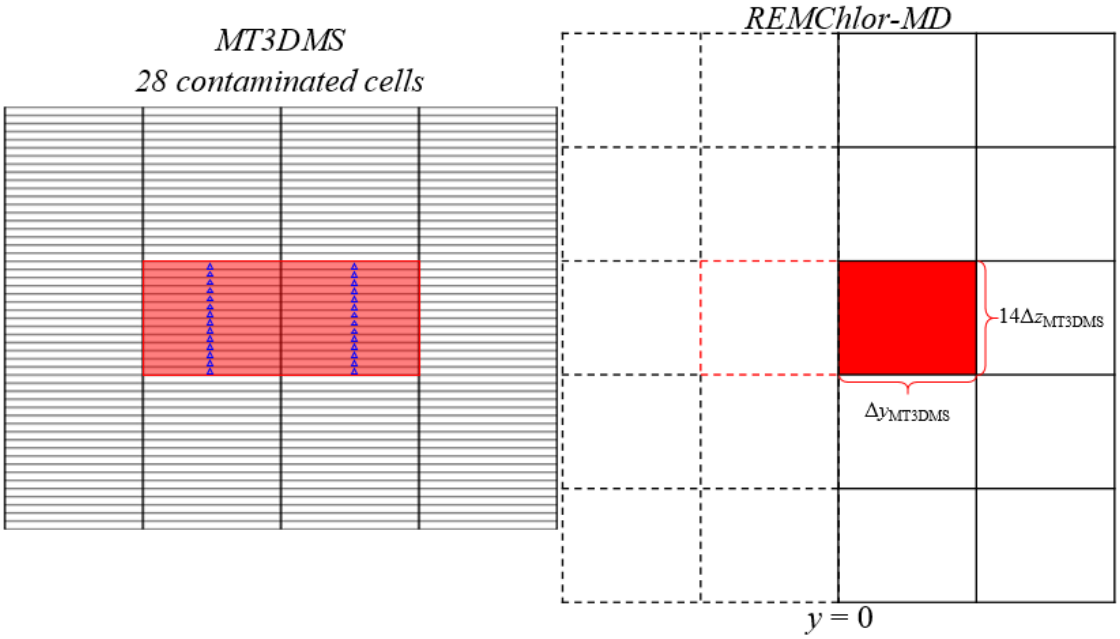

Figure 52. a) Grid spacing in MT3DMS, b) approximation of source area in MT3DMS (left), and grid spacing in REMChlor-MD (right) for random case.

After verifying the vertical extent of the plume in MT3DMS, a total of 27 cells in *z*-dir were estimated for the REMChlor-MD model in order to fit the concentration contours observed in the numerical simulation. The total number of gridblocks in the REMChlor-MD model for this case was 75,168.

The Darcy flux calculation followed the same steps as in the lens case, obtaining a value of 2.697 m/yr, which is a lower number in comparison with the previous scenario. This happened most likely because the transmissive zone pathways are interrupted by low permeability zones with more frequency than before, due to the randomized material distribution.

The individual source cell flow analysis yielded a mass rate calculated as 1.752 kg/yr, leading to a TCE source concentration of 0.026 kg/m^3 (~26000 ppb). As mentioned beforehand, the source was set as one cell in the *y* direction, so *lysource* is 1. With the estimated 27 layers, the source was placed in the middle layer, setting *lzsourcemax* and *lzsourcemin* as 14.

Since the spacing in *x* is big (Δx = 10.42 m), α_x will be neglected by REMChlor-MD, so only the dispersivities in *y* and *z* were defined. The values had to be higher than in the lens case due to the increased lateral and vertical spreading. Just as in the lens case, the transverse and vertical dispersivities were calibrated with the numerical simulation plume extents. Several values of α_y and α_z were defined until the TCE concentration contours from the MT3DMS and REMChlor-MD models were similar, for α_y = 2 m and α_z = 0.014 m.

The sand volume fraction was set equal to the value proportioned by the T-PROGS distribution of 0.351. The diffusion length was estimated with the volume weighted mean

procedure explained in the lens case, calculating 1.214 m from the three faces shown below in Figure 53. The matrix diffusion area was then estimated from Equation 43 as 70.611 m^2. The number of time steps was set as 860 because of the Δt of 0.5 yrs previously defined.

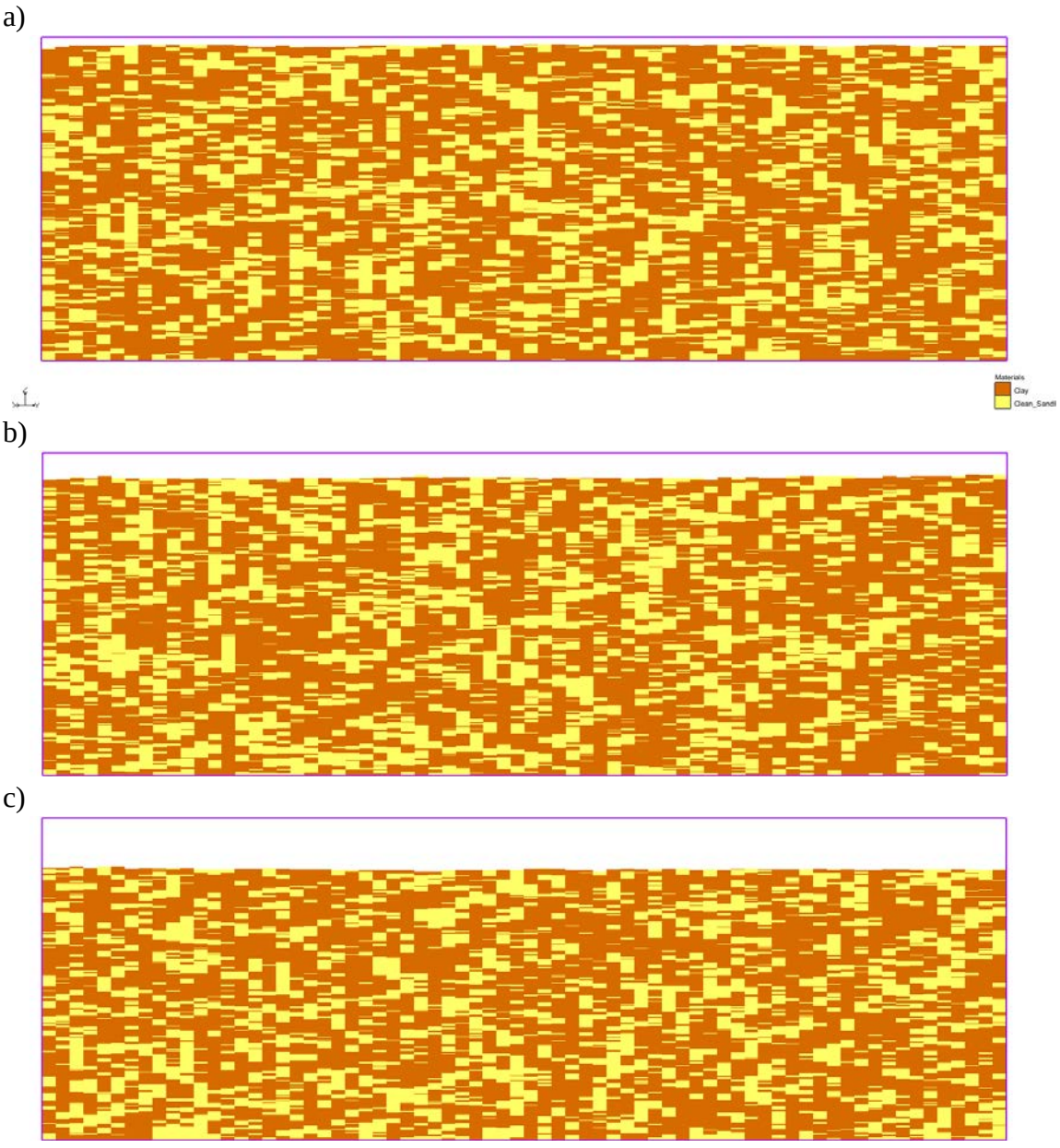

Figure 53. MT3DMS/MODFLOW model faces selected for estimation of *L* in random case for a) j=16, b) j=39, and c) j=71.

The input parameters used in the REMChlor-MD model are listed in Table 21. Those variables not mentioned above were kept the same from the lens case.

Table 21. Input parameters in REMChlor model for random case.

Description	Value
****Source terms****	
Initial source zone concentration, C_0 (kg/m^3)	2.56E-2
Initial source zone mass, m_{t0} (kg)	100
Gamma exponent, Γ	0
Fraction of source mass removed, *xremove*	1
Remediation start time, t_1 (yr)	30
Remediation end time, t_2 (yr)	30.1
Source zone decay rate constant (1/yr)	0
Source containing cells in *y*, *lysource*	1
Top layer number in *z*, *lzsourcemax*	14
Bottom layer number in *z*, *lzsourcemin*	14
Darcy velocity, v_d (m/yr)	2.697
****Transport terms in high K zone****	
High *K* zone porosity, ϕ	0.3
High *K* zone tortuosity, τ	0.669
High *K* zone longitudinal dispersivity, α_x (m)	5
High *K* zone transverse dispersivity, α_y (m)	2
High *K* zone vertical dispersivity, α_z (m)	0.014
High *K* zone retardation, *R*	1
****Decay terms in High K zone****	
Zone 1 length for plume decay, x_1	1000
Zone 2 length for plume decay, x_2	2000
Period 1 for plume decay, $tplume_1$ (yr)	250
Period 2 for plume decay, $tplume_2$ (yr)	300
****Transport terms in low K zone****	
Matrix diffusion flag, *md*	2
Low *K* zone porosity, ϕ_l	0.5
Low *K* zone tortuosity, τ_l	0.794
Low *K* zone retardation, R_l	1
Diffusion coefficient, *D* (m^2/yr)	3.15E-2
Matrix diffusion area, A_{md} (m^2)	70.611
Sand volume fraction, ~~V_f~~	0.351

Table 21 continued

Description	Value
Characteristic diffusion length, L (m)	1.214
******Finite Difference Parameters******	
Δx (m)	10.424
Δy (m)	8.796
Δz (m)	1.44
Number of elements, *nx*	87
Number of *y* cells, *ny*	32
Number of layers, *nz*	27
Δt (yr)	0.5
Number of time steps	860

The REMChlor-MD model ran in 2 minutes, 50 seconds. The longer run time was expected due to the bigger size of the model. This time is still negligible when compared to the approximated 70 h run time for the MT3DMS numerical simulations.

7.2.3. Testing

The comparison of mass discharge rate over time between the MT3DMS and REMChlor-MD models is shown in Figure 54, with the curves from REMChlor-MD and MT3DMS displaying the fast rise and decrease of TCE mass discharge rate followed by tailing behavior seen in the lens case. The calculated coefficient of determination of 0.912, suggests that the response of the REMChlor-MD model matches the overall behavior of the mass discharge rate in the random system. However, the REMChlor-MD curve is shifted slightly to the right, indicating that the mass is leaving the random scenario at a slower pace than what the numerical simulation proposes.

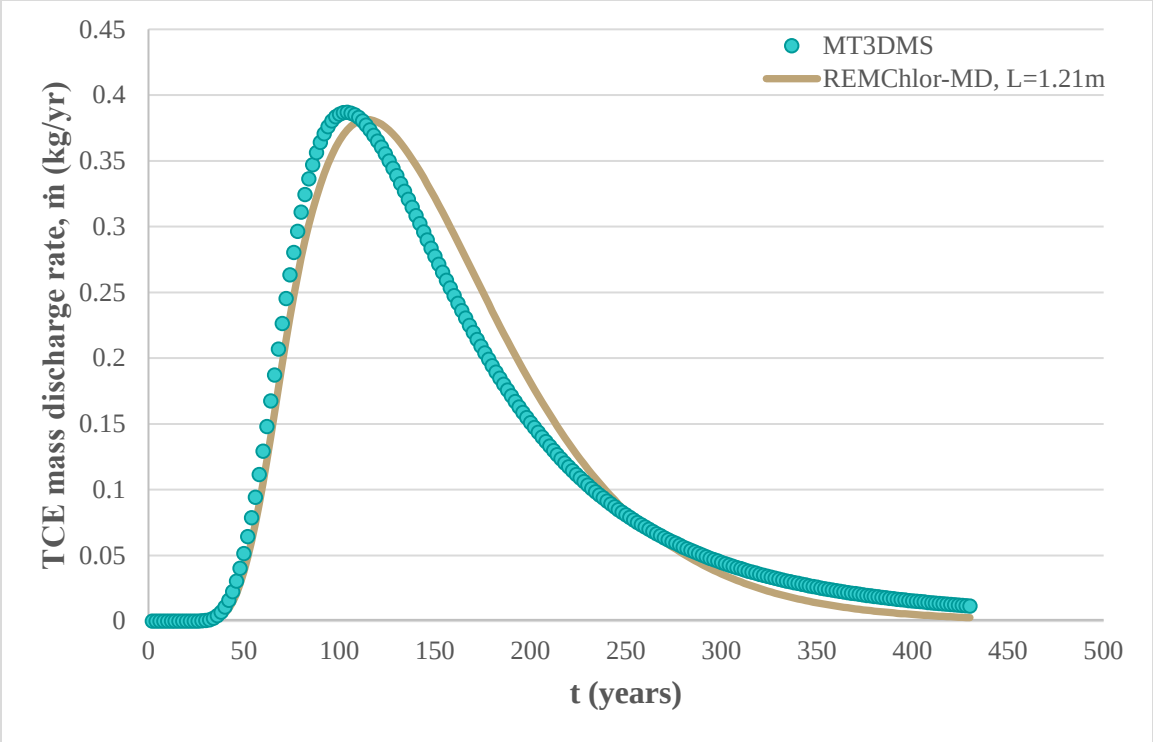

Figure 54. TCE mass discharge rate vs time profile comparing the MT3DMS model with REMChlor-MD for random case with L = 1.21 m.

The TCE average outlet concentration profile is shown in Figure 55 below, where, just as in the lens case the outlet concentrations were low due to the concentrated zone of the plume not reaching the model boundary. The target concentration was 1 ppb again, with REMChlor-MD reaching concentrations below this value at about 272 years, whereas the MT3DMS model required about 278 years to do the same. The 6-year difference in arrival times between the two models is approximately 2.2%.

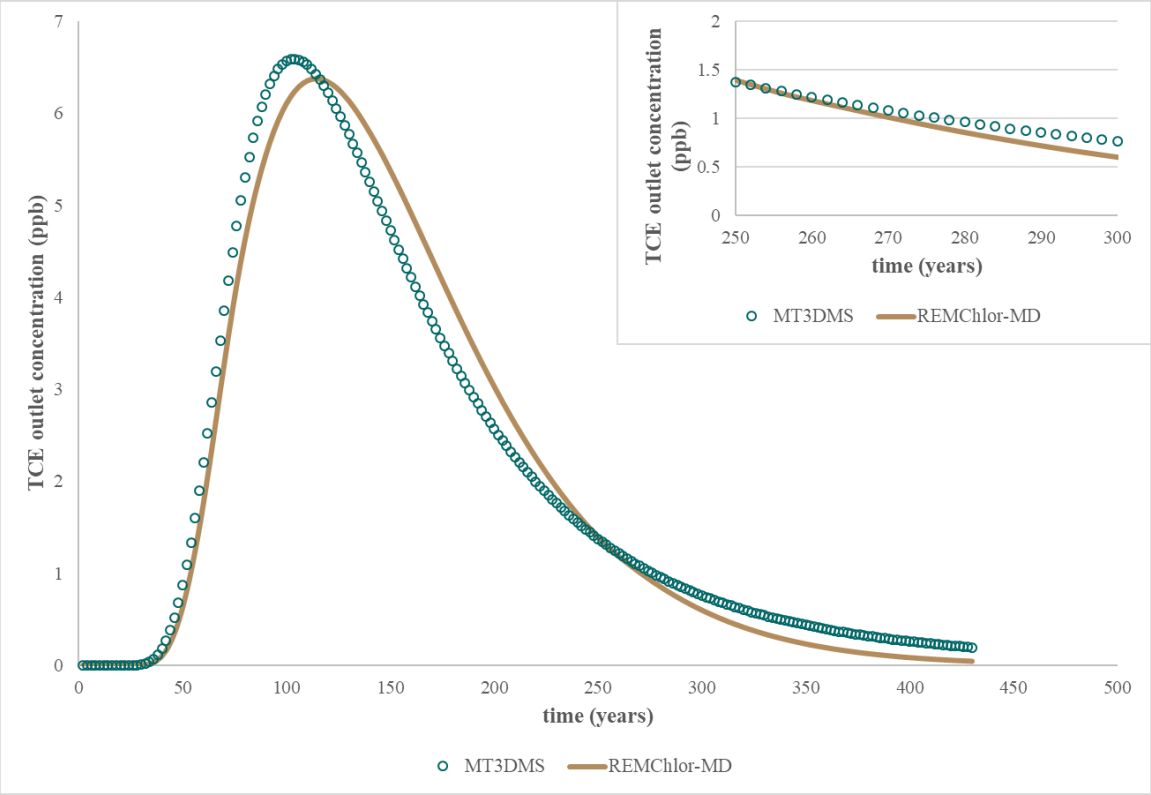

Figure 55. TCE outlet concentration vs time profile comparing the MT3DMS model with REMChlor-MD for random case with L = 1.21 m. Inset: zoomed-in view of tail for arrival times comparison.

The fit of the model was improved some by reducing the available area for mass transfer. According to Equation 43, this is done by raising the diffusion length. Using small increments in L, an optimum value of 1.35 m was calibrated, resulting in the solid line shown in Figure 56 below. The REMChlor-MD results using the calibrated diffusion length display an improvement in the overall shape of the mass discharge rate profile. However, this improvement comes at the cost of achieving lower values for the maximum mass rate leaving the system. This is reflected in the coefficient of determination, with a recalculated value of 0.903.

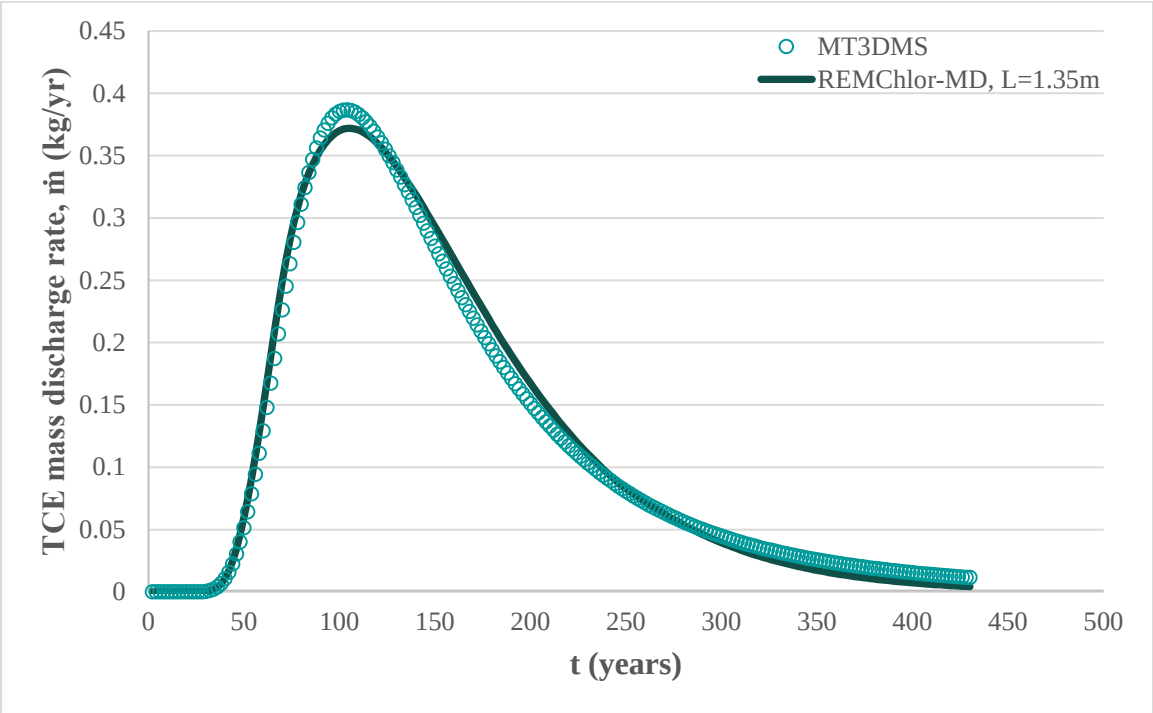

Figure 56. TCE mass discharge rate vs time profile comparing the REMChlor-MD and MT3DMS model for random case with L = 1.35 m.

As discussed in the simulation of experiments in Chapter 4, the negative effect on the estimation of R^2 due to the reduction in the fit of the higher order of magnitude values is bigger than the improvement of the parameter caused by a better match of the model at lower order of magnitude values.

The TCE average outlet concentration curves observed in Figure 57 below show that the difference in arrival times between REMChlor-MD and MT3DMS was reduced to 4 years (~1.4%), since the REMChlor-MD simulation with diffusion length of 1.35 m required 274 years to reach values below 1 ppb.

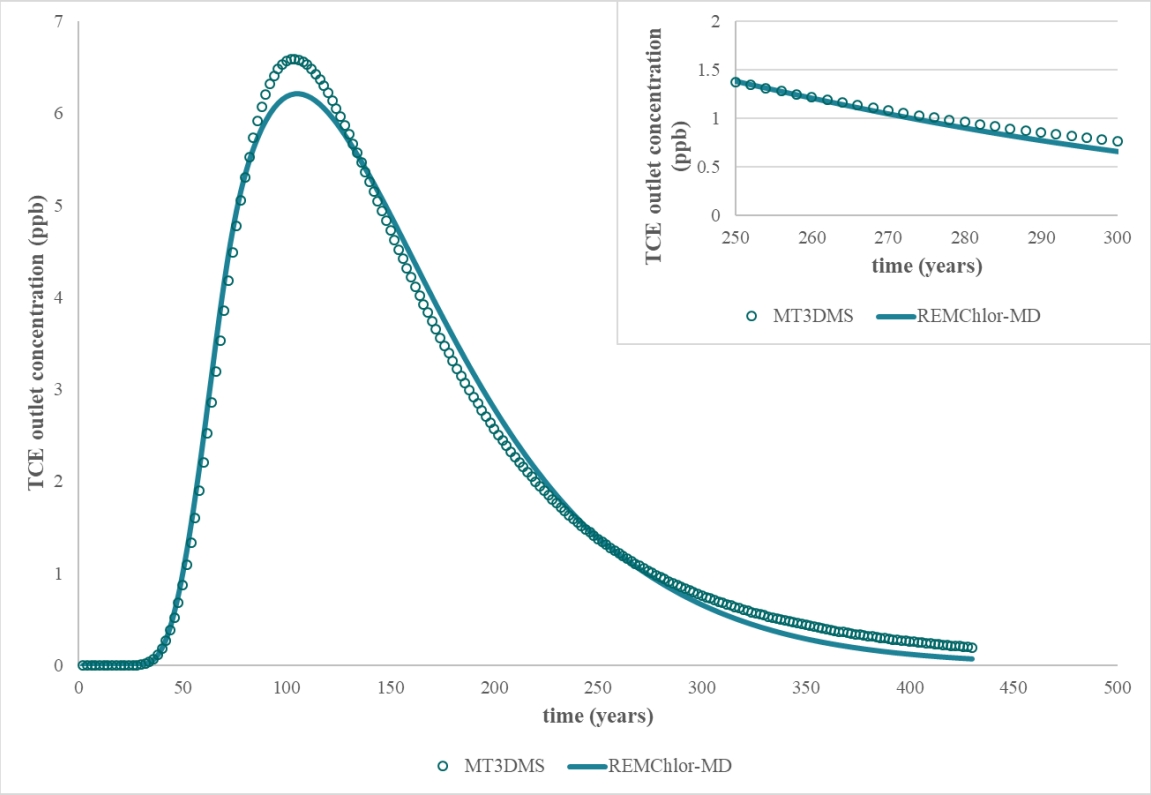

Figure 57. TCE outlet concentration vs time profile comparing the MT3DMS model with REMChlor-MD for random case with L = 1.35 m. Inset: zoomed-in view of tail for arrival times comparison.

The TCE concentration contours were generated for the random case in order to make a direct comparison of the plume with MT3DMS. The concentration distribution from the REMChlor-MD output file was input in Surfer® and horizontal and vertical slices were made to the model to create the 2-D concentration contours shown in Figure 58 through Figure 63. The layout of the graphs is the same as in the lens case, showing front views (plane *xz*) and map views (plane *xy*) of the TCE concentration contours at 10 years, 30 years, and 130 years. For each view, superimposed graphs are shown initially, followed by a comparison between the TCE plumes from the MT3DMS model and REMChlor-MD.

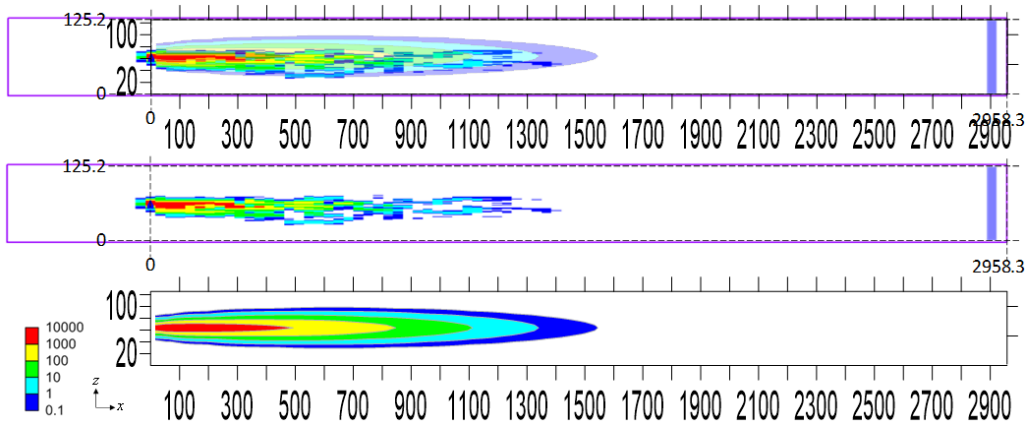

Figure 58. Comparison of MT3DMS (at i = 35) and REMChlor-MD (at first gridblock from center) TCE concentration contours in *xz* plane at *t* = 10yrs for random case. Above: REMChlor-MD contours over MT3DMS contours. Middle: MT3DMS contours. Below: REMChlor-MD contours.

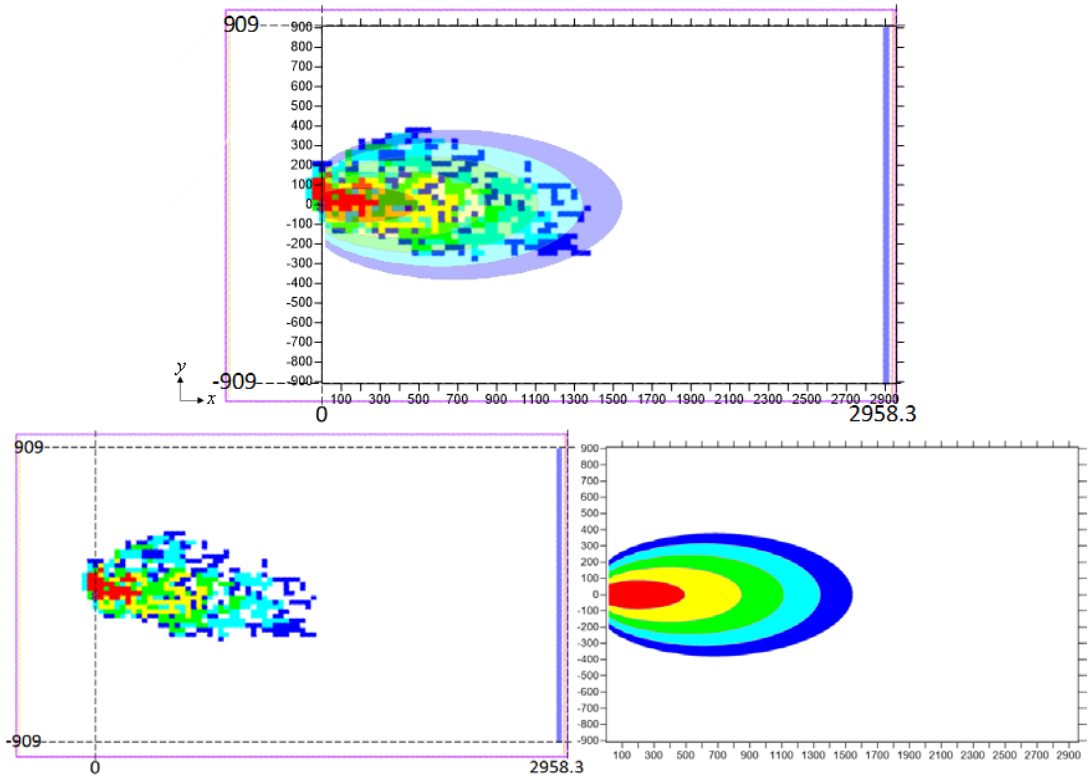

Figure 59. Comparison of MT3DMS (k = 200) and REMChlor-MD (layer #14) models in *xy* plane at *t* = 10yrs for random case. Above: REMChlor-MD contours over MT3DMS contours. Below: MT3DMS contours (left) and REMChlor-MD contours (right).

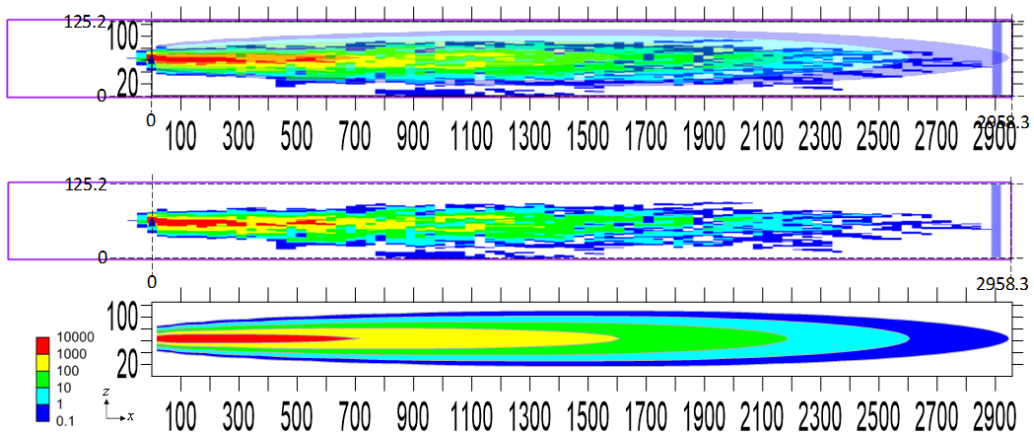

Figure 60. Comparison of MT3DMS (at i = 35) and REMChlor-MD (at first gridblock from center) TCE concentration contours in *xz* plane at *t* = 30yrs for random case. Above: REMChlor-MD contours over MT3DMS contours. Middle: MT3DMS contours. Below: REMChlor-MD contours.

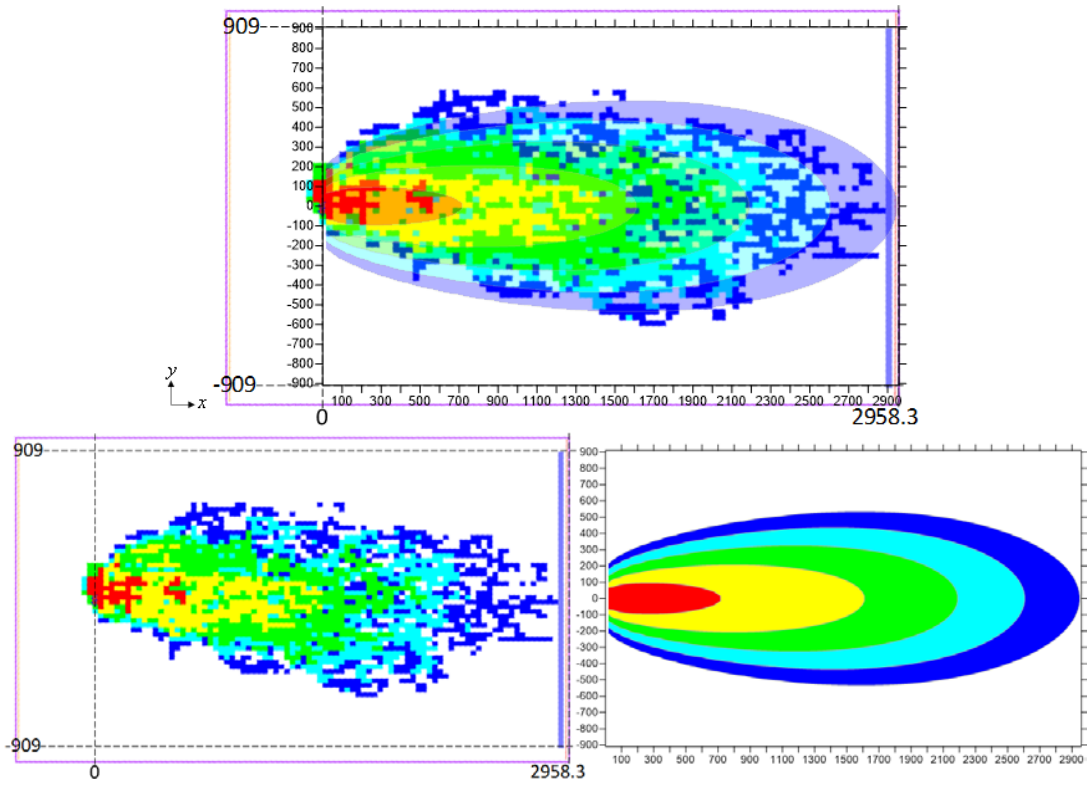

Figure 61. Comparison of MT3DMS (k = 200) and REMChlor-MD (layer #14) models in *xy* plane at *t* = 30yrs for random case. Above: REMChlor-MD contours over MT3DMS contours. Below: MT3DMS contours (left) and REMChlor-MD contours (right).

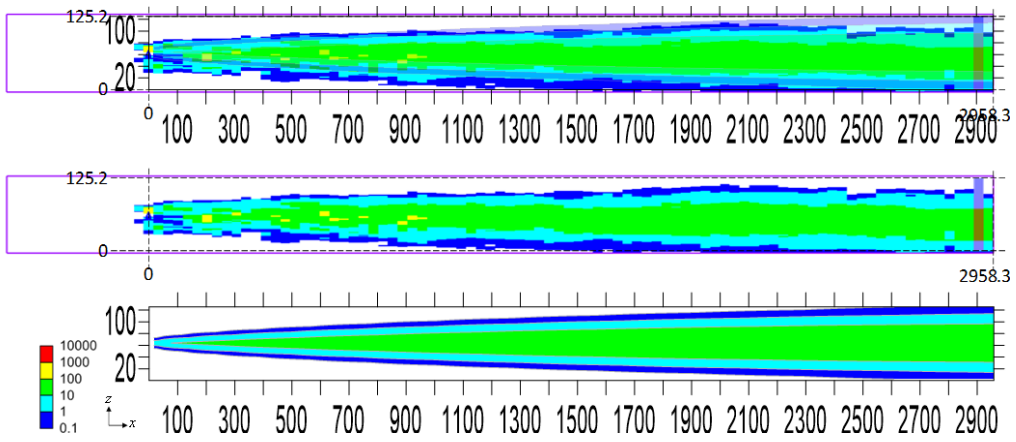

Figure 62. Comparison of MT3DMS (at i = 35) and REMChlor-MD (at first gridblock from center) TCE concentration contours in *xz* plane at *t* = 130yrs for random case. Above: REMChlor-MD contours over MT3DMS contours. Middle: MT3DMS contours. Below: REMChlor-MD contours.

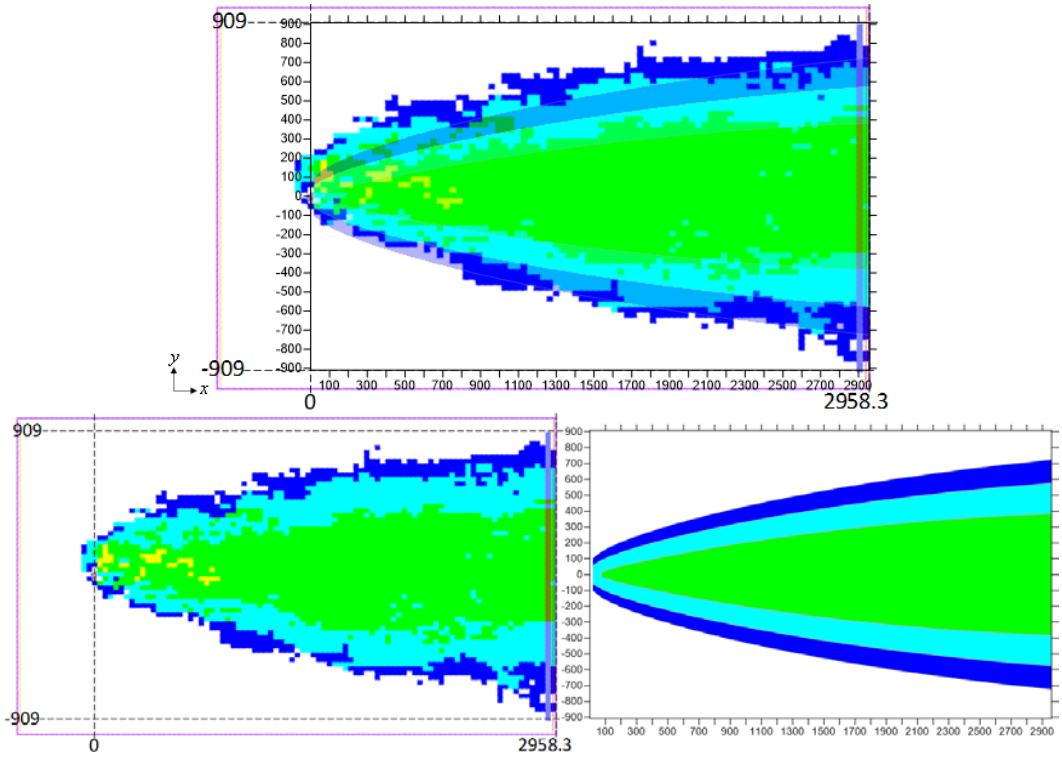

Figure 63. Comparison of MT3DMS (k = 200) and REMChlor-MD (layer #14) models in *xy* plane at *t* = 130yrs for random case. Above: REMChlor-MD contours over MT3DMS contours. Below: MT3DMS contours (left) and REMChlor-MD contours (right).

The plume extents estimated with REMChlor-MD display a good match to the MT3DMS model contours, corroborating the calibrated values of the transverse and vertical dispersivities. There is some deviation at later times but the consideration of REMChlor-MD showing results for only the high permeability materials remains. This becomes important due to the matrix diffusion effects because the low permeability areas store contaminant mass for long periods of time, resulting in higher concentration contours displayed in MT3DMS.

8. CONCLUSIONS AND RECOMMENDATIONS

This research consisted of assessing the accuracy of the implementation of Vinsome and Westerveld (1980) semi-analytical method to the process of matrix diffusion for finite embedded heterogeneity scenarios in groundwater chemical transport modeling.

The execution of the semi-analytical method in a Visual Basic program in Excel® was tested against experimental results from published laboratory scale flow chamber studies, and with simple geometry numerical simulations developed in MT3DMS. The results obtained showed good-to-excellent visual and quantitative agreement, indicating good accuracy of the matrix diffusion semi-analytical/numerical method for most practical purposes.

A FORTRAN version of the semi-analytical method, REMChlor-MD tested against fine grid numerical simulations provided great results, for systems with highly complex heterogeneities present. This becomes particularly important taking into account that this type of setup is closer to real life scenarios, where the exact heterogeneity of field sites is usually unknown.

Three geometric parameters were used in the semi-analytical method for finite embedded heterogeneities: the high permeability material volume fraction (V_f), the high/low permeability material interface area (A_{md}), and the characteristic average diffusion length (L). A geometrical relationship was defined to reduce the number of matrix diffusion parameters to define in the upcoming REMChlor-MD version to only two: V_f and L. The results obtained using this "2-parameter" approach provided a decent match with the fine-grid simulation data without calibration, and a good match with small adjustments to L.

The semi-analytical method implementation proved to be extremely efficient, providing great match to experimental results and numerical simulations with run times ranging from fractions of seconds up to less than three minutes, depending on the size of the model and the simulated periods of time. This is outstanding considering the fine grid MT3DMS numerical simulations used as base of comparison using a little under three million gridblocks took up to 70h to run the mass transport simulation. The efficiency of the semi-analytical method is due to the fitting function approximation for the low permeability areas, allowing the effects of complex heterogeneity to be approximated in a coarse grid.

Recommendations

Some recommendations for future research based on this study include:

- Compare REMChlor-MD and MT3DMS for T-PROGS scenario incorporating sorption and degradation.
- Consider more realistic scenarios for the implementation of the method, such as field sites to study and develop the parameterization of the semi-analytical method with field data.
- Assess the feasibility of a fitting function containing a multiple time-dependent penetration depth to improve the response of the semi-analytical method around the concentration reversal period.
- Implement the matrix diffusion semi-analytical/numerical method in commercial chemical transport models like MT3DMS (Zheng and Wang, 1999).

APPENDICES

Appendix A: Cubic spline interpolation

The simulated data in section 5.2 was equally distributed in 0.5 days spacing whereas the experimental dataset had an independent variable that was not equally distributed. The program SRS1 Cubic Spline for Excel from © SRS1 Software (SRS1 Software LLC, 2015) was used to interpolate the data from the semi-analytical model results to match the time series of the experimental data.

The graphs shown in Figure A.1 through Figure A.3 present the spline interpolation results alongside the original simulated data for the different cases studied in sections 5.2 and 5.3.

a)

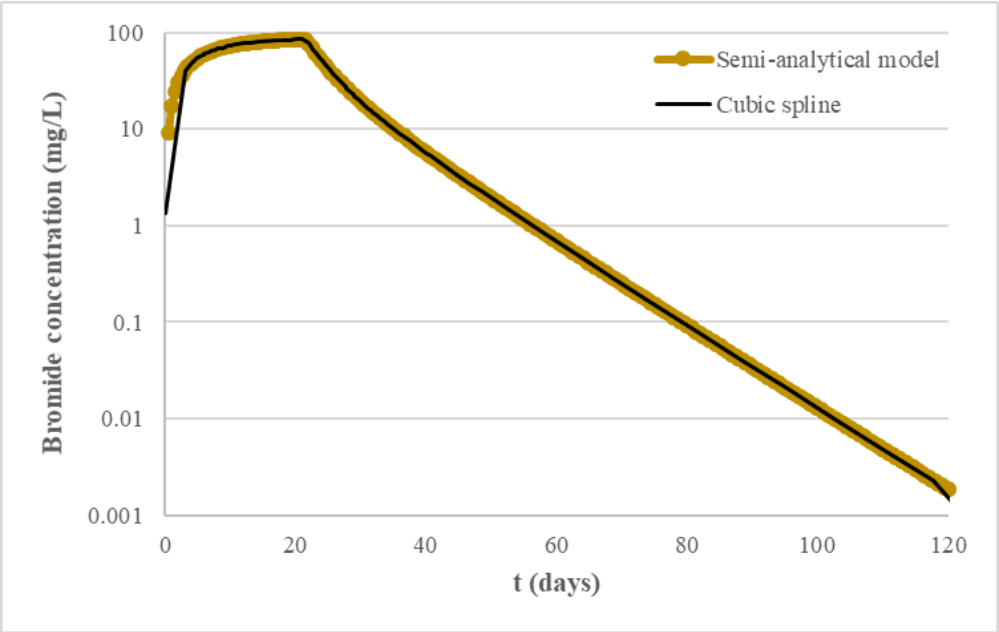

b)

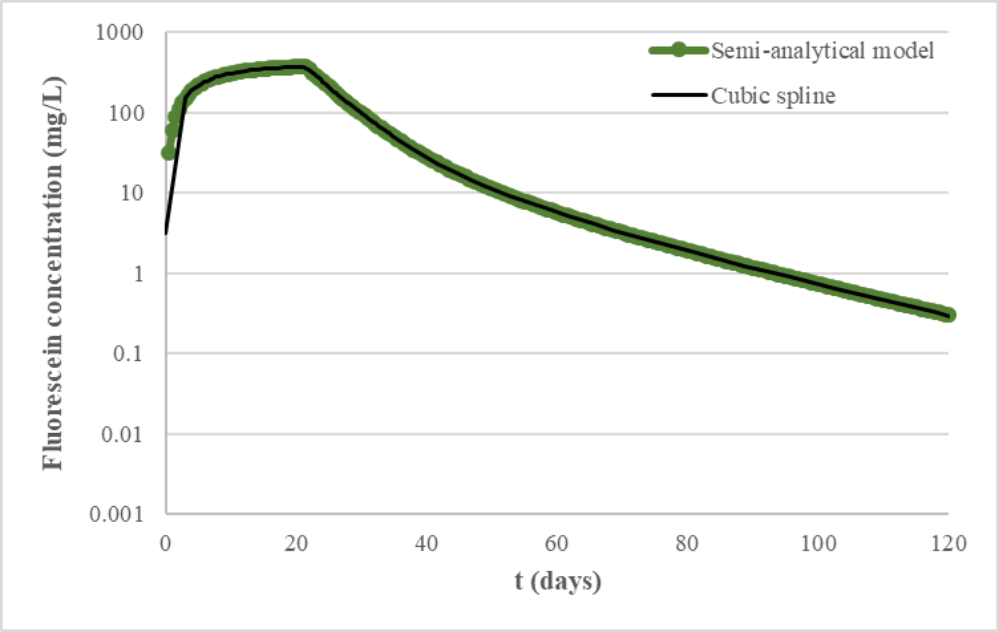

Figure A.1 Comparison of cubic spline with one gridblock simulated data in suspended clay lenses case for a) Bromide and b) Fluorescein.

a)

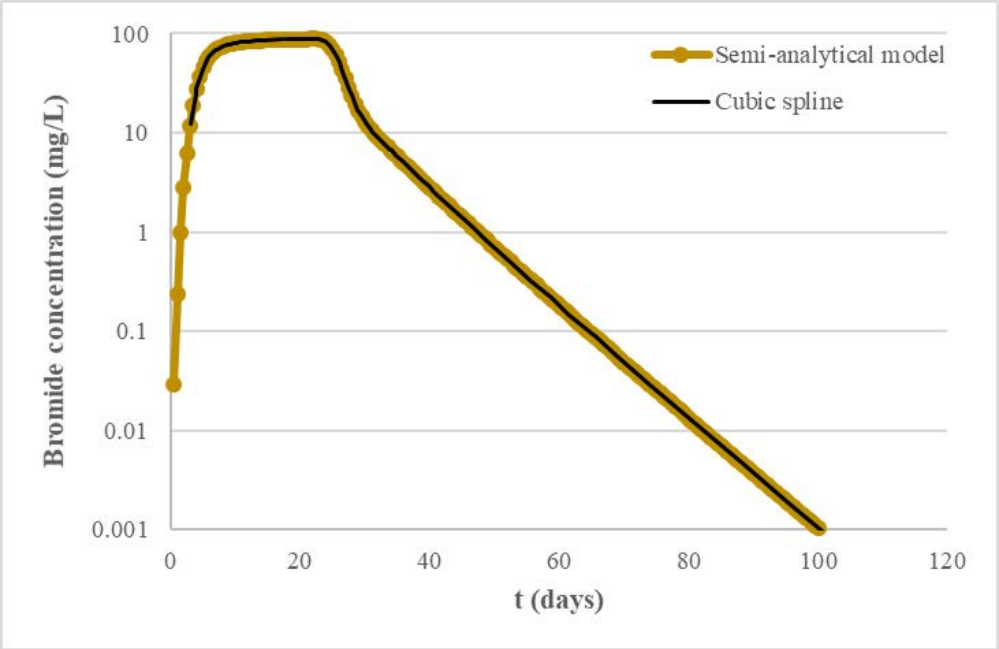

b)

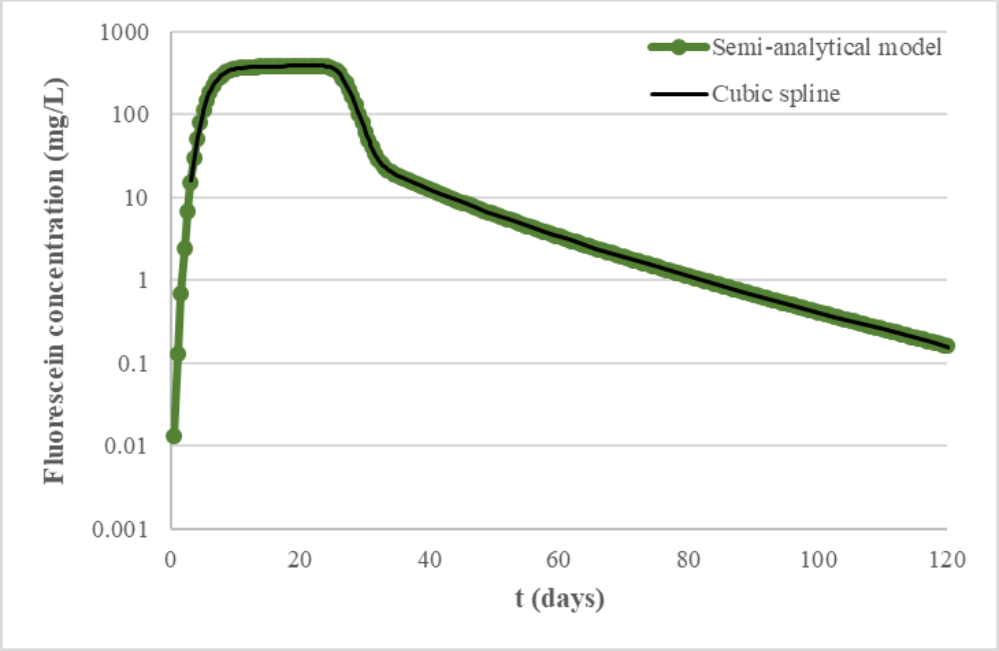

Figure A.2 Comparison of cubic spline with 50-gridblock simulated data in suspended clay lenses case for a) Bromide and b) Fluorescein.

a)

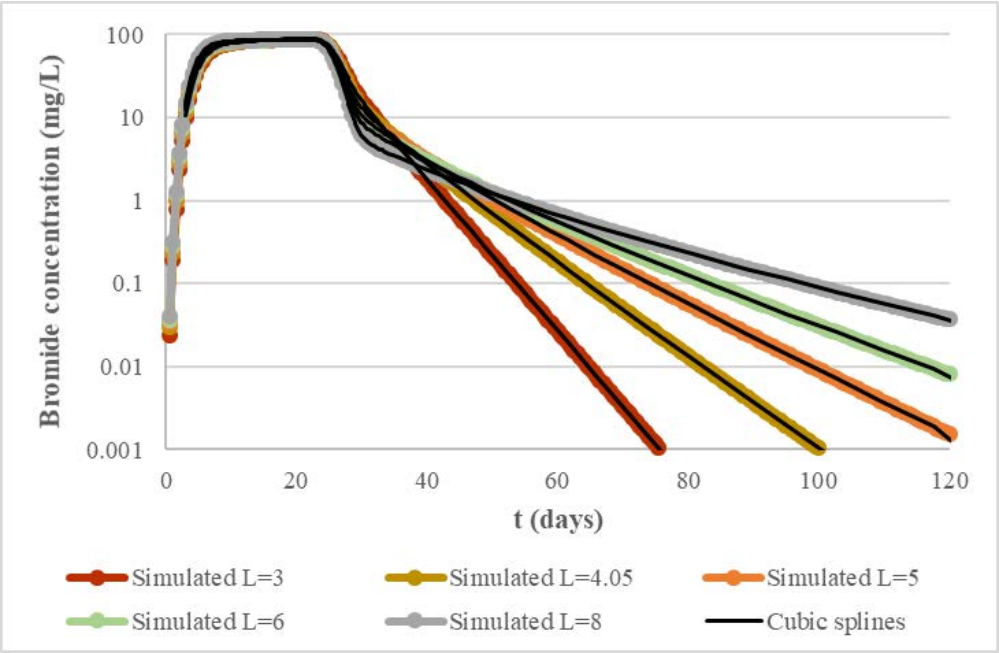

b)

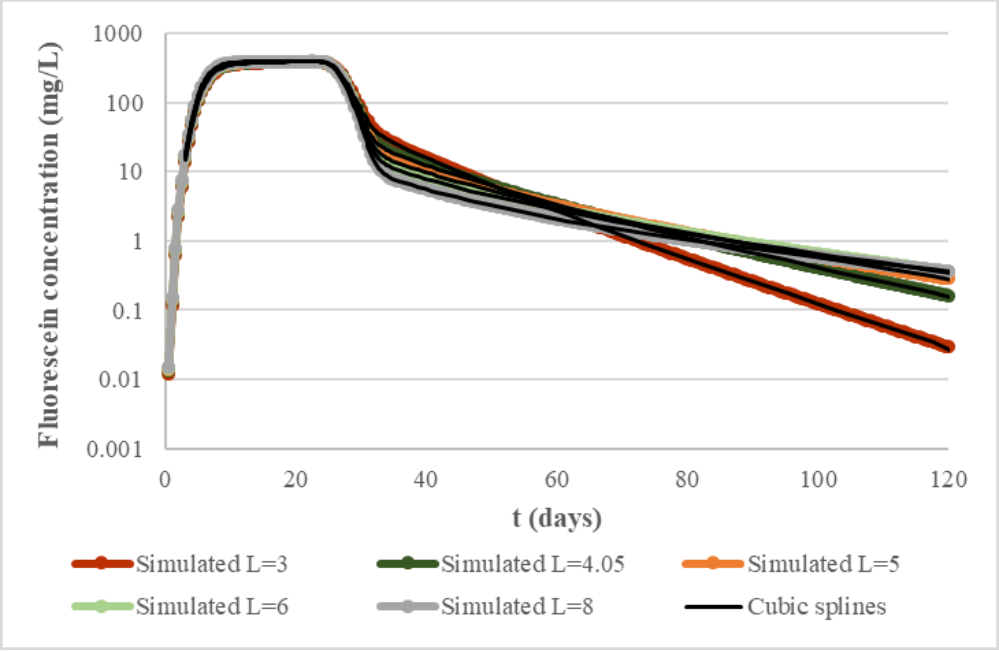

Figure A.3 Comparison of cubic splines with simulated data in diffusion length study for a) Bromide and b) Fluorescein.

Appendix B: Borehole data for T-PROGS simulation

The data for the boreholes used in Chapter 7 shown below was taken from the "Borehole Editor" window in GMS:

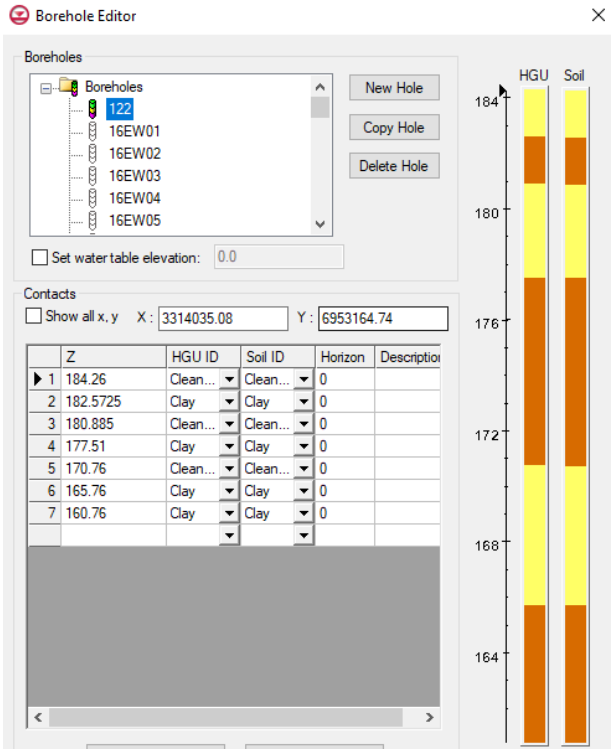

Figure B.1 Data for Borehole 122.

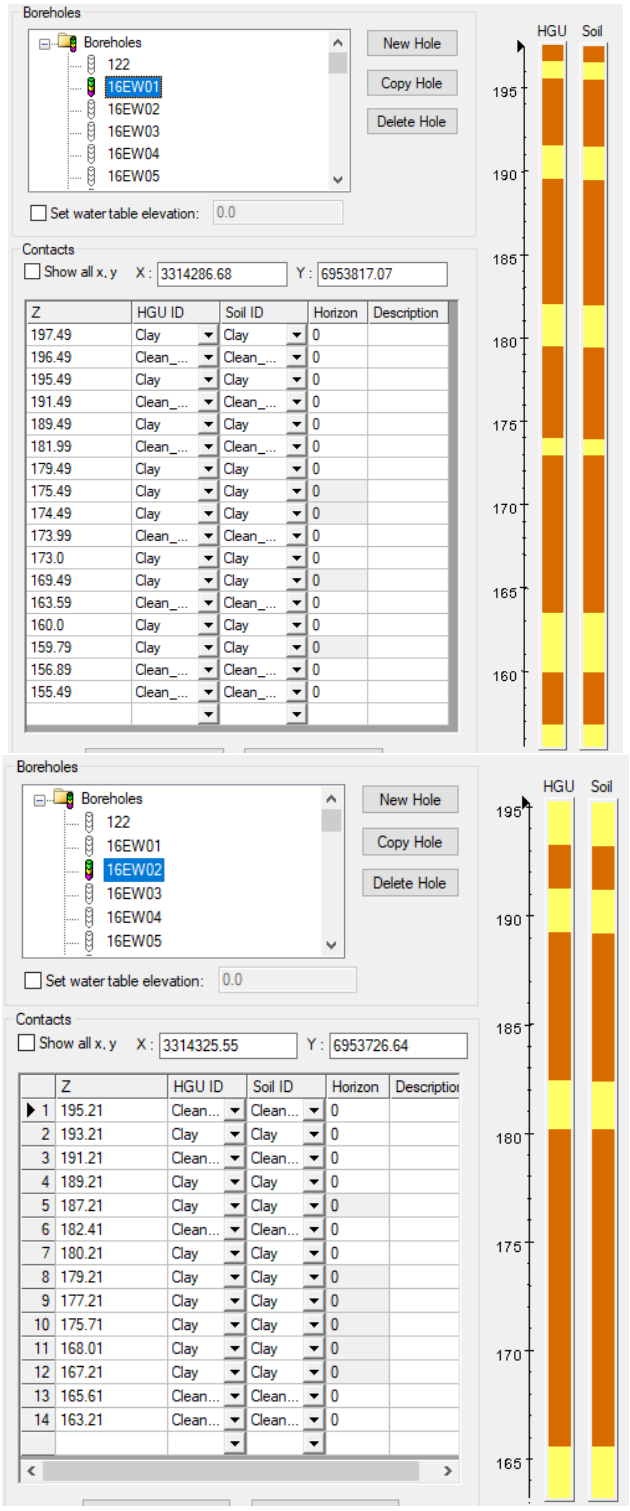

Figure B.2 Data for Boreholes 16EW01 (above) and 16EW02 (below).

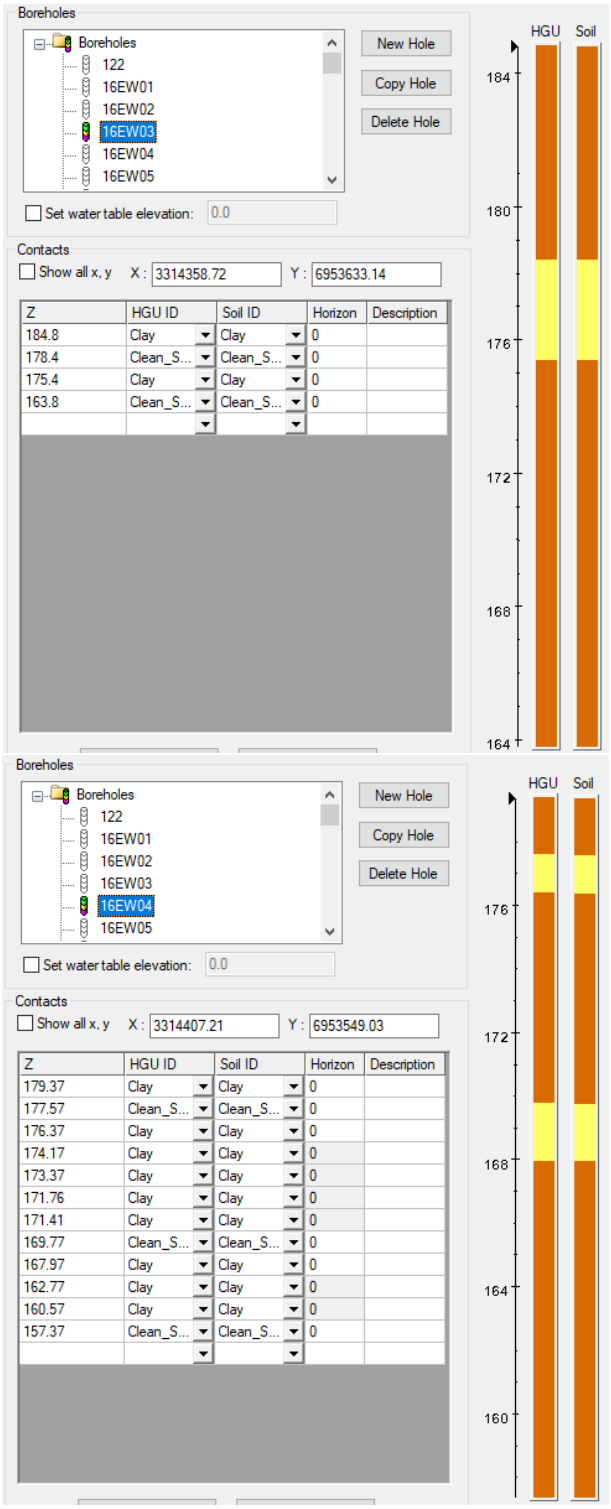

Figure B.3 Data for Boreholes 16EW03 (above) and 16EW04 (below).

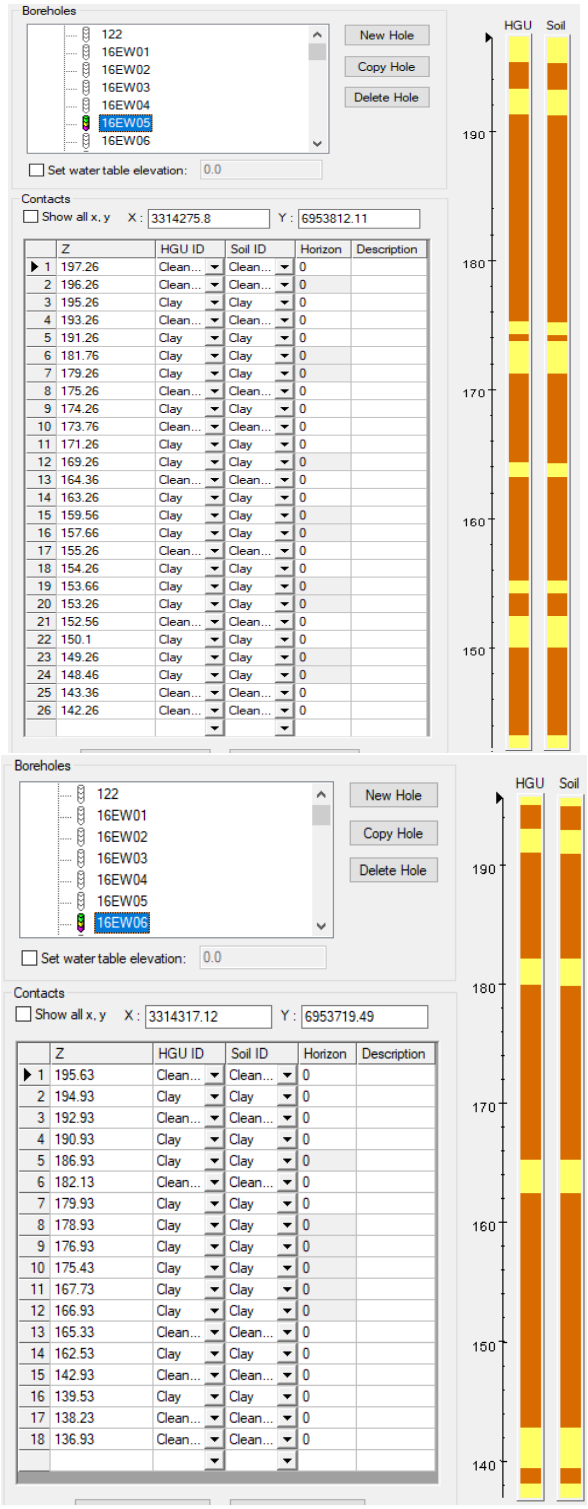

Figure B.4 Data for Boreholes 16EW05 (above) and 16EW06 (below).

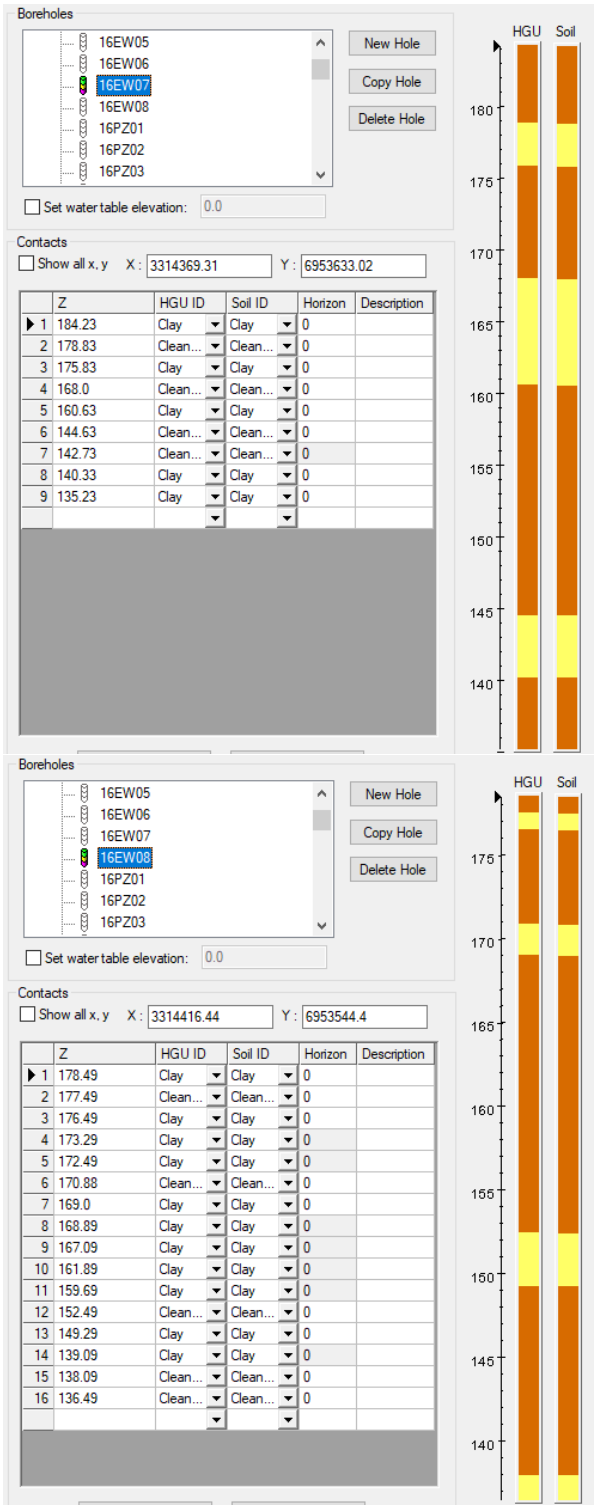

Figure B.5 Data for Boreholes 16EW07 (above) and 16EW08 (below).

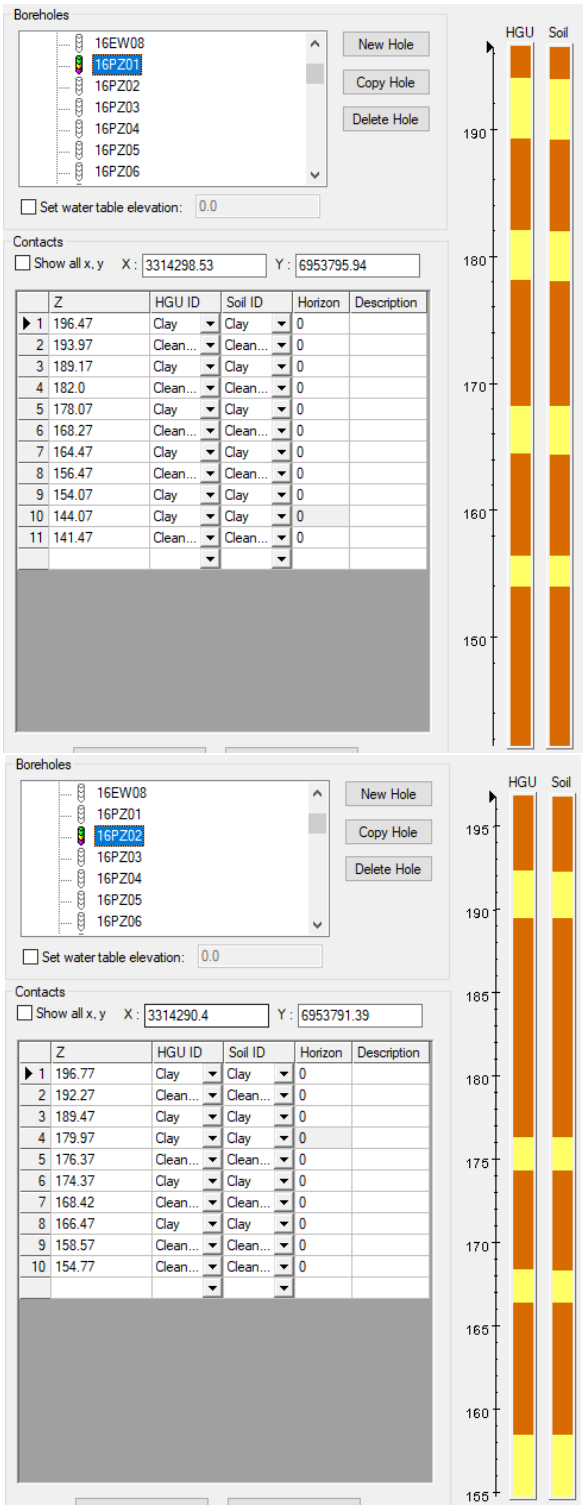

Figure B.6 Data for Boreholes 16PZ01 (above) and 16PZ02 (below).

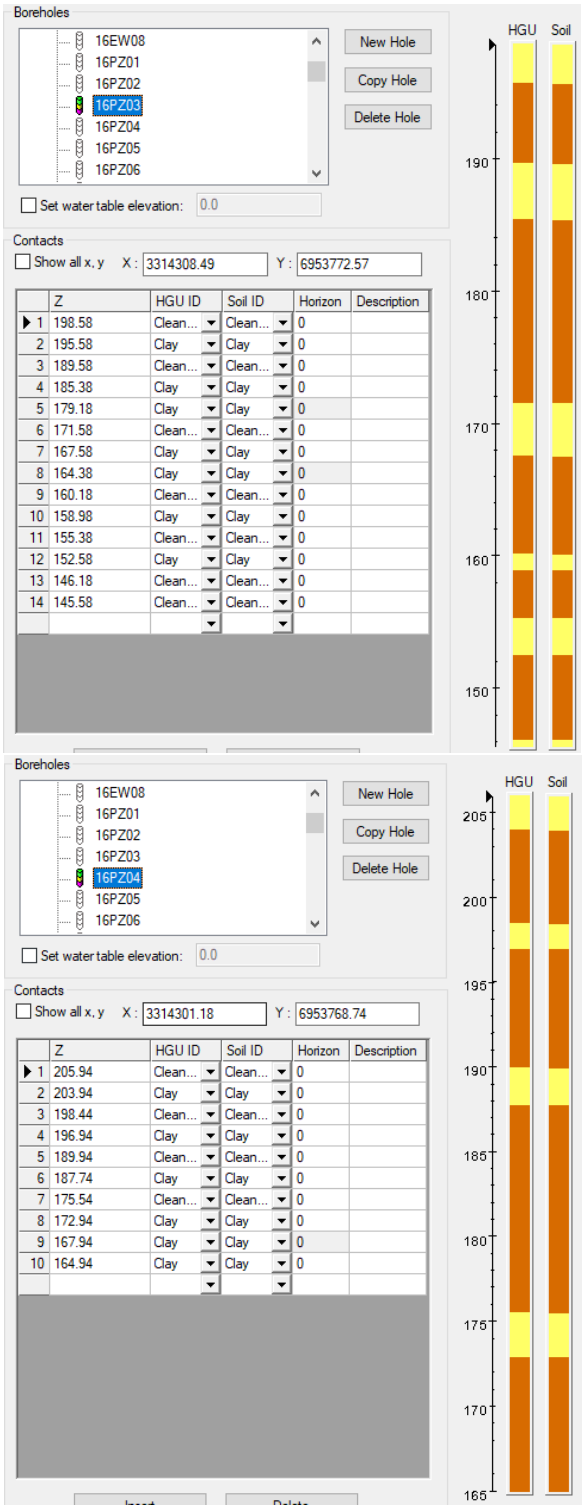

Figure B.7 Data for Boreholes 16PZ03 (above) and 16PZ04 (below).

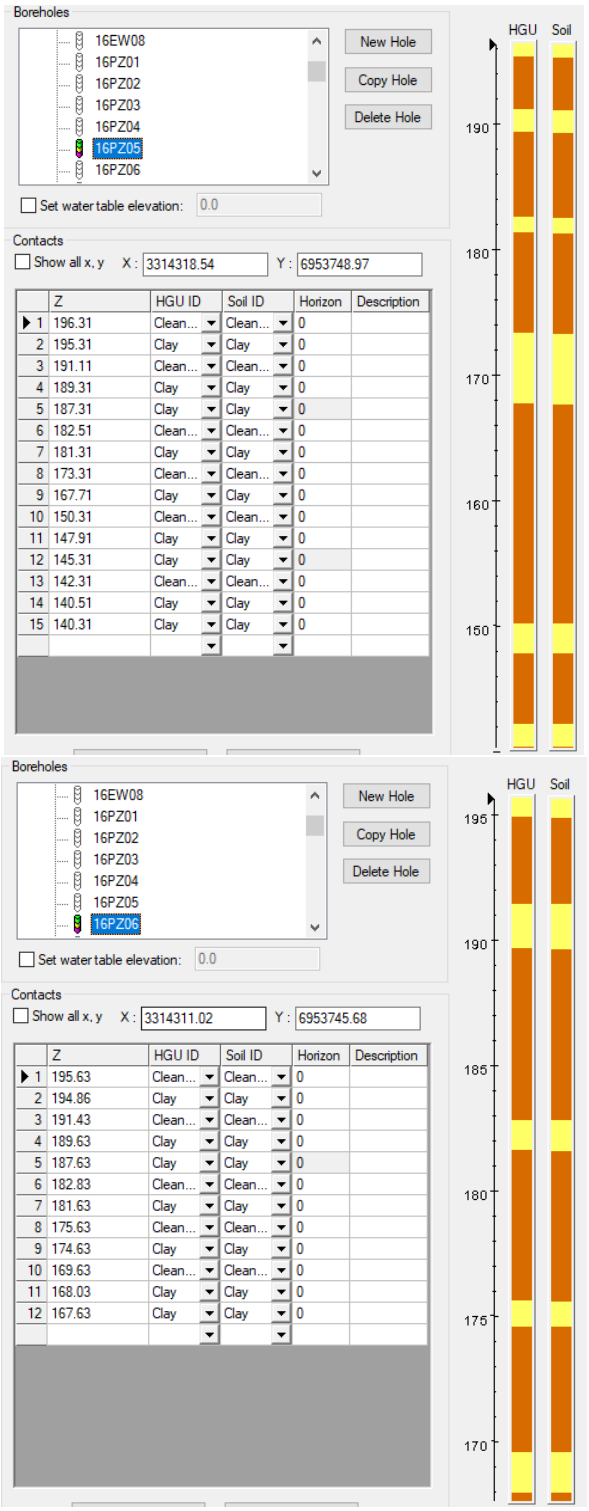

Figure B.8 Data for Boreholes 16PZ05 (above) and 16PZ06 (below).

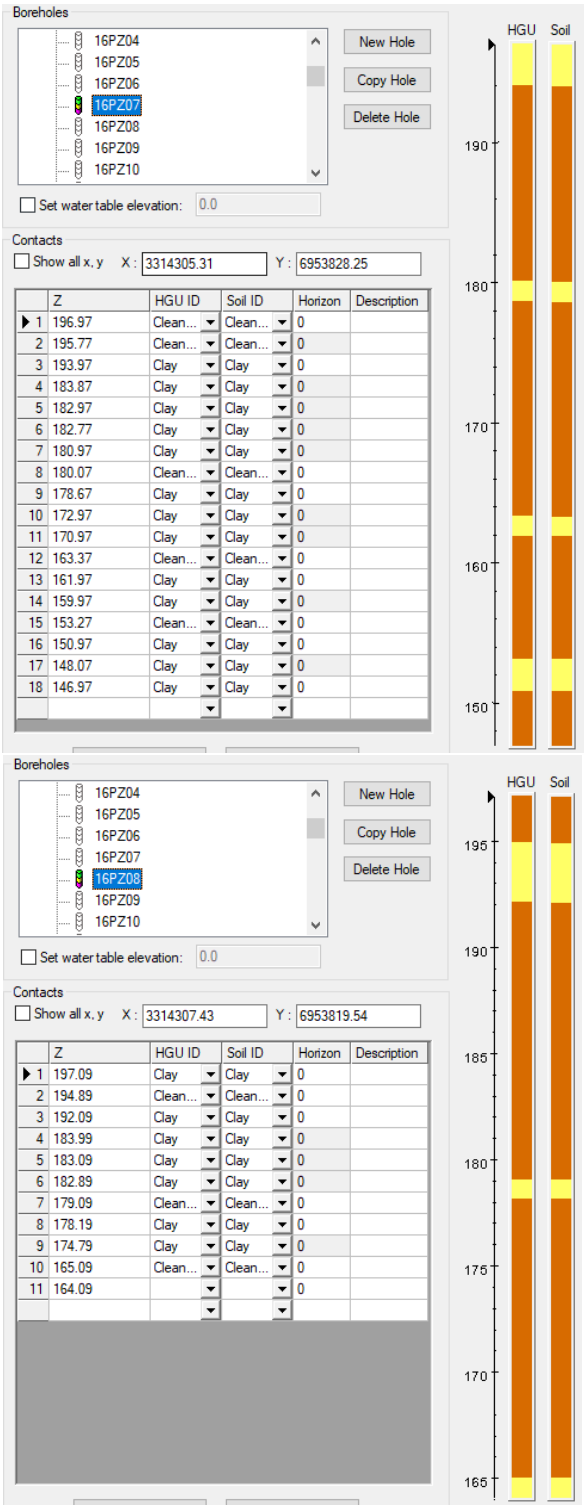

Figure B.9 Data for Boreholes 16PZ07 (above) and 16PZ08 (below).

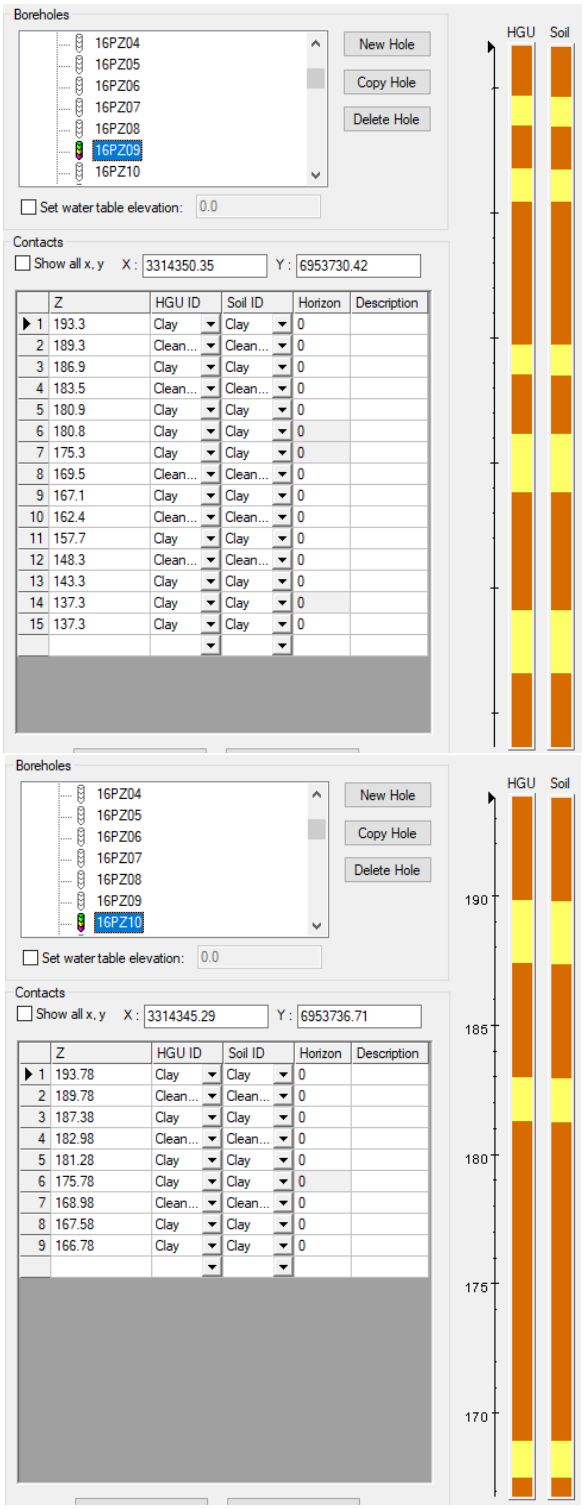

Figure B.10 Data for Boreholes 16PZ09 (above) and 16PZ10 (below).

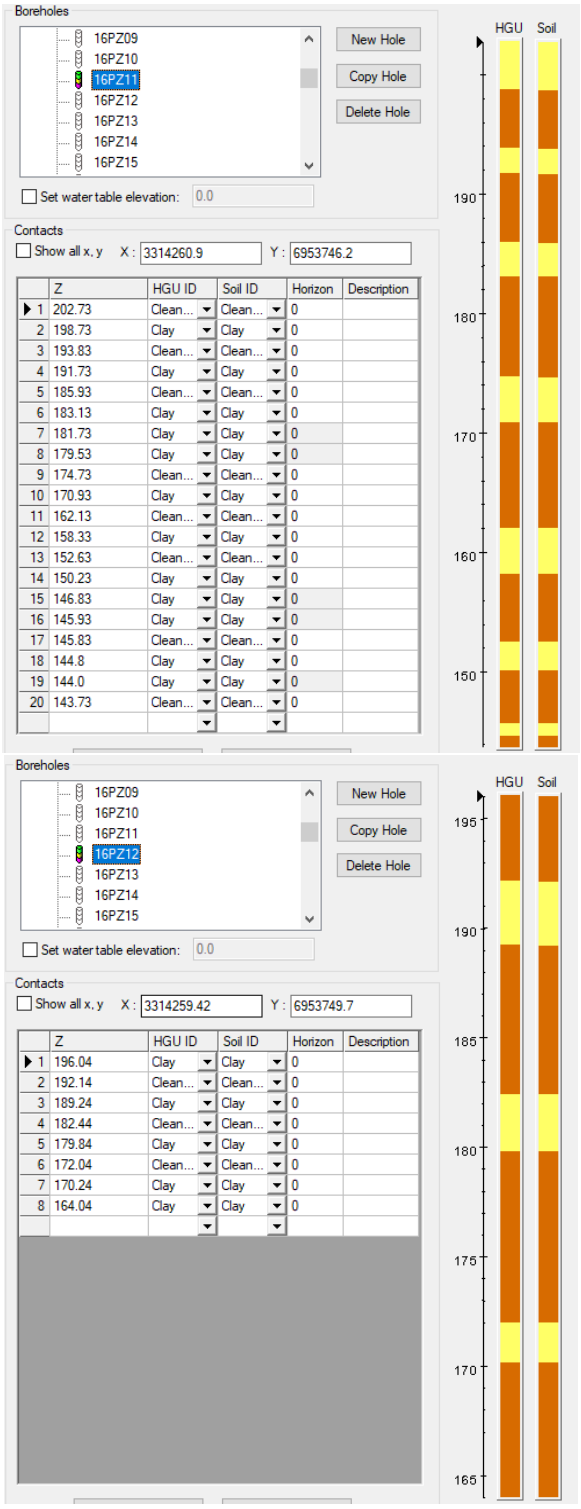

Figure B.11 Data for Boreholes 16PZ11 (above) and 16PZ12 (below).

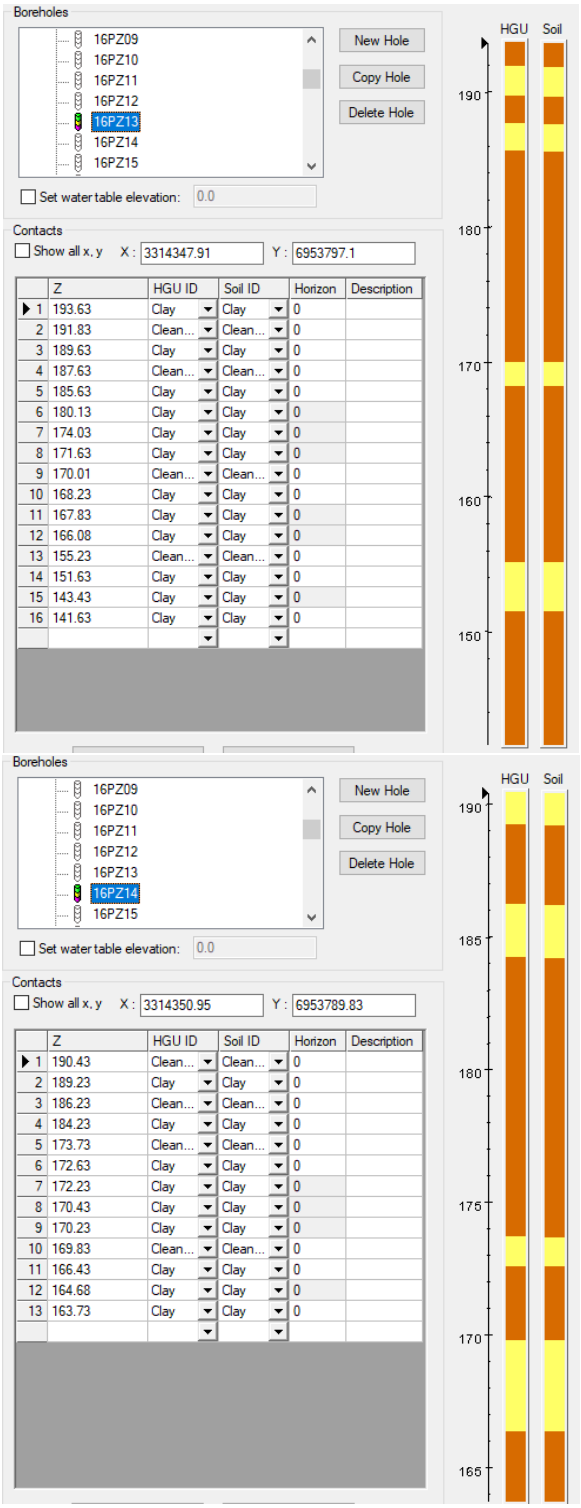

Figure B.12 Data for Boreholes 16PZ13 (above) and 16PZ14 (below).

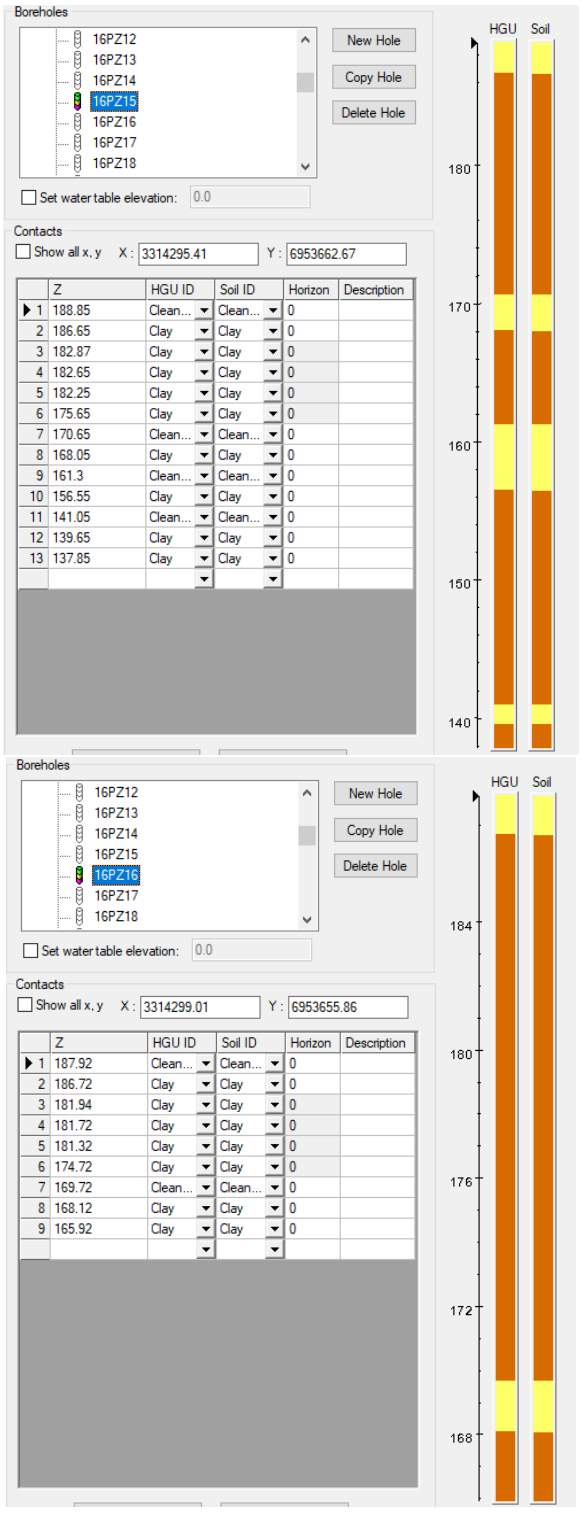

Figure B.13 Data for Boreholes 16PZ15 (above) and 16PZ16 (below).

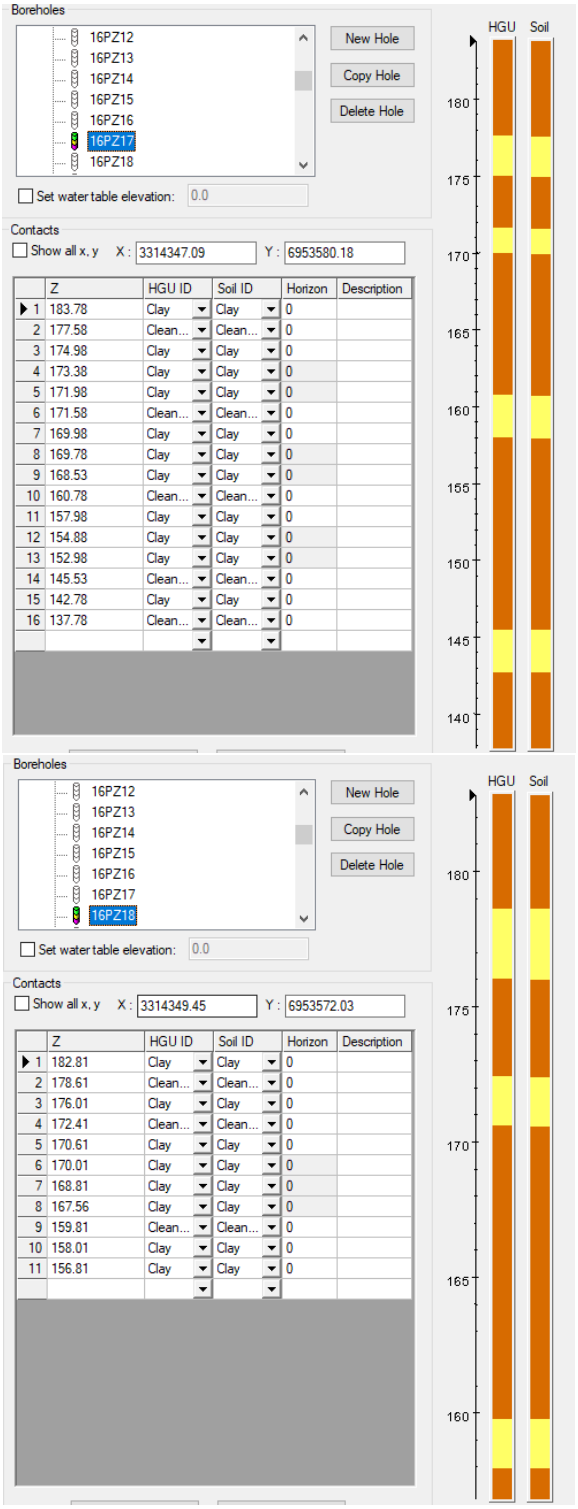

Figure B.14 Data for Boreholes 16PZ17 (above) and 16PZ18 (below).

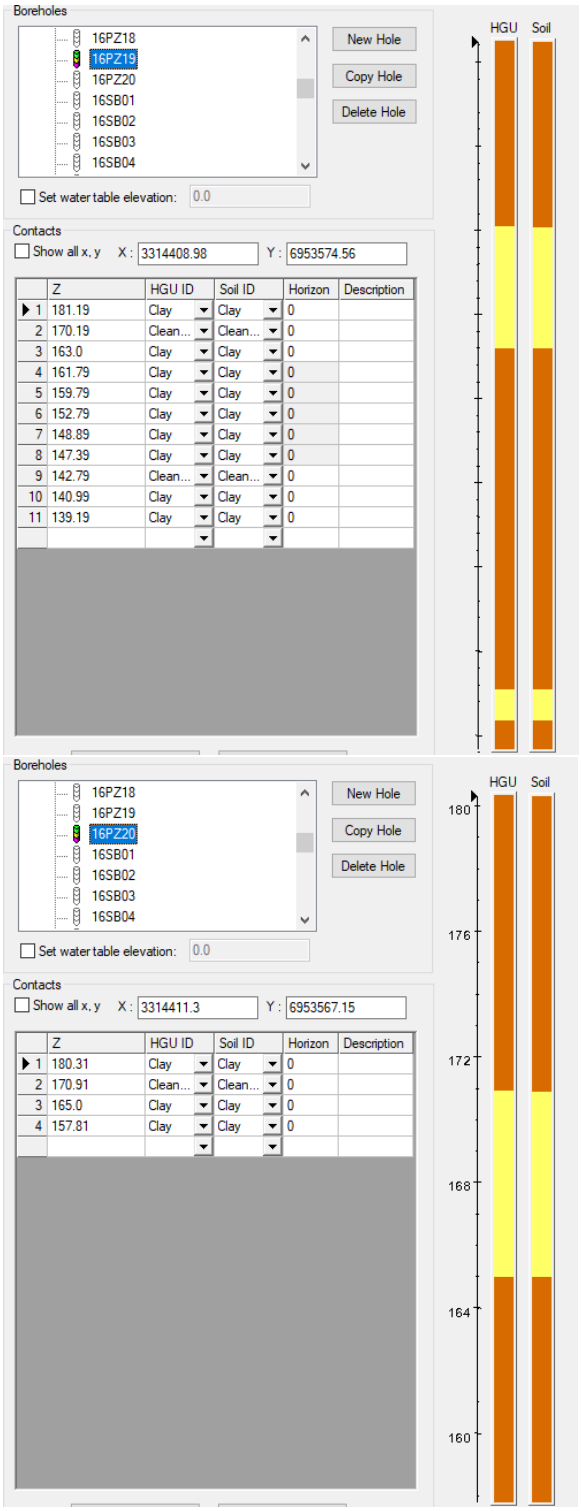

Figure B.15 Data for Boreholes 16PZ19 (above) and 16PZ20 (below).

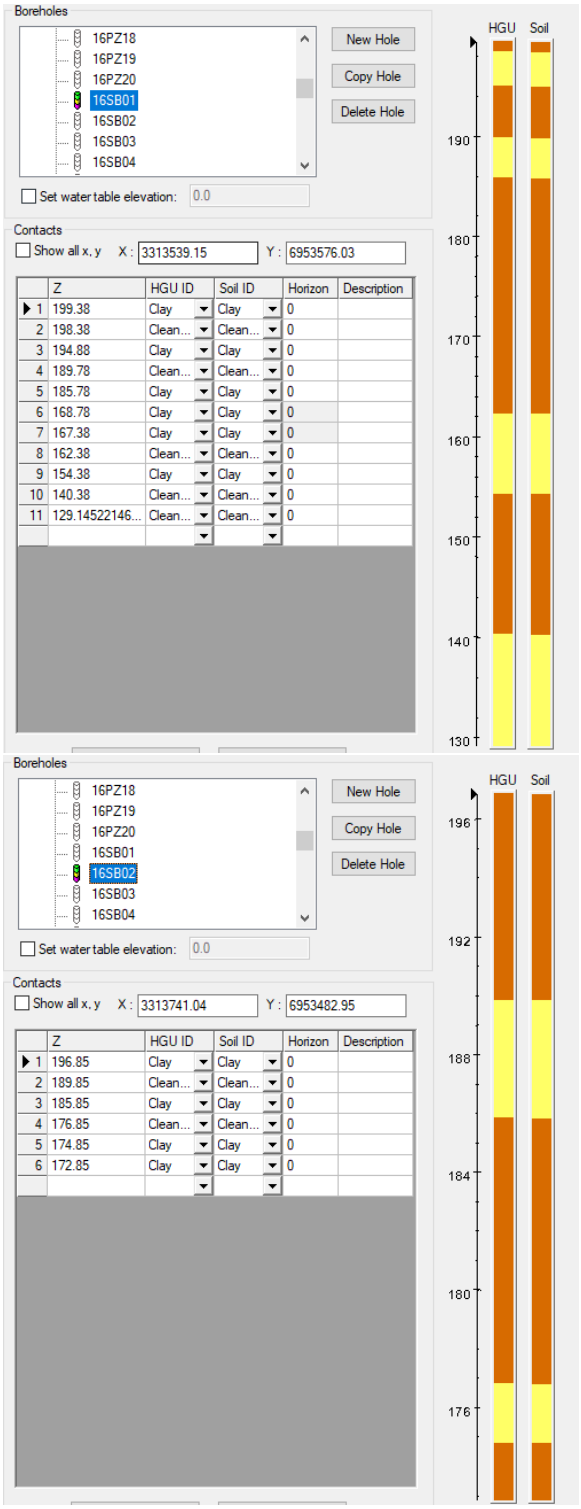

Figure B.16 Data for Boreholes 16SB01 (above) and 16SB02 (below).

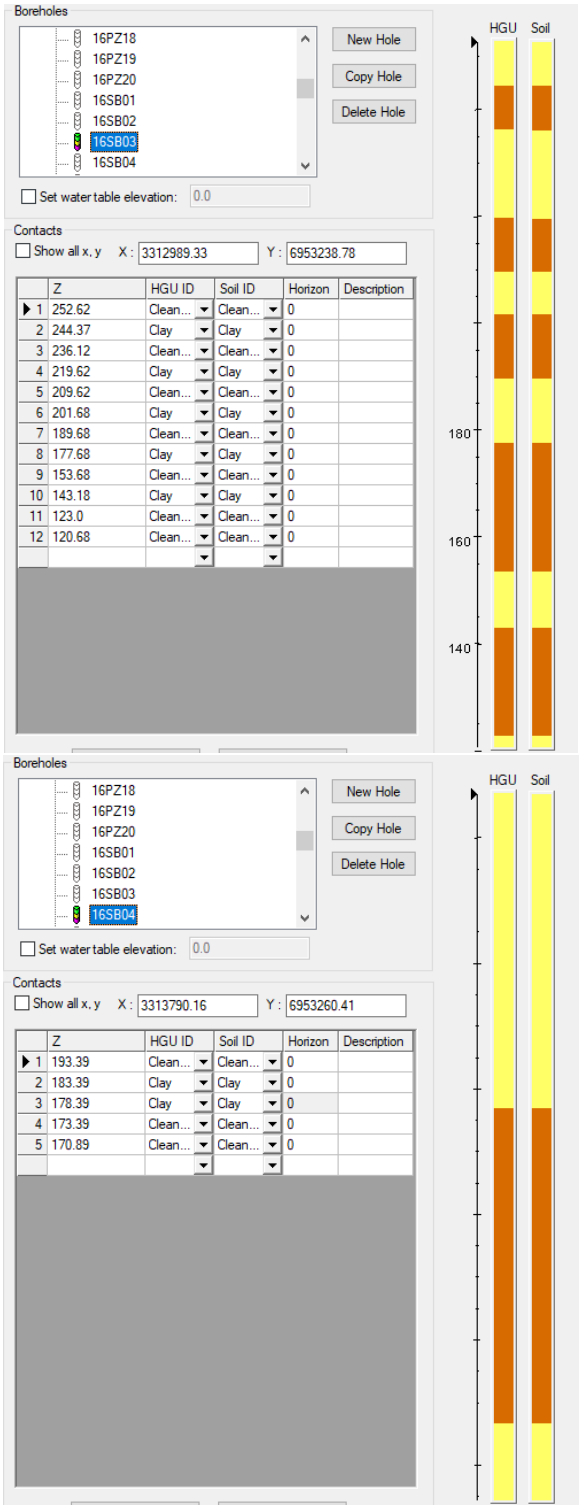

Figure B.17 Data for Boreholes 16SB03 (above) and 16SB04 (below).

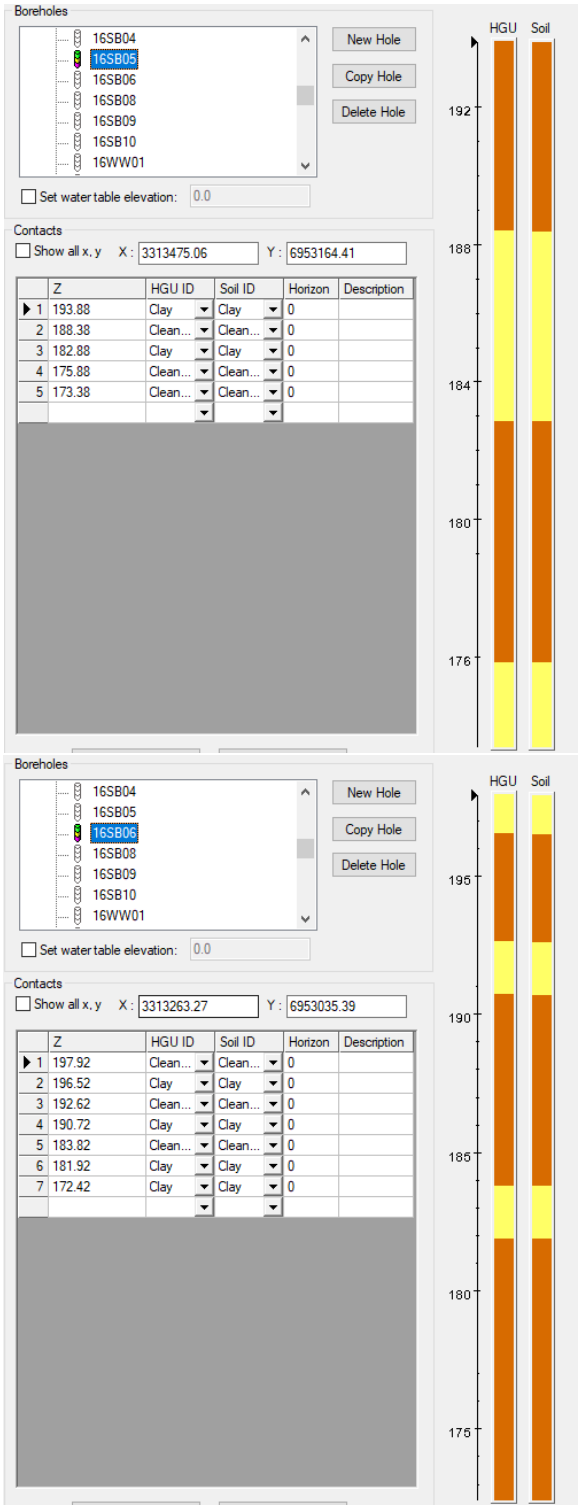

Figure B.18 Data for Boreholes 16SB05 (above) and 16SB06 (below).

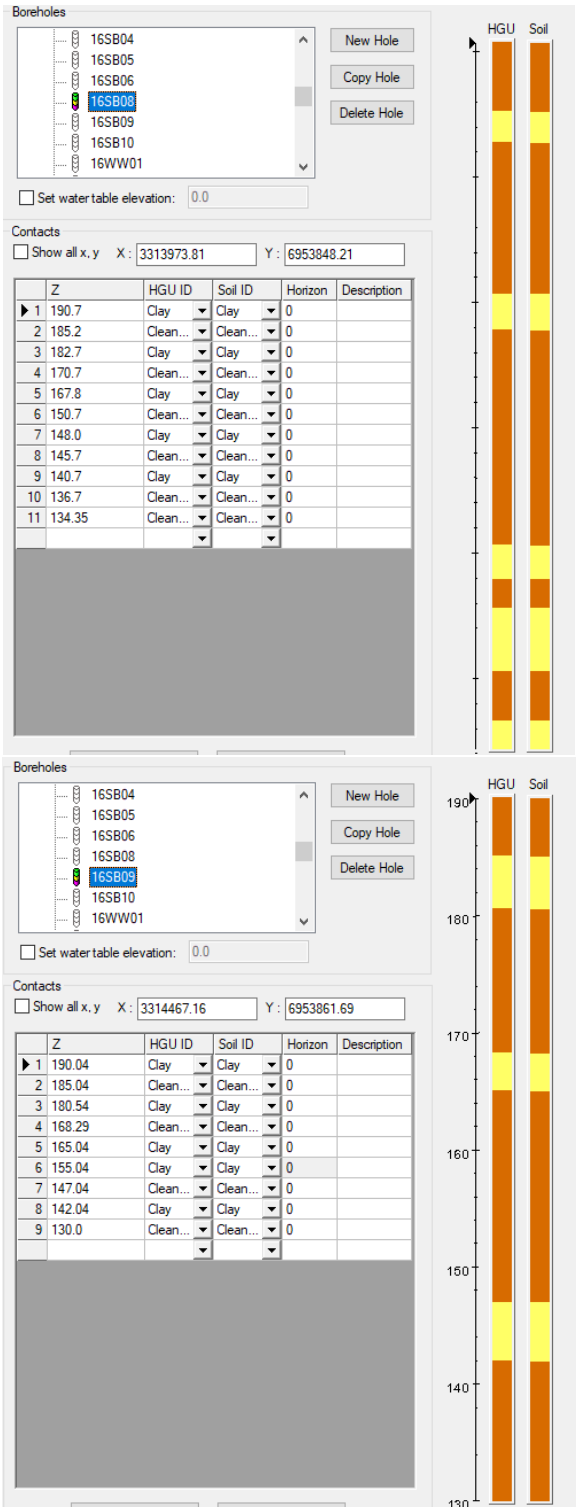

Figure B.19 Data for Boreholes 16SB08 (above) and 16SB09 (below).

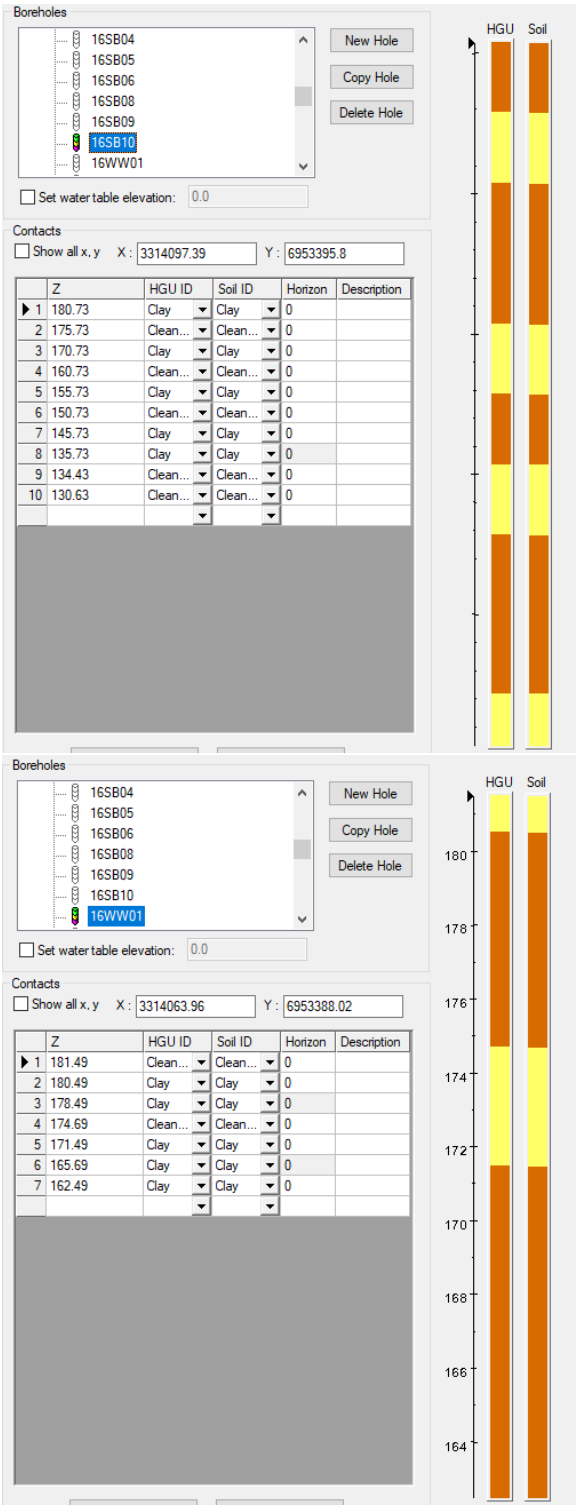

Figure B.20 Data for Boreholes 16SB10 (above) and 16WW01 (below).

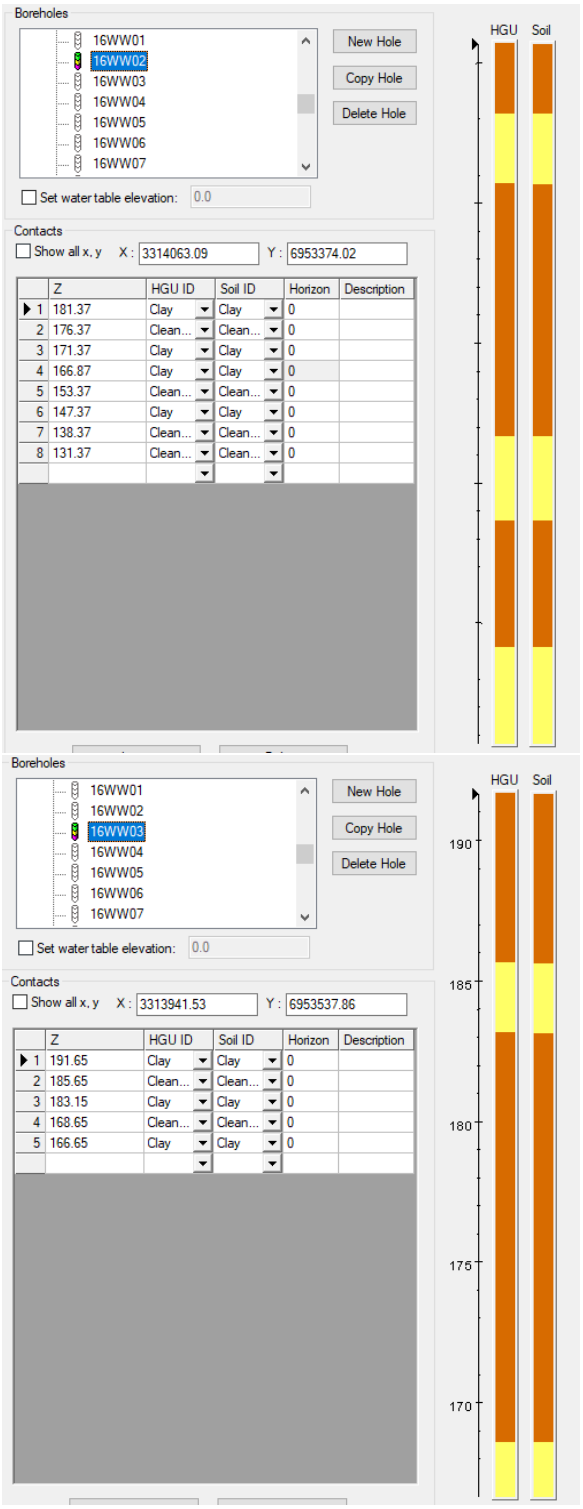

Figure B.21 Data for Boreholes 16WW02 (above) and 16WW03 (below).

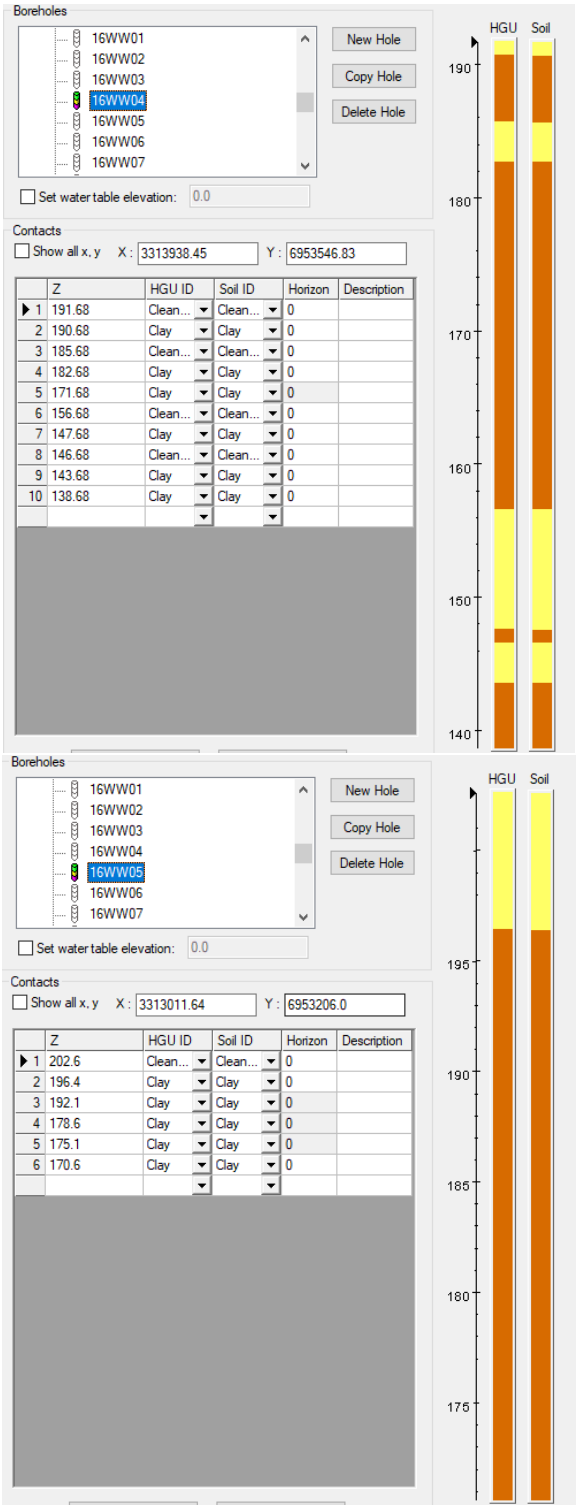

Figure B.22 Data for Boreholes 16WW04 (above) and 16WW05 (below).

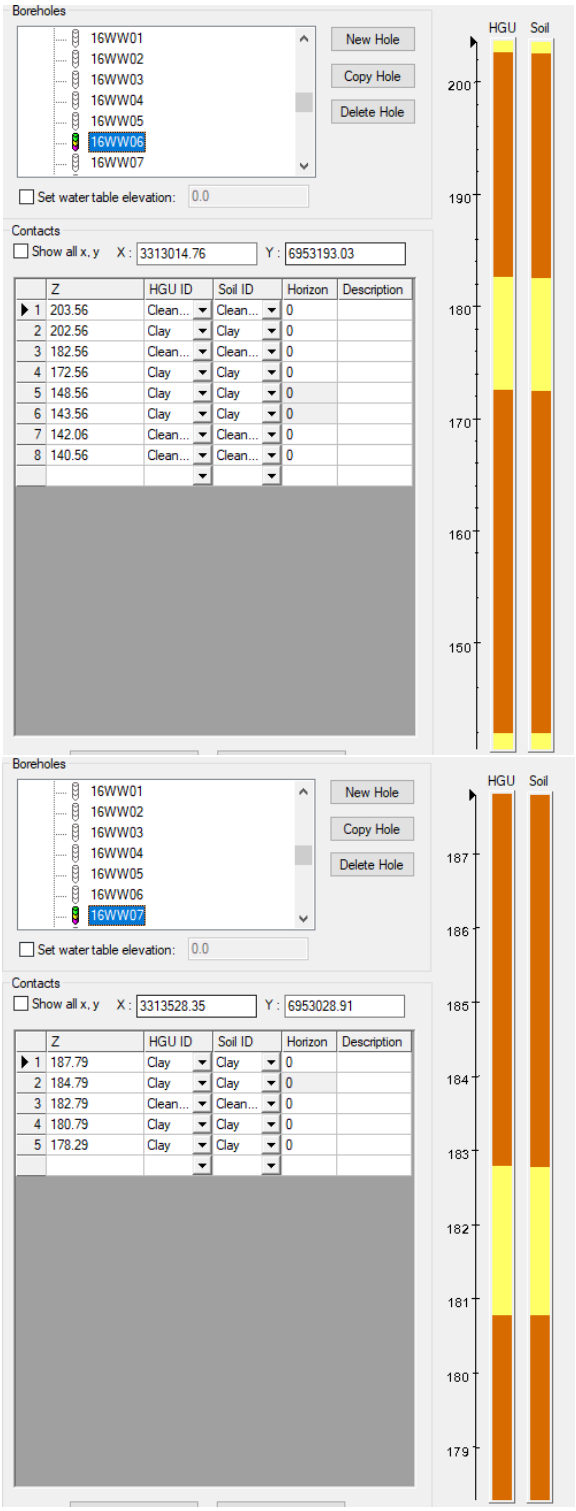

Figure B.23 Data for Boreholes 16WW06 (above) and 16WW07 (below).

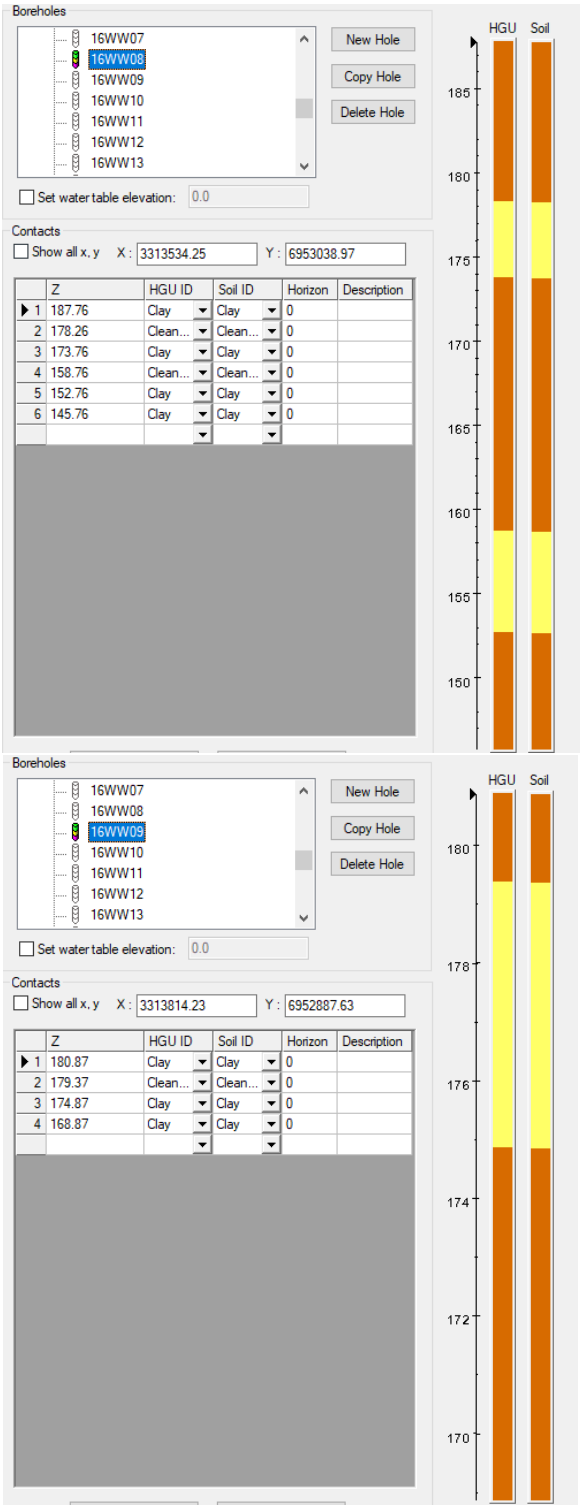

Figure B.24 Data for Boreholes 16WW08 (above) and 16WW09 (below).

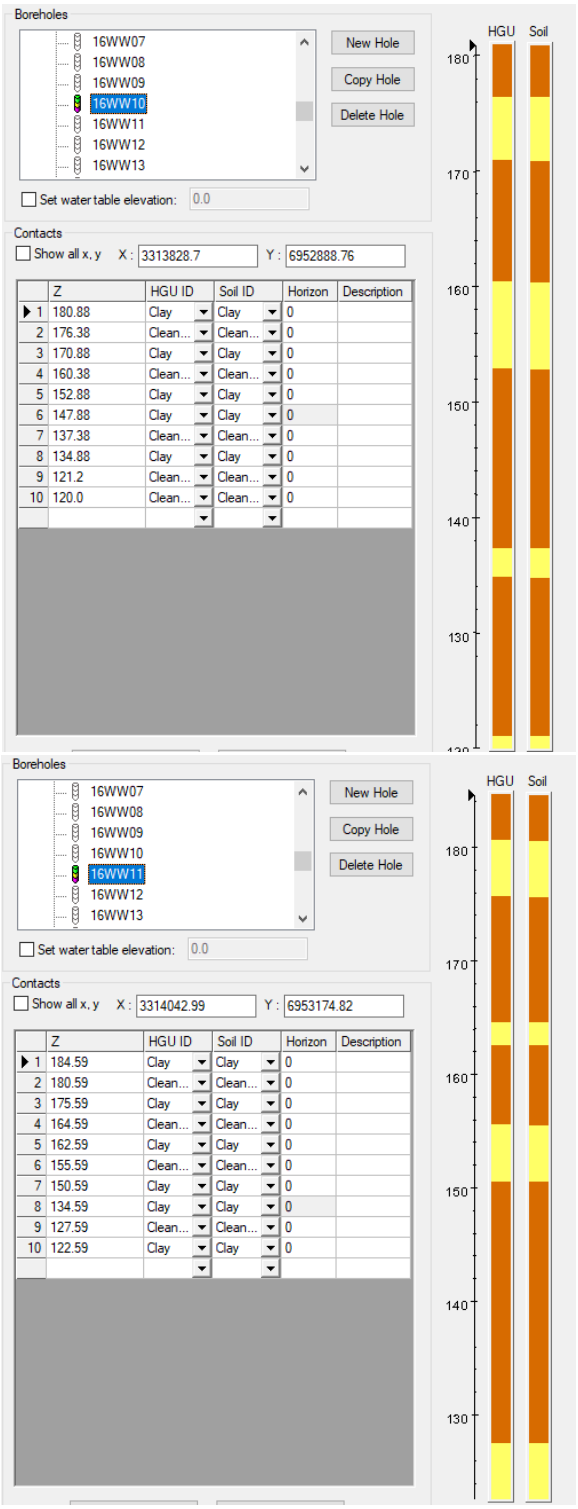

Figure B.25 Data for Boreholes 16WW10 (above) and 16WW11 (below).

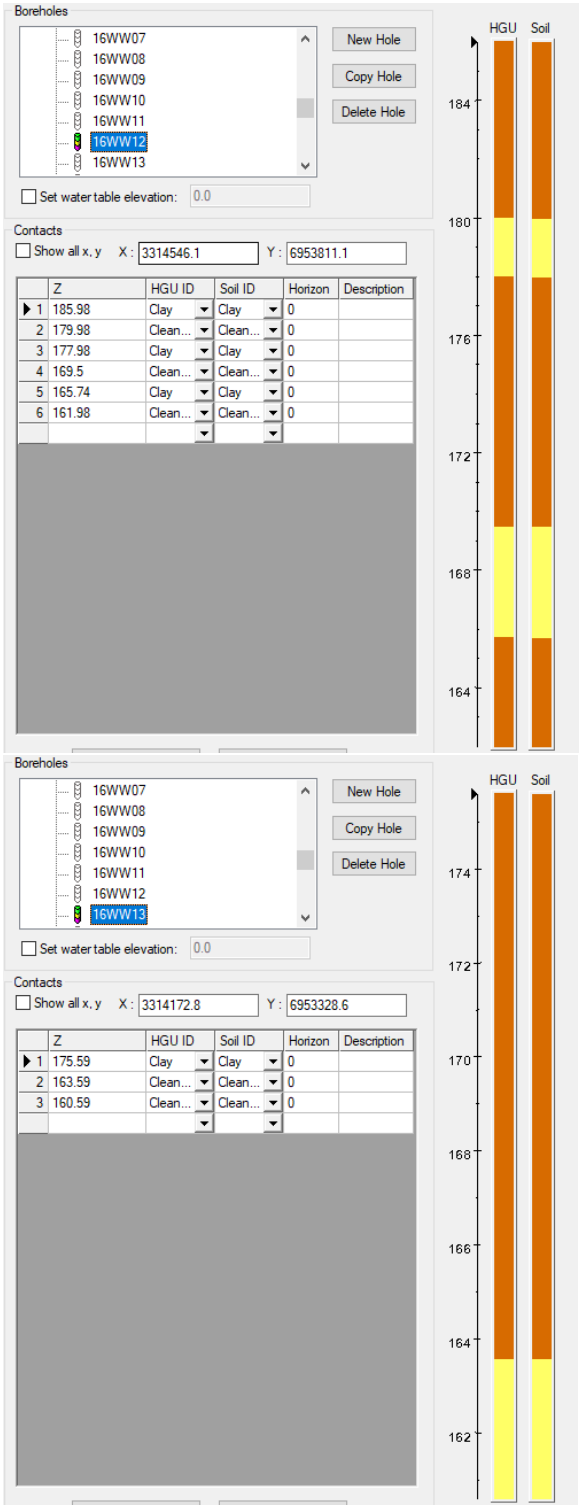

Figure B.26 Data for Boreholes 16WW12 (above) and 16WW13 (below).

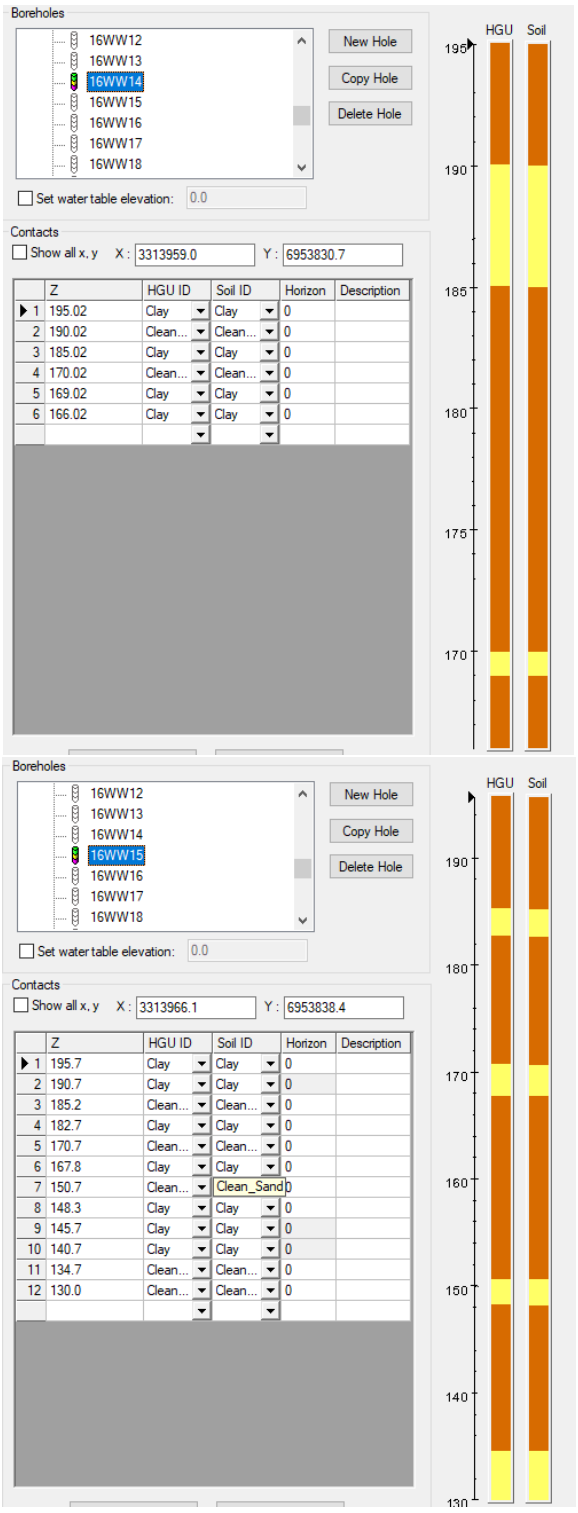

Figure B.27 Data for Boreholes 16WW14 (above) and 16WW15 (below).

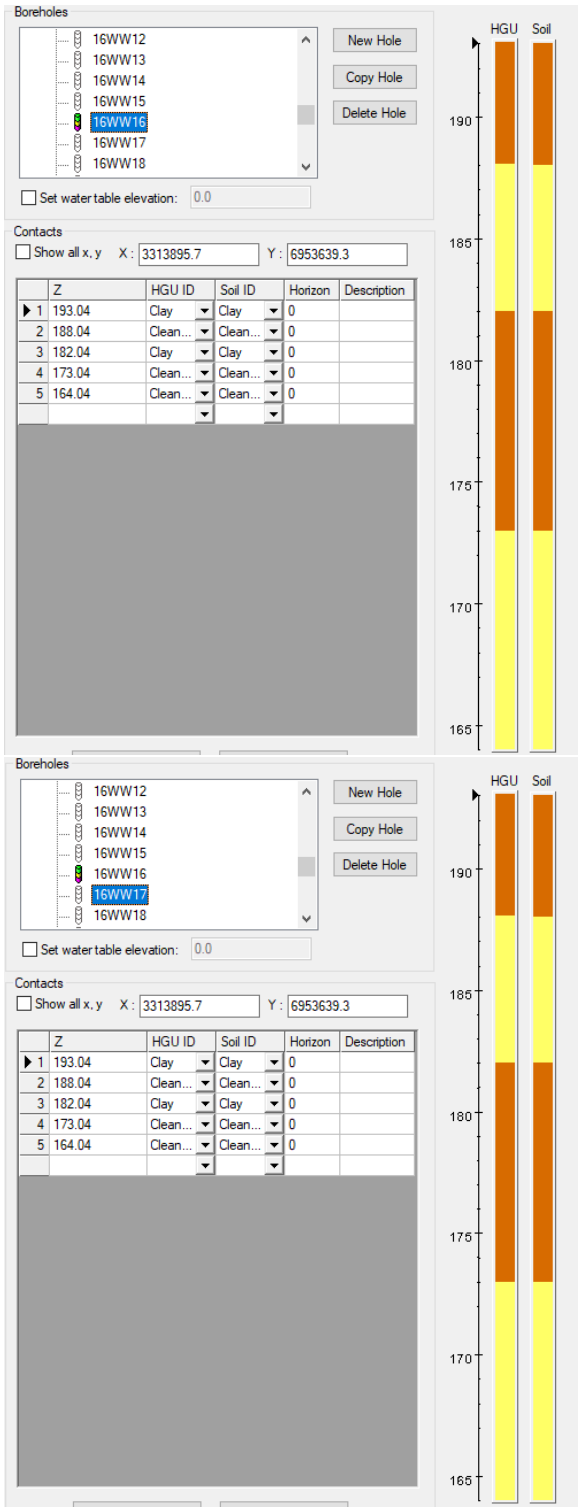

Figure B.28 Data for Boreholes 16WW16 (above) and 16WW17 (below).

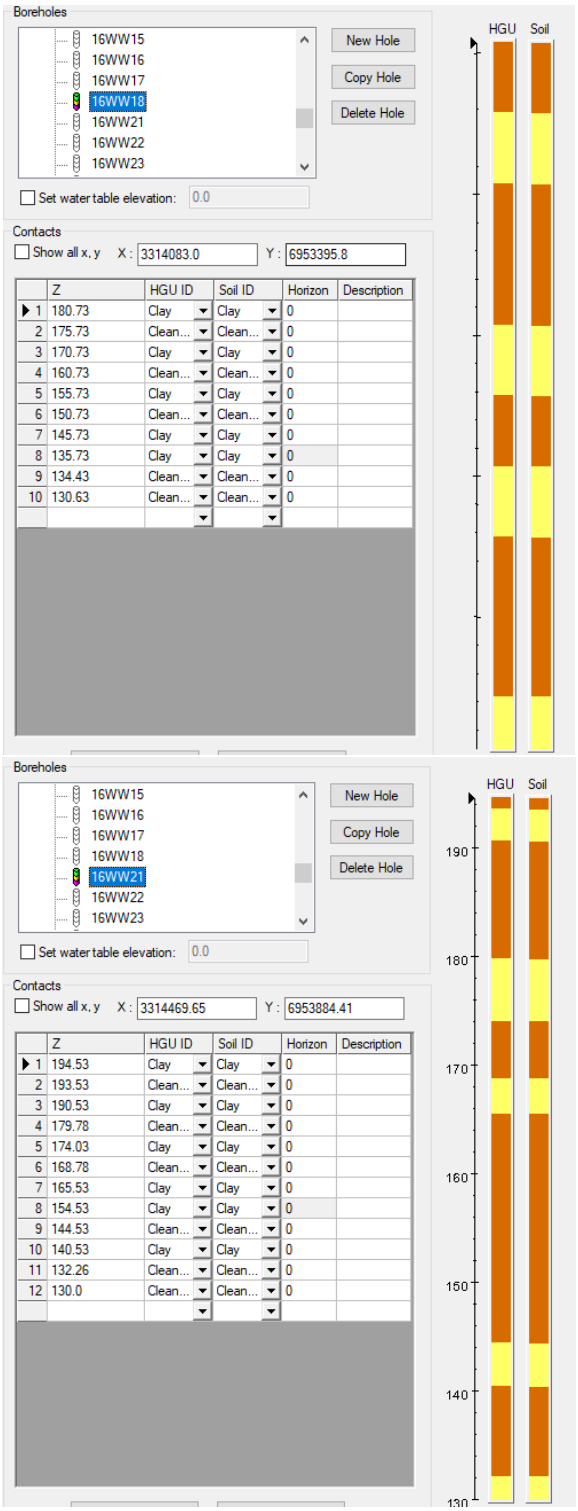

Figure B.29 Data for Boreholes 16WW18 (above) and 16WW21 (below).

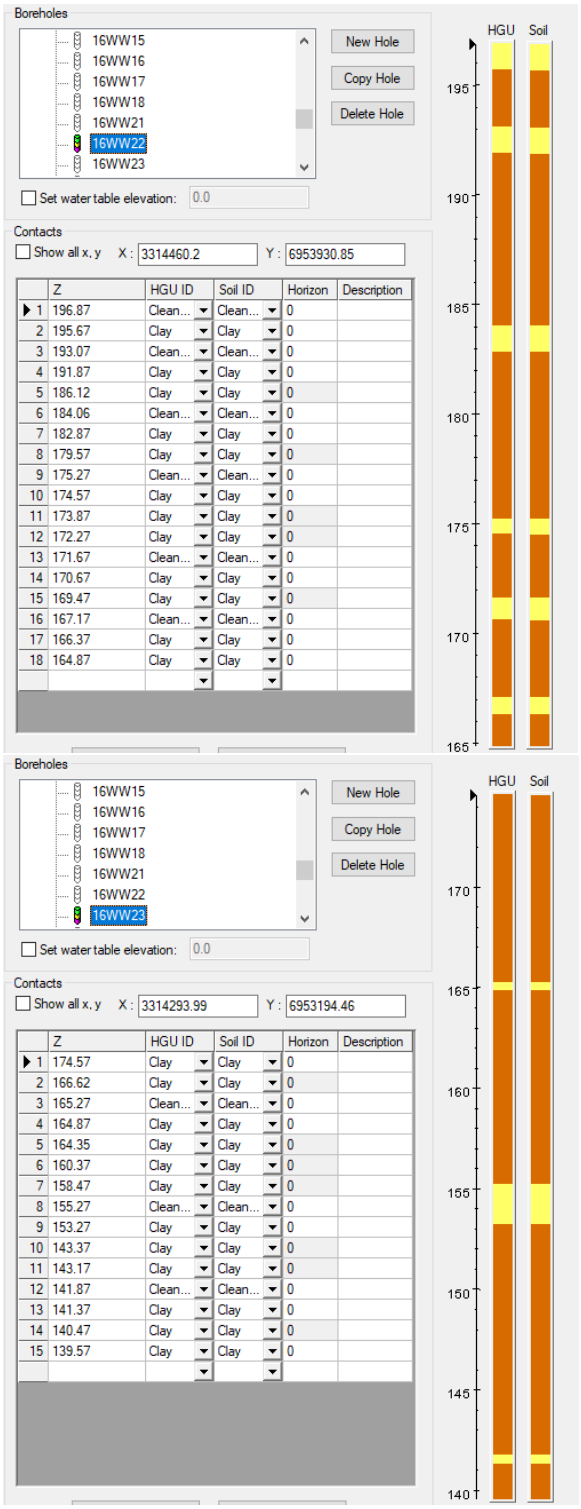

Figure B.30 Data for Boreholes 16WW22 (above) and 16WW23 (below).

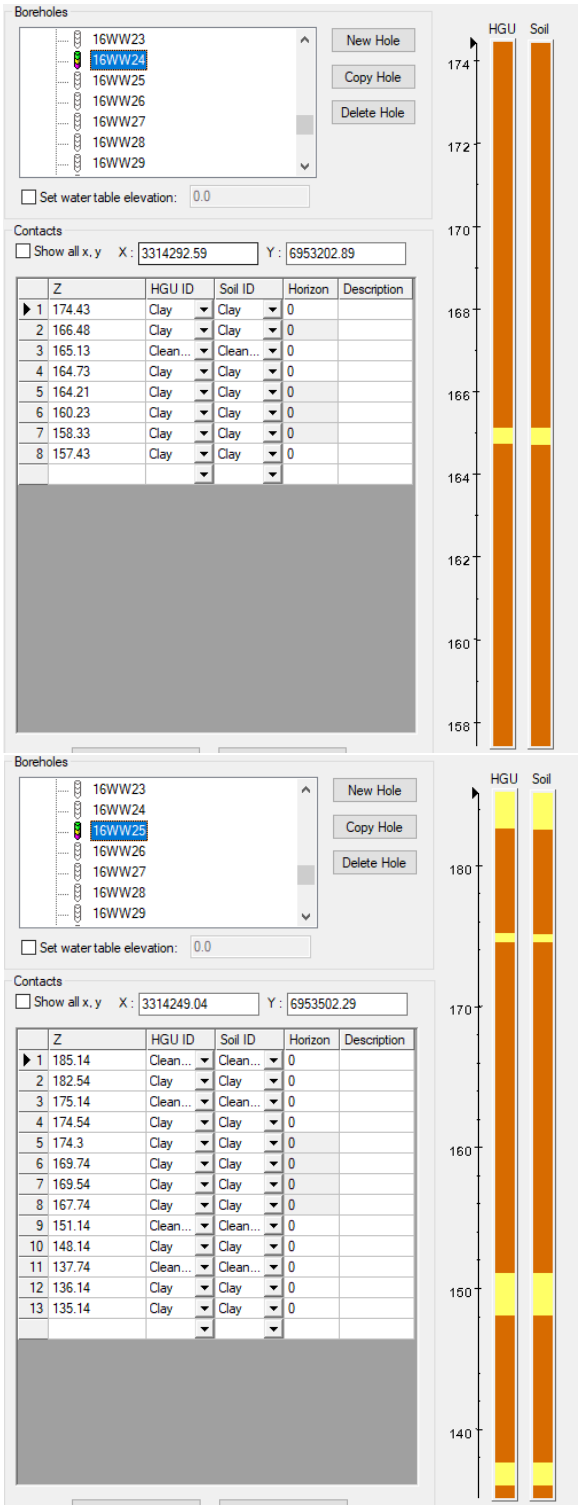

Figure B.31 Data for Boreholes 16WW24 (above) and 16WW25 (below).

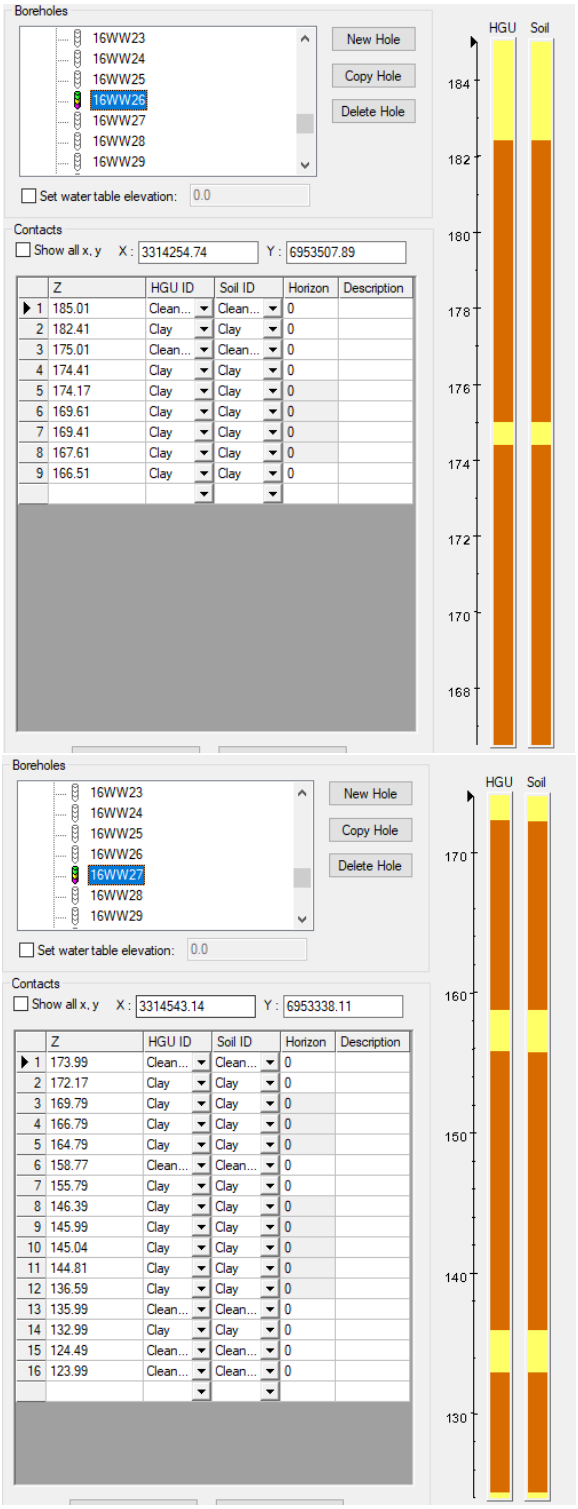

Figure B.32 Data for Boreholes 16WW26 (above) and 16WW27 (below).

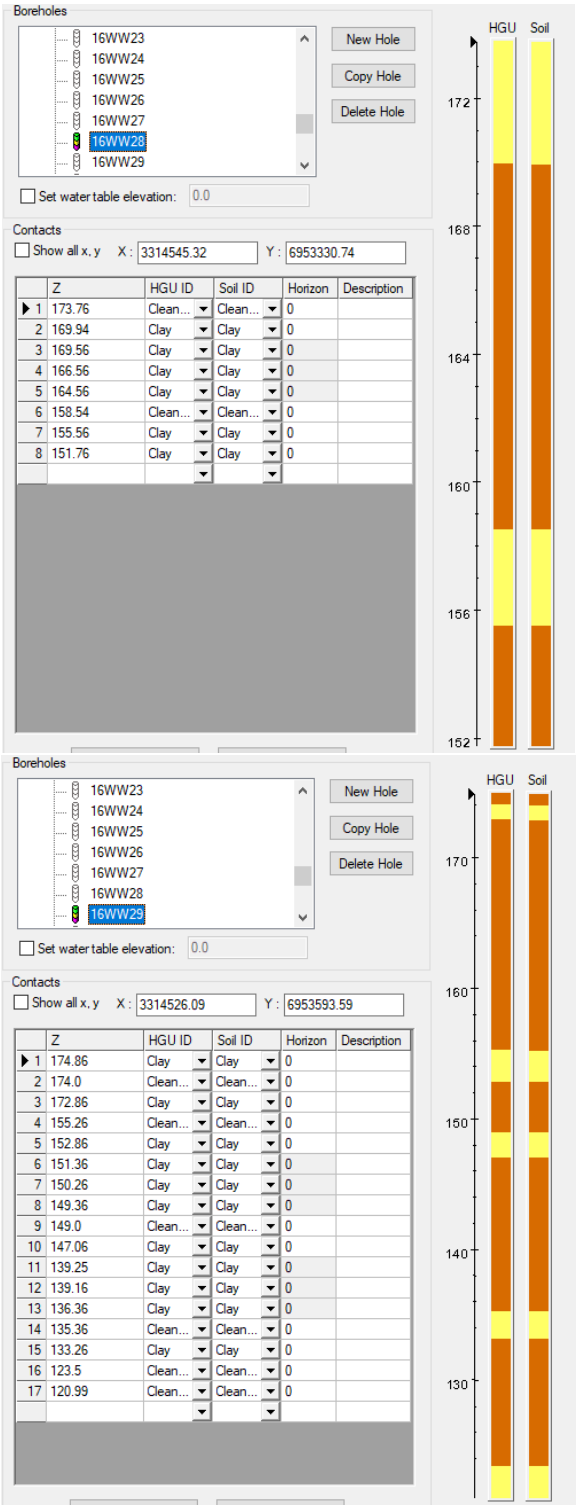

Figure B.33 Data for Boreholes 16WW28 (above) and 16WW29 (below).

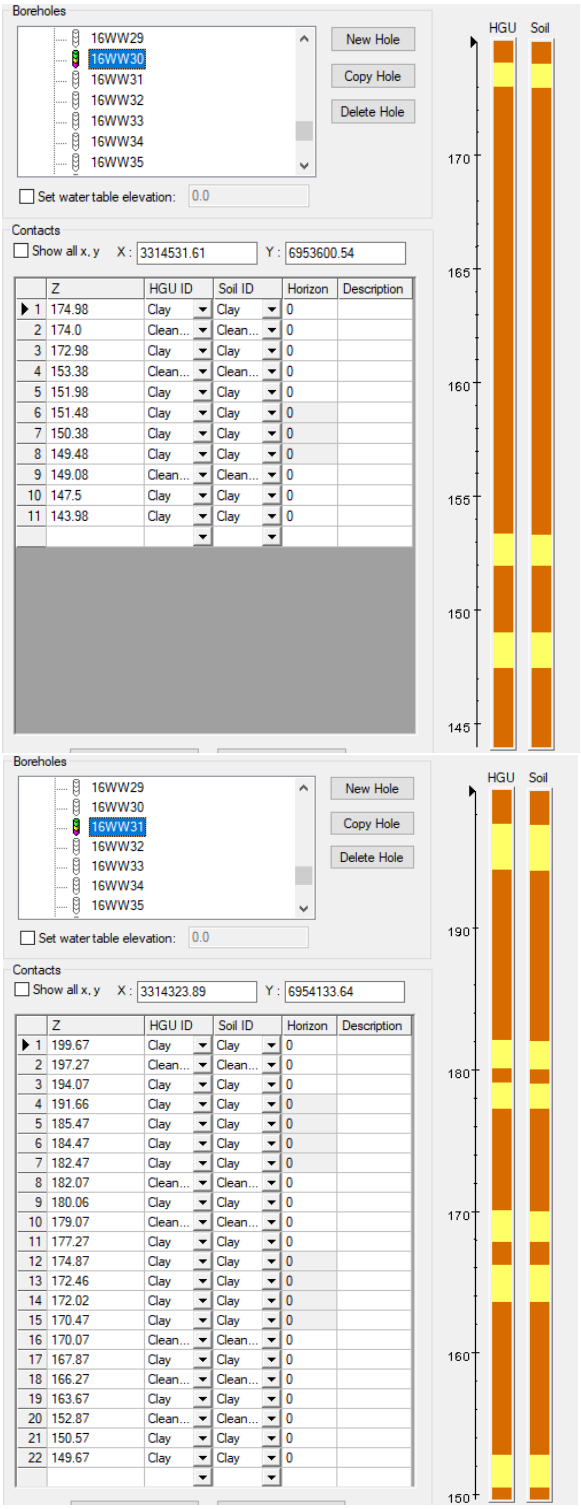

Figure B.34 Data for Boreholes 16WW30 (above) and 16WW31 (below).

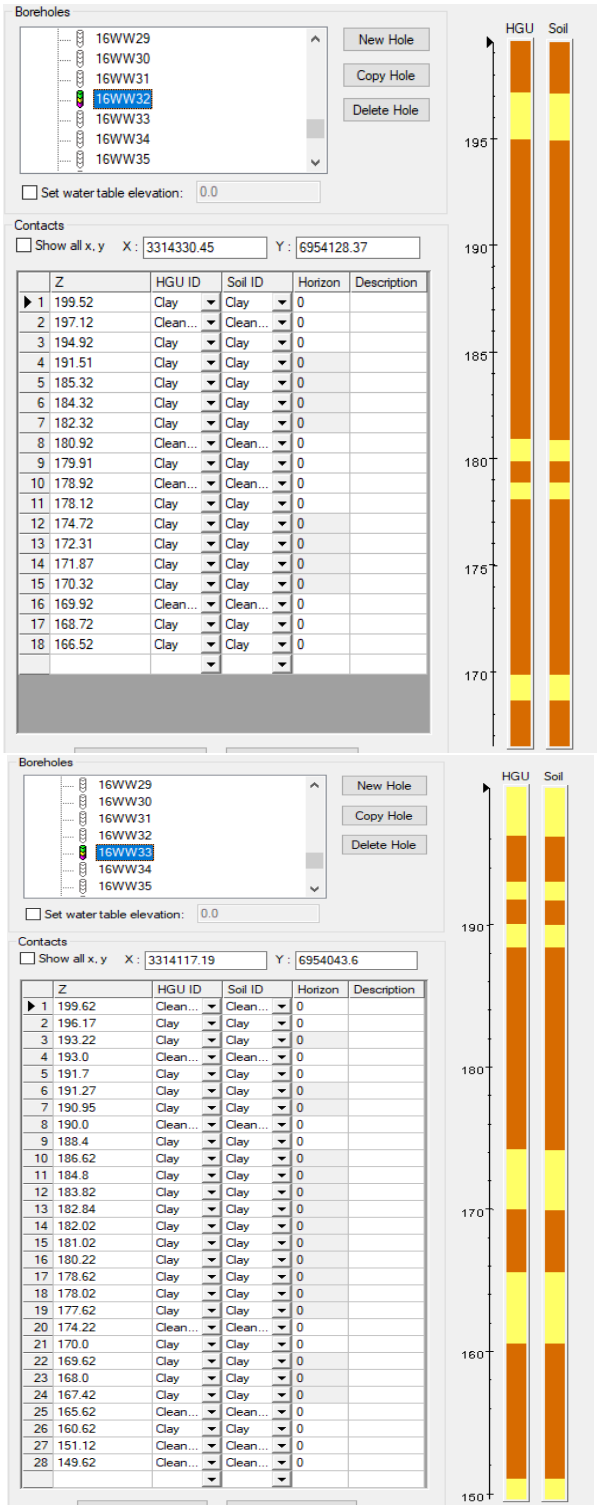

Figure B.35 Data for Boreholes 16WW32 (above) and 16WW33 (below).

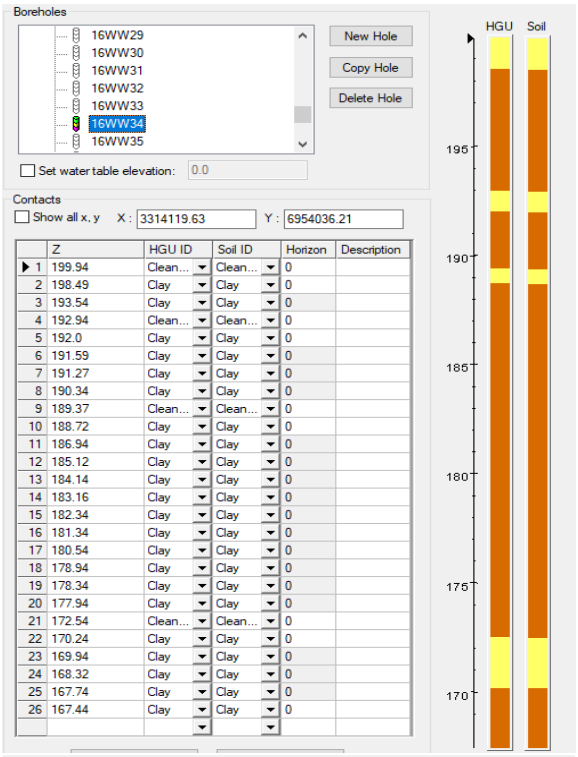

Figure B.36 Data for Boreholes 16WW34 (above) and 16WW35 (below).

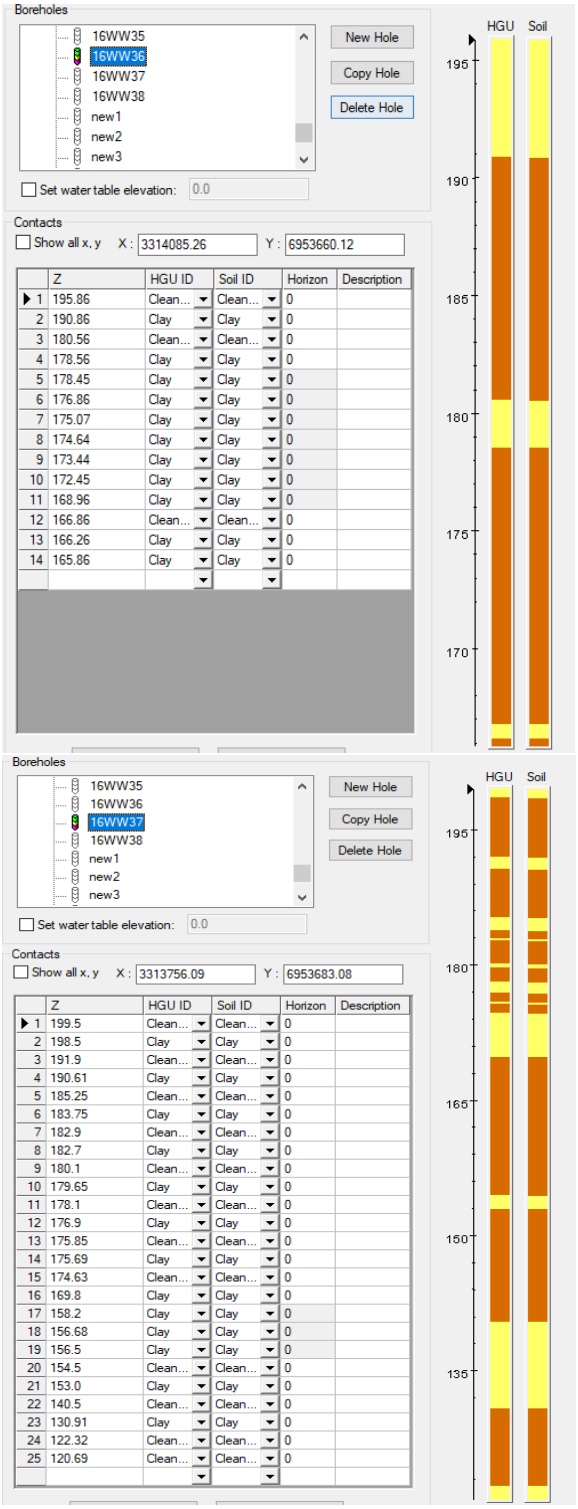

Figure B.37 Data for Boreholes 16WW36 (above) and 16WW37 (below).

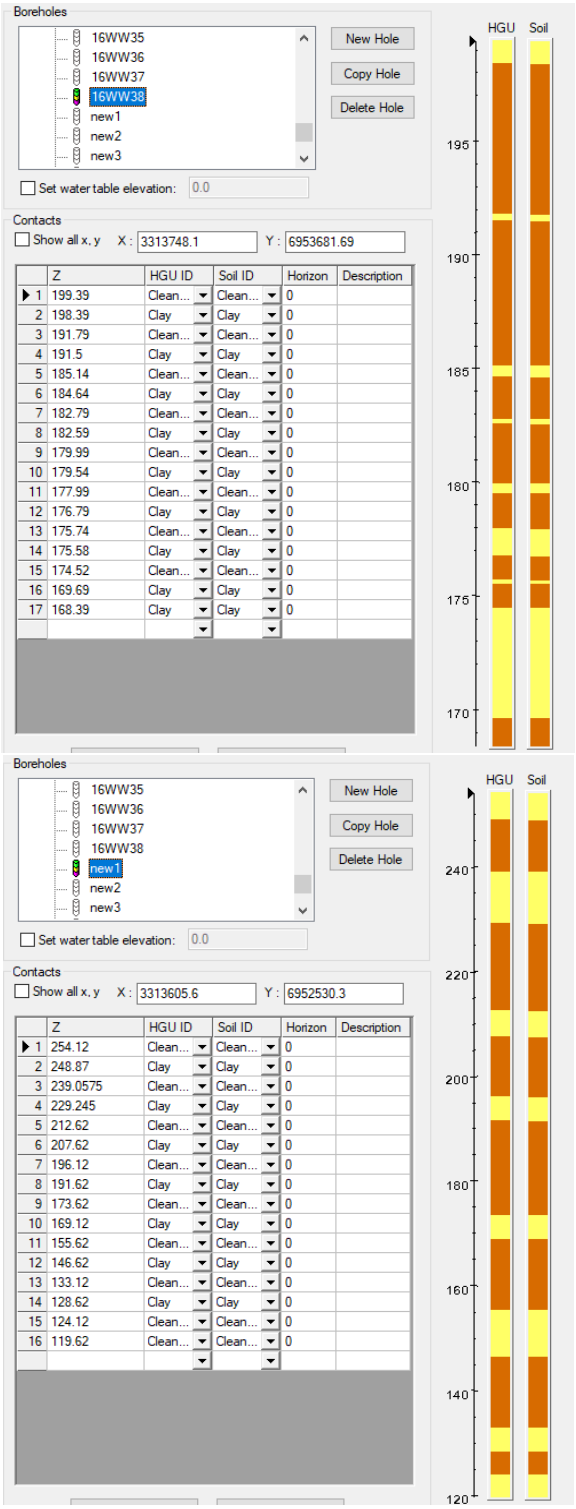

Figure B.38 Data for Boreholes 16WW38 (above) and new1 (below).

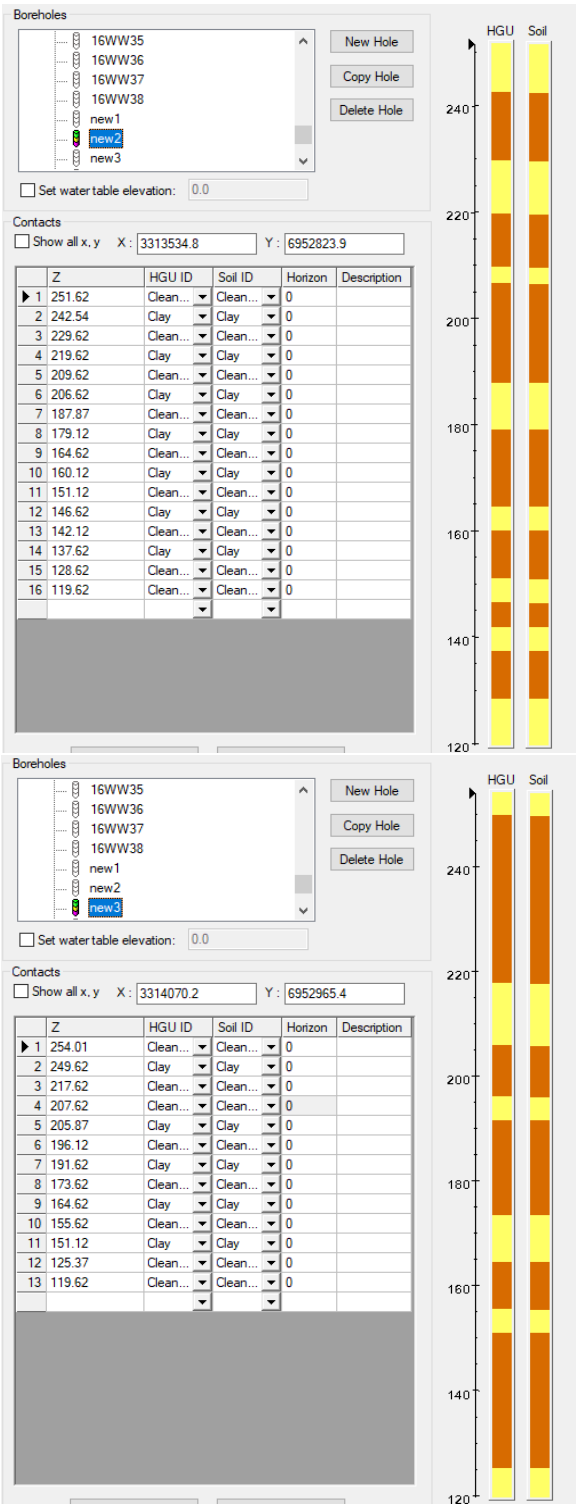

Figure B.39 Data for Boreholes new2 (above) and new3 (below).

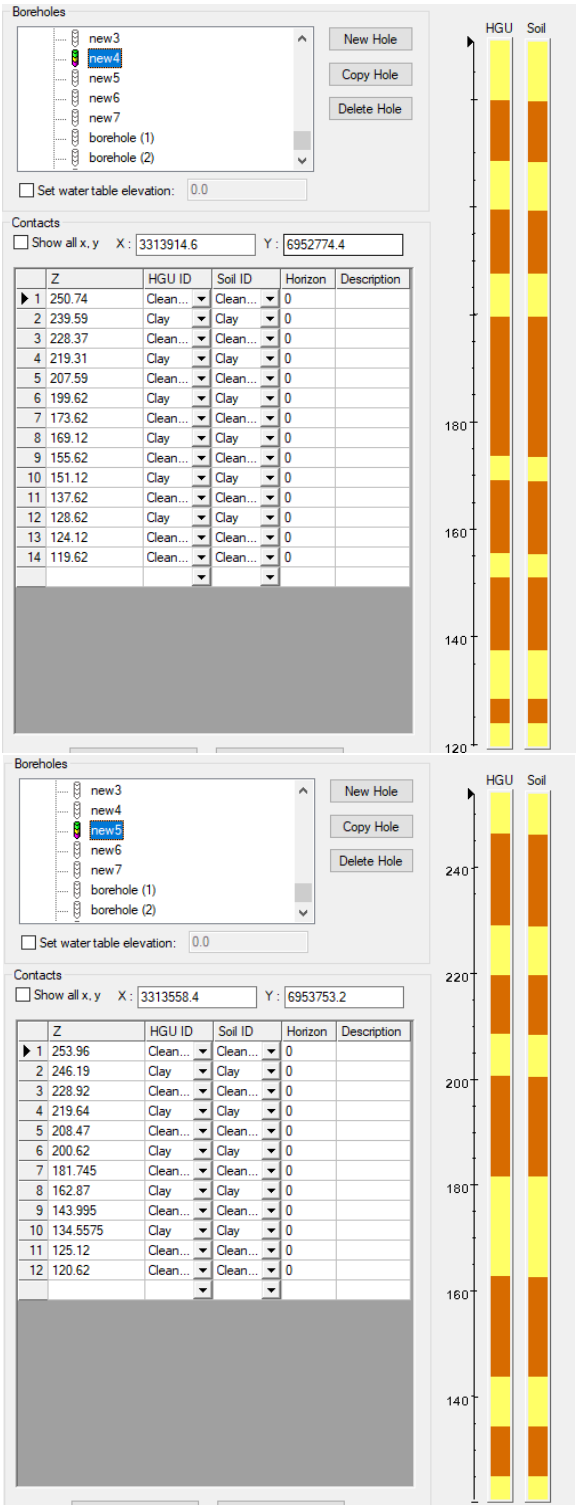

Figure B.40 Data for Boreholes new4 (above) and new5 (below).

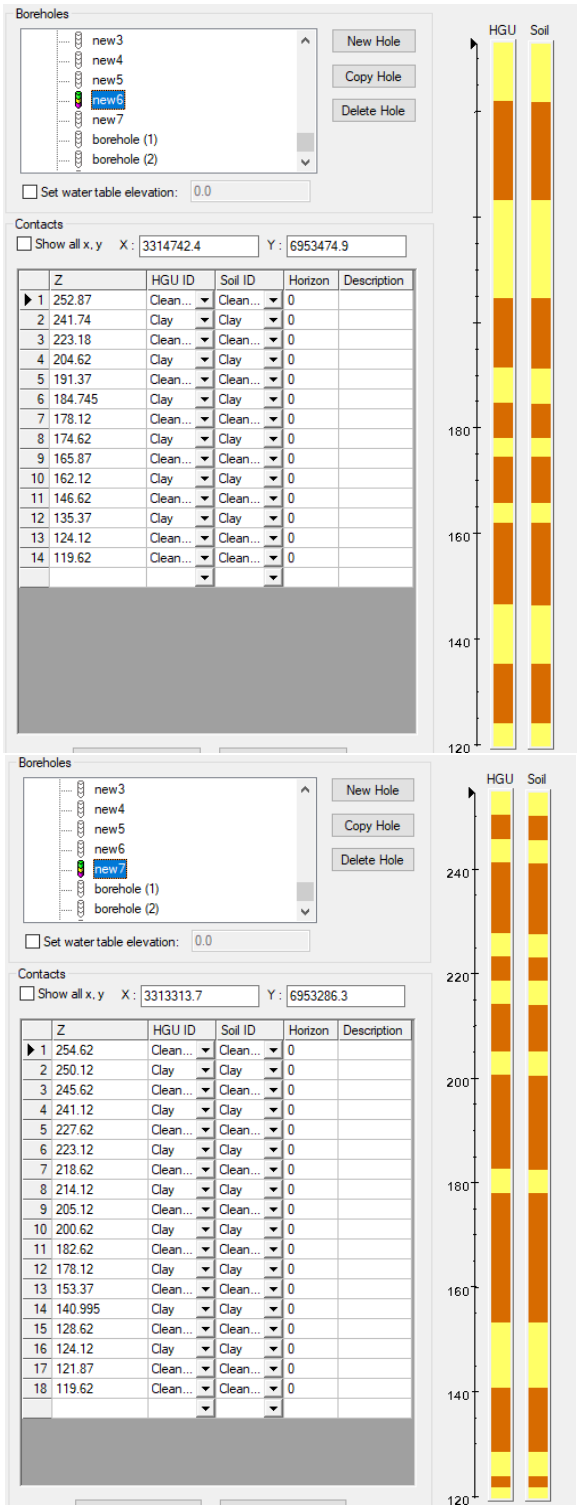

Figure B.41 Data for Boreholes new6 (above) and new7 (below).

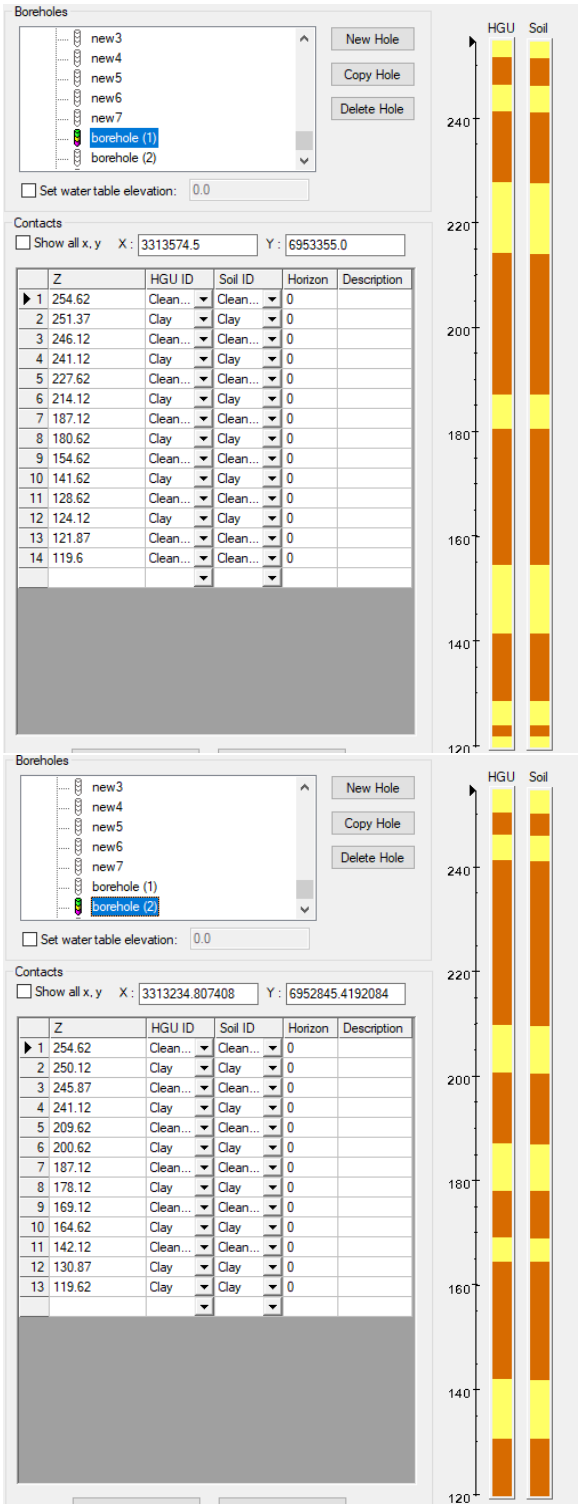

Figure B.42 Data for Boreholes borehole (1) (above) and borehole (2) (below).

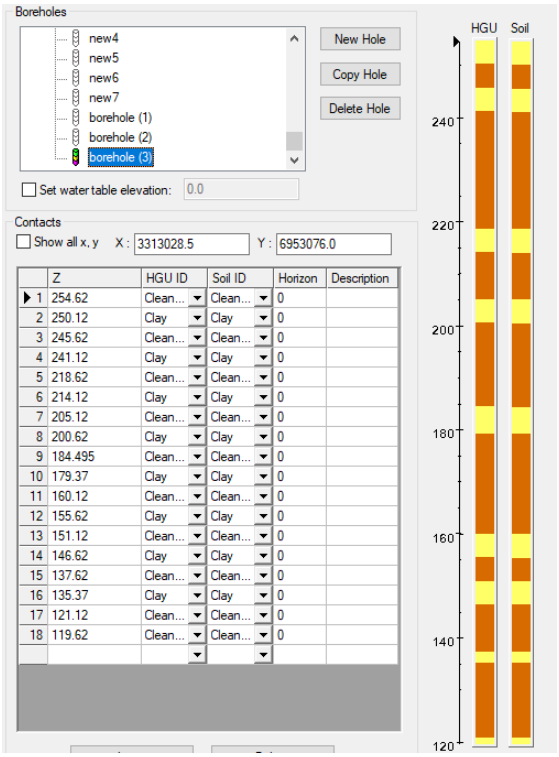

Figure B.43 Data for Boreholes borehole (1) (above) and borehole (2) (below).

REFERENCES

Adidharma, H., Temyanko, V., 2007. 5.1 Interpolation, in: Mathcad for chemical engineers (Ed.), Mathcad for Chemical Engineers. Trafford Publishing, pp. 59-64.

Anderson, D.R., 2010. 14.3 Coefficient of determination, in: Anonymous Statistics for Business and Economics. South-Western Cengage Learning, pp. 500-506.

AQUAVEO, 2017. GMS: GMS User Manual 10.2. 2017.

AQUAVEO, 2016. GMS 10.2 Tutorial. T-PROGS.

Ataie-Ashtiani, B., Hosseini, S.A., 2005. Numerical errors of explicit finite difference approximation for two-dimensional solute transport equation with linear sorption. Environmental Modelling & Software 20, 817-826.

Ball, W.P., Liu, C., Xia, G., Young, D.F., 1997. A diffusion-based interpretation of tetrachloroethene and trichloroethene concentration profiles in a groundwater aquitard. Water Resour. Res. 33, 2741-2757.

Bear, J., Nichols, E., Kulshrestha, A., Ziagos, J., 1994. Effect of Contaminant Diffusion into and out of Low-Permeability Zones. Effect of contaminant diffusion into and out of low-permeability zones UCRL-ID-115626.

Brunner, P., Simmons, C.T., 2012. HydroGeoSphere: A Fully Integrated, Physically Based Hydrological Model. Ground Water 50, 170-176.

Carle, S.F., 1999. T-PROGS: Transition probability geostatistical software. University of California, Davis, CA 84.

Chapman, S.W., Parker, B.L., 2013. Chapter 5.0 Type site Simulations, in: Sale, T., Parker, B.L., Newell, C.J., Devlin, J.F. (Eds.), State-of-the-Science-Review: Management of Contaminants Stored in Low Permeability Zones. SERDP Project ER-1740, pp. 79.

Chapman, S.W., Parker, B.L., 2005. Plume persistence due to aquitard back diffusion following dense nonaqueous phase liquid source removal or isolation. Water Resour. Res. 41.

Chapman, S.W., Parker, B.L., Sale, T.C., Doner, L.A., 2012. Testing high resolution numerical models for analysis of contaminant storage and release from low permeability zones. J. Contam. Hydrol. 136–137, 106-116.

Choudhry, M., Lizzio, M., 2004. 7.1 Cubic splines, in: Anonymous Advanced Fixed Income Analysis. Butterworth-Heinemann, pp. 118-139.

Domenico, P.A., Schwartz, F.W., 1998. Physical and Chemical Hydrogeology. Wiley, New York.

Doner, L.A., 2008. Tools to Resolve Water Quality Benefits of Upgradient Contaminant Flux Reduction. (Unpublished Master's Thesis). Colorado State University, Fort Collins, Colorado.

Falta, R.W., 2008. Methodology for comparing source and plume remediation alternatives. Groundwater 46, 272-285.

Falta, R., Stacy, M., Ahsanuzzaman, A., Wang, M., Earle, R., 2007. REMChlor Remediation Evaluation Model for Chlorinated Solvents User's Manual Version 1.0, Center for Subsurface Modeling Support, Ada, OK .

Falta, R.W., 2005. Dissolved Chemical Discharge from Fractured Clay Aquitards Contaminated by DNAPLS, in: Faybishenko, B., Witherspoon, P.A., Gale, J. (Eds.), Dynamics of Fluids and Transport in Fractured Rock. American Geophysical Union, Washington, D. C., pp. 165-174.

Falta, R.W., Wang, W., 2017. A semi-analytical method for simulating matrix diffusion in numerical transport models. J. Contam. Hydrol. 197, 39-49.

Fanchi, J.R., 2005. Principles of Applied Reservoir Simulation. Gulf Professional Publishing.

Fetter, C.W., 2008. *Contaminant Hydrogeology*, 2, illustrated, reprint ed. Waveland Press, Incorporated.

Foster, S.S., 1975. The Chalk groundwater tritium anomaly—a possible explanation. Journal of Hydrology 25, 159-165.

Freeze, R.A., Cherry, J.A., 1979. Groundwater. Prentice-Hall, Englewood Cliffs, NJ.

Gillham, R.W., Sudicky, E.A., Cherry, J.A., Frind, E.O., 1984. An Advection-Diffusion Concept for Solute Transport in Heterogeneous Unconsolidated Geological Deposits. Water Resour. Res. 20, 369-378.

Golden Software, 2017. Surfer® Powerful contouring, gridding & surface mapping system. Full User's Guide, 106.

Goodall, D.C., Quigley, R., 1977. Pollutant migration from two sanitary landfill sites near Sarnia, Ontario. Canadian Geotechnical Journal 14, 223-236.

Hadley, P.W., Newell, C., 2014. The New Potential for Understanding Groundwater Contaminant Transport. Groundwater 52, 174-186.

Howard, K.W.F., Gelo, K.K., 2002. Chapter 2. Intensive groundwater use in urban areas: the case of megacities., in: Llamas, M.R., Custodio, E. (Eds.), Intensive use of Groundwater: Challenges and Opportunities, Ilustrated ed. CRC Press, pp. 35.

Liu, C., Ball, W.P., 2002. Back diffusion of chlorinated solvent contaminants from a natural aquitard to a remediated aquifer under well-controlled field conditions: Predictions and measurements. Groundwater 40, 175-184.

Mackay, D.M., Cherry, J.A., 1989. Groundwater contamination: Pump-and-treat remediation. Environ. Sci. Technol. 23, 630-636.

McDonald, M.G., Harbaugh, A.W., 1988. A modular three-dimensional finite-difference ground-water flow model, 586.

Millington, R., Quirk, J., 1961. Permeability of porous solids. Transactions of the Faraday Society 57, 1200-1207.

Narasimhan, T., Witherspoon, P., 1976. An integrated finite difference method for analyzing fluid flow in porous media. Water Resour. Res. 12, 57-64.

National Research Council, 1994. Alternatives for Ground Water Cleanup. National Academies Press.

Pankow, J.F., Cherry, J.A., 1996. Dense chlorinated solvents and other DNAPLs in groundwater: History, behavior, and remediation.

Parker, B.L., Chapman, S.W., Guilbeault, M.A., 2008. Plume persistence caused by back diffusion from thin clay layers in a sand aquifer following TCE source-zone hydraulic isolation. Journal of Contaminant Hydrology 102, 86-104.

Pruess, K., Wu, Y., 1988. A semi-analytical method for heat sweep calculations in fractured reservoirs. LBL-24463.

Pruess, K., Wu, Y., 1993. A New Semi-Analytical Method for Numerical Simulation of Fluid and Heat Flow in Fractured Reservoirs. SPE Advanced Technology Series 1, 63-72.

Rasa, E., Chapman, S.W., Bekins, B.A., Fogg, G.E., Scow, K.M., Mackay, D.M., 2011. Role of back diffusion and biodegradation reactions in sustaining an MTBE/TBA plume in alluvial media. Journal of Contaminant Hydrology 126, 235-247.

Rohatgi, A., 2017. WebPlotDigitizer.

Sale, T.C., Zimbron, J.A., Dandy, D.S., 2008. Effects of reduced contaminant loading on downgradient water quality in an idealized two-layer granular porous media. Journal of Contaminant Hydrology 102, 72-85.

Schwartz, F.W., Zhang, H., 2003. 3.1 Porosity of a soil or rock, in: Anonymous Fundamentals of Groundwater, illustrated ed. John Wiley & Sons, New York, pp. 42-44.

Seyedabbasi, M.A., Newell, C.J., Adamson, D.T., Sale, T.C., 2012. Relative contribution of DNAPL dissolution and matrix diffusion to the long-term persistence of chlorinated solvent source zones. J. Contam. Hydrol. 134, 69-81.

Solley, W.B., Pierce, R.R., Perlman, H.A., 1998. Estimated use of Water in the United States in 1995. US Geological Survey.

SRS1 Software LLC, 2015. SRS1 Cubic Spline for Excel. 2017.

Sudicky, E., Frind, E., 1982. Contaminant transport in fractured porous media: Analytical solutions for a system of parallel fractures. Water Resour. Res. 18, 1634-1642.

Sudicky, E.A., Gillham, R.W., Frind, E.O., 1985. Experimental Investigation of Solute Transport in Stratified Porous Media: 1. The Nonreactive Case. Water Resour. Res. 21, 1035-1041.

Tang, D., Frind, E., Sudicky, E.A., 1981. Contaminant transport in fractured porous media: Analytical solution for a single fracture. Water Resour. Res. 17, 555-564.

Travis, C., Doty, C., 1990. ES&T Views: Can contaminated aquifers at superfund sites be remediated? Environ. Sci. Technol. 24, 1464-1466.

Trefry, M.G., Muffels, C., 2007. FEFLOW: A Finite-Element Ground Water Flow and Transport Modeling Tool. Ground Water 45, 525-528.

VanLoon, G.W., 2000. Environmental Chemistry: A Global Perspective. Oxford University Press, Oxford; New York.

Vinsome, P., Westerveld, J., 1980. A simple method for predicting cap and base rock heat losses in'thermal reservoir simulators. J Can Pet Technol 19.

Wang, W., 2014. Comparison of Analytical, Numerical and Semi-Analytical Methods for Modeling Matrix Diffusion Effects in Aquitards.

Yang, M., Annable, M.D., Jawitz, J.W., 2015. Back Diffusion from Thin Low Permeability Zones. Environ. Sci. Technol. 49, 415-422.

Yang, M., Annable, M.D., Jawitz, J.W., 2014. Light reflection visualization to determine solute diffusion into clays. J. Contam. Hydrol. 161, 1-9.

Zheng, C., Bennett, G.D., 2002. Applied Contaminant Transport Modeling. Wiley-Interscience New York.

Zheng, C., Wang, P.P., 1999. MT3DMS: A Modular Three-Dimensional Multispecies Transport Model for Simulation of Advection, Dispersion, and Chemical Reactions of Contaminants in Groundwater Systems; Documentation and User's Guide. SERDP-99-1.